

Lecture Notes in Physics

Founding Editors: W. Beiglböck, J. Ehlers, K. Hepp, H. Weidenmüller

Editorial Board

R. Beig, Vienna, Austria
W. Beiglböck, Heidelberg, Germany
W. Domcke, Garching, Germany
B.-G. Englert, Singapore
U. Frisch, Nice, France
F. Guinea, Madrid, Spain
P. Hänggi, Augsburg, Germany
W. Hillebrandt, Garching, Germany
R. L. Jaffe, Cambridge, MA, USA
W. Janke, Leipzig, Germany
H. v. Löhneysen, Karlsruhe, Germany
M. Mangano, Geneva, Switzerland
J.-M. Raimond, Paris, France
D. Sornette, Zurich, Switzerland
S. Theisen, Potsdam, Germany
D. Vollhardt, Augsburg, Germany
W. Weise, Garching, Germany
J. Zittartz, Köln, Germany

The Lecture Notes in Physics

The series Lecture Notes in Physics (LNP), founded in 1969, reports new developments in physics research and teaching – quickly and informally, but with a high quality and the explicit aim to summarize and communicate current knowledge in an accessible way. Books published in this series are conceived as bridging material between advanced graduate textbooks and the forefront of research and to serve three purposes:

- to be a compact and modern up-to-date source of reference on a well-defined topic
- to serve as an accessible introduction to the field to postgraduate students and nonspecialist researchers from related areas
- to be a source of advanced teaching material for specialized seminars, courses and schools

Both monographs and multi-author volumes will be considered for publication. Edited volumes should, however, consist of a very limited number of contributions only. Proceedings will not be considered for LNP.

Volumes published in LNP are disseminated both in print and in electronic formats, the electronic archive being available at springerlink.com. The series content is indexed, abstracted and referenced by many abstracting and information services, bibliographic networks, subscription agencies, library networks, and consortia.

Proposals should be sent to a member of the Editorial Board, or directly to the managing editor at Springer:

Christian Caron
Springer Heidelberg
Physics Editorial Department I
Tiergartenstrasse 17
69121 Heidelberg / Germany
christian.caron@springer.com

J. Strzałko
J. Grabski
P. Perlikowski
A. Stefański
T. Kapitaniak

Dynamics of Gambling: Origins of Randomness in Mechanical Systems



Jarosław Strzałko
Technical University of Lodz
Division of Dynamics
Stefanowskiego 1/15
90-924 Lodz
Poland
jstrzalk@poczta.onet.pl

Juliusz Grabski
Technical University of Lodz
Division of Dynamics
Stefanowskiego 1/15
90-924 Lodz
Poland
julgrabs@p.lodz.pl

Przemysław Perlikowski
Technical University of Lodz
Division of Dynamics
Stefanowskiego 1/15
90-924 Lodz
Poland
przemyslaw.perlikowski@p.lodz.pl

Andrzej Stefański
Technical University of Lodz
Division of Dynamics
Stefanowskiego 1/15
90-924 Lodz
Poland
steve@p.lodz.pl

Tomasz Kapitaniak
Technical University of Lodz
Division of Dynamics
Stefanowskiego 1/15
90-924 Lodz
Poland
tomaszka@p.lodz.pl

Strzałko J., et al., *Dynamics of Gambling: Origins of Randomness in Mechanical Systems*, Lect. Notes Phys. 792 (Springer, Berlin Heidelberg 2009),
DOI 10.1007/978-3-642-03960-7

Lecture Notes in Physics ISSN 0075-8450 e-ISSN 1616-6361
ISBN 978-3-642-03959-1 e-ISBN 978-3-642-03960-7
DOI 10.1007/978-3-642-03960-7
Springer Heidelberg Dordrecht London New York

Library of Congress Control Number: 2009938265

© Springer-Verlag Berlin Heidelberg 2009

This work is subject to copyright. All rights are reserved, whether the whole or part of the material is concerned, specifically the rights of translation, reprinting, reuse of illustrations, recitation, broadcasting, reproduction on microfilm or in any other way, and storage in data banks. Duplication of this publication or parts thereof is permitted only under the provisions of the German Copyright Law of September 9, 1965, in its current version, and permission for use must always be obtained from Springer. Violations are liable to prosecution under the German Copyright Law.

The use of general descriptive names, registered names, trademarks, etc. in this publication does not imply, even in the absence of a specific statement, that such names are exempt from the relevant protective laws and regulations and therefore free for general use.

Cover design: Integra Software Services Pvt. Ltd., Pondicherry

Printed on acid-free paper

Springer is part of Springer Science+Business Media (www.springer.com)

to
Jagoda, Aldona, Renata, Marzena, Gosia
– our wives

Preface

Our everyday life is influenced by many unexpected (difficult to predict) events usually referred as a chance. Probably, we all are as we are due to the accumulation point of a multitude of chance events. Gambling games that have been known to human beings nearly from the beginning of our civilization are based on chance events. These chance events have created the dream that everybody can easily become rich. This pursuit made gambling so popular.

This book is devoted to the dynamics of the mechanical randomizers and we try to solve the problem why mechanical device (roulette) or a rigid body (a coin or a die) operating in the way described by the laws of classical mechanics can behave in such a way and produce a pseudorandom outcome.

During mathematical lessons in primary school we are taught that the outcome of the coin tossing experiment is random and that the probability that the tossed coin lands heads (tails) up is equal to $1/2$. Approximately, at the same time during physics lessons we are told that the motion of the rigid body (coin is an example of such a body) is fully deterministic. Typically, students are not given the answer to the question *Why this duality in the interpretation of the simple mechanical experiment is possible?*

Trying to answer this question we describe the dynamics of the gambling games based on the coin toss, the throw of the die, and the roulette run. The dynamics of this type of gambling can be described in terms of the Newtonian mechanics, so one can expect that the outcome can be predicted. We give evidence that from the point of view of dynamical systems this dynamics is predictable. However, due to high (but finite) sensitivity to initial conditions the very precise devices are necessary to predict the outcome, so practically this outcome is pseudorandom. Our studies do not give the general answer to the famous Albert Einstein's question *Does the God play dice?* which is connected with all the events in the whole universe but give evidence to the negative answer to the simpler question *Does the God play dice in the casino?* We give evidence that the pseudorandomness in mechanical systems can be fully understood in terms of nonlinear dynamics as temporal sensitivity to the initial conditions generated by nonsmooth properties of the randomizers.

This book is mainly for mathematicians and physicists interested in nonlinear phenomena. It can also be read by all interested in such chance problems as only basic classical mechanics is necessary to understand most of the text. It is also

addressed to gamblers but our results cannot be directly used to make fortune in the casino. However our results can help to understand that the betting systems that claim to be winning (particularly popular for roulette) are nothing more than charlatanism.

The book is organized as follows. Typical mechanical randomizers like a coin, a die, and a roulette are described in Chap. 2. In Chap. 3 we derive the equations of motion which allow to describe the dynamics of the gambling based on the coin toss, the throw of the die, and the roulette run. Chapter 4 explains why according to the theory of the dynamical systems this gambling is predictable but practically unpredictable. Finally, in Chap. 5 we discuss the origin of randomness in mechanical systems.

We would like to acknowledge the helpful discussions with Eric Mosekilde, Giusseppe Rega, Ko-Choong Woo, Marian Wiercigroch, and Serhiy Yanchuk. We are thankful to Franciszek Wójcik, Piotr Borkowski, and Piotr Dmuchowski of the Department of Electrical Apparatus, Technical University of Łódź, for allowing us to use their high speed camera.

Łódź

*Jarosław Strzałko
Juliusz Grabski
Przemysław Perlikowski
Andrzej Stefański
Tomasz Kapitaniak*

Contents

1	Introduction	1
1.1	Gambling and Gaming	1
1.2	A Short History	2
1.3	Coin	6
1.4	Dice	7
1.5	Roulette	11
1.6	Other Mechanical Randomizers	14
1.7	Dynamics and Predictability	17
1.7.1	Sensitive Dependence on Initial Conditions	18
1.7.2	Fractal Basin Boundaries	19
References		21
2	General Motion of a Rigid Body	23
2.1	Basic Equations of Motion of a Rigid Body	23
2.1.1	Dynamics Equations in General Form	23
2.1.2	Newton–Euler Equations	25
2.2	Precession of a Body	26
2.2.1	Precession of Symmetric Top	27
2.2.2	Torque-Free Motion of Spherical Top	29
2.3	Orientation of a Rigid Body	30
2.3.1	Euler Angles and Other Conventions	31
2.3.2	Euler’s Parameters	34
2.4	Air Resistance Forces and Moments	35
2.5	Modeling of Bodies Impact	37
References		39
3	Equations of the Randomizer’s Dynamics	41
3.1	Equations of the Coin Toss	41
3.1.1	Free Fall of a Coin	41
3.1.2	Coin Motion in the Air	46
3.1.3	Coin Bounces on the Floor	64

3.2	Equations of the Die Throw	67
3.2.1	Free Fall of a Die	67
3.2.2	Die Bounces on the Table	69
3.3	Equations of the Roulette Run	71
3.3.1	Spinning Wheel Motion Analysis	73
3.3.2	The Ball Motion on Fixed Wheel Surfaces	74
3.3.3	Collision of the Ball with a Deflector ($C_{(Dk)}$)	80
3.3.4	Free Fall of the Ball (F)	83
3.3.5	Landing of the Ball	84
3.3.6	Collision of the Ball with Rotating Conical Surface ($C_{(CC)}$) ..	88
3.3.7	Rolling of the Ball on the Spinning Wheel ($R_{(RC)}$)	91
3.3.8	The Ball Landing in the Pocket ($L_{(Pk)}$)	93
	References	95
4	Dynamics and Predictability	97
4.1	Experimental Observations	97
4.2	Simplified Models	101
4.2.1	Keller's Model	101
4.2.2	Precession of a Coin	105
4.2.3	Plane Motion Model of a Cubic Die	108
4.2.4	Nagler–Richter's Model of a Die	110
4.3	Coin Tossing Simulation	112
4.4	Simulations of the Die Throw	117
4.4.1	Free Fall Probability Distribution	118
4.4.2	Simulation of Dice Bouncing on the Table	126
4.5	Simulation of the Roulette Run	130
4.6	On the Predictability of Mechanical Randomizer	136
	References	141
5	Nature of Randomness in Mechanical Systems	143
5.1	Randomness and Determinism	143
5.2	Why the Tossed Coin or Die Can Approximate the Random Process? ..	145
5.3	Why the Impacts Induce Pseudorandomness?	148
	References	149
Index	151

Chapter 1

Introduction

Abstract The definitions of gambling and gaming are given. We discuss the main differences between these terms. A brief history of gambling is presented. Physical models of the considered mechanical randomizers, namely the coin, the dice, and the roulette are introduced. We discuss under which conditions they can be fair.

1.1 Gambling and Gaming

Gambling is the wagering of money or something of material value on an event with an uncertain outcome with the primary intent of winning additional money and/or material goods [1]. Usually, the outcome of the wager is known within a short period.

The term gaming [2] is connected with gambling and this typically refers to the instances in which the gambling activity has been permitted by law. Gaming companies offer legal gambling activities to the public [3]. However this distinction is not always universally used in the English-speaking world. For example, in the United Kingdom, the regulator of gambling activities is called the Gambling Commission (not the Gaming Commission) [4].

The Catholic and Jewish traditions set aside days for gambling, although religious authorities generally disapprove of gambling to some extent. Gambling can have adverse social consequences. Tijms [5] suggested that the creation of the first pair of dice had a similar impact on the mobility of goods in the preindustrial economy as the invention of a wheel. For these social and religious reasons, most legal jurisdictions limit gambling. Some Islamic nations prohibit gambling; most other countries regulate it [6].

Nowadays in most countries the jurisdictions, both local and national, either ban or control gambling by limited licensing. Such regulation generally leads to the creation of illegal gambling casinos and the development of gambling tourism. In the official casinos gambling can be performed through materials that are given a value but is not real money. The involvement of governments, through regulation and taxation, has led to a close connection between many governments and gaming organizations, where legal gambling provides significant government revenue, such as in Monaco or Macau.

Gambling in the United States currently is legal. However, it is due to each state to regulate or prohibit this practice. In Nevada gambling has been legal since 1931 giving the state its economic development since then. Las Vegas is the world capital of gambling. Gambling became legal in Atlantic City and New Jersey in 1976 while Tunica, Mississippi, had to wait till 1990. Thanks to U.S. Supreme Court decision in 1987 many native American tribes have built their casinos on the tribal lands participating in the benefits. As the tribes are sovereign nations the state laws restricting gambling do not refer to them. In such cases they have to obey federal law. Gambling is legalized in almost all states in the form of a state-run lottery.

There is general legislation requiring that the odds in gaming devices are statistically random, to prevent the manufacturers from making some high-payoff results impossible. Since these high payoffs have very low probability, a house bias can quite easily be missed unless checking the odds carefully [7].

Finally, it should be mentioned that gambling like any other behavior which involves variation in brain chemistry can become psychologically addictive and harmful behavior with some people [8]. Reinforcement schedules may also make gamblers persist in gambling even after repeated losses. The Russian writer Fiodor Dostoevsky in his novel *The Gambler* described the psychological implications of gambling and how gambling can affect gamblers. On the other hand gambling interest of Gerollamo Cardano created foundations of the modern probability theory.

In this book we consider such examples of gambling as a toss of a coin, a throw of a die, and a roulette run. In all these cases gambling is connected with mechanical devices. We focus on the description of gambling in terms of the classical mechanics and theory of dynamical systems.

1.2 A Short History

Gambling is perhaps as old as our civilization. Dice have been used for gambling for at least a few millenia. The earliest archaeological evidences are from India, where the examples of dice have been found in the neighborhood of Harappan and are dated back to the third millennium BC. Dice are also mentioned in the great Hindu epic, the Mahabharata, where Yudhisthira plays a game of dice against the Kauravas for the northern kingdom of Hastinapura. The use of dice is believed to have spread later to Persia and through the Middle East to Greece and Roman Europe.

In Egypt a board game called astragulus have been invented around 3500 BC. In this game players tossed four-sided sheep bones. It remained in use right up to the Middle Ages and can be considered as a precursor to the modern-day dice games.

There are several biblical references to “casting lots” which indicate that gambling was very popular, particularly at the times of King David. The most known reference is perhaps the following case of Jonah (Jonah 1:1-17) [9].

But Jonah ran away from the Lord and headed for Tarshish. He went down to Joppa, where he found a ship bound for that port. After paying the fare, he went aboard and sailed for Tarshish to flee from the Lord. Then the Lord sent a great wind on the sea, and such a violent storm arose that the ship threatened to break up. All the sailors were afraid and each

cried out to his own god. And they threw the cargo into the sea to lighten the ship. Then the sailors said to each other, “come, let us cast lots to find out who is responsible for this calamity.” They cast lots and the lot fell on Jonah. “pick me up and throw me into the sea,” he replied, “and it will become calm. I know it is my fault that this great storm has come upon you.”.... Then they took Jonah and threw him overboard, and the raging sea grew calm. But the Lord provided a great fish to swallow Jonah, and Jonah was inside the fish three days and three nights.

Gambling with three or sometimes two dice was a very popular form of amusement for Greek upper class and was an almost invariable accompaniment to symposia. At the luxurious days of the Roman Empire, the Romans were passionate gamblers, and dicing was a favorite form of amusement, though it was forbidden, except during the holidays of Saturnalia. A pair of bone made cubic dice from the first century AD, which have been found during the excavations in Pompeii is shown in Fig. 1.1 (left). The Romans also used an icosahedral dice. The image of such a die from the second century AD is shown in Fig. 1.1 (right). Comparing Roman dice with contemporary set shown in Fig. 1.2, one can notice that dice design is basically unchanged to our days.

During the Middle Ages, dicing became the favorite pastime of the knights, and both dicing schools and guilds of dicers existed. It is possible to find hundreds of references to the dice gambling in the chronicles from this time. For example, the sons of the English King William the Conqueror, William (future William II Rufus) and Henry (future Henry I) were playing dice while plotting against their third brother Robert (future Duke of Normandy) as it is given in the chronicle of Orderic



Fig. 1.1 The Roman dice: a pair of cubic dice (*left*), icosahedral die (*right*)



Fig. 1.2 A set of contemporary dice

Vitalis [10]. In France both knights and ladies were especially given to dicing. This persisted through repeated legislation, including the edicts of St. Louis in 1254 and 1256. At the end of feudalism the German mercenaries called “landsknechts” were considered as the most notorious dicing gamblers of their time.

The invention of roulette in modern version is ascribed to Blaise Pascal. Earlier the Greeks spun shields on sword points, and the Roman emperor Augustus had rotating chariot wheel installed in the gaming room of his palace [11]. Although these games employed a wheel and a stationary pointer, the modern version roulette device utilizes a more complicated mechanism with a rotor and a ball revolving in counterdistinction to each other.

The story about Pascal inventing roulette is connected with his search for the formula to a curve known as the cycloid which took place in the Port-Royal monastery in the spring of 1657. Pascal defined this curve as the line described by a nail on the rim of a rolling wheel as it rises from the ground and falls again to meet it. In his famous treatise *Histoire de la roulette* he stated that as this “considers the rolling of wheels” it should be called “roulette.”

It is not known whether Pascal experimented with the rolling wheels but his treatise on roulette had a significant impact on modern mathematics. Ten years after Pascal’s death Gottfried Leibnitz generalized his equations and created the integral calculus.

The first form of roulette was devised in 18th century France. The roulette wheel is believed to be a fusion of the English wheel games Roly-Poly, Ace of Hearts, and E.O., the Italian board games of Hoca and Biribi, and “Roulette” from an already existing French board game of that name.

The game has been played in its current form since as early as 1765 in Paris. A police lieutenant Gabriel de Sartine referred to roulette as a gambling device immune to cheating which was introduced into casinos of Paris. The earliest description of the roulette game in its current form is found in a French novel “*La Roulette, ou le Jour*” by Jaques Lablee, which describes a roulette wheel in the Palais Royal in Paris in 1796. The description included the house pockets, “There are exactly two slots reserved for the bank, whence it derives its sole mathematical advantage.” It then goes on to describe the layout with, “...two betting spaces containing the bank’s two numbers, zero and double zero.” The book was published in 1801. An even earlier reference to a game of this name was published in regulations for New France (Canada) in 1758, which banned the games of “dice, hoca, faro, and roulette” [11, 12].

During the French Revolution of 1789 royalist emigrants brought roulette wheels to Bath and other British resorts. By the early 19th century the game spread all over Europe, particularly to such spa as Wiesbaden, Bad Homburg, Baden-Baden, Saxon-les-Bains, and Spa itself. In 1843, in the German spa casino town of Homburg, fellow Frenchmen Franois and Louis Blanc introduced the single “0” style roulette wheel in order to compete against other casinos offering the traditional wheel with single and double zero house pockets.

The popularity of the German casinos which result in the impoverishing of French emigrants and minor German nobility forced the Prussian government to

close them in 1872. After it Louis Blanc simply packed up his gambling equipment and transported it from Bad Homburg to the principality of Monaco. At that time Monte Carlo, the capital of this independent nation, was described as “two or three streets upon precipitous rocks, eight hundred wretches dying of hunger, a tumble-down castle, and a battalion of French troops” [11]. It was here that the single zero roulette wheel became the premier game, and over the years was exported around the world, except in the United States where the double zero wheel had remained dominant. Some call roulette the “King of Casino Games”, probably because it was associated with the glamour of the casinos in Monte Carlo. A legend tells that François Blanc supposedly bargained with the devil to obtain the secrets of roulette. The legend is based on the fact that the sum of all the numbers on the roulette wheel (from 1 to 36) is 666, which is the “Number of the Beast.” Roulette became the main attraction of Monte Carlo, which ruled supreme as the world center of gambling up until the rise of Las Vegas after the World War II.

Roulette first reached the United States, like many goods of French origin, via New Orleans. It was played extensively on the paddle-wheel steamers that plied the Mississippi. It was here, because of rampant cheating by both operators and gamblers, the wheel eventually was placed on top of the table to prevent devices being hidden in the table or wheel, and the betting layout was simplified. This eventually evolved into the American style roulette game as different from the traditional French game. The American game developed in the gambling dens across the new territories where makeshift games had been set up, whereas the French game evolved with style and leisure in Monte Carlo. However, it is the American style layout with its simplified betting and fast cash action, using either a single or double zero wheel, that now dominates in most casinos around the world.

During the first part of the 20th century, the only important casino towns of note were Monte Carlo with the traditional single zero French wheel and Las Vegas with the American double zero wheel. In the 1970s, casinos began to flourish around the world. By 2008 there were several hundred casinos worldwide offering roulette games. The double zero wheel is found in the United States, South America, and the Caribbean, while the single zero wheel is predominant elsewhere [12].

Gambling games always attract the attention of the scientists. Gerollamo Cardano (1501–1576), Galileo Galilei (1564–1642), and Christiaan Huygens (1629–1695) wrote the books on the dice games. Cardano, who was an ardent gambler, wrote a handbook for gamblers entitled *Liber de Ludo Aleae* (*The Book of Games of Chance*). In this work he introduced the concept of the set of outcomes of an experiment and in the case in which all outcomes are equally probable, he defined the probability of any one favorable event as the ratio of the number of possible outcomes. This result marked an enormous leap forward in the development of the probability theory. Using the results of Cardano, Galilei was able to explain to the Grand Duke of Tuscany, his benefactor, why it is that when tossing three dice, the chance of the sum being 10 is greater than the chance of the sum being 9. The appropriate probabilities are, respectively, $27/216$ and $25/216$. Blaise Pascal (1623–1662) and Pierre-Simon de Fermat (1601–1665) exchanged letters discussing the mathematical analysis of problems related to the dice games

contributing to the further development of the probability theory. Huygens in his book *Van Rekening in Spelen van Gelunck* (*On Reasoning in Games of Chance*) published in 1660 introduced the concept of expected value, which plays a key role in the probability theory. He also unified various problems that had been solved earlier by Pascal and Fermat. In the 20th century this problem attracted the attention of Henri Poincaré (1854–1912) and Eberhard Hopf (1902–1983), who are nowadays recognized as the pioneers of the nonlinear dynamics.

1.3 Coin

Coin tossing is a simple and fair way of deciding between two arbitrary options. It is assumed that it provides even odds to both sides involved, requiring little effort and preventing the dispute from escalating into a struggle. It is used widely in sport and to decide about arbitrary factors such as which side of the field a team will start the game from, or which side will attack or defend initially. In team sports (soccer, American football, ice hockey, etc.) it is often the team captain who makes the call, while the referee usually tosses a coin. A spectacular case took place in 1968 European Football (Soccer) Championship. The semi-final game between Italy and the Soviet Union finished 0–0 after an extra-time. At that time penalty shots-out were not introduced and the decision was reached to toss a coin to see who gets to the final, rather than play a replay. Italy won and went on to become the European champion.

In some jurisdictions, a coin is tossed to decide between two candidates who poll an equal number of votes in an election or two companies tendering the equal prices for a project (such a situation occurred in Toronto in 2003). In more casual settings, a coin tossing is used simply to resolve the arguments between friends or family members.

It is commonly taken for granted that the toss of a coin is *random*. This statement is fundamental in the probability theory [13–15] and usually two types of coins are mathematically distinguished. The coin is *fair* if the probability of heads and tails is equal, i.e., $\text{Prob}(\text{heads}) = \text{Prob}(\text{tails}) = 1/2$. The coin has the known *bias* $\theta \in (0, 1]$ if $\text{Prob}(\text{heads}) = 1/2(1 + \theta)$. Tossing the coin is frequently used to describe the problems concerning random walks on scenery [16–18]. The random walk is an example of a stochastic process going on in time, namely the motion of a particle which is randomly hoping backward or forward [19]. Backward or forward steps can be determined by tossing a coin.

One of the random walk problem is a variation of gambler ruin game [20–24] in which a rich player gambles with a set amount of money while the poor one starts out with zero capital and is allowed to toss a coin in order to try to win the money. If the coin is heads, the poor player wins a dollar but if it is tails, the player loses a dollar. The poor player is always allowed to win the first toss and is allowed to toss n times, even when the amount of money lost reaches zero. The studies of Cooper [25, 26] show that the dynamics in this process is chaotic as the result of the fluctuations in the variance of the amount of money [25] and can model the on-off intermittency. Coin tossing can also be considered as a billiard problem [27].

The physical definition of the fair coin is completely lacking. One cannot expect the detailed characteristic to be general for every coin as many sizes and shapes of real coins exist. We consider that the coin is a rigid body with the round shape and assume that the physical equivalence of the fair coin is an *ideal coin* with uniform mass distribution and the equivalence of the coin with bias is an *imperfect coin* with nonuniform mass distribution. In both cases the coin has *no intrinsic randomness* and what is relevant is the relation of the initial position (initial conditions) of the coin to the precision of the coin tosser.

A coin can be modeled as a rigid body, namely a cylinder with a radius r and height h as shown in Fig. 1.3. In the case of an ideal coin the geometrical center of the cylinder B and the center of the mass C coincide (i.e., $\xi_c = 0, \eta_c = 0, \zeta_c = 0$). For the imperfect coin the center of the mass is located at the distance $\xi_c \neq 0, \eta_c \neq 0, \zeta_c \neq 0$ from the geometrical center B .

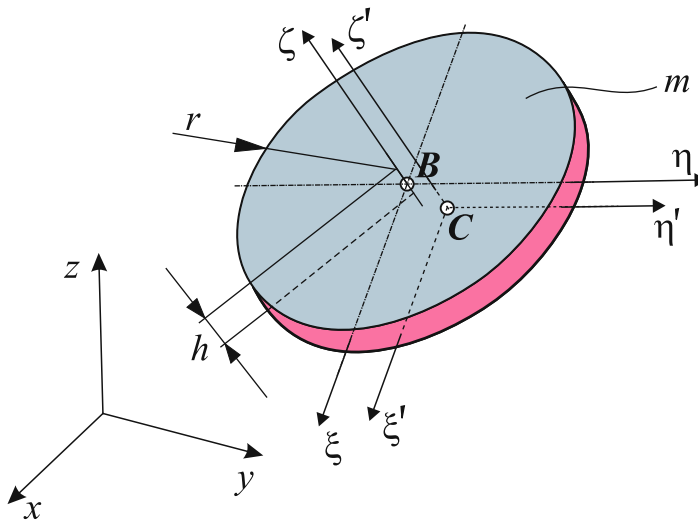


Fig. 1.3 Three-dimensional model of the imperfect coin

1.4 Dice

A throw of a fair die is commonly considered as a paradigm for chance. The die is usually a cube of a homogeneous material. The symmetry suggests that such a die has the same chance of landing on each of its six faces after a vigorous roll so it is considered to be fair. Generally, a die with a shape of convex polyhedron is fair by symmetry if and only if it is symmetric with respect to all its faces [28]. The polyhedra with this property are called the isohedra. Every isohedron has an even number of faces [29]. The commonly known examples of isohedra are tetrahedron, hexahedron (cube), octahedron, dodecahedron, and icosahedron which are also used as the shapes for dice. Typical isohedra are shown in Fig. 1.4.

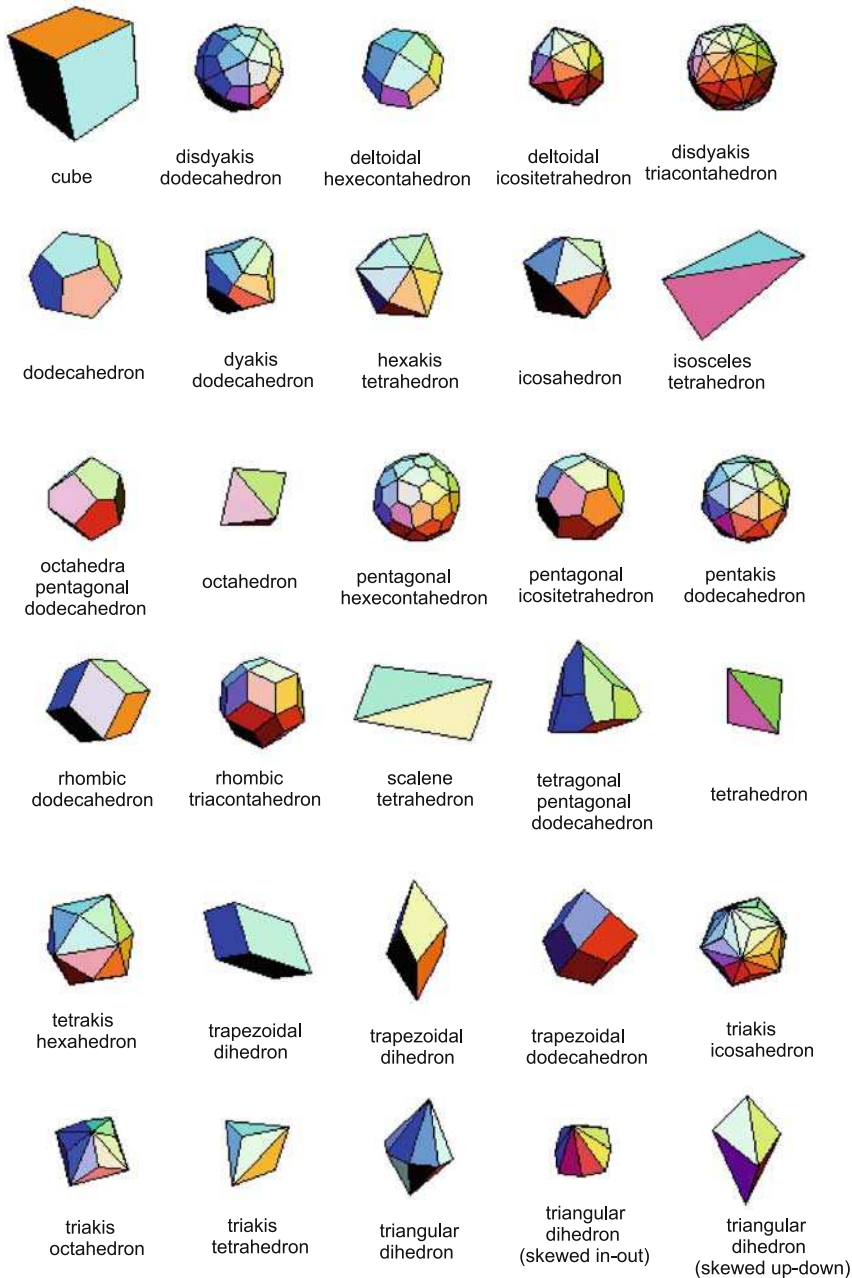


Fig. 1.4 Dice of isohedral shapes

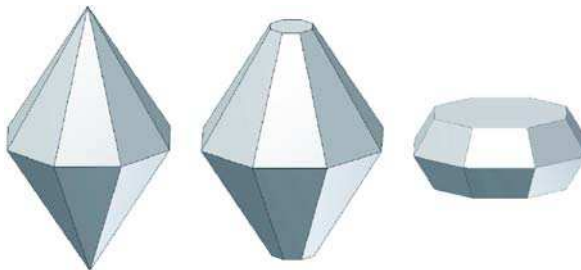


Fig. 1.5 Construction of the die which is fair by continuity

Diaconis and Keller [28] show that there are not symmetric polyhedra which are fair by continuity. As an example they consider the dual of n -prism which is a di-pyramid with $2n$ identical triangular faces from which two tips have been cut with two planes parallel to the base and equidistant from it as shown in Fig. 1.5.

If the cuts are close to the tips (Fig. 1.5b), the solid has a very small probability of landing on one of two tiny new faces. However, if the cuts are near the base (Fig 1.5c), the probability of landing on them is high. Therefore, by continuity there must be the cuts for which new and old faces have equal probability. In [28] it is suggested that the locations of these cuts depend upon the mechanical properties of the die and the table and can be found either experimentally or by the analysis based on the classical mechanics.

However, these definitions are not considering the dynamics of the die motion during the throw.

The faces of the dice are labeled in the well-defined way. Typical dice, their net images with face numbers, face colors, and vertex symbols are shown in Figs. 1.6, 1.7, 1.8, 1.9, and 1.10. In Chap. 4 we use the colors to distinguish die faces in our simulation.

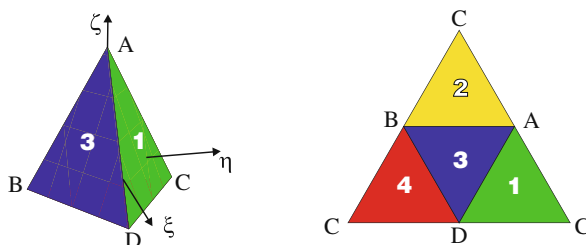


Fig. 1.6 Net image of the tetrahedron die with vertex symbols, face numbers, and face colors

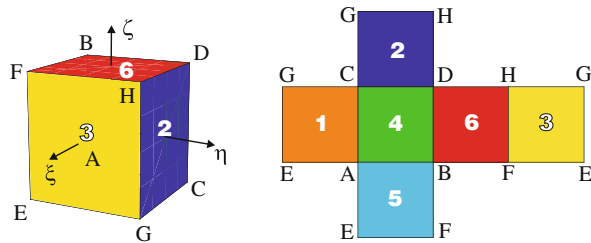


Fig. 1.7 Net image of the hexahedron (cube) die with vertex symbols, face numbers, and face colors

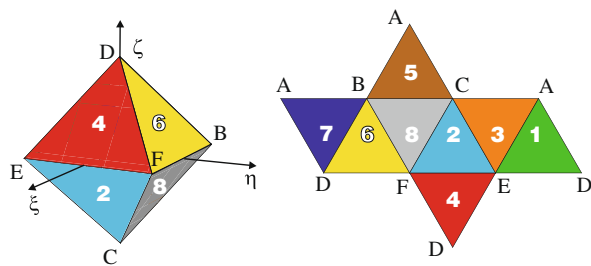


Fig. 1.8 Net image of the octahedron die with vertex symbols, face numbers, and face colors

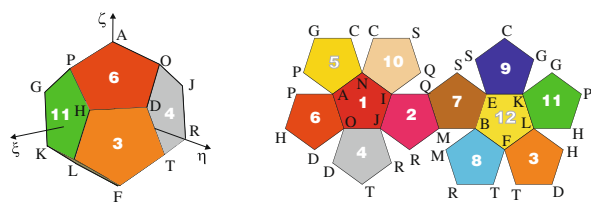


Fig. 1.9 Net image of the dodecahedron die with vertex symbols, face numbers, and face colors

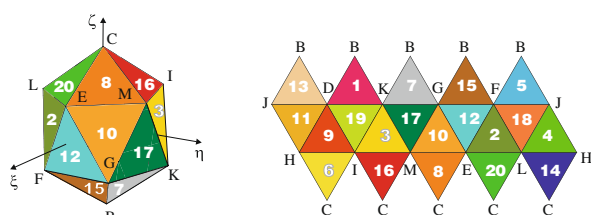


Fig. 1.10 Net image of the icosahedron die with vertex symbols, face numbers, and face colors

1.5 Roulette

Roulette is a casino and gambling game named after the French word meaning “small wheel.” In the game, the players may choose to place bets on either number, a range of numbers, the color red or black, or whether the number is odd or even. To determine the winning number and color, a croupier spins a wheel in one direction, then spins a ball in the opposite direction around a tilted circular track running around the circumference of the wheel. The ball eventually loses momentum and falls on to the wheel and into one of 37 (in European roulette) or 38 (in American roulette) colored and numbered pockets on the wheel [12]. An example of roulette wheel is shown in Fig. 1.11.

The pockets of the roulette wheel are numbered from 1 to 36, alternating between red and black. There is a green pocket numbered 0 (zero). In American roulette, there is a second green pocket marked 00. Pocket number order on the roulette wheel adheres to the following clockwise sequence: single zero wheel: 0-32-15-19-4-21-2-25-17-34-6-27-13-36-11-30-8-23-10-5-24-16-33-1-20-14-31-9-22-18-29-7-28-12-35-3-26 and double zero wheel: 0-28-9-26-30-11-7-20-32-17-5-22-34-15-3-24-36-13-1-00-27-10-25-29-12-8-19-31-18-6-21-33-16-4-23-35-14-2.

Players can place a variety of “inside” bets (selecting the number of the pocket the ball will land in or range of pockets based on their position) and “outside” bets (including bets on various positional groupings of pockets, pocket colors, or whether it is odd or even) [11, 12]. The payout odds for each type of a bet is based on its probability. The roulette table usually imposes minimum and maximum bets, and these rules usually apply separately for all of a player’s “inside” and “outside” bets for each spin. For “inside” bets at roulette tables, some casinos may use separate table chips of various colors to distinguish the players at the table. The players can continue to place bets until the dealer announces “no more bets” or “rien ne va plus.”

When a winning number and color is determined by the roulette wheel, the dealer will place a marker on that winning number on the roulette table layout. When the marker is on the table, no players may place bets, collect bets, or remove any bets from the table. The dealer will then sweep away all other losing bets either by hand or rake and determine all of the payouts to the remaining inside and outside winning



Fig. 1.11 Roulette wheel

bets. When the dealer has finished making the payouts, the marker is removed from the board where the players collect their winnings and make new bets.

The cloth cover with the betting areas on a roulette table is known as a “layout.” The French style layout is a single zero (shown in Fig. 1.12 (left)) and the American style layout (shown in Fig. 1.12 (right)) is usually a double zero. The American style roulette table with a wheel at one end is now used in most casinos all over the world. The French style table with a wheel in the center and a layout on either side is rarely found outside Monte Carlo.

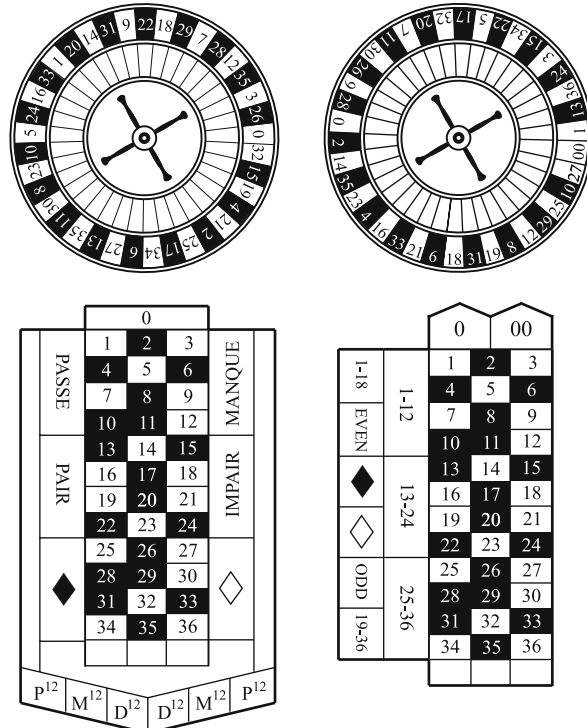


Fig. 1.12 The layout of roulette table

In the casino game of roulette there are the following types of bets [12]:

- Inside bets
 1. Straight-up: a single number bet. The chip is placed entirely on the middle of a number square.
 2. Split: a bet on two adjoining numbers, either on the vertical or horizontal (as in 14–17 or 8–9). The chip is placed on the line between these numbers.
 3. Street: a bet on three numbers on a single horizontal line. The chip is placed on the edge of the line of a number at the end of the line (either the left or the right, depending on the layout).

- 4. Corner (or square): a bet on four numbers in a square layout (as in 11–12–14–15). The chip is placed at the horizontal and vertical intersection of the lines between the four numbers.
- 5. Six line: a bet on two adjoining streets, with the chip placed at the corresponding intersection, as if in between where two street bets would be placed.
- 6. Trio: a bet on the intersecting point between 0, 1, and 2 or 00, 2, and 3.
- Outside bets (outside bets typically have smaller payouts with better odds at winning)
 - 1. 1–18: a bet on one of the first low 18 numbers coming up.
 - 2. 19–36: a bet on one of the last high 18 numbers coming up.
 - 3. Red or black: a bet on which color the roulette wheel will show.
 - 4. Even or odd: a bet on an even or odd number.
 - 5. Dozen bets: a bet on the first (1–12), second (13–24), or third group (25–36) of 12 numbers.
 - 6. Column bets: a bet on all 12 numbers on any of the three vertical lines (such as 1–4–7–10 on down to 34). The chip is placed on the space below the final number in this string.

In the early American gambling saloons, the house would set the odds on roulette tables at 27 for 1. This meant that on a \$1 bet you would get \$27 and the house would keep your initial dollar. Today most casino odds are set by law, and they have to be either 34 to 1 or 35 to 1. This means that the house pays you \$34 or \$35 and you get to keep your original \$1 bet. The house average or house edge (also called the expected value) is the amount the player loses relatively to any bet made, on average. If a player bets on a single number in the American game there is a probability of 1/38 that the player wins 35 times the bet and a 37/38 chance that the player loses his bet. The expected value is

$$-1 \cdot \frac{37}{38} + 35 \cdot \frac{1}{38} = -0.0526, \quad (1.1)$$

i.e., 5.26% house edge. For European roulette, a single number wins 1/37 and loses 36/37 and the expected value is

$$-1 \cdot \frac{36}{37} + 35 \cdot \frac{1}{37} = -0.0270, \quad (1.2)$$

i.e., 2.70% house edge [5, 12].

The green squares on the roulette wheel and on the table are technically the only house edge. Outside bets will always lose when a single or double zero come up. However, the house also has an edge on inside bets because the payouts are always set at 35 to 1 when you mathematically have a 37 to 1 chance of winning a straight bet on a single number. To understand the house edge on inside bets [12], imagine

placing straight \$1 wagers on all inside numbers on a roulette table (including 0 and 00) to assure a win. The player would only get back 35 times his/her original bet having spent \$38. The only exception is a five number bet where the house edge is considerably higher (7.89% on an American wheel), and the “even money” bets in some European games where the house edge is halved because only half the stake is lost when a zero comes up. The house edge is not the same as the hold. The hold is the total amount of cash the table changes for chips minus the chips taken away from the table – in other words, the actual “win” amount for the casino. The Casino Control Commission in Atlantic City releases a monthly report showing the win/hold amounts for each casino. The average win/hold for double zero wheels is between 21 and 30%, significantly more than 5.26%/2.70% of all players money because the players are making repeated bets after winning and losing portions of their total money.

A player with a certain total amount of money may not win or lose all his money instantly, so the total of all bets they make will often be greater than the total of the money they actually started to play with. The house edge applies to each bet made; not the total money, which means the player can end up losing significantly more than 5.26% of his starting money. For example, it is likely that a player with \$100 making \$10 bets on red will be able to bet more than 10 times, because sometimes he wins. He may end up betting a total of 20 times on red. This means the expected value is $20 \times \$10 \times 5.26\% = \10.52 , over 10% of his money is now in the “hold” despite the game having a 5.26% house advantage. A player who continually bets until he runs out of money will give the house 100% hold [12].

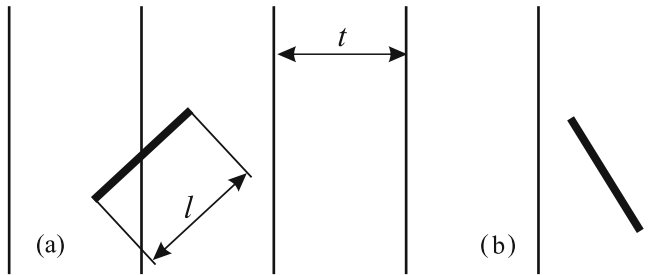
The analysis of the dynamical behavior of roulette goes back to Poincaré [30]. His results suggest that as the roulette ball is spun more and more vigorously the outcome number is independent of the initial conditions (initial conditions are washed out). For large number of trials the numbers become close to the uniform distribution. Later studies [11, 31] suggest that the real roulette may not be vigorous enough to wash out the initial conditions.

1.6 Other Mechanical Randomizers

The toss of the coin, the throw of the die, and the roulette run belong to the group of classical randomization mechanical systems. Other well-known elements in this group are, e.g., Buffon’s needle and pinball machine.

Buffon’s needle problem has been posed in the 18th century by Georges-Louis Leclerc, Conte de Buffon, in the following way: *Suppose we have a floor made of parallel strips of wood, each the same width, and we drop a needle onto the floor. What is the probability that the needle will lie across a line between two strips?*

Using integral geometry, the problem can be solved to get a Monte Carlo method to approximate π . The (a) needle lies across a line, while the (b) needle does not. The problem in more mathematical terms is given a needle of length l dropped on a plane ruled with parallel lines t units apart (Fig. 1.13), what is the probability that

**Fig. 1.13** Buffon's needle

the needle will cross a line? Let x be the distance from the center of the needle to the closest line, let θ be the acute angle between the needle and the lines, and let $t \geq l$. The probability density function of x ($0 \leq x \leq t/2$) is $\frac{2}{t}dx$ and the probability density function of θ ($0 \leq \theta \leq \pi/2$) is $\frac{2}{\pi}d\theta$. The two random variables, x and θ , are independent, so the joint probability density function is the product $\frac{4}{t\pi}dxd\theta$. The needle crosses a line if

$$x \leq \frac{l}{2} \sin \theta. \quad (1.3)$$

Integrating the joint probability density function gives the probability that the needle will cross a line:

$$\int_{\theta=0}^{\pi/2} \int_{x=0}^{(l/2)\sin\theta} \frac{4}{t\pi} dx d\theta = \frac{2l}{t\pi}. \quad (1.4)$$

For n needles dropped when h of them are crossing lines, this probability is

$$\frac{h}{n} = \frac{2l}{t\pi}, \quad (1.5)$$

which can be solved to get an estimate for π

$$\pi = \frac{2ln}{th}. \quad (1.6)$$

Now suppose $t < l$. In this case, integrating the joint probability density function, we obtain

$$\int_{\theta=0}^{\pi/2} \int_{x=0}^{m(\theta)} \frac{4}{t\pi} dx d\theta, \quad (1.7)$$

where $m(\theta)$ is the minimum between $(l/2) \sin \theta$ and $t/2$. Thus, performing the above integration, we see that, when $t < l$, the probability that the needle will cross a line is

$$\frac{h}{n} = \frac{2l}{t\pi} - \frac{2}{t\pi} \left\{ \sqrt{l^2 - t^2} + t \sin^{-1} \frac{t}{l} \right\} + 1. \quad (1.8)$$

An Italian mathematician, Mario Lazzarini performed the Buffon's needle experiment in 1901. Tossing a needle 3408 times, he attained the well-known estimate $355/113$ for π , which is a very accurate value, differing from π by no more than 3×10^{-7} . This is an impressive result, but is something of a cheat, as follows. Lazzarini chose the needles whose length was $5/6$ of the width of the strips of wood. In this case, the probability that the needles will cross the lines is $5/3\pi$. Thus if one was to drop n needles and get h crossings, one would estimate π as

$$\pi \approx \frac{5}{3} \frac{n}{h}. \quad (1.9)$$

π is very nearly $355/113$; in fact, there is no better rational approximation with fewer than 5 digits in the numerator and denominator. So if one had n and h such that $355/113 = (5/3)(n/h)$ or equivalently $h = 113n/213$ one would derive an unexpectedly accurate approximation to π , simply because the fraction $355/113$ happens to be so close to the correct value. But this can be easily arranged. To do this, one should pick n as a multiple of 213, because then $113n/213$ is an integer; one then drops n needles and hopes for exactly $h = 113n/213$ successes. If one drops 213 needles and happens to get 113 successes, then one can triumphantly report an estimate of π accurate to six decimal places. If not, one can just do 213 more trials and hope for a total of 226 successes; if not, just repeat as necessary. Lazzarini performed $3408 = 213 \times 16$ trials, making it seem likely that this is the strategy he used to obtain his “estimate.”

Hopf studies of Buffon's needle [32–34] show independence of the successive outcomes but also give the examples when the initial conditions are not washed out. More details on these studies can be found in [35–38].

The pinball machine schematically shown in Fig. 1.14 is also known as a Galton apparatus or probability machine. In this machine a ball is falling through a lattice of pins under the influence of the gravity. The pins are stick horizontally out of the vertical wall. Falling down the ball hits several pins before it finally terminates in one of the pockets. At the collisions the ball loses a portion of its initial energy and due to the friction between the ball and a pin the ball starts to rotate. It is generally assumed to produce a binomial probability distribution at the bottom where the balls fall down.

Figure 1.15 shows a histogram for distribution of 4014 balls over the 22 slots of the machine at the Technical University of Denmark. Also indicated in this figure is the binomial distribution corresponding to the number of layers in the machine. The experimental distribution appears to deviate from the binomial distribution by producing fewer outcomes in the center and more on the sides. This deviation is statistically significant [39].

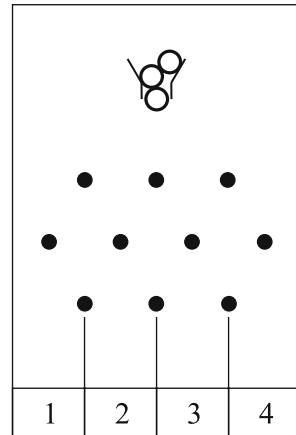
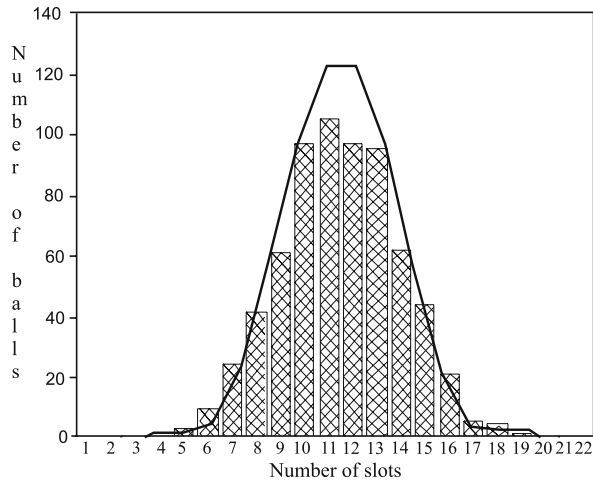
Fig. 1.14 Pinball machine

Fig. 1.15 Average distribution of balls in the 22 slots machine in the experiment performed at the Technical University of Denmark [39]



Pinball machine is often used to demonstrate how uncertainty arises in physical and other systems [19]. The dynamics of the simple pinball machine has been studied in [39].

1.7 Dynamics and Predictability

The dynamics of the mechanical randomizers is described by perfectly deterministic laws of classical mechanics which map initial conditions (position, configuration, momentum, and angular momentum) at the beginning of the motion into one of the final configurations defined by (i) the face of the coin, (ii) the number on the face on which the die lands, or (iii) the number of the roulette pocket. From the point of view of the dynamical systems the outcome from the mechanical randomizer is

deterministic, but as the initial condition–final configuration mapping is strongly nonlinear (as it will be shown in Chap. 3), one can expect deterministic unpredictability due to the sensitive dependence on the initial conditions and fractal boundaries between the basins of different final configurations.

1.7.1 Sensitive Dependence on Initial Conditions

Sensitive dependence on initial conditions and chaotic behavior of the system can be defined using Lyapunov exponents. In mathematics the Lyapunov exponent (named after the Russian mathematician Aleksandr Lyapunov) of a dynamical system is a quantity that characterizes the rate of separation of the nearby trajectories. Consider n -dimensional dynamical system given by

$$\dot{x} = f(x), \quad (1.10)$$

where $x \in R^n$. Quantitatively, two trajectories in phase space $x_1(t)$ and $x_2(t)$ with initial separation $|\delta z_0|$ diverge as

$$|\delta z(t)| \approx e^{\lambda t} |\delta z_0|, \quad (1.11)$$

where λ is the Lyapunov exponent. The rate of separation can be different for different orientations of initial separation vector. Thus, there is a whole spectrum of Lyapunov exponents and the number of them is equal to the number of dimensions of the phase space (the number of the first-order differential equations which are necessary to describe the dynamics). The largest Lyapunov exponent (LLE)

$$\lambda_{max} = \lim_{t \rightarrow \infty} \frac{1}{t} \ln \frac{|\delta z(t)|}{|\delta z_0|} \quad (1.12)$$

determines the predictability of a dynamical system. When the sum of all Lyapunov exponents is negative and the LLE is positive then a dynamical system is characterized by sensitive dependence on the initial conditions and is called chaotic.

LLE (1.12) is defined as the limit when time t goes to infinity, so to calculate Lyapunov exponents one has to have sufficiently (theoretically infinitely) long trajectory. Practical calculations are terminated when the limit in (1.12) saturates to the fixed value which has not changed with time.

In the case of mechanical randomizer the time of the system evolution is finite, as a coin, a die, or a roulette ball terminates its motion in a finite time so one cannot use the theory of chaotic systems to direct explanation of the observed behavior. However, in Chap. 4 we give evidence of temporal sensitive dependence on initial conditions which can be observed for the coin (die) during the bounces on the table. In Chap. 5 we show that in the case of no energy dissipation during the coin toss (throw of the die), i.e., when the air resistance is neglected and elastic impacts are assumed, the infinite process of the coin (die) bounces on the table is chaotic.

1.7.2 Fractal Basin Boundaries

As we will see in Chap. 3 the equations of motion of mechanical randomizer are Newton–Euler’s equations, with no external source of random influence, i.e., the fluctuations of air, thermodynamic or quantum fluctuations of the coin, die, or ball. One can construct a mapping of the initial conditions to a final observed configuration. The initial conditions are position, configuration, momentum, and angular momentum at the beginning of the motion. The final configuration depends on the kind of randomizer. In the case of the tossed coin there are three possible final configurations after bouncing on the floor: the coin terminates flat on the surface with its heads side up, its tails side up, or the coin balances on its edge. For n face die there are n possible final configurations (the die can land on one of its faces F_i ($i = 1, 2, \dots, n$)). For the roulette there are 37 or 38 final configurations defined by the number of the pocket in which the ball terminates. Theoretically, for the case of dice one can also expect unstable final configurations in which a die balances on one of its edges or vertices. In the roulette the ball balances between two pockets in unstable final configuration.

The flow given by the equations of motion maps all possible initial conditions into one of the final configurations. The set of initial conditions that is mapped onto the particular configuration creates its basin of attraction. For the coin the set of initial conditions that is mapped onto the heads configuration creates *heads basin of attraction* while the set of initial conditions mapped onto tails configuration creates *tails basin of attraction*. The boundary that separates heads and tails basins consists of initial conditions mapped onto the coin standing on the edge configuration. For infinitely thin coin this set is a set of zero measure and thus with probability 1 the coin ends up either heads or tails. For the finite thinness of the coin this measure is not zero but the probability of edge configuration to be stable is low. For n face die there are n basins of attraction. The initial conditions that are mapped onto the i th face configuration create i th face basin of attraction $\beta(F_i)$. The boundaries that separate the basins of different faces consist of initial conditions mapped onto the die standing on its edges or vertices configuration and are the sets of zero measure. Roulette has 37 or 38 basins of attraction separated by the zero measure boundaries.

Let us indicate all possible final configurations in different colors. The space of all possible initial conditions has been divided into small boxes. The center of each box has been taken as the initial condition in the simulations of the randomizer trajectory. After the identification of the final configuration the box is painted with an appropriate color. This procedure allows for the identification of the basin of attraction of each final configuration. Of course one has to consider very small boxes and for better visualization it is necessary to consider 2D cross section of the initial condition space.

The possibility that the boundaries between the basins of different faces is fractal, particularly intermingled ones is worth investigating (see Fig. 1.16). Near a given basin boundary, if the initial conditions are given with the uncertainty ε , then a fraction $f(\varepsilon)$ of initial conditions give an unpredictable outcome. For the smooth basin boundaries this fraction can be easily estimated (upper circle in

Fig. 1.16a) and when the distance of the initial conditions from the basin boundary is larger than ε the result of the throw can be easily predicted (lower circle in Fig. 1.16a).

The basin boundaries can also be fractal [40]. A fractal is generally “a rough or fragmented geometric shape that can be split into parts, each of which is (at least approximately) a reduced-size copy of the whole,” a property called self-similarity. The term was coined by Mandelbrot in 1975 [41]. Fractal basin boundaries are discontinuous (for example, an uncountable sequence of disjoint stripes) or continuous (a snowflake structure). For the fractal basin boundary (Fig. 1.16b) the level of unpredictability increases. There are regions of the initial condition space where it is impossible to set the initial conditions with any finite inaccuracy ε and be sure of the final state prediction (for example, the region indicated by the circle in Fig. 1.16b).

The analysis of the structure of the basin boundaries allows us to identify the condition under which a randomizer is predictable.

Definition 1.1. The mechanical randomizer is predictable if for almost all initial conditions x_0 there exists an open set U ($x_0 \in U$) which is mapped into the given final configuration.

Assume that the initial condition x_0 is a set with the inaccuracy ε . Consider a ball B centered at x_0 with a radius ε . Definition 1.1 implies that if $B \subset U$ then randomizer is predictable.

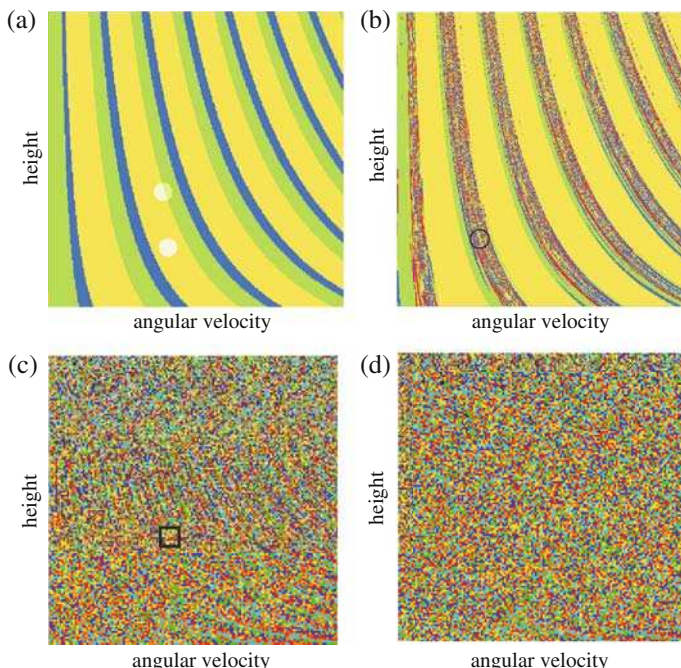


Fig. 1.16 Tetrahedral dice basin of attraction

From the point of view of the predictability of the die throw the possibility of the occurrence of the intermingled basins is the most interesting [42–45]. Let us briefly explain the term of the intermingled basins of attraction. A basin $\beta(F_i)$ is called the riddled one when for any point in $\beta(F_i)$, a ball in the phase space of arbitrarily small radius has a nonzero fraction of its volume in some other (say $\beta(F_j)$) basin. The basin $\beta(F_j)$ may or may not be riddled by the basin $\beta(F_i)$. If for all i, j the basin $\beta(F_j)$ is also riddled by the basin $\beta(F_i)$ such basins are called the intermingled ones.

As an example of the intermingled basin of attraction let us consider Fig. 1.16c. In the neighborhood of any initial conditions which lead to any of the final configurations there are points which lead to all other configurations. In this case the structure of the basin is self-similar (for example, enlarge the square in Fig. 1.16c and observe the structure shown in Fig. 1.16d).

Definition 1.2. The mechanical randomizer is fair by dynamics if in the neighborhood of any initial condition leading to one of the n final configurations $F_1, \dots, F_i, \dots, F_n$, where $i = 1, \dots, n$, there are sets of points $\beta(F_1), \dots, \beta(F_i), \dots, \beta(F_n)$, which lead to all other possible configurations and a measures of sets $\beta(F_i)$ are equal.

This definition implies that for the infinitely small inaccuracy of the initial conditions all final configurations are equally probable.

In Chap. 4 we give evidence of the coin toss, the die throw, and the roulette run are predictable in the sense of Definition 1.1, so they are not fair by dynamics. Chapter 5 presents examples that under unrealistic condition of the lack of energy dissipations mechanical randomizer becomes unpredictable and fair by dynamics.

References

1. United Kingdom Office of Public Sector Information: Definition as gaming. <http://www.opsi.gov.uk/acts1990/Ukpga-19900026-en1.htm> (2009). Cited 10 Apr 2009 1
2. Wikipedia. <http://en.wikipedia.org/wiki/Gambling> (2009). Cited 10 Apr 2009 1
3. Gambling Law US. <http://www.gambling-law-us.com> (2009). Cited 10 Apr 2009 1
4. UK Gambling Commission. <http://www.gamblingcommission.gov.uk> (2009). Cited 10 Apr 2009 1
5. Tijms H.: Understanding Probability. Cambridge University Press, Cambridge (2007) 1, 13
6. International Association of Gaming Regulators: Members. <http://www.iagr.org/members-members.htm> (2009). Cited 10 Apr 2009 1
7. Nevada State Gaming Control Board: Technical Standards. <http://gaming.nv.gov/stats-regshistory.htm-tech-standards> 2
8. Maclin, O.H., Dixon, M.R.: A computerized simulation for investigating gambling behavior during roulette play. *Behav. Res. Methods, Instrum. Comput.* **36** (1), 96–100 (2004) 2
9. The Holy Bible. The Gideons International, Lutterworth (2000) 2
10. Mason, E., King Rufus: The Life and Murder of William II of England. The History Press, Port Stroud (2008) 4
11. Bass, T.: The Eudaemonic Pie. Houghton-Mifflin, Boston (1985) 4, 5, 11, 14
12. Wikipedia. <http://en.wikipedia.org/wiki/Roulette> 4, 5, 11, 12, 13, 14
13. Feller, W.: An Introduction to Probability: Theory and Examples. Wiley, New York (1957) 6

14. Jaynes, E.T.: Probability Theory: The Logic of Science. Cambridge University Press, Cambridge (1996) 6
15. Kerrich, J.E.: An Experimental Introduction to the Theory of Probability. J. Jorgensen, Copenhagen (1946) 6
16. Harris, M., Keane, M.: Random coin tossing. *Probab. Theory Related Fields* **109**, 27–34 (1997) 6
17. Benjamini, I., Kesten, H.: Distinguishing sceneries by observing the scenery along a random walk. *J. Anal. Math.* **69**, 97 (1996) 6
18. Howard, D.: Orthogonality of measures induced by random walks with scenery. *Combin. Probab. Comput.* **5**, 247 (1996) 6
19. Haken, H.: Synergetic. Springer, Berlin (1978) 6, 17
20. Rocha, A.L., Stern, F.: The asymmetric n -player gambler's ruin problem with equal initial fortunes. *Adv. Appl. Math.* **33**, 512 (2004) 6
21. Kmet, A., M. Petkovsek, M.: Gambler's ruin problem in several dimensions. *Adv. Appl. Math.* **28**, 107 (2002) 6
22. Itoh, Y., Maechara, H.A.: A variation to the ruin problem. *Math. Japan* **47**, 97 (1998) 6
23. Harik, G., Cantu-Paz, E., Goldberg, D., Miller, B.: The gambler's ruin problem, genetic algorithms, and the sizing of populations. *Evol. Comput.* **7**, 231 (1999) 6
24. Duan, Z., L. Howard, L.: A modified gambler's ruin problem of polyethylene chains in the amorphous region. *Proc. Natl. Acad. Sci. U.S.A.* **93**, 100007 (1996) 6
25. Cooper, C.: Strange attractors in a chaotic coin flip simulation. *Chaos, Solitons Fractals* **30**, 1–12 (2006) 6
26. Cooper, C.: A note on on-off intermittency in a chaotic flip simulation. *Comput. Graph.* **31**, 137–145 (2007) 6
27. Balzass, N.L., Chatterjee, R., Jakson, A.D.: Coin tossing as a billiard problem. *Phys. Rev. E* **52**, 3608 (1995) 6
28. Diaconis, P., Keller, J.B.: Fair dice. *Amer. Math. Monthly* **96**, 337–339 (1989) 7, 9
29. Grunbaum, B.: On polyhedra in E^3 having all faces congruent. *Bull. Res. Council Israel* **8F**, 215–218 (1960) 7
30. Poincaré, H.: Calcul de Probabilités. George Carre, Paris (1896) 14
31. Barnhart, R.: Beating the Wheel: Wining Strategies at Roulette. Lyle and Stuart, New York, (1992) 14
32. Hopf, E.: On causality, statistics and probability. *J. Math. Phys.*, **13**, 51 (1934) 16
33. Hopf, E.: Über die Bedeutung der Willkürlichen Funktionen für die Wahrscheinlichkeitstheorie. Jahresbericht Deutsche Mathematische Verlag **46**, 179 (1936) 16
34. Hopf, E.: Ein Verteilungsproblem bei dissipativen dynamischen Systemen. *Mathematische Annalen* **114**, 161 (1937) 16
35. von Plato, J.: Creating Modern Probability: Its Mathematics, Physics and Philosophy in Historical Perspective. Cambridge University Press, Cambridge (1994) 16
36. Lindley, T.F.: Is it the coin that is biased? *Philosophy* **56**, 403 (1981) 16
37. Stevens, M.: Bigger than Chaos: Understanding Complexity through Probability. Harvard University Press, Cambridge (2003) 16
38. Engel, E.: A Road to Randomness in Physical Systems. Springer, New York (1992) 16
39. Hansen, L.-U., Christensen, M., Mosekilde, E.: Deterministic analysis of the probability machine, *Phys. Scr.* **51**, 35–45 (1995) 16, 17
40. McDonald, S.W., Grebogi, C., Ott, E., Yorke, J.A.: Fractal basin boundaries. *Physica*, **17D**, 125–153 (1985) 20
41. Mandelbrot, B.B.: Fractal Geometry of Nature. Freeman, San Francisco (1982) 20
42. Sommerer, J.C., Ott, E.: Riddled basins. *Nature* **365**, 136 (1993) 21
43. Ott, E., Alexander, J.C., Kan, I., Sommerer, J.C., Yorke, J.A.: The transition to chaotic attractors with riddled basins. *Physica D* **76**, 384 (1994) 21
44. Alexander, J.C., Yorke, J.A., You, Z., Kan, I.: Riddled basins. *Int. J. Bifur. Chaos* **2**, 795 (1992) 21
45. Kapitaniak, T., Maistrenko, Yu., Stefanski, A., Brindley, J.: Bifurcations from locally to globally riddled basins. *Phys. Rev. E* **57**, R6253 (1998) 21

Chapter 2

General Motion of a Rigid Body

Abstract The tools that allow the description of the motion of the rigid body are recalled. We used both Euler's angles and Euler's parameters (normalized quaternions) to describe the orientations of the body. Precession of the rigid body and air resistance and the dissipation of the energy at successive collisions are discussed.

2.1 Basic Equations of Motion of a Rigid Body

In the motion analysis of a coin, a die, and roulette ball free (unconstrained) body motion and constraint body motion are analyzed. Free body motion is described by dynamics equations of a rigid body [1–7]. At the instant of the body (coin, die, ball) contact with surroundings (base, table, wheel) some additional equations – constraint equations – are necessary.

2.1.1 Dynamics Equations in General Form

The general form of body dynamics equations can be derived from body linear momentum and angular momentum laws

$$\frac{d\mathbf{Q}}{dt} = \mathbf{F} \quad \text{and} \quad \frac{d\mathbf{K}}{dt} = \mathbf{M}, \quad (2.1)$$

where \mathbf{F} , \mathbf{M} are vectors of body external force and moments whereas \mathbf{Q} , \mathbf{K} are vectors of linear momentum and angular momentum of body defined by

$$\mathbf{Q} = \int_V \mathbf{v} \rho dV \quad \text{and} \quad \mathbf{K} = \int_V \mathbf{r} \times \mathbf{v} \rho dV. \quad (2.2)$$

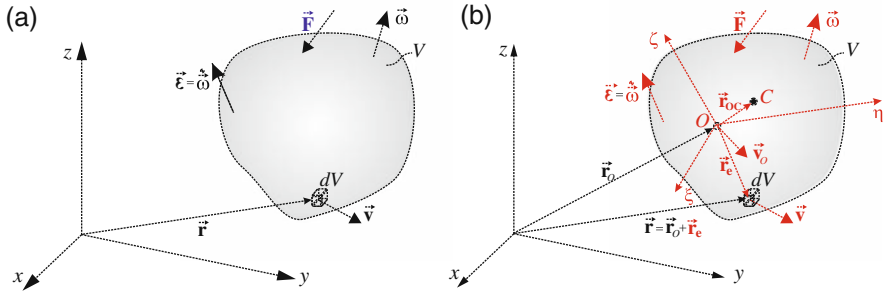


Fig. 2.1 Body point position (\mathbf{r}) and velocity (\mathbf{v}) vectors: (a) in the inertial frame xyz , and (b) in the body embedded frame $O\xi\eta\zeta$

In (2.2) V denotes a body volume (Fig. 2.1), \mathbf{r} position vector¹ of a body point (volume dV), \mathbf{v} velocity vector of the point described in inertial frame xyz , and ρ body material density.

Using the velocity vector \mathbf{v}_o represented by the components in the body embedded frame ($\xi\eta\zeta$) to describe body point velocity vector ($\mathbf{v} = \mathbf{v}_o + \boldsymbol{\omega} \times \mathbf{r}_e$) on the basis of (2.1), (2.2) we obtain the general form of body dynamics equations:

$$m\dot{\mathbf{v}}_o + m\mathbf{R}_{oc}^T \tilde{\boldsymbol{\omega}} + m\tilde{\boldsymbol{\Omega}}\mathbf{v}_o + m\tilde{\boldsymbol{\Omega}}^T \tilde{\boldsymbol{\Omega}}\mathbf{R}_{oc} = \mathbf{F}, \quad (2.3)$$

$$m\mathbf{R}_{oc}\dot{\mathbf{v}}_o + \mathbf{J}_o \dot{\boldsymbol{\omega}} + m\mathbf{R}_{oc}\tilde{\boldsymbol{\Omega}}\mathbf{v}_o + \tilde{\boldsymbol{\Omega}}\mathbf{J}_o \tilde{\boldsymbol{\omega}} = \mathbf{M}_o. \quad (2.4)$$

In the mentioned equations m is the mass of body, $\dot{\mathbf{v}}_o$ and $\tilde{\boldsymbol{\omega}}$ are column matrices of vectors² $\dot{\mathbf{v}}_o$, $\boldsymbol{\omega}$ components, \mathbf{R}_{oc} and $\tilde{\boldsymbol{\Omega}}$ are antisymmetric matrices representing the vectors \mathbf{r}_{oc} and $\boldsymbol{\omega}$, \mathbf{J}_o is inertia matrix of the body including mass moments of inertia of the body with respect to $O\xi\eta\zeta$ frame. \mathbf{F} and \mathbf{M}_o are column matrices of vectors \mathbf{F} , \mathbf{M}_o components in $O\xi\eta\zeta$ frame.

We get a special form of body dynamics equations introducing the body embedded frame $C\xi\eta\zeta$, where C is the body mass center (Fig. 2.2), and using the mass center velocity vector ($\mathbf{v}_c = [v_{c\xi} \ v_{c\eta} \ v_{c\zeta}]^T$) instead of \mathbf{v}_o :

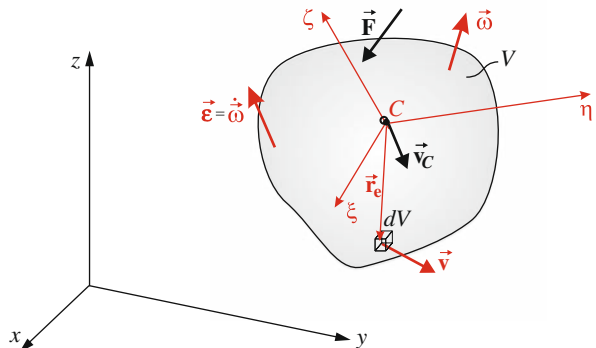
$$m\dot{\mathbf{v}}_c + m\tilde{\boldsymbol{\Omega}}\mathbf{v}_c = \mathbf{F}, \quad (2.5)$$

$$\mathbf{J}_c \dot{\boldsymbol{\omega}} + \tilde{\boldsymbol{\Omega}} \mathbf{J}_c \tilde{\boldsymbol{\omega}} = \mathbf{M}_c. \quad (2.6)$$

¹ In most of figures the vector quantities are denoted with an arrow above the symbol.

² The symbol $\boldsymbol{\omega}$ is used for the angular velocity vector, and $\tilde{\boldsymbol{\omega}}$ for its matrix representation, i.e., the column matrix of the angular velocity components. For the square matrix representing the angular velocity vector ($\boldsymbol{\omega}$) the symbol $\tilde{\boldsymbol{\Omega}}$ is used.

Fig. 2.2 Body mass center velocity vector (\vec{v}_c) and external force \mathbf{F} in the inertial frame xyz , angular velocity and acceleration vectors in the body embedded frame ($C\xi\eta\xi$)



2.1.2 Newton–Euler Equations

The simplest equations describing dynamics of a rigid body are the well-known form of the Newton–Euler equations based on body linear momentum and angular momentum laws

$$\frac{d\mathbf{Q}}{dt} = \mathbf{F} \quad \text{and} \quad \frac{d\mathbf{K}_c}{dt} = \mathbf{M}_c , \quad (2.7)$$

where \mathbf{K}_c and \mathbf{M}_c are vectors of angular momentum of a body and body force moments with respect to the body mass center (C). Newton–Euler equations have the form:

$$m\dot{v}_c = \mathbf{F} , \quad (2.8)$$

$$\mathbf{J}_c\ddot{\omega} + \tilde{\boldsymbol{\Omega}}\mathbf{J}_c\dot{\omega} = \mathbf{M}_c , \quad (2.9)$$

where the mass center velocity and external force are expressed by vector components with respect to the inertial frame (xyz), i.e., $v_c = [\dot{x} \quad \dot{y} \quad \dot{z}]^T$, $\mathbf{F} = [f_x \quad f_y \quad f_z]^T$, whereas \mathbf{J}_c , $\tilde{\boldsymbol{\Omega}}$, and \mathbf{M}_c are described in the frame $C\xi\eta\xi$.

On the other hand, it is more convenient to describe the rotations of a body (2.4) by their components with respect to the body embedded frame ($C\xi\eta\xi$).

Equations (2.8) and (2.9) are general equations of motion and are suitable for the dynamics analysis of any body, i.e., a nonsymmetric and nonhomogeneous body. In the case in which the forces \mathbf{F} are independent of the angular velocity of the body and moments \mathbf{M}_c are not the functions of body mass center accelerations, (2.8) and (2.9) are uncoupled. This happens when the air resistance of a body is neglected.

The scalar form of a body dynamics equations obtained from the general equation (2.8) and (2.9) can be written in the well-known form of Newton–Euler equations:

$$m\ddot{x} = f_x , \quad m\ddot{y} = f_y , \quad m\ddot{z} = f_z , \quad (2.10)$$

$$\begin{aligned} J_\xi \dot{\omega}_\xi + (J_\zeta - J_\eta) \omega_\eta \omega_\zeta - J_{\xi\zeta} \dot{\omega}_\zeta - J_{\xi\eta} \dot{\omega}_\eta + J_{\eta\zeta} (\omega_\zeta^2 - \omega_\eta^2) + \\ + (J_{\xi\eta} \omega_\zeta - J_{\xi\zeta} \omega_\eta) \omega_\xi = M_{C\xi} , \end{aligned}$$

$$\begin{aligned} J_\eta \dot{\omega}_\eta + (J_\xi - J_\zeta) \omega_\xi \omega_\zeta - J_{\xi\eta} \dot{\omega}_\xi - J_{\eta\zeta} \dot{\omega}_\zeta + J_{\xi\zeta} (\omega_\xi^2 - \omega_\zeta^2) + \\ + (J_{\eta\zeta} \omega_\xi - J_{\xi\eta} \omega_\zeta) \omega_\eta = M_{C\eta} , \end{aligned} \quad (2.11)$$

$$\begin{aligned} J_\zeta \dot{\omega}_\zeta + (J_\eta - J_\xi) \omega_\xi \omega_\eta - J_{\eta\zeta} \dot{\omega}_\eta - J_{\xi\zeta} \dot{\omega}_\xi + J_{\xi\eta} (\omega_\eta^2 - \omega_\xi^2) + \\ + (J_{\xi\zeta} \omega_\eta - J_{\eta\zeta} \omega_\xi) \omega_\zeta = M_{C\zeta} . \end{aligned}$$

The moments of inertia in this case are determined with respect to the body embedded frame $C\xi\eta\zeta$ with the origin in the body mass center and in the general case, for a nonsymmetric or nonhomogeneous body, the inertia products are nonzero terms, because the axes $C\xi\eta\zeta$ will not be principal axes.

In the case of symmetric body the axes $C\xi\eta\zeta$ are principal axes ($J_{\xi\eta} = 0$, $J_{\eta\zeta} = 0$, $J_{\xi\zeta} = 0$) and from (2.11) we obtain

$$J_\xi \frac{d\omega_\xi}{dt} - (J_\eta - J_\zeta) \omega_\eta \omega_\zeta = M_{C\xi} ,$$

$$J_\eta \frac{d\omega_\eta}{dt} - (J_\zeta - J_\xi) \omega_\xi \omega_\zeta = M_{C\eta} , \quad (2.12)$$

$$J_\zeta \frac{d\omega_\zeta}{dt} - (J_\xi - J_\eta) \omega_\xi \omega_\eta = M_{C\zeta} .$$

Expressing ω_ξ , ω_η , ω_ζ in terms of Euler angles $(\varphi, \vartheta, \psi)$ or in normalized quaternions (e_0, e_1, e_2, e_3) one can obtain the motion equations in the chosen coordinates.

2.2 Precession of a Body

The term precession is used to indicate that the body angular velocity vector rotates during the motion.

In general case of a body motion we use (2.11) to describe the body rotation. There are no analytical solution of (2.11) in general case but we can solve these equations numerically for any data and obtain the body motion as well as the changes in angular velocity vector ($\boldsymbol{\omega}$) and angular momentum vector (\mathbf{K}_c). Some exemplary results of such solutions for torque-induced body motion are shown in Fig. 2.3 where vectors $\boldsymbol{\omega}$ and \mathbf{K}_c are depicted for some time instant. We can see that both vectors change their directions and values during the body motion. From presented cases follow that these bodies undergo precession (i.e., the vector $\boldsymbol{\omega}$ rotates).

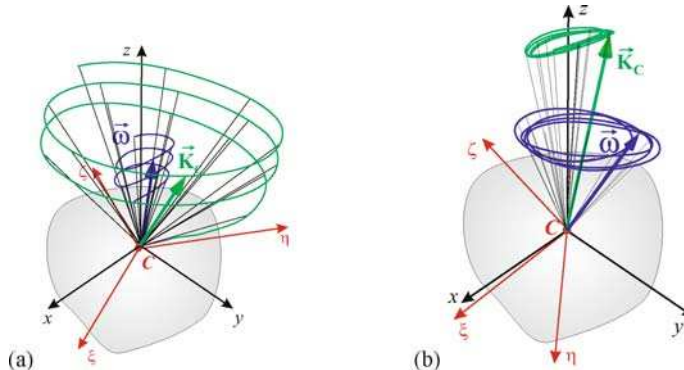


Fig. 2.3 The precessing nonsymmetric body: changes of angular momentum (\mathbf{K}_c) and angular velocity ($\boldsymbol{\omega}$) vectors direction due to nonzero moments of external forces: (a) for $M_{C\xi} \neq 0, M_{C\eta} \neq 0, M_{C\zeta} \neq 0$ and (b) for $M_{C\xi} \neq 0, M_{C\eta} \neq 0, M_{C\zeta} = 0$

Beyond the torque-induced precession torque-free precession is also possible. In the case of torque-free motion of a body the moment of external forces with respect to the body mass center is zero ($\mathbf{M}_c = \mathbf{0}$) and from (2.7) we have $d\mathbf{K}_c/dt = \mathbf{0}$. It means that the body angular momentum vector with respect to the mass center is constant vector and there are no changes in the value neither in the direction of \mathbf{K}_c ($\mathbf{K}_c = \text{const}$).

For some special cases – for symmetric bodies and zero moments of external forces ($\mathbf{M}_c = \mathbf{0}$) – an analytical solution of (2.11) can be obtained [4]. We present such solutions for symmetric top³ (which is the model of ideal coin) and spherical top⁴ (which is the model of ideal die and torque-free motion of a roulette ball).

2.2.1 Precession of Symmetric Top

Taking into account the symmetry of body (symmetric top) $J_\xi = J_\eta = J_1, J_\zeta = J_3, J_{\xi\eta} = J_{\xi\zeta} = J_{\eta\zeta} = 0$ and assuming zero value of forces moment acting on the body ($M_{C\xi} = M_{C\eta} = M_{C\zeta} = 0$), from (2.12) we get the following equations:

³ A symmetric top is a body in which two moments of inertia are the same. There are two classes of symmetric tops, oblate symmetric top with $J_\xi = J_\eta < J_\zeta$ and prolate symmetric top (cigar shaped) with $J_\xi = J_\eta > J_\zeta$. (A body is an asymmetric top if all three moments of inertia are different.)

⁴ A spherical top is a special case of a symmetric top (although it need not be spherical) with equal moment of inertia about all three axes ($J_\xi = J_\eta = J_\zeta$).

$$\begin{aligned} J_\xi \dot{\omega}_\xi - (J_1 - J_3) \omega_\zeta \omega_\eta &= 0 , \\ J_1 \dot{\omega}_\eta - (J_3 - J_1) \omega_\zeta \omega_\xi &= 0 , \\ J_3 \dot{\omega}_\zeta &= 0 . \end{aligned} \quad (2.13)$$

Solving (2.13) together with initial conditions (i.e., the initial angular velocity components $\omega_\xi(0) = \omega_{\xi 0}$, $\omega_\eta(0) = \omega_{\eta 0}$, $\omega_\zeta(0) = \omega_{\zeta 0}$) we obtain the components of angular velocity of the body in the form

$$\begin{aligned} \omega_\xi(t) &= \omega_{\eta 0} \sin \left(\frac{J_1 - J_3}{J_1} \omega_{\zeta 0} t \right) + \omega_{\xi 0} \cos \left(\frac{J_1 - J_3}{J_1} \omega_{\zeta 0} t \right) , \\ \omega_\eta(t) &= \omega_{\eta 0} \cos \left(\frac{J_1 - J_3}{J_1} \omega_{\zeta 0} t \right) - \omega_{\xi 0} \sin \left(\frac{J_1 - J_3}{J_1} \omega_{\zeta 0} t \right) , \\ \omega_\zeta(t) &= \omega_{\zeta 0} . \end{aligned} \quad (2.14)$$

For symmetric top the vector $\boldsymbol{\omega}$ has constant value

$$\omega = \sqrt{\omega_{\xi 0}^2 + \omega_{\eta 0}^2 + \omega_{\zeta 0}^2} . \quad (2.15)$$

From (2.14) arise that $\omega_\zeta(t)$ is time independent and two other components can be transformed to the following form:

$$\begin{aligned} \omega_\xi(t) &= \omega_\tau \sin (\omega_p t + \varphi_\tau) , \\ \omega_\eta(t) &= \omega_\tau \cos (\omega_p t + \varphi_\tau) , \end{aligned} \quad (2.16)$$

with the constant coefficients

$$\omega_p = \frac{J_1 - J_3}{J_1} \omega_{\zeta 0} , \quad \omega_\tau = \sqrt{\omega_{\xi 0}^2 + \omega_{\eta 0}^2} , \quad \varphi_\tau = \arctg \frac{\omega_{\xi 0}}{\omega_{\eta 0}} . \quad (2.17)$$

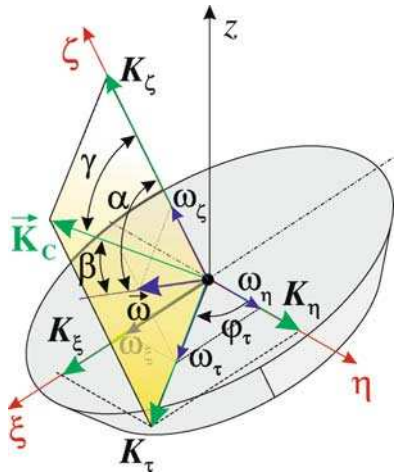
From presented solutions (2.14), (2.15), (2.16), and (2.17) it follows that for the symmetric top its angular momentum vector (\mathbf{K}_c) has components obtained as

$$\begin{aligned} K_\xi(t) &= J_1 \omega_\tau \sin (\omega_p t + \varphi_\tau) , \\ K_\eta(t) &= J_1 \omega_\tau \cos (\omega_p t + \varphi_\tau) , \\ K_\zeta(t) &= J_3 \omega_{\zeta 0} , \end{aligned} \quad (2.18)$$

and the constant value as

$$K_c = \sqrt{J_1^2(\omega_{\xi 0}^2 + \omega_{\eta 0}^2) + J_3^2 \omega_{\zeta 0}^2} . \quad (2.19)$$

Fig. 2.4 Torque-free precession of symmetric top: vectors of angular velocity (ω) and angular momentum (\mathbf{K}_c)



We can also obtain the angle γ between the symmetry axis of the body (ζ) and the angular momentum vector (\mathbf{K}_c) and the angle α between ζ and the vector $\tilde{\omega}$ (see Fig. 2.4) as

$$\gamma = \arccos \frac{J_3 \omega_{\zeta 0}}{K_c} = \text{const} , \quad \alpha = \arccos \frac{\omega_{\zeta 0}}{\omega} = \text{const} . \quad (2.20)$$

The angles γ and α have constant value, but they are measured from axis ζ which moves (changes its direction). While the angular momentum vector \mathbf{K}_c has constant value and direction in the spatial frame xyz we can use the angle $\beta = \alpha - \gamma$ to obtain the orientation of the vector $\tilde{\omega}$ with respect to the fixed vector \mathbf{K}_c . From (2.20) we have

$$\beta = \alpha - \gamma = \arcsin \frac{(J_3 - J_1) \omega_{\zeta 0} \omega_\tau}{K_c \omega} = \text{const} . \quad (2.21)$$

The vectors of angular velocity and angular momentum for symmetric top are also presented in Fig. 2.5, where ω and \mathbf{K}_c are shown in the spatial frame xyz as well as in the body embedded frame $\xi\eta\zeta$. The angular velocity vector ω in the spatial frame xyz rotates around the angular momentum vector (Fig. 2.5a). Both vectors rotate in the body embedded frame $\xi\eta\zeta$ (Fig. 2.5b).

2.2.2 Torque-Free Motion of Spherical Top

For torque-free motion of spherical top ($J_\xi = J_\eta = J_\zeta = J_1$), (2.13) simplify to the form

$$J_1 \dot{\omega}_\xi = 0 , \quad J_1 \dot{\omega}_\eta = 0 , \quad J_1 \dot{\omega}_\zeta = 0 , \quad (2.22)$$

Fig. 2.5 The precessing symmetric top: angular momentum (\vec{K}_C) and angular velocity (ω) vectors in (a) spatial frame xyz and (b) body embedded frame $\xi\eta\xi$

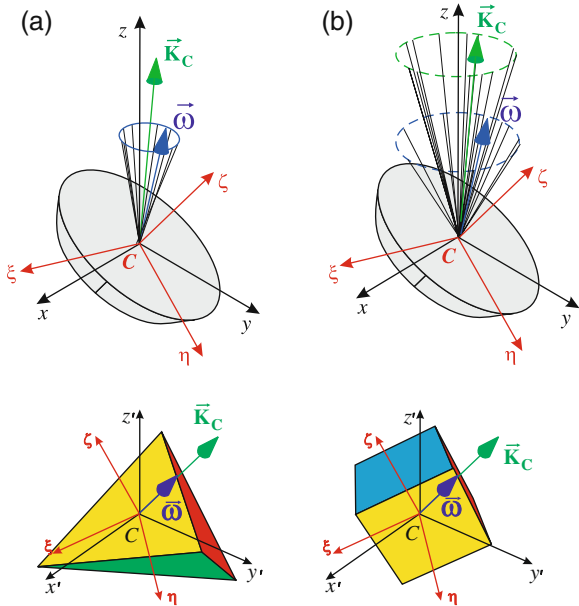


Fig. 2.6 Torque-free motion of spherical tops: constant angular momentum (\vec{K}_C) and angular velocity (ω) vectors' directions and values for a ball, tetrahedron die, and cubic die (no precession motion)

and we get the solution: $\omega_\xi = \omega_{\xi 0}$, $\omega_\eta = \omega_{\eta 0}$, $\omega_\zeta = \omega_{\zeta 0}$. It means that the angular momentum vector (\vec{K}_C) and angular velocity vector (ω) have constant values and directions during the body motion. We will call such a motion as no precession motion. Illustration of this case is shown in Fig. 2.6.

2.3 Orientation of a Rigid Body

The orientation of a rigid body (orientation of a body embedded frame $\xi\eta\xi$) with respect to the local reference frame $x'y'z'$ is described by [3, 5, 8–10]

$$\mathbf{r} = \mathbf{R} \mathbf{r}', \quad (2.23)$$

where

- \mathbf{r} – the column matrix representing the vector \mathbf{r} of the position coordinates of an arbitrary point A (Fig. 2.7) of the body before its rotation (in the initial position),
- \mathbf{r}' – the column matrix of coordinates of the same point of the body after its rotation (in the final position),
- \mathbf{R} – the rotation matrix (representing the orientation of the local frame $\xi\eta\xi$, with respect to the frame $x'y'z'$).

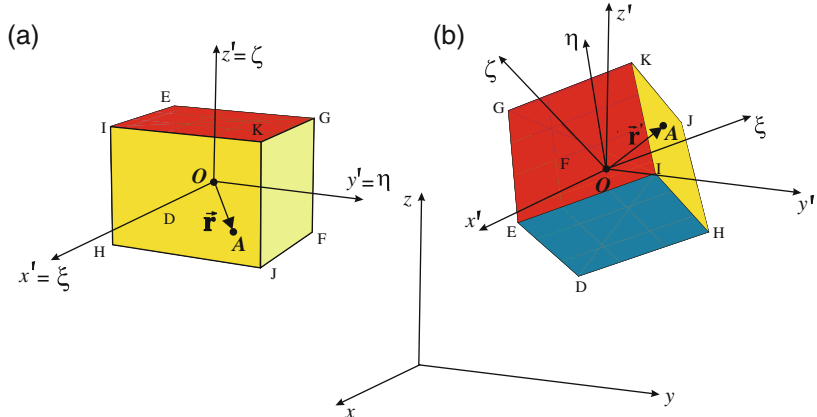


Fig. 2.7 Point A position vectors: (a) \mathbf{r} – in the initial position and (b) \mathbf{r}' – in the final position

The inverse transformation is defined by

$$\mathbf{r}' = \mathbf{R}^{-1} \mathbf{r} = \mathbf{R}^T \mathbf{r} \quad (2.24)$$

(\mathbf{R}^{-1} is the inverse matrix of \mathbf{R} , and $\mathbf{R}^{-1} = \mathbf{R}^T$, whereas \mathbf{R}^T is the transpose matrix of \mathbf{R}).

The matrix \mathbf{R} can be expressed in different ways. Its form depends on the coordinates that are chosen for the body orientation description. The elements of the rotation matrix (\mathbf{R}) are cosines of the angles between the axes of body reference frames $x'y'z'$ and $\xi\eta\zeta$ (Fig. 2.7b)

$$\mathbf{R} = \begin{bmatrix} \cos \vartheta(x', \xi) \cos \vartheta(x', \eta) \cos \vartheta(x', \zeta) \\ \cos \vartheta(y', \xi) \cos \vartheta(y', \eta) \cos \vartheta(y', \zeta) \\ \cos \vartheta(z', \xi) \cos \vartheta(z', \eta) \cos \vartheta(z', \zeta) \end{bmatrix}. \quad (2.25)$$

On the basis of the rotation matrix (\mathbf{R}) it is possible to define the matrix (or angular velocity tensor) that contains the components of the body angular velocity vector ($\tilde{\boldsymbol{\Omega}} = \dot{\mathbf{R}}\mathbf{R}^T$), which is necessary in the dynamic analysis of the body. Matrix $\tilde{\boldsymbol{\Omega}}$ is obtained in the xyz reference frame. We use the symbol $\tilde{\boldsymbol{\Omega}}_\xi$ for the body angular velocity matrix defined by the components in the body embedded frame $\xi\eta\zeta$. This matrix is expressed as $\tilde{\boldsymbol{\Omega}}_\xi = \mathbf{R}^T \tilde{\boldsymbol{\Omega}} \mathbf{R}$.

2.3.1 Euler Angles and Other Conventions

In what follows, we adapt the conventions of [1, 7, 9, 11] which are different from the ones used in [6]. Using Euler angles (or any other from 12 possible conventions of specifying the relative orientation of a body) the rotation matrix \mathbf{R} is the composition of three consecutive rotations: $\varphi_1, \varphi_2, \varphi_3$, around axes $\xi\eta\zeta$ of the frame embedded and fixed in the body

$$R = R_1(\varphi_1)R_2(\varphi_2)R_3(\varphi_3), \quad (2.26)$$

whereas $R_1(\varphi_1)$, $R_2(\varphi_2)$, $R_3(\varphi_3)$ are the matrices of successive rotations around ξ , η , and ζ axes.

The definition of Euler angles is not unique. In works of various authors different sets of angles describe the body orientations and other naming conventions for the same angles are used. These conventions depend on the axes about which the rotations are carried out and on the rotation sequences. Basic definitions, names, and expressions used in this work are briefly presented below. For the rotation of the body of value φ_i around the ξ axis (Fig. 2.8) the rotation matrix has the following form:

$$R_\xi(\varphi_i) = \begin{bmatrix} 1 & 0 & 0 \\ 0 & \cos \varphi_i & -\sin \varphi_i \\ 0 & \sin \varphi_i & \cos \varphi_i \end{bmatrix}. \quad (2.27)$$

For the rotation of value φ_i around the η axis

$$R_\eta(\varphi_i) = \begin{bmatrix} \cos \varphi_i & 0 & \sin \varphi_i \\ 0 & 1 & 0 \\ -\sin \varphi_i & 0 & \cos \varphi_i \end{bmatrix}. \quad (2.28)$$

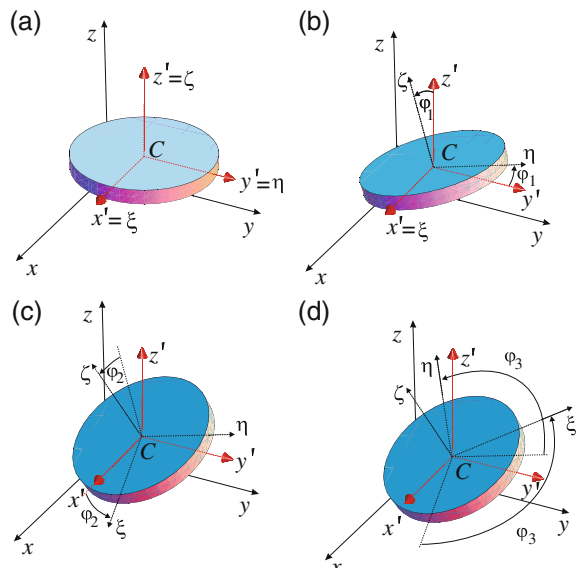


Fig. 2.8 Initial position of a body (a) and the rotation sequence: φ_1 – around the ξ (b), φ_2 – around the η (c), φ_3 – around the ζ (d)

The rotation of value φ_i around the ζ axis leads to

$$R_\zeta(\varphi_i) = \begin{bmatrix} \cos \varphi_i & -\sin \varphi_i & 0 \\ \sin \varphi_i & \cos \varphi_i & 0 \\ 0 & 0 & 1 \end{bmatrix}. \quad (2.29)$$

Depending on the order of rotations around the sequence of chosen axes there are 12 possible variants of this method determining the position of a body in space. Denoting the axes $\xi\eta\zeta$ of the body embedded frame by symbols 1, 2, 3 ($\xi \rightarrow 1, \eta \rightarrow 2, \zeta \rightarrow 3$), possible rotation sequences can be represented as follows: 121 ($\xi\text{-}\eta\text{-}\xi$), 123 ($\xi\text{-}\eta\text{-}\zeta$), 131 ($\xi\text{-}\zeta\text{-}\xi$), 132 ($\xi\text{-}\zeta\text{-}\eta$), 212 ($\eta\text{-}\xi\text{-}\eta$), 213 ($\eta\text{-}\xi\text{-}\zeta$), 231 ($\eta\text{-}\zeta\text{-}\xi$), 232 ($\eta\text{-}\zeta\text{-}\eta$), 312 ($\zeta\text{-}\xi\text{-}\eta$), 313 ($\zeta\text{-}\xi\text{-}\zeta$), 321 ($\zeta\text{-}\eta\text{-}\xi$), 323 ($\zeta\text{-}\eta\text{-}\zeta$).

Classical Euler angles are: $\varphi_1 = \psi$, $\varphi_2 = \vartheta$, $\varphi_3 = \varphi$, that indicate consecutively the rotations: by angle $\varphi_1 = \psi$ around the ζ axis, by $\varphi_2 = \vartheta$ around the new position of the ξ axis, and by $\varphi_3 = \varphi$ around the ζ (rotation sequence is abbreviated as $\zeta\text{-}\xi\text{-}\zeta$ or 313). The rotation matrix R for such angles is obtained by substituting into (2.26) the following rotational matrices:

$$R_1(\varphi_1) = R_\zeta(\psi), \quad R_2(\varphi_2) = R_\xi(\vartheta), \quad R_3(\varphi_3) = R_\zeta(\varphi), \quad (2.30)$$

that means

$$R = R_\zeta(\psi)R_\xi(\vartheta)R_\zeta(\varphi). \quad (2.31)$$

In Table 2.1 the set of 12 possible rotation sequences and the singularity condition for each case and values of angles causing singularities in numerical solutions are presented. These singularities arise in the inversion process of the matrix B , which is used to calculate the generalized velocities \dot{q} on the basis of body angular velocity $\tilde{\omega}$ ($\dot{q} = B^{-1}\tilde{\omega}$).

Table 2.1 Singularity condition in the numerical analysis of the rigid body dynamics ($k = 0, 1, \dots$)

Rotation sequence	Singularity condition	Angle indicating singularity
121	$-\sin \varphi_2 = 0$	$\varphi_2 = \pm k\pi$
123	$\cos \varphi_2 = 0$	$\varphi_2 = \frac{\pi}{2} \pm k\pi$
131	$-\sin \varphi_2 = 0$	$\varphi_2 = \pm k\pi$
132	$-\cos \varphi_2 = 0$	$\varphi_2 = \frac{\pi}{2} \pm k\pi$
212	$-\sin \varphi_2 = 0$	$\varphi_2 = \pm k\pi$
213	$-\cos \varphi_2 = 0$	$\varphi_2 = \frac{\pi}{2} \pm k\pi$
231	$\cos \varphi_2 = 0$	$\varphi_2 = \frac{\pi}{2} \pm k\pi$
232	$-\sin \varphi_2 = 0$	$\varphi_2 = \pm k\pi$
312	$\cos \varphi_2 = 0$	$\varphi_2 = \frac{\pi}{2} \pm k\pi$
313	$-\sin \varphi_2 = 0$	$\varphi_2 = \pm k\pi$
321	$-\cos \varphi_2 = 0$	$\varphi_2 = \frac{\pi}{2} \pm k\pi$
323	$-\sin \varphi_2 = 0$	$\varphi_2 = \pm k\pi$

2.3.2 Euler's Parameters

An alternative to Euler's angles and similar conventions of body orientation description are Euler's parameters (also called Euler symmetric parameters and known in mathematics as normalized quaternions) [9, 10, 12]. They are very useful in representing the rotations due to some advantages in comparison to other representations. The main advantage of Euler parameters is that they do not produce any singularities in numerical solutions of body motion equations.

In the matrix notation Euler's parameters are represented by the column matrix

$$\mathbf{p} = \begin{bmatrix} e_0 \\ e_1 \\ e_2 \\ e_3 \end{bmatrix} = \begin{bmatrix} \cos \frac{\phi}{2} \\ v_1 \sin \frac{\phi}{2} \\ v_2 \sin \frac{\phi}{2} \\ v_3 \sin \frac{\phi}{2} \end{bmatrix}, \quad (2.32)$$

or, shortly

$$\mathbf{p} = \begin{bmatrix} e_0 \\ \mathbf{e} \end{bmatrix} = \begin{bmatrix} \cos \frac{\phi}{2} \\ \mathbf{v}^o \sin \frac{\phi}{2} \end{bmatrix}. \quad (2.33)$$

The basis of this method of body orientation description is well known as the Euler theorem stating that any rotation of the rigid body can be expressed as a single rotation about some axis. The axis can be represented by 3D vector \mathbf{v}^o (Fig. 2.9). The vector \mathbf{v}^o is a unit vector and it remains unchanged during the body rotation. The rotation angle ϕ is a scalar value.

The rotation matrix (2.25) can be expressed by Euler parameters as [10]

$$\mathbf{R} = (2e_0^2 - 1)\mathbf{I} + 2\mathbf{ee}^T + 2e_0\mathbf{E}, \quad (2.34)$$

in which \mathbf{I} is the identity matrix of dimensions (3×3) and the matrix \mathbf{E} has the form

$$\mathbf{E} = \begin{bmatrix} 0 & -e_3 & e_2 \\ e_3 & 0 & -e_1 \\ -e_2 & e_1 & 0 \end{bmatrix}. \quad (2.35)$$

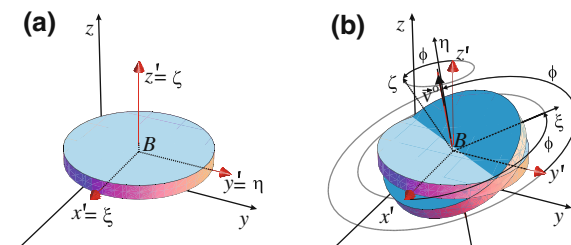


Fig. 2.9 The body rotation by ϕ – around the vector \mathbf{v}^o

The expanded form of the matrix R (2.34) – expressed by unit quaternions (e_0, \dots, e_3) – has the following form:

$$R = \begin{bmatrix} -1 + 2e_0^2 + 2e_1^2 & 2e_1e_2 - 2e_0e_3 & 2e_0e_2 + 2e_1e_3 \\ 2e_1e_2 + 2e_0e_3 & -1 + 2e_0^2 + 2e_2^2 & -2e_0e_1 + 2e_2e_3 \\ -2e_0e_2 + 2e_1e_3 & 2e_0e_1 + 2e_2e_3 & -1 + 2e_0^2 + 2e_3^2 \end{bmatrix}. \quad (2.36)$$

The antisymmetric matrix $\tilde{\Omega}_\xi$ ($\tilde{\Omega}_\xi = R^\top \dot{R}$) containing scalar components of the coin angular velocity vector – in the body embedded frame $\xi\eta\zeta$ – has the form

$$\tilde{\Omega}_\xi = 2 \begin{bmatrix} 0 - \dot{e}_3e_0 + \dot{e}_2e_1 - \dot{e}_1e_2 + \dot{e}_0e_3 & \dot{e}_2e_0 + \dot{e}_3e_1 - \dot{e}_0e_2 - \dot{e}_1e_3 \\ 0 & -\dot{e}_1e_0 + \dot{e}_0e_1 + \dot{e}_3e_2 - \dot{e}_2e_3 \\ \text{asym.} & 0 \end{bmatrix}. \quad (2.37)$$

The angular velocity vector of the coin $\tilde{\omega}_\xi$ in the body embedded frame $\xi\eta\zeta$ is expressed by the column matrix

$$\tilde{\omega}_\xi = \begin{bmatrix} \omega_\xi \\ \omega_\eta \\ \omega_\zeta \end{bmatrix} = 2 \begin{bmatrix} \dot{e}_1e_0 - \dot{e}_0e_1 - \dot{e}_3e_2 + \dot{e}_2e_3 \\ \dot{e}_2e_0 + \dot{e}_3e_1 - \dot{e}_0e_2 - \dot{e}_1e_3 \\ \dot{e}_3e_0 - \dot{e}_2e_1 + \dot{e}_1e_2 - \dot{e}_0e_3 \end{bmatrix}, \quad (2.38)$$

whereas

$$\dot{\tilde{\omega}}_\xi = \begin{bmatrix} \dot{\omega}_\xi \\ \dot{\omega}_\eta \\ \dot{\omega}_\zeta \end{bmatrix} = 2 \begin{bmatrix} -e_1\ddot{e}_0 + e_0\ddot{e}_1 + e_3\ddot{e}_2 - e_2\ddot{e}_3 \\ -e_2\ddot{e}_0 - e_3\ddot{e}_1 + e_0\ddot{e}_2 + e_1\ddot{e}_3 \\ -e_3\ddot{e}_0 + e_2\ddot{e}_1 - e_1\ddot{e}_2 + e_0\ddot{e}_3 \end{bmatrix}. \quad (2.39)$$

The column matrix containing xyz scalar components of the coin angular velocity vector (i.e., the components in fixed spatial frame) has the form

$$\tilde{\omega} = \begin{bmatrix} \omega_x \\ \omega_y \\ \omega_z \end{bmatrix} = 2 \begin{bmatrix} \dot{e}_1e_0 - \dot{e}_0e_1 + \dot{e}_3e_2 - \dot{e}_2e_3 \\ \dot{e}_2e_0 - \dot{e}_3e_1 - \dot{e}_0e_2 + \dot{e}_1e_3 \\ \dot{e}_3e_0 + \dot{e}_2e_1 - \dot{e}_1e_2 - \dot{e}_0e_3 \end{bmatrix}. \quad (2.40)$$

Using Euler's parameters allows to avoid singularities in numerical solutions of body rotation problems. The coin dynamics is one of such problems. The equations of coin dynamics are presented in the following sections. Special attention is paid to the coin dynamics description in quaternions.

2.4 Air Resistance Forces and Moments

To define the right-hand sides of (2.3)–(2.4) or (2.8)–(2.9) the components of the forces acting on the body and moments of these forces with respect to the $C\xi\eta\zeta$ frame axis should be determined.

The determination of the air resistance forces acting on the body is cumbersome due to its variable velocity and a change in the Reynolds number ($Re = \frac{2rv}{v}$) that follows during the toss [13]. (A range of changes in the Reynolds number is wide because of variations in the body velocity: $Re \ll 1$ in the initial stage of its motion (during its fall with a zero initial velocity), $Re \cong 10^4$ – at the velocity of the mass center $v = 10$ m/s and the coin radius $r = 0.01$ m.)

For detailed information on the aerodynamics and fluid mechanics pertinent to this section, see [13–17].

On the basis of kinematic relations for a rigid body, a distribution of velocities on outer surfaces of the body is determined. It has been assumed that the air resistance occurs only on this part of the body surface on which the velocity vectors of its points have a sense compliant with the normal vector to this surface and directed outward from the body. The air resistance force vector \mathbf{f}_r will be determined as a sum of resistance forces (\mathbf{f}_i) on all planes of a body

$$\mathbf{f}_r = \sum_{i=1}^{n_s} \mathbf{f}_i . \quad (2.41)$$

Each of the vectors \mathbf{f}_i is treated as a sum of two components originating from tangential (parallel) and normal (perpendicular) forces to the body surface (S_i). This results in the necessity of using various air resistance coefficients λ_τ for the forces $\mathbf{f}_{i\tau}$ (of the tangential direction (air friction forces)) and λ_n – for the forces \mathbf{f}_{in} in the normal direction (air pressure forces). Hence

$$\mathbf{f}_i = \mathbf{f}_{i\tau} + \mathbf{f}_{in} , \quad (2.42)$$

where $\mathbf{f}_{i\tau}$ and \mathbf{f}_{in} are determined from the relations

$$\mathbf{f}_{i\tau} = -\lambda_\tau \int_{S_i} |\mathbf{v}_{Ai\tau}|^b \mathbf{v}_{Ai\tau} dS_i , \quad (2.43)$$

$$\mathbf{f}_{in} = -\lambda_n \int_{S_i} |\mathbf{v}_{Ain}|^b \mathbf{v}_{Ain} s_i dS_i . \quad (2.44)$$

The symbols used in formulas (2.43)–(2.44) denote, respectively, $\mathbf{v}_{Ai\tau}$ – vector comprising the velocity components tangential to the surface on which the point A_i is situated, \mathbf{v}_{Ain} – vector of velocity components perpendicular to this surface, $|\mathbf{v}_{Ai\tau}|$ and $|\mathbf{v}_{Ain}|$ refer to the values of velocity vectors, and b is a real number that belongs to the range $< 0, 1 >$ (for $b = 0$, the air resistance is linearly dependent on velocity, whereas for $b = 1$, resistance depends on the square of velocity). The functions s_i that occur in (2.44) are described by the following relation:

$$s_i = \frac{1}{2} \operatorname{sign}(\mathbf{v}_{Ain}^T \tilde{\boldsymbol{\eta}}_i^o) (1 + (\mathbf{v}_{Ain}^T \tilde{\boldsymbol{\eta}}_i^o)) \quad (i = 1, 2, 3) , \quad (2.45)$$

where η_i^o are unit vectors, normal to the body surfaces under consideration, directed outward from the body.

The functions s_i allow for the determination of regions in which the air resistance components normal to the surface act. It has been assumed that normal components of resistance forces do not occur in these regions where the velocity vector of points situated on the surface is directed inward the body. The air resistance forces perpendicular to the body surface occur in these body points in which the following condition is satisfied:

$$\mathbf{v}_{Ain}^T \tilde{\eta}_i^o > 0 \quad (i = 1, 2, 3). \quad (2.46)$$

The effect of application of the functions s_i is illustrated in Fig. 3.5.

After the determination of forces, the moments of these forces with respect to the center of mass C (or the chosen pole B) should be determined. The total moment of air resistance forces with respect to the point B has been presented as a sum of the moments m_i originating from resistance forces on all surfaces of the body

$$m_{rB} = \sum_{i=1}^{n_s} m_i, \quad (2.47)$$

where m_i is determined as follows:

$$m_i = -\lambda_n \int_{S_i} |\mathbf{v}_{Ain}|^b R^T R_{BAi} \mathbf{v}_{Ain} s_i dS_i - \lambda_\tau \int_{S_i} |\mathbf{v}_{Ait}|^b R^T R_{BAi} \mathbf{v}_{Ait} dS_i. \quad (2.48)$$

R_{BAi} in (2.48) denotes antisymmetrical matrix including the components of the vector⁵ r_{BAi} .

2.5 Modeling of Bodies Impact

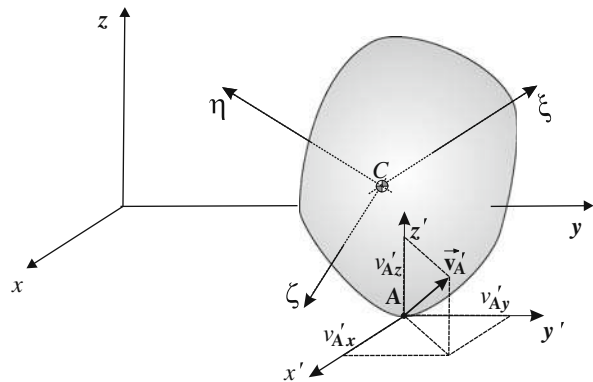
Let us consider that the body collides with a floor when the point A on its surface touches the floor as shown in Fig. 2.10. In the rigid body dynamics the most common model of collision of bodies is based on Newton's hypothesis [5, 7]

$$-\chi = \frac{\dot{v}_{Az}}{v_{Az}}, \quad (2.49)$$

where χ is the coefficient of restitution ($0 < \chi < 1$), A stands for the body point which makes contact with the floor at the instant of impact (Fig. 2.10), v_{Az} and

⁵ In many textbooks – for example, in [10] – following notation is used $R_{BAi} = \tilde{r}_{BAi}$.

Fig. 2.10 Velocity vector \mathbf{v}'_A of the point A after the collision and its scalar components $v_{A\tau}'$, v_{Av}' , v_{Az}'



v_{Az} are projections of the velocity of the point A on the direction (z) normal to the impact surface, respectively, before and after the impact.

Assumption (2.49) means that we include energy losses during the collision and only the momentum is conserved. (In a purely elastic collision of bodies ($\chi = 1$) kinetic energy, linear and angular momentum are conserved.) On the basis of Newton hypothesis we can calculate z component of the reaction force impulse (S_z).

Besides Newton's hypothesis to analyze the phenomena that accompany the impact the laws of linear momentum and angular momentum theorems of a body, as well as supplementary constraint equations, have been employed.

The position of the colliding point (A) in the body embedded frame is described by ξ_A , η_A , ζ_A . Assuming that the collision time is negligibly short the position and the orientation of body after the impact are the same as before the impact.

To describe the motion after the impacts we will use the additional frame with an origin at point A and axis: z' – parallel to the fixed axis z and axes τ , v in the ground plane (Fig. 2.10).

Mosekilde [18] and Feldberg et al. [19] proposed to obtain the value of χ considering free vibrations of dumped oscillator described by equation $m\ddot{z} + \kappa\dot{z} + kz = 0$. It means that during the collision the body vibrates on visco-elastic foundation (κ and k are foundation damping and elasticity coefficients). The illustration for such a model is shown in Fig. 2.11 and sample results are presented in Fig. 2.12.

Comparing the oscillations velocity v_z for $t_0 = 0$ and $t_1 = T/2$ (where $T = 4\pi/\sqrt{\frac{4km-\kappa^2}{m^2}}$) one finds (Fig. 2.12)

Fig. 2.11 Body on visco-elastic foundation

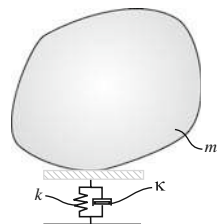
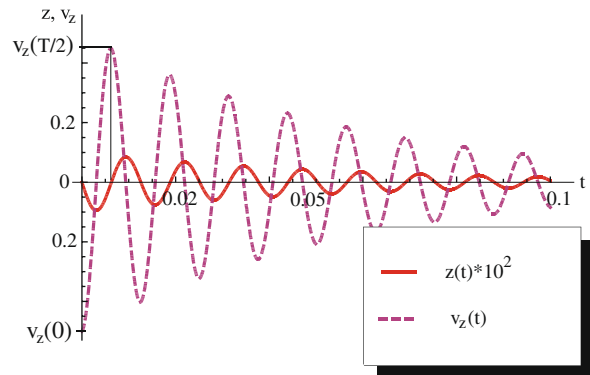


Fig. 2.12 Displacement and velocity of dumped oscillator



$$\chi = \frac{v_z(T/2)}{v_z(0)} = e^{-\frac{2\pi\kappa}{\sqrt{4km-\kappa^2}}} . \quad (2.50)$$

To obtain additional constraint equations we have to consider the model of the contact between the colliding bodies. For specific collision cases (coin, dice, roulette ball) constraint equations are different and are presented in next sections.

References

1. Arnold, V.I.: Mathematical Methods of Classical Mechanics. Springer, New York (1989) 23, 31
2. Beatty, M.F., Jr.: Principles of Engineering Mechanics. Plenum Press, New York (1986) 23
3. Landau, L., Lifschitz, E.: Mechanics. Pergamon Press, Oxford (1976) 23, 30
4. Kittel, C., Knight, W.D., Ruderman, M.A.: Mechanica. Berkeley Physics Course – Volume 1. McGraw-Hill, New York (1965) 23, 27
5. Roth, E.J.: Dynamics of a System of Rigid Bodies. Dover, New York (1960) 23, 30, 37
6. Wittaker, E.T.: Analytical Dynamics of Particles and Rigid Bodies. Cambridge University Press, Cambridge (1937) 23, 31
7. Goldstein, H.: Classical Mechanics. Addison-Wesley, Reading (1950) 23, 31, 37
8. Montgomery, R.: How much does a rigid body rotate? Amer. J. Phys. **59**, 394 (1991) 30
9. Diebel, J.: Representing Attitude: Euler Angles, Unit Quaternions, and Rotation Vectors. <http://ai.stanford.edu/~diebel/>. Cited 15 May 2007 30, 31, 34
10. Nikrevesh, P.E.: Computer-Aided Analysis of Mechanical Systems. Prentice-Hall, Englewood Cliffs, NJ (1988) 30, 34, 37
11. Marsden, J.E., Ratiu, T.S.: Introduction to Mechanics and Symmetry. Springer, New York (1994) 31
12. Altman, S.L.: Rotations, Quaternions, and Double Groups. Oxford University Press, Oxford (1986) 34
13. Long, L., Weiss, H.: The velocity dependence of aerodynamic drag: A primer for mathematicians. Amer. Math. Monthly **106**, 127 (1999) 36
14. Landau, L., Lifschitz E.: Fluid Mechanics. Butterworth and Heinemann, New York (1987) 36
15. McCormick, B.: Aerodynamics, Aeronautics and Flight Mechanics. Wiley, London (1995) 36
16. Thompson, P.A.: Compressible Fluid Dynamics. McGraw-Hill, London (1972) 36
17. White, F.M.: Viscous Fluid Flows. McGraw-Hill, London (1991) 36
18. Mosekilde, E.: Topics in Nonlinear Dynamics: Applications to Physics, Biology and Economic Systems. World Scientific, Singapore (1996) 38
19. Feldberg, R., Szymkat, M., Knudsen, C., Mosekilde, E.: Iterated-map approach to die tossing. Phys. Rev. A **42**/*8*, 4493 (1990) 38

Chapter 3

Equations of the Randomizer's Dynamics

Abstract Basing on the Newton–Euler laws of mechanics we derive the equations which describe the dynamics of the coin toss, the die throw, and roulette run. The equations for full 3D models and for lower dimensional simplifications are given. The influence of the air resistance and energy dissipation at the impacts is described. The obtained equations allow for the numerical simulation of the randomizer's dynamics and define the mapping of the initial conditions into the final outcome.

3.1 Equations of the Coin Toss

3.1.1 Free Fall of a Coin

In the case of a cylinder-shaped coin (or modeled by the cylindrical body) of homogeneous material its center of mass (point C) is situated in the geometrical center of the cylinder (in point B). The body embedded frame axes (ξ , η , ζ) are the axes passing through the center of the mass (Fig. 3.1). As the products of inertia are zeros, these axes are the central axes, and the inertia matrix of the coin (J_c) is a diagonal matrix.

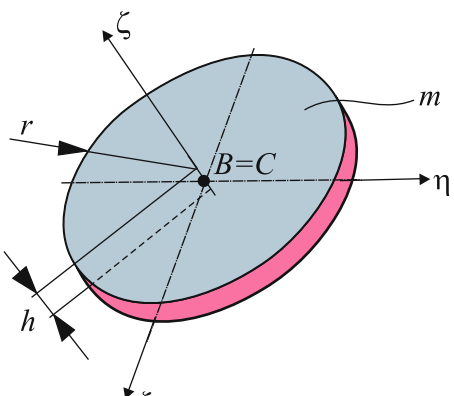


Fig. 3.1 Three-dimensional model of the ideal coin

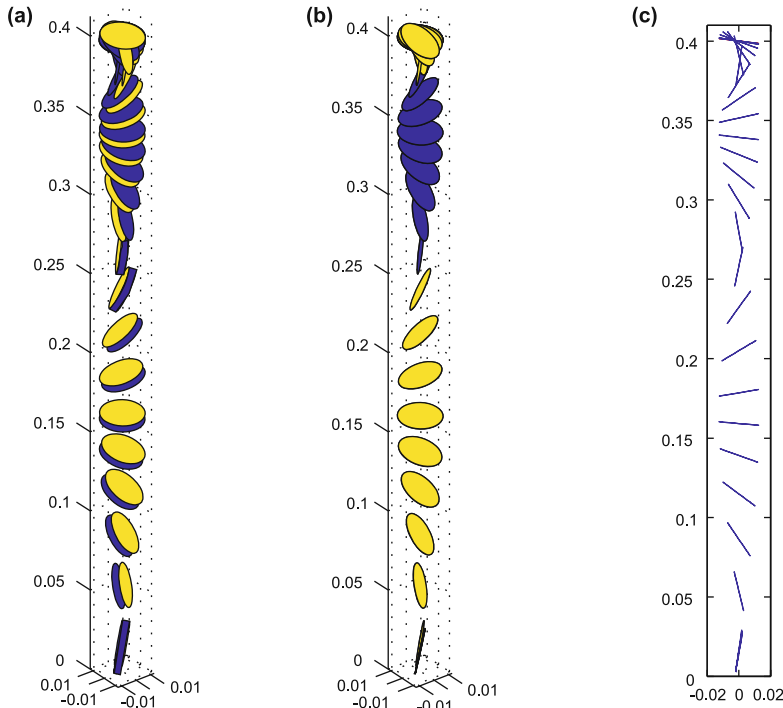


Fig. 3.2 Coin models: (a) 3D coin model; (b) 2D coin model; and (c) 1D coin model

Besides 3D coin model we will consider the simplified models of 2D coin (thin disk, $h = 0$) in the space motion and 1D coin model – disk performing plane motion – in the vertical plane (Fig. 3.2c). (It should be mentioned here that our 1D model in [1–3] was called the 2D one.)

Newton–Euler equations in matrix form ((2.8) and (2.9)) are general equations of motion and are suitable for the dynamic analysis of any body, i.e., a nonsymmetric and nonhomogeneous body. In the case in which the forces \mathbf{F} are independent of the angular velocity of the body and moments \mathbf{m}_c are not the functions of the center of mass accelerations, (2.8) and (2.9) are uncoupled. This happens when air resistance is neglected.

The scalar form of the Newton–Euler equations is described by (2.10) and (2.11).

The full equations of motion for the cases of (i) imperfect, (ii) ideal 3D coin as well as for (iii) 2D and (iv) 1D coin models are shown below. In all equations Euler parameters (normalized quaternions) have been applied.

3.1.1.1 The Equations of Motion of an Imperfect Coin

The first three scalar equations obtained from the general equation (2.10) are common for all coin models:

$$m\ddot{x} = f_x , \quad m\ddot{y} = f_y , \quad m\ddot{z} = f_z . \quad (3.1)$$

If the air resistance of a coin is taken into account then all force components (f_x , f_y , f_z) have nonzero values. (Air resistance forces and their moments are derived in the next section.) In the case of free fall of a body the component f_z is the only force acting on the coin ($f_z = -mg$).

The equations describing the changes in the spatial orientation of the coin obtained from (2.11), expressed in Euler parameters, have the following form [4]:

$$\begin{aligned} & 2((-e_1\dot{e}_0 + e_0\dot{e}_1 + e_3\dot{e}_2 - e_2\dot{e}_3)(2J_{\xi\eta}(-e_3\dot{e}_0 + e_2\dot{e}_1 - e_1\dot{e}_2 + e_0\dot{e}_3) + \\ & + 2J_{\xi\xi}(e_2\dot{e}_0 + e_3\dot{e}_1 - e_0\dot{e}_2 - e_1\dot{e}_3)) + (-e_3\dot{e}_0 + e_2\dot{e}_1 - e_1\dot{e}_2 + e_0\dot{e}_3) + \\ & \times (2J_{\eta\xi}(-e_3\dot{e}_0 + e_2\dot{e}_1 - e_1\dot{e}_2 + e_0\dot{e}_3) + 2J_{\xi}(-e_2\dot{e}_0 - e_3\dot{e}_1 + e_0\dot{e}_2 + e_1\dot{e}_3)) - \\ & - (-e_2\dot{e}_0 - e_3\dot{e}_1 + e_0\dot{e}_2 + e_1\dot{e}_3)(2J_{\eta}(-e_3\dot{e}_0 + e_2\dot{e}_1 - e_1\dot{e}_2 + e_0\dot{e}_3) + \\ & + 2J_{\eta\xi}(-e_2\dot{e}_0 - e_3\dot{e}_1 + e_0\dot{e}_2 + e_1\dot{e}_3)) + J_{\xi\xi}(e_3\ddot{e}_0 - e_2\ddot{e}_1 + e_1\ddot{e}_2 - e_0\ddot{e}_3) + \\ & + J_{\xi\eta}(e_2\ddot{e}_0 + e_3\ddot{e}_1 - e_0\ddot{e}_2 - e_1\ddot{e}_3) + J_{\xi}(-e_1\ddot{e}_0 + e_0\ddot{e}_1 + e_3\ddot{e}_2 - e_2\ddot{e}_3)) = M_{\xi}, \end{aligned} \quad (3.2)$$

$$\begin{aligned} & 4J_{\xi}(e_3\dot{e}_0 - e_2\dot{e}_1 + e_1\dot{e}_2 - e_0\dot{e}_3)(-e_1\dot{e}_0 + e_0\dot{e}_1 + e_3\dot{e}_2 - e_2\dot{e}_3) + \\ & + 4J_{\xi}(-e_3\dot{e}_0 + e_2\dot{e}_1 - e_1\dot{e}_2 + e_0\dot{e}_3)(-e_1\dot{e}_0 + e_0\dot{e}_1 + e_3\dot{e}_2 - e_2\dot{e}_3) + \\ & + 4J_{\eta\xi}(e_2\dot{e}_0 + e_3\dot{e}_1 - e_0\dot{e}_2 - e_1\dot{e}_3)(e_1\dot{e}_0 - e_0\dot{e}_1 - e_3\dot{e}_2 + e_2\dot{e}_3) + \\ & + J_{\xi\xi}(-4(e_3\dot{e}_0 - e_2\dot{e}_1 + e_1\dot{e}_2 - e_0\dot{e}_3)^2 + \\ & + 4(e_1\dot{e}_0 - e_0\dot{e}_1 - e_3\dot{e}_2 + e_2\dot{e}_3)^2) + 2J_{\eta\xi}(e_3\ddot{e}_0 - e_2\ddot{e}_1 + e_1\ddot{e}_2 - e_0\ddot{e}_3) + \\ & + 2J_{\eta}(-e_2\ddot{e}_0 - e_3\ddot{e}_1 + e_0\ddot{e}_2 + e_1\ddot{e}_3) - 2J_{\xi\eta}(2(e_3\dot{e}_0 - e_2\dot{e}_1 + e_1\dot{e}_2 - e_0\dot{e}_3) + \\ & \times (e_2\dot{e}_0 + e_3\dot{e}_1 - e_0\dot{e}_2 - e_1\dot{e}_3) - e_1\ddot{e}_0 + e_0\ddot{e}_1 + e_3\ddot{e}_2 - e_2\ddot{e}_3) = M_{\eta}, \end{aligned} \quad (3.3)$$

$$\begin{aligned} & 2((-e_2\dot{e}_0 - e_3\dot{e}_1 + e_0\dot{e}_2 + e_1\dot{e}_3)(2J_{\xi\eta}(-e_2\dot{e}_0 - e_3\dot{e}_1 + e_0\dot{e}_2 + e_1\dot{e}_3) + \\ & + 2J_{\eta}(-e_1\dot{e}_0 + e_0\dot{e}_1 + e_3\dot{e}_2 - e_2\dot{e}_3)) - (-e_1\dot{e}_0 + e_0\dot{e}_1 + e_3\dot{e}_2 - e_2\dot{e}_3) + \\ & \times (2J_{\xi}(-e_2\dot{e}_0 - e_3\dot{e}_1 + e_0\dot{e}_2 + e_1\dot{e}_3) + 2J_{\xi\eta}(-e_1\dot{e}_0 + e_0\dot{e}_1 + e_3\dot{e}_2 - e_2\dot{e}_3)) + \\ & + (-e_3\dot{e}_0 + e_2\dot{e}_1 - e_1\dot{e}_2 + e_0\dot{e}_3)(2J_{\xi\xi}(-e_2\dot{e}_0 - e_3\dot{e}_1 + e_0\dot{e}_2 + e_1\dot{e}_3) + \\ & + 2J_{\eta\xi}(e_1\dot{e}_0 - e_0\dot{e}_1 - e_3\dot{e}_2 + e_2\dot{e}_3)) + J_{\xi}(-e_3\ddot{e}_0 + e_2\ddot{e}_1 - e_1\ddot{e}_2 + e_0\ddot{e}_3) + \\ & + J_{\eta\xi}(e_2\ddot{e}_0 + e_3\ddot{e}_1 - e_0\ddot{e}_2 - e_1\ddot{e}_3) + J_{\xi\xi}(e_1\ddot{e}_0 - e_0\ddot{e}_1 - e_3\ddot{e}_2 + e_2\ddot{e}_3)) = M_{\xi}. \end{aligned} \quad (3.4)$$

The right-hand side quantities (M_{ξ} , M_{η} , M_{ξ}) denote the moments of air resistance forces with respect to the body embedded axes (central axes $C\xi$, $C\eta$, $C\xi$). The formulas defining these moments for 3D imperfect coin model in the general form ($\mathbf{m}_c = [M_{\xi} \ M_{\eta} \ M_{\xi}]^T$) as well as for particular coin models are presented in Sect. 2.4.

The additional equation that has to be satisfied (constraint equation) in the case when Euler parameters are used as coordinates takes the following form:

$$\dot{e}_0^2 + \dot{e}_1^2 + \dot{e}_2^2 + \dot{e}_3^2 + e_0\ddot{e}_0 + e_1\ddot{e}_1 + e_2\ddot{e}_2 + e_3\ddot{e}_3 = 0 . \quad (3.5)$$

The equations of motion for the imperfect model of a coin (3.1), (3.2), (3.3), and (3.4) after some substitutions allow to write the equations for the cases of ideal 3D coin as well as for 2D and 1D coin models.

3.1.1.2 The Equations of Motion of an Ideal Coin

The equations describing the changes in the spatial orientation of the symmetrical coin obtained from (3.2), (3.3), and (3.4) for $J_\xi = J_\eta = \frac{mr^2}{4} + \frac{mh^2}{12}$, $J_\zeta = \frac{mr^2}{2}$, and $J_{\xi\eta} = J_{\eta\zeta} = J_{\zeta\xi} = 0$, expressed with Euler parameters, are as follows:

$$2 \left(mr^2 (e_3\dot{e}_0 - e_2\dot{e}_1 + e_1\dot{e}_2 - e_0\dot{e}_3) (e_2\dot{e}_0 + e_3\dot{e}_1 - e_0\dot{e}_2 - e_1\dot{e}_3) - \frac{1}{6}m(h^2 + 3r^2) (e_3\dot{e}_0 - e_2\dot{e}_1 + e_1\dot{e}_2 - e_0\dot{e}_3) (e_2\dot{e}_0 + e_3\dot{e}_1 - e_0\dot{e}_2 - e_1\dot{e}_3) - \frac{1}{12}m(h^2 + 3r^2) (e_1\ddot{e}_0 - e_0\ddot{e}_1 - e_3\ddot{e}_2 + e_2\ddot{e}_3) \right) = M_\xi , \quad (3.6)$$

$$\begin{aligned} \frac{1}{6}m(12r^2(e_3\dot{e}_0 - e_2\dot{e}_1 + e_1\dot{e}_2 - e_0\dot{e}_3)(-e_1\dot{e}_0 + e_0\dot{e}_1 + e_3\dot{e}_2 - e_2\dot{e}_3) + \\ + 2(h^2 + 3r^2)(e_3\dot{e}_0 - e_2\dot{e}_1 + e_1\dot{e}_2 - e_0\dot{e}_3)(e_1\dot{e}_0 - e_0\dot{e}_1 - e_3\dot{e}_2 + e_2\dot{e}_3) - \\ - (h^2 + 3r^2)(e_2\ddot{e}_0 + e_3\ddot{e}_1 - e_0\ddot{e}_2 - e_1\ddot{e}_3)) = M_\eta , \end{aligned} \quad (3.7)$$

$$\begin{aligned} \frac{1}{3}m((h^2 + 3r^2)(e_3\dot{e}_0 - e_2\dot{e}_1 + e_1\dot{e}_2 - e_0\dot{e}_3)(e_2\dot{e}_0 + e_3\dot{e}_1 - e_0\dot{e}_2 - e_1\dot{e}_3) + \\ + (h^2 + 3r^2)(e_2\dot{e}_0 + e_3\dot{e}_1 - e_0\dot{e}_2 - e_1\dot{e}_3)(-e_1\dot{e}_0 + e_0\dot{e}_1 + e_3\dot{e}_2 - e_2\dot{e}_3) + \\ + 3r^2(-e_3\ddot{e}_0 + e_2\ddot{e}_1 - e_1\ddot{e}_2 + e_0\ddot{e}_3)) = M_\zeta . \end{aligned} \quad (3.8)$$

3.1.1.3 The Equations of a 2D Coin Model

For the 2D ($h = 0$) imperfect coin model the products of inertia $J_{\eta\zeta} = J_{\zeta\xi} = 0$ are used in (3.2), (3.3), and (3.4). Only one off-diagonal element of a coin inertia matrix remains nonzero ($J_{\xi\eta} \neq 0$). After these substitutions:

$$\begin{aligned} 2(2J_\zeta(-e_3\dot{e}_0 + e_2\dot{e}_1 - e_1\dot{e}_2 + e_0\dot{e}_3)(-e_2\dot{e}_0 - e_3\dot{e}_1 + e_0\dot{e}_2 + e_1\dot{e}_3) - \\ - 2J_\eta(-e_3\dot{e}_0 + e_2\dot{e}_1 - e_1\dot{e}_2 + e_0\dot{e}_3)(-e_2\dot{e}_0 - e_3\dot{e}_1 + e_0\dot{e}_2 + e_1\dot{e}_3) + \\ + 2J_{\xi\eta}(-e_3\dot{e}_0 + e_2\dot{e}_1 - e_1\dot{e}_2 + e_0\dot{e}_3)(-e_1\dot{e}_0 + e_0\dot{e}_1 + e_3\dot{e}_2 - e_2\dot{e}_3) + \\ + J_{\xi\eta}(e_2\ddot{e}_0 + e_3\ddot{e}_1 - e_0\ddot{e}_2 - e_1\ddot{e}_3) + J_\xi(-e_1\ddot{e}_0 + e_0\ddot{e}_1 + e_3\ddot{e}_2 - e_2\ddot{e}_3)) = M_\xi , \end{aligned} \quad (3.9)$$

$$\begin{aligned} 4J_\zeta(e_3\dot{e}_0 - e_2\dot{e}_1 + e_1\dot{e}_2 - e_0\dot{e}_3)(-e_1\dot{e}_0 + e_0\dot{e}_1 + e_3\dot{e}_2 - e_2\dot{e}_3) + \\ + 4J_\xi(-e_3\dot{e}_0 + e_2\dot{e}_1 - e_1\dot{e}_2 + e_0\dot{e}_3)(-e_1\dot{e}_0 + e_0\dot{e}_1 + e_3\dot{e}_2 - e_2\dot{e}_3) + \\ + 2J_\eta(-e_2\ddot{e}_0 - e_3\ddot{e}_1 + e_0\ddot{e}_2 + e_1\ddot{e}_3) - 2J_{\xi\eta}(2(e_3\dot{e}_0 - e_2\dot{e}_1 + e_1\dot{e}_2 - e_0\dot{e}_3) \\ \times (e_2\dot{e}_0 + e_3\dot{e}_1 - e_0\dot{e}_2 - e_1\dot{e}_3) - e_1\ddot{e}_0 + e_0\ddot{e}_1 + e_3\ddot{e}_2 - e_2\ddot{e}_3) = M_\eta , \end{aligned} \quad (3.10)$$

$$\begin{aligned}
& 4J_\eta(e_3\dot{e}_0 - e_2\dot{e}_1 + e_1\dot{e}_2 - e_0\dot{e}_3)(e_2\ddot{e}_0 + e_3\dot{e}_1 - e_0\dot{e}_2 - e_1\dot{e}_3) + \\
& + 4J_{\xi\eta}(e_2\dot{e}_0 + e_3\dot{e}_1 - e_0\dot{e}_2 - e_1\dot{e}_3)^2 + 4J_{\xi\eta}(e_3\dot{e}_0 - e_2\dot{e}_1 + e_1\dot{e}_2 - e_0\dot{e}_3) \\
& \times (-e_1\dot{e}_0 + e_0\dot{e}_1 + e_3\dot{e}_2 - e_2\dot{e}_3) + 4J_\xi(e_2\dot{e}_0 + e_3\dot{e}_1 - e_0\dot{e}_2 - e_1\dot{e}_3) \\
& \times (-e_1\dot{e}_0 + e_0\dot{e}_1 + e_3\dot{e}_2 - e_2\dot{e}_3) + 2J_\zeta(-e_3\ddot{e}_0 + e_2\ddot{e}_1 - e_1\ddot{e}_2 + e_0\ddot{e}_3) = M_\zeta .
\end{aligned} \quad (3.11)$$

3.1.1.4 The Equations of a 1D Coin Model

Let us assume that the coin is thin ($h = 0$, $J_{\xi\xi} = J_{\eta\xi} = 0$), it rotates only around the ξ -axis ($\omega_\eta = \omega_\zeta = 0$ and $\dot{\omega}_\eta = \dot{\omega}_\zeta = 0$), what means that ξ remains horizontal during motion. In this case one obtains 1D model of the coin shown in Fig. 3.3 and general equations (3.1), (3.2), (3.3), and (3.4) can be simplified as follows:

$$m\ddot{x} = f_x, \quad m\ddot{y} = f_y, \quad m\ddot{z} = f_z, \quad (3.12)$$

$$2J_\xi(-e_1\ddot{e}_0 + e_0\ddot{e}_1 + e_3\ddot{e}_2 - e_2\ddot{e}_3) = M_\xi, \quad (3.13)$$

$$-2J_{\xi\eta}(-e_1\ddot{e}_0 + e_0\ddot{e}_1 + e_3\ddot{e}_2 - e_2\ddot{e}_3) = M_\eta, \quad (3.14)$$

$$-4J_{\xi\eta}(e_1\dot{e}_0 - e_0\dot{e}_1 - e_3\dot{e}_2 + e_2\dot{e}_3)^2 = M_\zeta. \quad (3.15)$$

It is possible to show that last three equations are identical with $J_\xi\ddot{\vartheta} = M_\xi$, $-J_{\xi\eta}\dot{\vartheta} = M_\eta$, $0 = M_\zeta$, i.e., with the dynamic equations describing the rotations of a rigid body ($J_{\xi\xi} = J_{\eta\xi} = 0$) in plane motion – expressed in rotation angle ϑ (one of the Euler angles). In this case the body rotates by ϑ about the ξ axis parallel to x what means that the rotation angle ϕ is equal to ϑ ($\phi = \vartheta$) and the unit vector

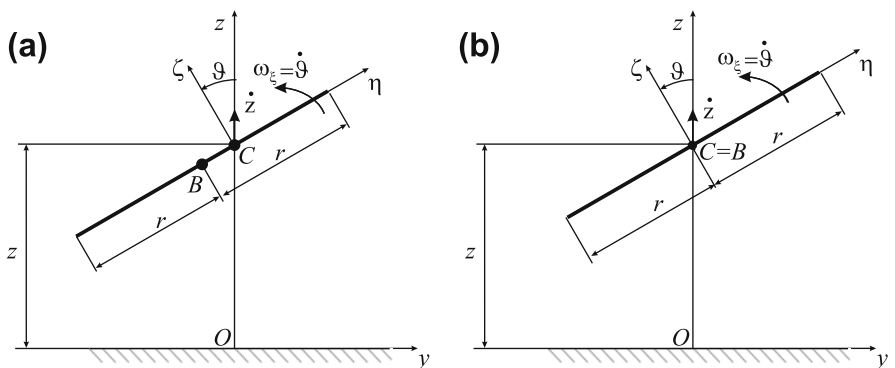


Fig. 3.3 One-dimensional coin models (yz projection): (a) an imperfect coin and (b) an ideal coin

\mathbf{v} has the x -axis direction ($v_1 = 1, v_2 = 0, v_3 = 0$). Euler parameters (2.32) are as follows:

$$\mathbf{p} = \begin{bmatrix} e_0 \\ e_1 \\ e_2 \\ e_3 \end{bmatrix} = \begin{bmatrix} \cos \frac{\vartheta}{2} \\ v_1 \sin \frac{\vartheta}{2} \\ 0 \\ 0 \end{bmatrix}. \quad (3.16)$$

Substituting $e_0 = \cos \frac{\vartheta}{2}, e_1 = \sin \frac{\vartheta}{2}, e_2 = e_3 = 0$ into (3.13), (3.14), and (3.15) leads to

$$-e_1\ddot{e}_0 + e_0\ddot{e}_1 + e_3\ddot{e}_2 - e_2\ddot{e}_3 = \frac{\ddot{\vartheta}}{2} \left(\sin^2 \frac{\vartheta}{2} + \cos^2 \frac{\vartheta}{2} \right) = \frac{\ddot{\vartheta}}{2}, \quad (3.17)$$

$$e_1\dot{e}_0 - e_0\dot{e}_1 - e_3\dot{e}_2 + e_2\dot{e}_3 = -\frac{\dot{\vartheta}}{2} \left(\sin^2 \frac{\vartheta}{2} + \cos^2 \frac{\vartheta}{2} \right) = -\frac{\dot{\vartheta}}{2}, \quad (3.18)$$

hence

$$J_{\xi}\ddot{\vartheta} = M_{\xi}, \quad -J_{\xi\eta}\ddot{\vartheta} = M_{\eta}, \quad -J_{\xi\eta}\dot{\vartheta}^2 = M_{\zeta}. \quad (3.19)$$

In Fig. 3.3 1D models of an imperfect coin and an ideal coin are shown.

Assuming that the coin is symmetric with respect to the $\eta\zeta$ plane ($J_{\xi\eta} = 0$) we find the dynamic equations of the plane motion of the coin in the form

$$\begin{aligned} m\ddot{x} &= f_x, & m\ddot{y} &= f_y, & m\ddot{z} &= f_z \\ J_{\xi}\ddot{\vartheta} &= M_{\xi}, & 0 &= M_{\eta}, & 0 &= M_{\zeta}. \end{aligned} \quad (3.20)$$

It should be mentioned here that although in a 1D model the coin reminds us of a bar (as in Fig. 3.3) in (3.20) one has to consider the moment of inertia for a cylinder or a disk, i.e., $J_{\xi} = \frac{mr^2}{4} + \frac{mh^2}{12}$ or $J_{\eta} = \frac{mr^2}{4}$. Substituting the bar moment of inertia $J_{\xi} = J_{\eta} = \frac{ml^2}{12}$ into (3.20) one solves the problem of the plane motion of the bar [1, 2]. Such model can be used in the discussion of the mechanical randomizers but cannot be used as model of a tossed coin.

3.1.2 Coin Motion in the Air

A cylindrical model of the coin with a base radius r and a height h , performing a general motion, is subject of analysis (Fig. 3.4). On the basis of kinematic relations for a rigid body, a distribution of velocities on outer surfaces of the cylinder is determined. It has been assumed that the air resistance occurs only on this part of the

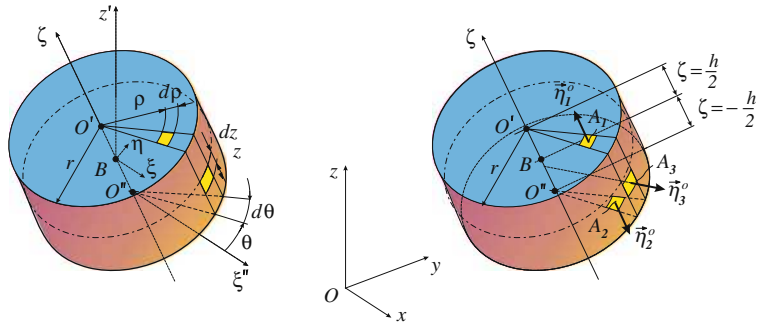


Fig. 3.4 Quantities used to determine air resistance forces \mathbf{f}_1 , \mathbf{f}_2 , and \mathbf{f}_3 (unit vectors of coin planes: η_1^o , η_2^o , and cylindrical outer surface η_3^o)

cylinder surface on which the velocity vectors of its points have a sense compliant with the normal vector to this surface and directed outward from the body.

The air resistance force vector \mathbf{f}_r is determined as a sum of resistance forces on both the cylinder base planes (\mathbf{f}_1 and \mathbf{f}_2) and resistance forces on the lateral surface (\mathbf{f}_3):

$$\mathbf{f}_r = \mathbf{f}_1 + \mathbf{f}_2 + \mathbf{f}_3 . \quad (3.21)$$

Vector \mathbf{f}_1 denotes the resistance forces occurring on one plane of the coin ($\zeta = \frac{h}{2}$), whereas \mathbf{f}_3 stands for the resistance forces on the second plane ($\zeta = -\frac{h}{2}$). Each of the vectors \mathbf{f}_1 , \mathbf{f}_2 , and \mathbf{f}_3 is treated as a sum of two components originating from tangential (parallel) and normal (perpendicular) forces to the body surface. This results in the necessity of using various air resistance coefficients λ_τ for the forces $\mathbf{f}_{1\tau}$, $\mathbf{f}_{2\tau}$ (of the tangential direction – air friction forces) and λ_n – for the forces \mathbf{f}_{in} in the normal direction (air pressure forces). Hence

$$\mathbf{f}_i = \mathbf{f}_{i\tau} + \mathbf{f}_{in} \quad (i = 1, 2, 3) , \quad (3.22)$$

where $\mathbf{f}_{i\tau}$ and $\mathbf{f}_{2\tau}$ are determined from the relation

$$\mathbf{f}_{i\tau} = -\lambda_\tau \int_0^r \left(\int_0^{2\pi} |\mathbf{v}_{Ait}|^b \mathbf{v}_{Ait} \rho d\theta \right) d\rho \quad (i = 1, 2) , \quad (3.23)$$

$$\mathbf{f}_{in} = -\lambda_n \int_0^r \left(\int_0^{2\pi} |\mathbf{v}_{Ain}|^b \mathbf{v}_{Ain} s_i \rho d\theta \right) d\rho \quad (i = 1, 2) , \quad (3.24)$$

and \mathbf{f}_{1n} and \mathbf{f}_{2n} are defined by

$$\mathbf{f}_{3\tau} = -\lambda_{\tau} \int_{-h/2}^{h/2} \left(\int_0^{2\pi} |\mathbf{v}_{A3\tau}|^b \mathbf{v}_{A3\tau} r d\theta \right) dz , \quad (3.25)$$

$$\mathbf{f}_{3n} = -\lambda_n \int_{-h/2}^{h/2} \left(\int_0^{2\pi} |\mathbf{v}_{A3n}|^b \mathbf{v}_{A3n} s_3 r d\theta \right) dz . \quad (3.26)$$

The symbols used in formulas (3.23), (3.24), (3.25), and (3.26) denote, respectively, r the radius of the coin, $\mathbf{v}_{A\tau}$ the vector comprising the velocity components tangential to the surface on which the point A_i is situated, and \mathbf{v}_{Ain} – vector of velocity components perpendicular to this surface, $|\mathbf{v}_{A\tau}|$ and $|\mathbf{v}_{Ain}|$ refer to the values of velocity vectors, and b is a real number that belongs to the range $[0, 1]$ (for $b = 0$, the air resistance is linearly dependent on velocity, whereas for $b = 1$ resistance depends on the square of velocity). The functions s_i that occur in formula (3.24) are described by (2.45), i.e.,

$$s_i = \frac{1}{2} \operatorname{sign}(\mathbf{v}_{Ain}^T \tilde{\boldsymbol{\eta}}_i^o) (1 + \operatorname{sign}(\mathbf{v}_{Ain}^T \tilde{\boldsymbol{\eta}}_i^o)) \quad (i = 1, 2, 3) , \quad (3.27)$$

where $\boldsymbol{\eta}_i^o$ are unit vectors, normal to the coin surfaces under consideration, directed outward from the coin (Fig. 3.4). The vectors $\boldsymbol{\eta}_i^o$ – in the xyz frame – are defined (in the matrix form) as follows:

$$\tilde{\boldsymbol{\eta}}_i^o = R \tilde{\boldsymbol{\eta}}_i \quad (i = 1, 2, 3) , \quad (3.28)$$

where

$$\tilde{\boldsymbol{\eta}}_1 = \begin{bmatrix} 0 \\ 0 \\ 1 \end{bmatrix} , \quad \tilde{\boldsymbol{\eta}}_2 = \begin{bmatrix} 0 \\ 0 \\ -1 \end{bmatrix} , \quad \tilde{\boldsymbol{\eta}}_3 = \begin{bmatrix} \cos \theta \\ \sin \theta \\ 0 \end{bmatrix} . \quad (3.29)$$

The effect of application of the functions s_i (3.27) is illustrated in Fig. 3.5.

3.1.2.1 The Velocity Fields on the Coin Surfaces

The symbol \mathbf{v}_{A1} denotes a column matrix that includes the coordinates of the velocity vector of the point A_1 , that is to say, of an arbitrary point situated on the plane $\zeta = \frac{h}{2}$ (Fig. 3.4). The components of this vector along the normal direction to the surface are represented by the matrix vector \mathbf{v}_{A1n} , whereas $\mathbf{v}_{A1\tau}$ includes the velocity components of the tangential direction to the surface where point A_1 is situated on. The tangential and normal components are determined from the relationship

$$\mathbf{v}_{A1n} = RH_1R^T \mathbf{v}_{A1} , \quad \mathbf{v}_{A1\tau} = \mathbf{v}_{A1} - \mathbf{v}_{A1n} , \quad (3.30)$$

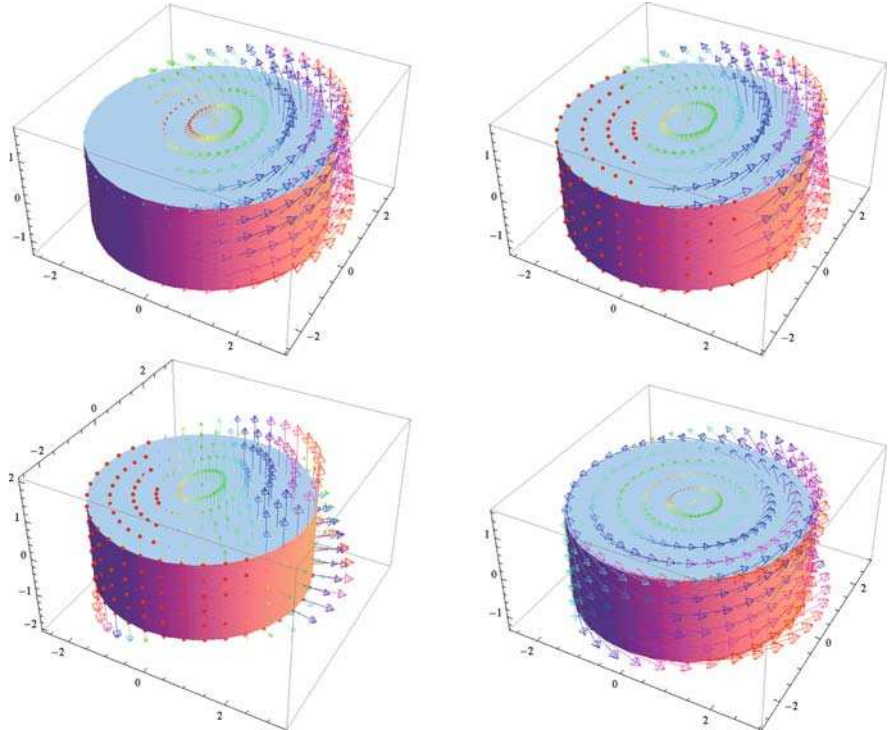


Fig. 3.5 Velocity vectors of points lying on the coin surfaces: (a) total velocities; (b) velocities with senses directed outward from the body; (c) normal components with senses directed outward from the body; and (d) tangential components of total velocities

where

$$\begin{aligned} \mathbf{v}_{A1} &= \mathbf{v}_B + \tilde{\boldsymbol{\Omega}} \mathbf{r}_{BA1}, & \mathbf{v}_B &= \mathbf{v}_C + \tilde{\boldsymbol{\Omega}} \mathbf{r}_{CB}, & \mathbf{v}_C &= [\dot{x} \quad \dot{y} \quad \dot{z}]^T, \\ \mathbf{r}_{BA1} &= \mathbf{R} \boldsymbol{\rho}_1, & \mathbf{r}_{CB} &= -\mathbf{R} \boldsymbol{\rho}_{BC}, \\ \boldsymbol{\rho}_1 &= [\rho \cos \theta \quad \rho \sin \theta \quad \frac{h}{2}]^T, & \boldsymbol{\rho}_{BC} &= [\xi_c \quad \eta_c \quad \zeta_c]^T, \end{aligned} \quad (3.31)$$

where \mathbf{R} is a transformation matrix of the coordinates from the frame $B\xi\eta\zeta$ (Fig. 3.4) into the frame xyz , and \mathbf{H}_1 is a zero–one matrix in the form

$$\mathbf{H}_1 = \begin{bmatrix} 0 & 0 & 0 \\ 0 & 0 & 0 \\ 0 & 0 & 1 \end{bmatrix}. \quad (3.32)$$

To avoid misunderstanding, let us add that the vectors (the column matrices) \mathbf{v}_{A1} , \mathbf{v}_B , \mathbf{v}_C , \mathbf{r}_{BA1} , \mathbf{r}_{CB} , \mathbf{v}_{A1n} , \mathbf{v}_{A1t} are defined by the coordinates in the xyz frame, the matrix $\tilde{\boldsymbol{\Omega}}$ is defined in the xyz frame, and the vectors $\boldsymbol{\rho}_1$, $\boldsymbol{\rho}_{BC}$ are determined by the coordinates in the moving frame $\xi\eta\zeta$. After the transformations that follow from formulas (3.30)

and (3.31), the expressions that define the components of velocity of individual points lying on the body surface are obtained.

Similarly, as for the plane $\zeta = \frac{h}{2}$, the tangential and normal components of the velocity v_{A_2} of the point A_2 lying on the plane $\zeta = -\frac{h}{2}$ (Fig. 3.4) are determined:

$$\begin{aligned} v_{A_{2n}} &= RH_1 R^T v_{A_2}, & v_{A_{2\tau}} &= v_{A_2} - v_{A_{2n}}, & v_{A_2} &= v_B + \tilde{\Omega} r_{BA_2}, \\ r_{BA_2} &= R\rho_2, & \rho_2 &= [\rho \cos \theta \quad \rho \sin \theta \quad -\frac{h}{2}]^T. \end{aligned} \quad (3.33)$$

The symbols $v_{A_{3n}}$, $v_{A_{3\tau}}$ denote the matrices of components of velocity of the point (A_3) lying on the lateral surface of the cylinder that are determined on the basis of the following relation:

$$\begin{aligned} v_{A_{3n}} &= RR_\theta H_3 R_\theta^T R^T v_{A_3}, & v_{A_{3\tau}} &= v_{A_3} - v_{A_{3n}}, \\ v_{A_3} &= v_B + \tilde{\Omega} r_{BA_3}, & r_{BA_3} &= R\rho_3, \end{aligned} \quad (3.34)$$

where ρ_3 is a vector that defines the position of this point in the frame $\xi\eta\zeta$:

$$\rho_3 = [r \cos \theta \quad r \sin \theta \quad z]^T, \quad (3.35)$$

and the matrix H_3 has the form as follows:

$$H_3 = \begin{bmatrix} 1 & 0 & 0 \\ 0 & 0 & 0 \\ 0 & 0 & 0 \end{bmatrix}. \quad (3.36)$$

Some sample results of the calculations of velocity of points lying on the coin surfaces and the effect of application of the functions s_1 , s_2 , and s_3 are presented in Fig. 3.5. The application of these functions in the calculation procedures allows for the determination of the regions where the components of resistance forces normal to each surface act. The components of air resistance forces tangential to the body surfaces are determined on the whole outer surface of the body. The normal components of resistance forces occur in these regions only when the velocity vector of points lying on the surface is directed outward from the body (in Fig. 3.5b, c, the velocity vectors with senses directed inward the body are shown as points).

3.1.2.2 Air Resistance Forces

The distribution of air resistance forces corresponds to the velocity distributions of points situated on outer surfaces of the coin. On the assumption that the resistance forces are proportional to velocity (that is to say, after the substitution of $b = 0$ in the formulas describing resistance forces), the distribution of forces normal to individual coin surfaces is such as in Fig. 3.5c, and the distribution of tangential

forces complies with Fig. 3.5d (the senses of resistance forces are opposite to the senses of the velocity vectors). On the basis of formulas (3.23) and (3.24), the resultant of the resistance forces acting on the first coin surface (including the point A_1 (Fig. 3.4)) is described as follows:

$$\begin{aligned} \mathbf{f}_1 = & -\lambda_n \int_0^r \left(\int_0^{2\pi} |\mathbf{v}_{A1n}|^b \mathbf{v}_{A1n} s_1 \rho d\theta \right) d\rho - \\ & - \lambda_\tau \int_0^r \left(\int_0^{2\pi} |\mathbf{v}_{A1\tau}|^b \mathbf{v}_{A1\tau} \rho d\theta \right) d\rho . \end{aligned} \quad (3.37)$$

As it has been mentioned before, the function s_1 allows for the selection of regions in which the resistance forces perpendicular to the body surface occur and are given by

$$s_1 = \frac{1}{2} \operatorname{sign}(\mathbf{v}_{A1n}^T \tilde{\boldsymbol{\eta}}_1^o) (1 + \operatorname{sign}(\mathbf{v}_{A1n}^T \tilde{\boldsymbol{\eta}}_1^o)) . \quad (3.38)$$

In a similar way, the resistance forces occurring on the second surface ($\zeta = -\frac{h}{2}$), where the point A_2 is situated (Fig. 3.4), are determined:

$$\begin{aligned} \mathbf{f}_2 = & -\lambda_n \int_0^r \left(\int_0^{2\pi} |\mathbf{v}_{A2n}|^b \mathbf{v}_{A2n} s_2 \rho d\theta \right) d\rho - \\ & - \lambda_\tau \int_0^r \left(\int_0^{2\pi} |\mathbf{v}_{A2\tau}|^b \mathbf{v}_{A2\tau} \rho d\theta \right) d\rho , \end{aligned} \quad (3.39)$$

with the function s_2 given by

$$s_2 = \frac{1}{2} \operatorname{sign}(\mathbf{v}_{A2n}^T \tilde{\boldsymbol{\eta}}_2^o) (1 + \operatorname{sign}(\mathbf{v}_{A2n}^T \tilde{\boldsymbol{\eta}}_2^o)) , \quad (3.40)$$

whereas $\tilde{\boldsymbol{\eta}}_2^o$ is a unit vector, normal to the coin surface ($\zeta = -\frac{h}{2}$) and directed outward from the coin (Fig. 3.4). The air resistance force (\mathbf{f}_3) arising on the lateral side of the cylinder is determined as follows:

$$\begin{aligned} \mathbf{f}_3 = & -\lambda_n \int_{-h/2}^{h/2} \left(\int_0^{2\pi} |\mathbf{v}_{A3n}|^b \mathbf{v}_{A3n} s_3 r d\theta \right) dz - \\ & - \lambda_\tau \int_{-h/2}^{h/2} \left(\int_0^{2\pi} |\mathbf{v}_{A3\tau}|^b \mathbf{v}_{A3\tau} r d\theta \right) dz . \end{aligned} \quad (3.41)$$

Function s_3 takes the form

$$s_3 = \frac{1}{2} \operatorname{sign}(\mathbf{v}_{A3n}^T \tilde{\eta}_3^o) (1 + \operatorname{sign}(\mathbf{v}_{A3n}^T \tilde{\eta}_3^o)) , \quad (3.42)$$

where η_3^o is a unit vector, normal to the cylindrical surface of the coin and directed outward from the coin.

Using formulas (3.37), (3.39) and (3.41) we are not able to obtain the resistance forces in an analytical form. It is not possible to find a closed form of integral of the terms containing the function sign (.). Therefore, the resistant forces have been integrated partly analytically and partly numerically.

The resultant vectors of tangential forces to each surface ($\mathbf{f}_{i\tau}$) can be presented in an explicit (analytical) form.

The resultant vector of the resistance forces \mathbf{f}_{1n} , normal to the plane $\zeta = \frac{h}{2}$, is determined on the basis of (3.37) as $\mathbf{f}_{1n} = -\lambda_n \int_0^r \left(\int_0^{2\pi} |\mathbf{v}_{A1n}|^b \mathbf{v}_{A1n} s_1 \rho d\varphi \right) d\rho$. As in the integrated expression, a selection function of the velocity s_1 occurs; the calculations are conducted numerically for the given numerical data. The numerical calculations are carried out for the discrete velocity field of points lying on the body surface. The integration is performed in these regions only where the velocities of the points (\mathbf{v}_{A1n}) are directed outward from the body (Fig. 3.5c).

Similarly, the resultant vectors of the forces \mathbf{f}_{2n} , \mathbf{f}_{3n} are determined numerically, and the vectors $\mathbf{f}_{2\tau}$, $\mathbf{f}_{3\tau}$ are determined explicitly.

3.1.2.3 Moments of Air Resistance Forces

The total moment of air resistance forces with respect to point B has been presented as a sum of the moments (m_1 and m_2) originating from resistance forces on both planes of the cylinder base and the moments of resistance forces on the cylindrical surface (m_3):

$$m_{rB} = m_1 + m_2 + m_3 , \quad (3.43)$$

whereas m_1 and m_2 are determined from formula (3.44) (for $i = 1, 2$)

$$\begin{aligned} m_i = & -\lambda_n \int_0^r \left(\int_0^{2\pi} |\mathbf{v}_{Ain}|^b \mathbf{R}^T \mathbf{R}_{BAi} \mathbf{v}_{Ain} s_i \rho d\theta \right) d\rho - \\ & - \lambda_\tau \int_0^r \left(\int_0^{2\pi} |\mathbf{v}_{Ait}|^b \mathbf{R}^T \mathbf{R}_{BAi} \mathbf{v}_{Ait} \rho d\theta \right) d\rho , \end{aligned} \quad (3.44)$$

and m_3 is expressed by the relation

$$\begin{aligned} m_3 = & -\lambda_n \int_{-h/2}^{h/2} \left(\int_0^{2\pi} |\mathbf{v}_{A3n}|^b R^T R_{BA3} \mathbf{v}_{A3n} s_3 r d\theta \right) dz - \\ & - \lambda_\tau \int_{-h/2}^{h/2} \left(\int_0^{2\pi} |\mathbf{v}_{A3\tau}|^b R^T R_{BA3} \mathbf{v}_{A3\tau} r d\theta \right) dz , \end{aligned} \quad (3.45)$$

where R_{BA1} , R_{BA2} , and R_{BA3} in formulas (3.44)–(3.45) denote antisymmetrical matrices including the components of the vectors, respectively, \mathbf{r}_{BA1} (3.31), \mathbf{r}_{BA2} (3.33), and \mathbf{r}_{BA3} (3.34) that can be expressed symbolically as $R_{BA1} = \tilde{\mathbf{r}}_{BA1}$, $R_{BA2} = \tilde{\mathbf{r}}_{BA2}$, $R_{BA3} = \tilde{\mathbf{r}}_{BA3}$.

Only the tangent components of resultant moment of air resistance forces m_{rB} are determined explicitly. The normal components are calculated numerically after the discretization of actual velocity field on the coin body.

3.1.2.4 Simplified Models of Coin–Air Interaction

If the thickness of the coin h is negligible in comparison to its radius r , then it can be assumed that $h \rightarrow 0$ in the computational model. Thus, the formulas generated in the previous section can be employed after the substitution of $h = 0$.

In this paragraph, we show how the formulas that describe air resistance for a simplified 2D model of the coin can be derived from the general relationships. In this way the relations that define not only the resultant of the air resistance forces tangential to the coin surface but also the resultant of normal forces can be determined explicitly. For a thin coin ($h = 0$), the velocities of points situated on both planes are identical:

$$\mathbf{v}_{A1} = \mathbf{v}_{A2} , \quad \mathbf{v}_{A1\tau} = \mathbf{v}_{A2\tau} , \quad \mathbf{v}_{A1n} = \mathbf{v}_{A2n} . \quad (3.46)$$

After the calculations in which the general relations (3.30) and (3.31) have been used, the normal components of velocity (for $h = 0$ and $\zeta_c = 0$) are obtained in the explicit form.

The velocity vectors of points situated on both planes of the 2D coin model have been depicted in Fig. 3.6.

3.1.2.5 Air Resistance Forces and Moments for a Thin Coin

While determining a sum of normal components of the resistance forces ($\mathbf{f}_{1n} + \mathbf{f}_{2n}$), acting on the planes at both sides of the coin, on the basis of (3.24) we obtain

$$\begin{aligned} \mathbf{f}_{1n} + \mathbf{f}_{2n} = & -\lambda_{n1} \int_0^r \left(\int_0^{2\pi} |\mathbf{v}_{A1n}|^b \mathbf{v}_{A1n} s_1 \rho d\theta \right) d\rho - \\ & - \lambda_{n2} \int_0^r \left(\int_0^{2\pi} |\mathbf{v}_{A2n}|^b \mathbf{v}_{A2n} s_2 \rho d\theta \right) d\rho . \end{aligned} \quad (3.47)$$

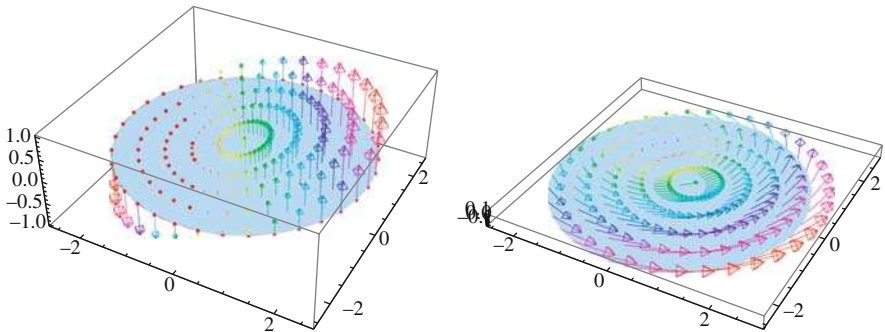


Fig. 3.6 Velocity vectors of points situated on the surfaces of the 2D coin model: (a) normal velocity components with senses outward from the body and (b) tangential components of total velocities

On the assumption that the coefficients λ_{n1} and λ_{n2} are identical ($\lambda_{n1} = \lambda_{n2} = \lambda_n$), relation (3.47) can be expressed as follows:

$$\mathbf{f}_{1n} + \mathbf{f}_{2n} = -\lambda_n \int_0^r \left(\int_0^{2\pi} |\mathbf{v}_{A1n}|^b \mathbf{v}_{A1n} (s_1 + s_2) \rho d\theta \right) d\rho . \quad (3.48)$$

From the properties of the functions s_1 (3.38) and s_2 (3.40), it results that in the case under consideration ($\mathbf{v}_{A1n} = \mathbf{v}_{A2n}$ and $\eta_1^o = -\eta_2^o$):

$$\begin{aligned} s_1 + s_2 &= \frac{1}{2} \text{sign}(\mathbf{v}_{A1n}^T \boldsymbol{\eta}_1^o) (1 + \text{sign}(\mathbf{v}_{A1n}^T \boldsymbol{\eta}_1^o)) + \\ &+ \frac{1}{2} \text{sign}(\mathbf{v}_{A1n}^T (-\boldsymbol{\eta}_1^o)) (1 + \text{sign}(\mathbf{v}_{A1n}^T (-\boldsymbol{\eta}_1^o))) = 1 . \end{aligned} \quad (3.49)$$

Thus, the resultant of the resistance forces with normal directions to the coin surface ($\mathbf{f}_{1n} + \mathbf{f}_{2n}$) can be expressed by the formula

$$\mathbf{f}_{1n} + \mathbf{f}_{2n} = -\lambda_n \int_0^r \left(\int_0^{2\pi} |\mathbf{v}_{A1n}|^b \mathbf{v}_{A1n} \rho d\theta \right) d\rho . \quad (3.50)$$

If it is additionally assumed that for the thin coin ($h = 0$), the air forces acting on the coin cylindrical surface are equal to zero ($\mathbf{f}_{3n} = 0$ and $\mathbf{f}_{3\tau} = 0$), one gets

$$\mathbf{f}_n = \mathbf{f}_{1n} + \mathbf{f}_{2n} + \mathbf{f}_{3n} = -\lambda_n \int_0^r \left(\int_0^{2\pi} |\mathbf{v}_{A1n}|^b \mathbf{v}_{A1n} \rho d\theta \right) d\rho . \quad (3.51)$$

The determination of the resultant of the forces tangential to the coin surface ($\mathbf{f}_\tau = \mathbf{f}_{1\tau} + \mathbf{f}_{2\tau} + \mathbf{f}_{3\tau}$), defined by (3.23), on the assumption that $\mathbf{f}_{3\tau} = 0$, $\mathbf{v}_{A1\tau} = \mathbf{v}_{A2\tau}$, and $\lambda_{\tau 1} = \lambda_{\tau 2} = \lambda_\tau$ leads to

$$\mathbf{f}_\tau = \mathbf{f}_{1\tau} + \mathbf{f}_{2\tau} + \mathbf{f}_{3\tau} = -2\lambda_\tau \int_0^r \left(\int_0^{2\pi} |\mathbf{v}_{A1\tau}|^b \mathbf{v}_{A1\tau} \rho d\theta \right) d\rho . \quad (3.52)$$

Similarly, as with the forces, the moments originating from the resistance forces acting on the lateral surface of the coin are neglected ($\mathbf{m}_3 = 0$) in the case of the thin coin. While determining a sum of the moments of normal components of resistance forces ($\mathbf{m}_1 + \mathbf{m}_2$), acting on the planes on both sides of the coin, on the basis of (3.44) (for $\mathbf{v}_{A1} = \mathbf{v}_{A2}$, $\lambda_{n1} = \lambda_{n2} = \lambda_n$, $\lambda_{\tau1} = \lambda_{\tau2} = \lambda_\tau$), we obtain the matrices

$$\mathbf{v}_{Bn} = \mathbf{v}_{1n} + \mathbf{v}_{2n} = -\lambda_n \int_0^r \left(\int_0^{2\pi} |\mathbf{v}_{A1n}|^b \mathbf{R}^\top \mathbf{R}_{BA1} \mathbf{v}_{A1n} \rho d\theta \right) d\rho , \quad (3.53)$$

$$\mathbf{v}_{B\tau} = \mathbf{v}_{1\tau} + \mathbf{v}_{2\tau} = -2\lambda_\tau \int_0^r \left(\int_0^{2\pi} |\mathbf{v}_{A1\tau}|^b \mathbf{R}^\top \mathbf{R}_{BA1} \mathbf{v}_{A1\tau} \rho d\theta \right) d\rho . \quad (3.54)$$

For the thin coin ($h = 0$), both tangential and normal components of the resistance force moment vector with respect to the point B (and the point C) can be defined explicitly.

3.1.2.6 Resistance Forces Acting on the Disk in Plane Motion

In this paragraph, the relations that describe resistance forces and their momenta for a plane motion of the thin coin, and the more general case of motion “without precession and self-rotation” (or, in other words, a screw motion about the axis moving with a translatory motion) are given.

The equations with the identical structure as the bar dynamics equations can be used to describe a motion of the coin model only in such a case when the coefficients occurring in these equations characterize the coin (the coin model in the form of the thin disk). These equations can be obtained as a special case of the dynamics equations of the 3D coin model, assuming that the disk thickness $h = 0$ and that the following restrictions $\omega_\eta = 0$, $\omega_\zeta = 0$ (angular velocity $\omega_\xi = \vartheta$) are imposed on the body motion. Moreover, it is assumed that the coin mass center moves along the axis η ($\eta_c \neq 0$, $\xi_c = 0$, $\zeta_c = 0$).

To perform such motion, it should be additionally assumed that the initial angular velocity of the coin has zero components $\omega_\eta(t = 0) = 0$, $\omega_\zeta(t = 0) = 0$ and the initial orientation $\vartheta(t = 0) = 0$ and $\psi(t = 0) = 0$.

We consider here the coin whose mass center (C) (and the geometrical center (B)) moves in the plane yz ($x = 0$), and the angular velocity vector is constantly perpendicular to the plane yz (the axis ξ keeps the constant direction; it is parallel to the axis x). The angles of spin and precession remain equal to zero ($\varphi = 0$, $\psi = 0$). The motion of such a coin is identical to the motion of the bar with the

same parameters as the coin and identical loadings generated by air resistance, i.e.,

$$f_n = -\pi r^2 \lambda_n \begin{bmatrix} 0 \\ \sin \vartheta (\eta_c \omega_\xi + \dot{y} \sin \vartheta - \dot{z} \cos \vartheta) \\ \cos \vartheta (\eta_c \omega_\xi + \dot{y} \sin \vartheta - \dot{z} \cos \vartheta) \end{bmatrix}, \quad (3.55)$$

$$f_r = -2\pi r^2 \lambda_r \begin{bmatrix} \dot{x} \\ \cos \vartheta (\dot{y} \cos \vartheta + \dot{z} \sin \vartheta) \\ \sin \vartheta (\dot{y} \cos \vartheta + \dot{z} \sin \vartheta) \end{bmatrix}. \quad (3.56)$$

The total moment of resistance forces with respect to the mass center (C), for the model of the thin, symmetrical coin under consideration, for $\omega_\eta = 0$, $\omega_\zeta = 0$ is determined as

$$m_c = -\frac{\pi r^2}{4} \lambda_n \begin{bmatrix} (r^2 + 4\eta_c^2)\omega_\xi + 4\eta_c(\dot{y} \sin \vartheta - \dot{z} \cos \vartheta) \\ 0 \\ 0 \end{bmatrix}, \quad (3.57)$$

and with respect to the geometrical center (point B) as

$$m_B = -\frac{\pi r^4}{4} \lambda_n \begin{bmatrix} \omega_\xi \\ 0 \\ 0 \end{bmatrix}. \quad (3.58)$$

(While deriving the above-mentioned formulas, it was assumed that the air resistance was linearly dependent on velocity, i.e., the case $b = 0$ is considered).

The effect of air resistance is better visible in the exemplary calculations conducted for an ideal coin ($\xi_c = 0$, $\zeta_c = 0$) with negligible thickness ($h = 0$) and with the assumption that the axes $\xi \eta \zeta$ are the main axes of inertia. The data assumed in the calculations are the same scaled parameters as in [1, 2] (i.e., $r = 1$ m, $m = 1$ kg, $g = 1$ m/s²). The coin falls from the assumed height z_0 with a zero initial velocity of the mass center and the assumed initial angular velocity $\omega_{\xi 0} = \dot{\vartheta}_0$ ($\omega_\eta = 0$, $\omega_\zeta = 0$). It has been also assumed in [1, 2] that air resistance is linearly dependent on velocity ($b = 0$). The values of components of resistance forces have been determined from relations (3.55)–(3.56). The total moment of resistance forces with respect to the geometrical center (B), for the model of the thin, ideal coin under analysis, has been obtained from (3.58).

Figure 3.7 presents an exemplary diagram showing changes in the acceleration (Fig. 3.7b) and the velocity (Fig. 3.7a) of the mass center of the coin, including the air resistance effect, whereas Fig. 3.8 depicts changes in the rotation angle ϑ (coin inclination angle) and the vertical component of the resistance force f_z . Solid lines

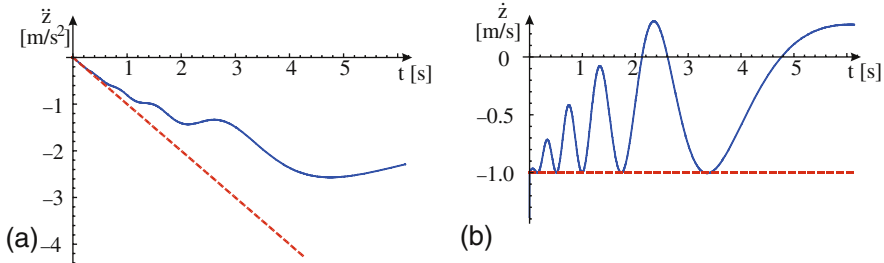


Fig. 3.7 Time series of the mass center of an ideal coin: (a) the acceleration, (b) the velocity ($r = 1$ m, $m = 1$ kg, $g = 1$ m/s²; air resistance characterized by $\lambda_n = 0.3, \lambda_\tau = 0$ — solid line, air resistance neglected – dashed line)

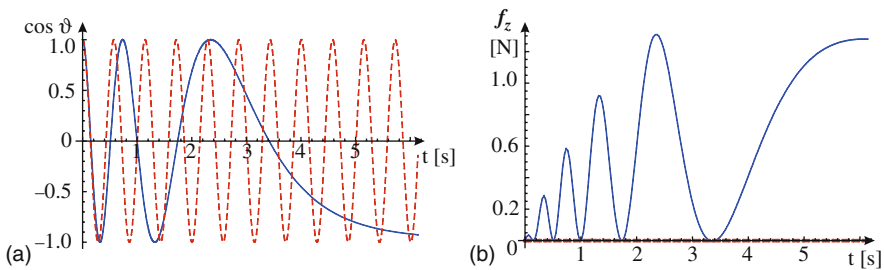


Fig. 3.8 Time series of (a) cosine ϑ (ϑ – coin inclination angle), (b) air resistance vertical component f_z ($r = 1$ m, $m = 1$ kg, $g = 1$ m/s²; air resistance characterized by $\lambda_n = 0.3, \lambda_\tau = 0$ — solid line, air resistance neglected – dashed line)

represent the cases where air resistance has been neglected, whereas the dashed lines have been calculated for air resistance characterized by $\lambda_n = 0.3, \lambda_\tau = 0$.

It follows from the comparison of results, including the effect of air resistance and neglecting the effect of these resistance forces, that an influence of resistance can be significant (as in the case of $\lambda_n = 0.3$ shown in Fig. 3.8). The velocity and acceleration of the mass center are not straight lines – as in the case where resistance is neglected – but they exhibit an oscillating character (similarly as the force f_z). The frequency of these oscillations decreases with a decrease in the coin angular velocity ($\dot{\vartheta}$). The plot of the function $\cos \vartheta$ points out to the fact that the changes in the angle ϑ occur slowly, and at the sufficiently long fall time, ϑ attains a constant value.

Generally, air resistance is a potential confounding factor. The air resistance causes the deviation of the trajectory of the mass center from the vertical axis and damps the rotation of the coin. In the case of the real coin, this deviation is small and only if the distance of the free fall is very long (a few tens of meters) the coin falls like a leaf, fluttering to the floor.

3.1.2.7 Resistance Forces Acting on the Thin Bar

To analyze the dynamics of the coin, which rotates about the horizontal axis, e.g., the ξ axis of the constant direction, a 1D model of the coin – a uniform bar [1] – can be employed. In [1] the length, the mass of the bar, and the gravitational acceleration are scaled as $l = 2$, $m = 1$, and $g = 1$, respectively. The structure of the bar is uniform, so its inertia moment is given as $J = 1/3$.

One can notice here that the direct application of the dynamics equations obtained for the bar in plane motion to model the coin motion is not obvious due to the differences in the geometry and differences in the mass distribution in the bar and the disk. For the equal mass m and the dimensions $l = 2r$, various values of the mass moment of inertia have to be used in the dynamics equations for the bar and the disk. The disk with a mass $m = 1 \text{ kg}$ and a radius $r = 1 \text{ m}$ has the inertia moment $J_\xi = \frac{1}{4} \text{ kg m}^2$, whereas for the bar of the same mass and a length $l = 2r$, we obtain $J_\xi = \frac{1}{3} \text{ kg m}^2$, assuming that the axis ξ goes through the body mass center.

For the bar with a negligible low thickness, performing a plane motion in the plane yz (Fig. 3.9), the resistance force f_r and its moment m_b can be expressed by the following relations:

$$f_r = -A_n \int_{-l}^l |v_{An}|^b v_{An} d\rho - A_\tau \int_{-l}^l |v_{At}|^b v_{At} d\rho , \quad (3.59)$$

$$m_b = -A_n \int_{-l}^l |v_{An}|^b R^T R_{BA} v_{An} d\rho - A_\tau \int_{-l}^l |v_{At}|^b R^T R_{BA} v_{At} d\rho , \quad (3.60)$$

where l denotes half the length of the bar, v_A is a vector that includes the velocity components of the point (A) lying at the distance ρ from its center (B), v_{An} and v_{At} are components of the column matrix v_A of the perpendicular and parallel directions to the coin surface, and b is a real number from the range $\langle 0, 1 \rangle$. The resistance coefficients for the bar have been denoted by A_n and A_τ , to distinguish them from the resistance coefficients for the disk, as they differ not only as far as values are concerned but they are expressed in various units as well.

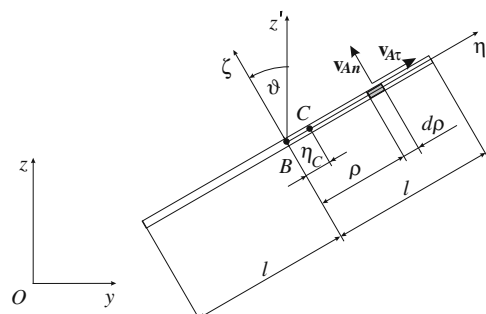


Fig. 3.9 One-dimensional coin model

The vectors (column matrices) occurring in (3.59) and (3.60) and the matrices R_{BA} , $\tilde{\Omega}$, R are thus given by the following relations:

$$\mathbf{v}_A = \mathbf{v}_B + \tilde{\Omega} \mathbf{r}_{BA}, \quad \mathbf{v}_B = \mathbf{v}_C + \tilde{\Omega} \mathbf{r}_{CB}, \quad \mathbf{v}_C = [0 \ \dot{y} \ \dot{z}]^T, \quad (3.61)$$

$$\mathbf{r}_{BA} = [0 \ \rho \cos \vartheta \ \rho \sin \vartheta]^T, \quad \mathbf{r}_{CB} = [0 \ -\eta_c \cos \vartheta \ -\eta_c \sin \vartheta]^T,$$

$$R_{BA} = \begin{bmatrix} 0 & -\rho \sin \vartheta & \rho \cos \vartheta \\ \rho \sin \vartheta & 0 & 0 \\ -\rho \cos \vartheta & 0 & 0 \end{bmatrix}, \quad (3.62)$$

$$\tilde{\Omega} = \begin{bmatrix} 0 & 0 & 0 \\ 0 & 0 & -\omega_\xi \\ 0 & \omega_\xi & 0 \end{bmatrix}, \quad R = \begin{bmatrix} 1 & 0 & 0 \\ 0 \cos \vartheta & -\sin \vartheta & 0 \\ 0 \sin \vartheta & \cos \vartheta & 0 \end{bmatrix}. \quad (3.63)$$

After some mathematical operations (and the substitution of $\omega_\xi = \dot{\vartheta}$), we obtain

$$\mathbf{v}_A = \begin{bmatrix} 0 \\ \dot{y} - (\rho - \eta_c)\dot{\vartheta} \sin \vartheta \\ \dot{z} + (\rho - \eta_c)\dot{\vartheta} \cos \vartheta \end{bmatrix}, \quad \mathbf{v}_{At} = \begin{bmatrix} 0 \\ \cos \vartheta (\dot{y} \cos \vartheta + \dot{z} \sin \vartheta) \\ \sin \vartheta (\dot{y} \cos \vartheta + \dot{z} \sin \vartheta) \end{bmatrix}, \quad (3.64)$$

$$\mathbf{v}_{An} = \begin{bmatrix} 0 \\ -\sin \vartheta ((\rho - \eta_c)\dot{\vartheta} - \dot{y} \sin \vartheta + \dot{z} \cos \vartheta) \\ \cos \vartheta ((\rho - \eta_c)\dot{\vartheta} - \dot{y} \sin \vartheta + \dot{z} \cos \vartheta) \end{bmatrix}. \quad (3.65)$$

The resultant resistance forces tangential and normal to the bar are defined by the formulas

$$\mathbf{f}_t = -4l \Lambda_t \begin{bmatrix} 0 \\ \cos \vartheta (\dot{y} \cos \vartheta + \dot{z} \sin \vartheta) \\ \sin \vartheta (\dot{y} \cos \vartheta + \dot{z} \sin \vartheta) \end{bmatrix}, \quad (3.66)$$

$$\mathbf{f}_n = -2l \Lambda_n \begin{bmatrix} 0 \\ \sin \vartheta (\eta_c \dot{\vartheta} + \dot{y} \sin \vartheta - \dot{z} \cos \vartheta) \\ -\cos \vartheta (\eta_c \dot{\vartheta} + \dot{y} \sin \vartheta - \dot{z} \cos \vartheta) \end{bmatrix}. \quad (3.67)$$

The vectors \mathbf{f}_t , \mathbf{f}_n and \mathbf{v}_A , \mathbf{v}_{At} , \mathbf{v}_{An} are defined in the frame xyz . The moment resultant vector \mathbf{m}_B ($\mathbf{m}_B = \mathbf{m}_{Bt} + \mathbf{m}_{Bn}$) is expressed through the components in the body

embedded frame $(\xi \eta \zeta)$ as follows:

$$\mathbf{m}_B = \mathbf{m}_{Br} + \mathbf{m}_{Bn} = \begin{bmatrix} 0 \\ 0 \\ 0 \end{bmatrix} + \begin{bmatrix} -\frac{2}{3}l^3 \Lambda_n \dot{\vartheta} \\ 0 \\ 0 \end{bmatrix} = -\frac{2}{3}l^3 \Lambda_n \begin{bmatrix} \dot{\vartheta} \\ 0 \\ 0 \end{bmatrix}. \quad (3.68)$$

Analogously, the vector \mathbf{m}_C ($\mathbf{m}_C = \mathbf{m}_{Cr} + \mathbf{m}_{Cn}$) is given by

$$\mathbf{m}_C = \begin{bmatrix} -\frac{2}{3}l \Lambda_n ((l^2 + 3\eta_C^2)\dot{\vartheta} + 3\eta_C \dot{y} \sin \vartheta - 3\eta_C \dot{z} \cos \vartheta) \\ 0 \\ 0 \end{bmatrix}. \quad (3.69)$$

In the case of symmetrical bar (the points B and C overlap), after the integration of (3.60), we obtain

$$\mathbf{m}_B = \mathbf{m}_{rB} = -\frac{2}{3}l^3 \Lambda_n [\dot{\vartheta} \ 0 \ 0]^T. \quad (3.70)$$

In Fig. 3.10 the results of the simulation of the bar motion for various air resistance coefficients in the normal direction to the bar (Λ_n) and in the tangential

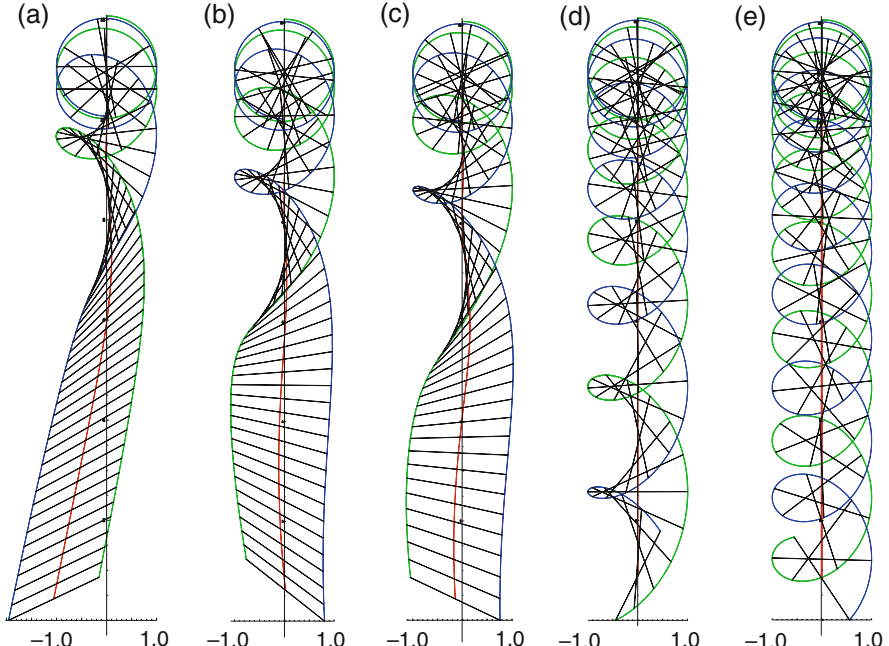


Fig. 3.10 Simulation of the bar motion – trajectory of the mass center and the trajectories of the bar ends for some values of coefficients Λ_n and Λ_τ : (a) for $\Lambda_n = 0.4$, $\Lambda_\tau = 0.1$; (b) for $\Lambda_n = 0.3$, $\Lambda_\tau = 0.075$; (c) for $\Lambda_n = 0.3$, $\Lambda_\tau = 0$; (d) for $\Lambda_n = 0.1$, $\Lambda_\tau = 0.025$; and (e) for $\Lambda_n = 0$, $\Lambda_\tau = 0$

direction (Λ_τ) are depicted. The trajectory of the mass center and the trajectories of the bar ends are shown. The differences in the motion for the assumed motion parameters are distinct. The fact that the influence of air resistance has been considered is followed by the changes in the body angular velocity. Moreover, it causes deflections of the mass center trajectory (as well as of other points of the body) from the trajectory obtained when this factor is neglected (Fig. 3.10e).

In Figs. 3.11 and 3.12 the changes in the velocity and acceleration of the bar mass center and the bar inclination cosine angle, as well as the vertical component of the total resistance force acting on the bar are shown. The results presented in Fig. 3.11 refer to two cases of the motion simulation for the data that differ in the resistance

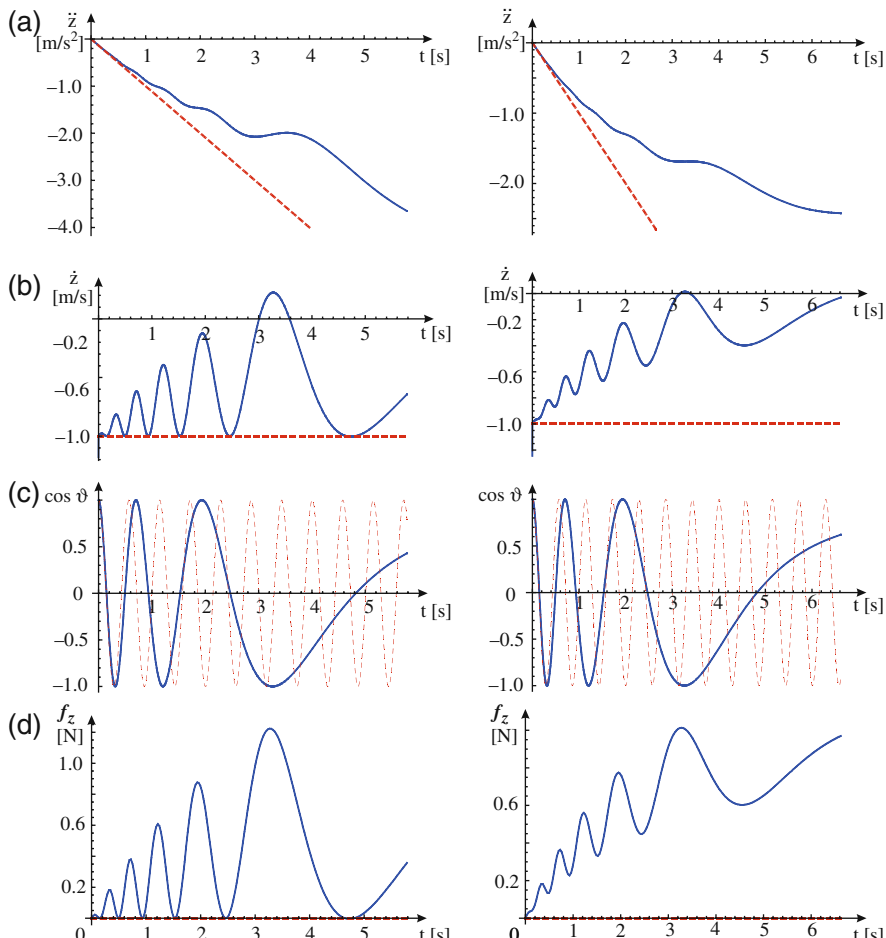


Fig. 3.11 Comparison of time series of: (a) velocity $\dot{z}(t)$; (b) acceleration $\ddot{z}(t)$; (c) cosine of bar inclination angle ($\cos \vartheta(t)$); and (d) vertical components of resistance force $f_z(t)$. Solid line (—) air resistance included (results for $\Lambda_n = 0.3$, $\Lambda_\tau = 0.0$ and for $\Lambda_n = 0.3$, $\Lambda_\tau = 0.075$), dashed line (---) air resistance omitted

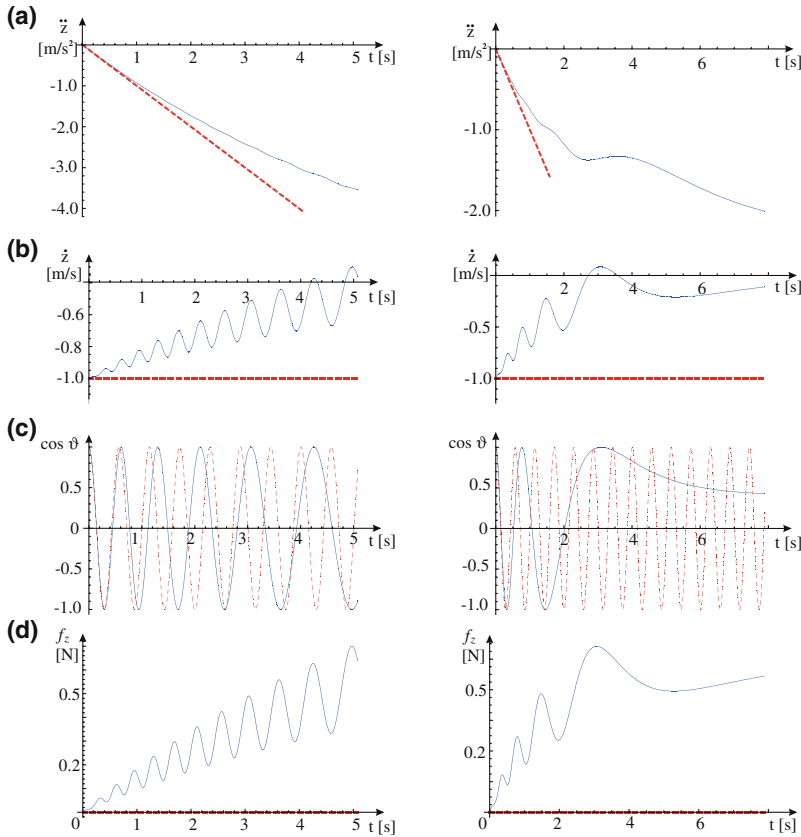


Fig. 3.12 Comparison of time series of (a) velocity $\dot{z}(t)$; (b) acceleration $\ddot{z}(t)$; (c) cosine of bar inclination angle ($\cos \vartheta(t)$); and (d) vertical component of resistance force $f_z(t)$. Solid line (—) air resistance included (results for $\Lambda_n = 0.1$, $\Lambda_\tau = 0.025$ and for $\Lambda_n = 0.4$, $\Lambda_\tau = 0.1$), dashed line (- - -) air resistance omitted

coefficient for the tangential direction (Λ_τ). It follows from the comparison of these figures that the fact that the air resistance is taken into consideration results in a change of the character of the velocity and acceleration of the bar mass center. In an appropriate plot instead of linear relations (a dashed line in the Fig. 3.11), nonlinear dependencies appear. These changes are caused by the action of resistance forces that exhibit an oscillating nature (Fig. 3.11d). It is worth noticing that the consideration of only normal components of resistance forces, i.e., $\Lambda_n > 0$, $\Lambda_\tau = 0$ results in the increase of the resultant resistance force (f_z), and then with the decrease to zero at the instant when the bar goes through the vertical position (for $\vartheta = 0, \pi, 2\pi, \dots$). If the tangential forces ($\Lambda_\tau > 0$) are taken into consideration, then air resistance can be analyzed also in the case when the bar is in the vertical position.

The results presented in Fig. 3.12 illustrate the remaining two cases of motion for which the mass center trajectory has been determined (Fig. 3.10). It follows from

the calculations that an increase in resistance coefficients leads to a disappearance of resistance force oscillations and consequently to a disappearance of oscillations of the mass center velocity and the bar angular velocity.

The results of the conducted calculations presented in Fig. 3.13 illustrate the differences in the behavior of the bar and the thin coin. At identical numerical parameters for both models $r = l/2 = 1$, $m = 1$ and for the same values of the resistance coefficients λ_n , Λ_n and λ_τ , Λ_τ , the motion simulations show different dynamical behaviors. The differences result from various values of inertia momenta and different values of resistance forces and their momenta for the bar and the disk (these differences follow from the different shapes of the models being compared). The conclusion that can be drawn on the basis of the analysis and simulations presented in this section is as follows: the thin disk that performs a plane motion is the proper 1D model of the coin. (The equations of the bar dynamics have the identical structure as for the case of the disk motion under consideration, but the coefficients that occur in them are defined by different relations.)

The 1D model can be an adequate model for the coin only in a particular case when

- the coin mass center moves along one plane,
- the vector of the coin total angular velocity is perpendicular to the plane determined by its mass center trajectory.

It follows from the considerations presented that the 1D coin model can be employed to analyze its dynamics even if air resistance is to be taken into account. The simulation of the coin toss conducted for 1D model is, however, restricted to such cases in which the coin angular velocity vector is horizontal and has a constant direction ($\omega = \dot{\vartheta}$).

The equations with the identical structure as the bar dynamic equations can be used to describe a motion of the coin model only in such a case when the coefficients

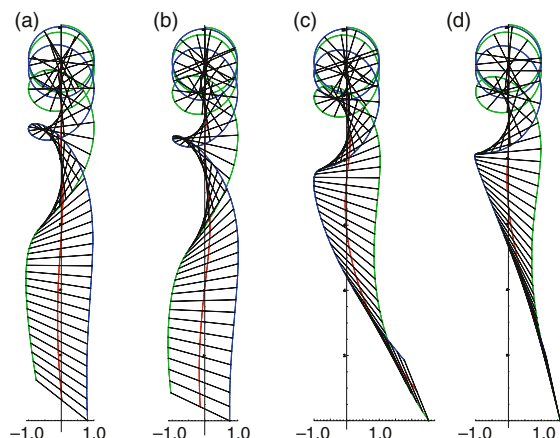


Fig. 3.13 Comparison of simulation results for the bar:
(a) $\Lambda_\tau = 0.075$; **(b)** $\Lambda_\tau = 0$ and thin disk; **(c)** $\lambda_\tau = 0$; **(d)** $\lambda_\tau = 0.075$ (coefficients $\Lambda_n = \lambda_n = 0.3$)

occurring in these equations characterize the coin (the coin model in the form of the thin disk).

3.1.3 Coin Bounces on the Floor

Let us consider that the imperfect coin collides with a floor when the point A on its edge touches the floor as shown in Fig. 3.14. Assuming Newton's hypothesis one gets

$$-\chi = \frac{v'_{Az}}{v_{Az}}, \quad (3.71)$$

where χ is the coefficient of restitution, A represents for the coin point in contact with the floor at the instant of impact (Fig. 3.14), v'_{Az} and v_{Az} are projections of the velocity of point A on the direction (z) normal to the impact surface, respectively, after and before the impact.

The position of point A in the body embedded frame is described by ξ_A , η_A , ζ_A (point A is located on the coin edge in one of the coin planes). To describe the impacts consider the additional frame with an origin at point A and axis: z' – parallel to the fixed axis z and axes τ , v in the ground plane (Fig. 3.14).

To analyze the phenomena that accompany the impact Newton's hypothesis, the laws of linear momentum and angular momentum theorems of a body, as well as constraint equations have been employed. These equations – expressed in Euler parameters – have the following form:

- Newton's hypothesis

$$\begin{aligned} & (2e_0^2 + 2e_3^2 - 1)(\omega'_\xi \eta_A - \omega'_\eta \xi_A) + (2e_0 e_1 + 2e_2 e_3)(\omega'_\xi \xi_A - \omega'_\xi \zeta_A) + \\ & + (2e_1 e_3 - 2e_0 e_2)(\omega'_\eta \zeta_A - \omega'_\zeta \eta_A) + \dot{z}' = \\ & = -\chi ((2e_0^2 + 2e_3^2 - 1)(\omega_\xi \eta_A - \omega_\eta \xi_A) + \\ & + (2e_0 e_1 + 2e_2 e_3)(\omega_\xi \xi_A - \omega_\xi \zeta_A) + (2e_1 e_3 - 2e_0 e_2)(\omega_\eta \zeta_A - \omega_\zeta \eta_A) + \dot{z}); \end{aligned} \quad (3.72)$$

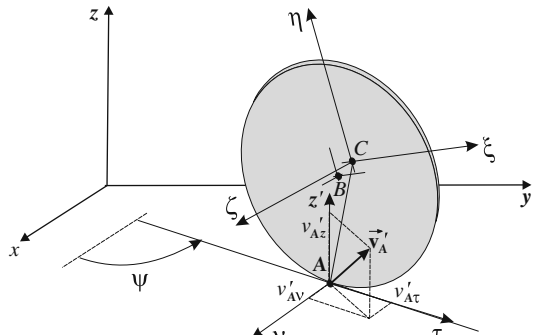


Fig. 3.14 Velocity vector v'_A of the point A after the collision and its scalar components v'_{At} , v'_{Av} , v'_{Az}

– linear momentum theorem

$$m\dot{x}' - S_x = m\dot{x}, \quad m\dot{y}' - S_y = m\dot{y}, \quad m\dot{z}' - S_z = m\dot{z}; \quad (3.73)$$

– angular momentum theorem

$$\begin{aligned} & 2\xi_A S_x e_0^2 - 2\eta_A S_z e_0^2 - 2e_2 \eta_A S_x e_0 - 2e_3 \xi_A S_x e_0 + \\ & + 2e_1 \eta_A S_y e_0 + 2e_1 \xi_A S_z e_0 + J_\xi \omega'_\xi - J_{\xi\eta} \omega'_\eta - \\ & - J_{\xi\zeta} \omega'_\zeta - 2e_1 e_3 \eta_A S_x + 2e_1 e_2 \xi_A S_x - 2e_2 e_3 \eta_A S_y + \\ & + 2e_2^2 \xi_A S_y - \xi_A S_y - 2e_3^2 \eta_A S_z + \eta_A S_z + 2e_2 e_3 \xi_A S_z = \\ & = J_\xi \omega_\xi - J_{\xi\eta} \omega_\eta - J_{\xi\zeta} \omega_\zeta, \end{aligned} \quad (3.74)$$

$$\begin{aligned} & -2\xi_A S_x e_0^2 + 2\xi_A S_z e_0^2 + 2e_2 \xi_A S_x e_0 - 2e_1 \xi_A S_y e_0 - \\ & - 2e_3 \xi_A S_y e_0 + 2e_2 \xi_A S_z e_0 - J_{\xi\eta} \omega'_\xi + J_\eta \omega_\eta - J_{\eta\zeta} \omega'_\zeta + \\ & + 2e_1 e_3 \xi_A S_x - 2e_1^2 \xi_A S_x + \xi_A S_x + 2e_2 e_3 \xi_A S_y - \\ & - 2e_1 e_2 \xi_A S_y + 2e_3^2 \xi_A S_z - \xi_A S_z - 2e_1 e_3 \xi_A S_z = \\ & = -J_{\xi\eta} \omega_\xi + J_\eta \omega_\eta - J_{\eta\zeta} \omega_\zeta, \end{aligned} \quad (3.75)$$

$$\begin{aligned} & 2\eta_A S_x e_0^2 - 2\xi_A S_y e_0^2 + 2e_3 \xi_A S_x e_0 + 2e_3 \eta_A S_y e_0 - \\ & - 2e_1 \xi_A S_z e_0 - 2e_2 \eta_A S_z e_0 - J_{\xi\zeta} \omega'_\xi - J_{\eta\zeta} \omega'_\eta + \\ & + J_\zeta \omega'_\zeta - 2e_1 e_2 \xi_A S_x + 2e_1^2 \eta_A S_x - \eta_A S_x - 2e_2^2 \xi_A S_y + \\ & + \xi_A S_y + 2e_1 e_2 \eta_A S_y - 2e_2 e_3 \xi_A S_z + 2e_1 e_3 \eta_A S_z = \\ & = -J_{\xi\zeta} \omega_\xi - J_{\eta\zeta} \omega_\eta + J_\zeta \omega_\zeta. \end{aligned} \quad (3.76)$$

S_x, S_y, S_z are the components of the impulse (\mathbf{S}) of base reaction (\mathbf{R}) defined in the fixed frame of coordinates (x, y, z) ; $\omega_\xi, \omega_\eta, \omega_\zeta$ denote the components of the angular velocity in the moving frame of reference ξ, η, ζ . There are nine unknowns in (3.72), (3.73), (3.74), (3.75), and (3.76). These equations are ordered in such a way that the unknown quantities $(\dot{x}', \dot{y}', \dot{z}', \omega'_\xi, \omega'_\eta, \omega'_\zeta, S_x, S_y, S_z)$ are on the left-hand side.

To obtain two additional equations we have to consider the model of the contact between the coin and the horizontal plane surface (ground, floor). According to Neimark and Fufaev [5] several different models of collision effect can be considered as shown in Fig. 3.15.

The individual cases differ as far as the values of the components of the velocity vector of the contact point (A) of the coin with the surface along the tangential direction (before the impact $(v_{A\tau})$ and after the impact $(v'_{A\tau})$) and along the normal direction (v_{Av} and v'_{Av}) or the impulse of the ground reaction (\mathbf{S}_{tv}) are concerned, namely

- (a) the coin with a sharp edge $v'_{Az} = -\chi v_{Az}, v'_{Av} = 0, v'_{A\tau} = v_{A\tau},$
- (b) the knurled coin $v'_{Az} = -\chi v_{Az}, v'_{Av} = v_{Av}, v'_{A\tau} = 0,$
- (c) the perfectly rough coin $v'_{Az} = -\chi v_{Az}, v'_{Av} = 0, v'_{A\tau} = 0,$
- (d) the smooth-frictionless coin (1) $v'_{Az} = -\chi v_{Az}, v'_{Av} = v_{Av}, v'_{A\tau} = v_{A\tau},$

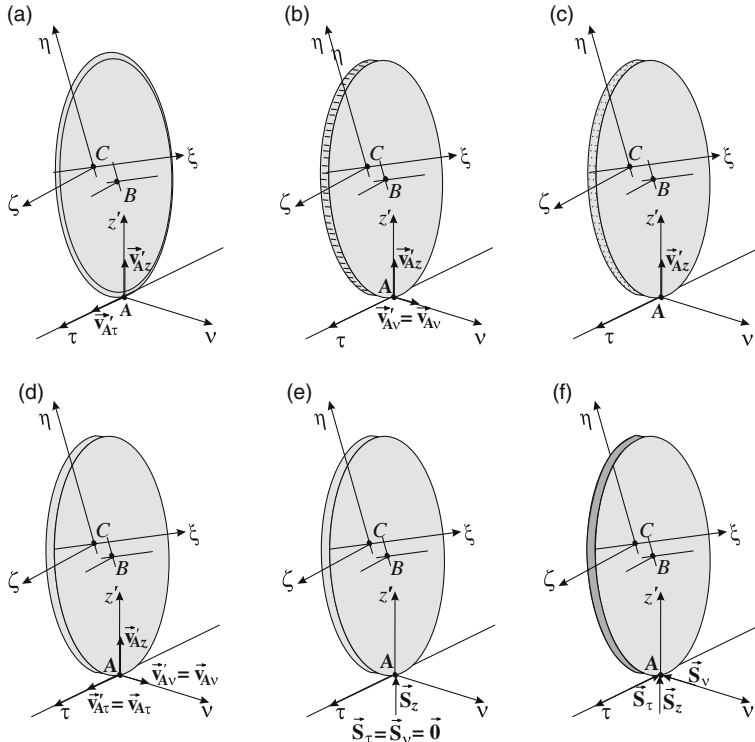


Fig. 3.15 Coin–surface collision models: (a) the coin with a sharp edge; (b) the knurled coin; (c) the perfectly rough coin; (d) the smooth (frictionless) coin (1); (e) the smooth (frictionless) coin (2); and (f) the rough coin with developed friction

(e) the smooth-frictionless coin (2) $v'_{Az} = -\chi v_{Az}$, $\mathbf{S}_{\tau v} = \mathbf{0}$,

(f) the rough coin with developed friction $v'_{Az} = -\chi v_{Az}$, $\mathbf{S}_{\tau v} = -\mu S_z \frac{\mathbf{v}_{\tau v}}{v_{\tau v}}$.

$\mathbf{S}_{\tau v}$ is the component on the floor reaction impulse located in the floor plane and μ the coefficient of dry friction between the coin and the floor.

The case of the perfectly rough coin conditions: $v'_{Av} = 0$, $v'_{A\tau} = 0$ imply the following constraint equations:

$$(2e_0e_2 + 2e_1e_3)(\omega'_\xi \eta_A - \omega'_\eta \xi_A) + (2e_1e_2 - 2e_0e_3)(\omega'_\xi \xi_A - \omega'_\xi \zeta_A) + (2e_0^2 + 2e_1^2 - 1)(\omega'_\eta \zeta_A - \omega'_\xi \eta_A) + \dot{x}' = 0 , \quad (3.77)$$

$$(2e_2e_3 - 2e_0e_1)(\omega'_\xi \eta_A - \omega'_\eta \xi_A) + (2e_0^2 + 2e_2^2 - 1)(\omega'_\xi \xi_A - \omega'_\xi \zeta_A) + (2e_1e_2 + 2e_0e_3)(\omega'_\eta \zeta_A - \omega'_\xi \eta_A) + \dot{y}' = 0 . \quad (3.78)$$

Solving (3.72), (3.73), (3.74), (3.75), (3.76), (3.77), and (3.78) one gets the components of velocity of the center of the coin mass after the collision \dot{x}' , \dot{y}' , \dot{z}' and the

components of the coin angular velocity $\omega'_\xi, \omega'_\eta, \omega'_\zeta$. Additionally, the components of the impulse reaction S_x, S_y, S_z are calculated.

In the case of a smooth ideal coin (3.72), (3.73), (3.74), (3.75), and (3.76) can be simplified as $J_{\xi\eta} = J_{\xi\zeta} = J_{\eta\zeta} = 0$ to the following form:

$$\begin{aligned} & (2e_0^2 + 2e_3^2 - 1)(\omega'_\xi \eta_A - \omega'_\eta \xi_A) + (2e_0 e_1 + 2e_2 e_3)(\omega'_\zeta \xi_A - \omega'_\xi \zeta_A) + \\ & + (2e_1 e_3 - 2e_0 e_2)(\omega'_\eta \xi_A - \omega'_\zeta \eta_A) + \dot{z}' = \\ & = -\chi ((2e_0^2 + 2e_3^2 - 1)(\omega_\xi \eta_A - \omega_\eta \xi_A) + \\ & + (2e_0 e_1 + 2e_2 e_3)(\omega_\zeta \xi_A - \omega_\xi \zeta_A) + (2e_1 e_3 - 2e_0 e_2)(\omega_\eta \zeta_A - \omega_\zeta \eta_A) + \dot{z}) , \end{aligned} \quad (3.79)$$

$$m(\dot{x}' - \dot{x}) = 0, \quad m(\dot{y}' - \dot{y}) = 0, \quad m(\dot{z}' - \dot{z}) = S_z, \quad (3.80)$$

$$J_\xi \omega'_\xi + (-2\eta_A e_0^2 + 2e_1 \xi_A e_0 - 2e_3^2 \eta_A + \eta_A + 2e_2 e_3 \xi_A) S_z = J_\xi \omega_\xi, \quad (3.81)$$

$$J_\eta \omega'_\eta + (2\xi_A e_0^2 + 2e_2 \zeta_A e_0 + 2e_3^2 \xi_A - \xi_A - 2e_1 e_3 \zeta_A) S_z = J_\eta \omega_\eta, \quad (3.82)$$

$$J_\zeta \omega'_\zeta (-2e_1 \xi_A e_0 - 2e_2 \eta_A e_0 - 2e_2 e_3 \xi_A + 2e_1 e_3 \eta_A) S_z = J_\zeta \omega_\zeta. \quad (3.83)$$

3.2 Equations of the Die Throw

3.2.1 Free Fall of a Die

In the analysis of dice dynamics we use Newton–Euler equations (in matrix form (2.8)–(2.9) and in scalar form (2.10)–(2.11)). The moments of inertia in these equations are determined with respect to the body embedded frame $C\xi\eta\zeta$ with the origin in the mass center and in the general case, for a nonsymmetric or nonhomogeneous die, the inertia products are nonzero terms, because the axes $C\xi\eta\zeta$ will not be principal axes. In the case of the symmetric die $C\xi\eta\zeta$ are principal axes, $J_{\xi\eta} = 0$, $J_{\eta\zeta} = 0$, $J_{\zeta\xi} = 0$, so we use (2.12).

For perfectly isohedral dice model (spherical tops [7]) we have $J_{\xi\eta} = 0$, $J_{\eta\zeta} = 0$, $J_{\zeta\xi} = 0$, $J_\xi = J_\eta = J_\zeta = J$ and (2.12) simplifies to

$$J \frac{d\omega_\xi}{dt} = M_{C\xi}, \quad J \frac{d\omega_\eta}{dt} = M_{C\eta}, \quad J \frac{d\omega_\zeta}{dt} = M_{C\zeta}. \quad (3.84)$$

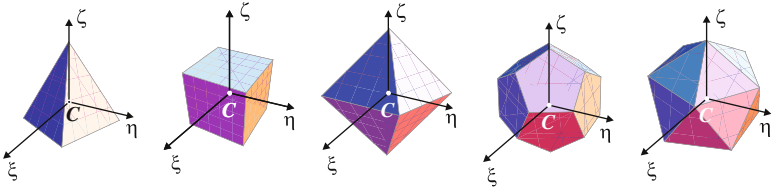


Fig. 3.16 Models of perfectly isohedral dice: tetrahedron (d4), hexahedron or cube (d6), octahedron (d8), dodecahedron (d12), icosahedron (d20), and bodies embedded frame ($C\xi\eta\zeta$)

Finally, for the models shown in Fig. 3.16 the dynamic equations of the die have the form

$$m \ddot{x} = f_x , \quad m \ddot{y} = f_y , \quad m \ddot{z} = f_z , \quad (3.85)$$

$$J \frac{d\omega_\xi}{dt} = M_{C\xi} , \quad J \frac{d\omega_\eta}{dt} = M_{C\eta} , \quad J \frac{d\omega_\zeta}{dt} = M_{C\zeta} . \quad (3.86)$$

Forces ($\mathbf{f} = [f_x \ f_y \ f_z]^T$) and their moments with respect to the body mass center ($\mathbf{M}_c = [M_{C\xi} \ M_{C\eta} \ M_{C\zeta}]^T$) originate from gravity, air-die interaction (drag), and die-table interaction (reactions in the collision time interval).

Some special numerical procedures for moments and products of inertia of polyhedron bodies were proposed in [7]. In our computations we have used *Mathematica*® 6 environment [8] and we got $J = ma^2/20$ for tetrahedron, $J = ma^2/6$ for cube, $J = ma^2/10$ for octahedron, $J = \frac{ma^2}{300} (95 + 39\sqrt{5})$ for dodecahedron, and $J = \frac{ma^2}{20} (3 + \sqrt{5})$ for icosahedron, where m denotes the die mass and a is the length of the die edge.

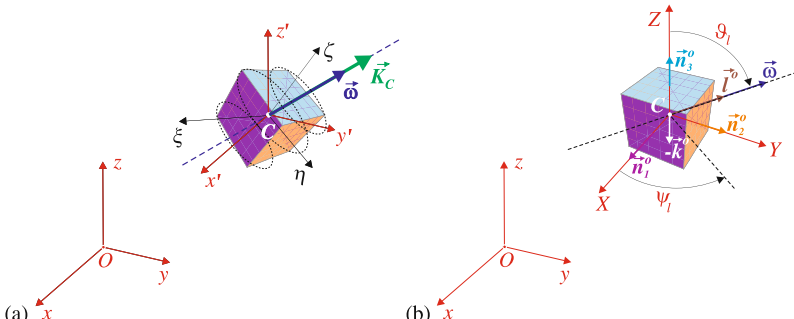


Fig. 3.17 Cube die: (a) body embedded frame $\xi\eta\zeta$, angular velocity ω , and angular momentum \mathbf{K}_C vectors and (b) orientation of die rotation axis \mathbf{l}^o and orientation vectors \mathbf{n}_i^o for faces 1, 2, and 3

Consider the die motion in 3D space described by the fixed frame $Oxyz$ as shown in Fig. 3.17a. Neglecting the influence of the air resistance one obtains (from (3.85) to (3.86)) Newton–Euler equations of the die motion in the following form:

$$m \ddot{x} = 0, \quad m \ddot{y} = 0, \quad m \ddot{z} = -mg, \quad (3.87)$$

$$J \frac{d\omega_\xi}{dt} = 0, \quad J \frac{d\omega_\eta}{dt} = 0, \quad J \frac{d\omega_\zeta}{dt} = 0, \quad (3.88)$$

where $\omega_\xi, \omega_\eta, \omega_\zeta$ are the components of the angular velocity vector $\boldsymbol{\omega}$.

The integrals of (3.87) and (3.88) are given in the form

$$\dot{x} = v_{0x} = const, \quad \dot{y} = v_{0y} = const, \quad \dot{z} = -gt + v_{0z}, \quad (3.89)$$

$$\omega_\xi = \omega_{0\xi} = const, \quad \omega_\eta = \omega_{0\eta} = const, \quad \omega_\zeta = \omega_{0\zeta} = const. \quad (3.90)$$

Equations (3.89) and (3.90) show that during the motion the angular velocity of the die $\boldsymbol{\omega}$ is constant and equal to its initial value $\boldsymbol{\omega}_0$. The orientation of the vector $\boldsymbol{\omega}$ in relation to the frames $C\xi\eta\zeta$ and $Oxyz$ is not changing as the components of angular velocity vector are constant (3.90). The directions of the angular velocity vector $\boldsymbol{\omega}$ and the angular momentum vector \mathbf{K}_C coincide and are constant during the motion as shown in Fig. 3.17a and depend only on the initial conditions.

The initial conditions are given by the initial position of die mass center $C - q_{10} = [x_0, y_0, z_0]^T$, its initial velocity $v_0 = [v_{0x}, v_{0y}, v_{0z}]^T$, initial orientation of the axes $(C\xi\eta\zeta) - q_{20} = [\psi_0, \vartheta_0, \varphi_0]^T$ (given by the Euler angles), and initial angular velocity column matrix $\tilde{\boldsymbol{\omega}}_0 = [\omega_{0\xi}, \omega_{0\eta}, \omega_{0\zeta}]^T$.

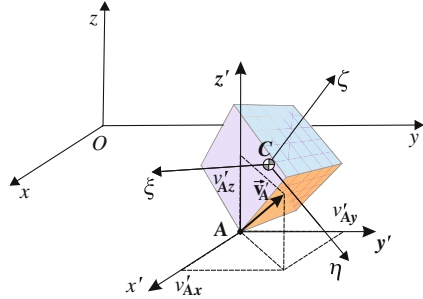
3.2.2 Die Bounces on the Table

To describe a collision of the die with a table we assume that (i) the table is modeled as flat, horizontal, elastic body (fixed to move); (ii) a friction force between the table and the die is omitted; (iii) only one point of the die is in contact with the table during each collision. Let us consider that the die collides with a table when the vertex A touches the floor as shown in Fig. 3.18. According to Newton's hypothesis one gets $\chi = v'_{Az}/v_{Az}$, where χ is the coefficient of restitution, v'_{Az} and v_{Az} are the projections of the velocity of the point A on the direction (z) normal to the impact surface, after and before the impact, respectively. The position of the point A in the body embedded frame is described by ξ_A, η_A, ζ_A . To describe the impacts we consider an additional frame with an origin at point A and the axes: $x'y'z'$ – parallel to the fixed axes xyz (Fig. 3.18). In the matrix form the velocity vector of the point A is described as $\mathbf{v}_A = \mathbf{v}_c + \tilde{\mathbf{\Omega}}_x \mathbf{R} \xi_A$, where $\mathbf{v}_c = [\dot{x} \ \dot{y} \ \dot{z}]^T$, $\xi_A = [\xi_A \ \eta_A \ \zeta_A]^T$, $\tilde{\mathbf{\Omega}}_x = \mathbf{R}^T \dot{\mathbf{R}}$, and the transformation matrix (in terms of Euler angles)

$$\mathbf{R} = \begin{bmatrix} c\varphi c\psi - c\vartheta s\varphi s\psi & -c\psi s\varphi - c\vartheta c\varphi s\psi & s\vartheta s\psi \\ c\vartheta c\psi s\varphi + c\varphi s\psi & c\vartheta c\varphi c\psi - s\varphi s\psi & -c\psi s\vartheta \\ s\vartheta s\varphi & c\varphi s\vartheta & c\vartheta \end{bmatrix}, \quad (3.91)$$

where $s \equiv \sin(\cdot)$ and $c \equiv \cos(\cdot)$ were used in (3.91) (also in (3.92)–(3.94)).

Fig. 3.18 Cube die velocity vector \vec{v}'_{Az} of the point A after collision and its scalar components v'_{Ax} , v'_{Ay} , v'_{Az}



In the analysis of the phenomena that accompany the impact besides Newton's hypothesis, the laws of linear momentum and angular momentum theorems of rigid body, as well as constraint equations have been employed. Modeling the contact between the die and the table we consider the case of the smooth frictionless die [5], i.e., the vector of the impulse base reaction \mathbf{S} has the following form $\mathbf{S} = [0, 0, S_z]^T$. The above assumptions result in the following relations:

$$\begin{aligned} \dot{z}' + \dot{\vartheta}'(-\xi_{AC}(\varphi + \psi)s\vartheta + c\vartheta c(\varphi + \psi)(\eta_{AC}\varphi + \xi_{AS}\varphi) + (\xi_{AC}\varphi + \\ -\eta_{AS}\varphi)s(\varphi + \psi)) + \dot{\psi}'s\vartheta (\xi_{AC}\vartheta c\psi s^2\varphi + \eta_{AC}c^2\frac{\vartheta}{2}c\psi s(2\varphi) - \eta_{AS}s^2\varphi s\psi + \\ + \xi_{AC}c^2\frac{\vartheta}{2}s(2\varphi)s\psi + c^2\varphi(-\xi_{AC}\psi + \eta_{AC}\vartheta s\psi) - \zeta_{AS}\vartheta s(\varphi + \psi)) = \\ = -\chi (\dot{z} + \dot{\vartheta}(-\xi_{AC}(\varphi + \psi)s\vartheta + c\vartheta c(\varphi + \psi)(\eta_{AC}\varphi + \\ + \xi_{AS}\varphi) + (\xi_{AC}\varphi - \eta_{AS}\varphi)s(\varphi + \psi)) + \dot{\psi}s\vartheta (\xi_{AC}\vartheta c\psi s^2\varphi + \eta_{AC}c^2\frac{\vartheta}{2}c\psi s(2\varphi) + \\ - \eta_{AS}s^2\varphi s\psi + \xi_{AC}c^2\frac{\vartheta}{2}s(2\varphi)s\psi + c^2\varphi(-\xi_{AC}\psi + \eta_{AC}\vartheta s\psi) - \zeta_{AS}\vartheta s(\varphi + \psi))) , \end{aligned} \quad (3.92)$$

$$\dot{x}' = \dot{x} , \quad \dot{y}' = \dot{y} , \quad m\dot{z}' - S_z = m\dot{z} , \quad (3.93)$$

$$J(\dot{\vartheta}'c\psi + \dot{\varphi}'s\vartheta s\psi) = J(\dot{\vartheta}c\psi + \dot{\varphi}s\vartheta s\psi) + S_z\eta_{AC}\vartheta - S_z\xi_{AC}\varphi s\vartheta ,$$

$$J(\dot{\vartheta}'s\psi - \dot{\varphi}'c\psi s\vartheta) = J(\dot{\vartheta}s\psi - \dot{\varphi}c\psi s\vartheta) - S_z\xi_{AC}\vartheta + S_z\xi_{AS}\vartheta s\varphi , \quad (3.94)$$

$$J(\dot{\varphi}'c\vartheta + \dot{\psi}') = J(\dot{\varphi}c\vartheta + \dot{\psi}) + S_z\xi_{AC}\varphi s\vartheta - S_z\eta_{AS}\vartheta s\varphi .$$

Equations (3.92), (3.93), and (3.94) allow the determination of the die velocity components after the collision (\dot{x}' , \dot{y}' , \dot{z}' , ω'_ξ , ω'_η , ω'_ζ) and the floor reaction impulse S_z . The die motion after the collisions is given by (3.87)–(3.88) with new initial velocities: \dot{x}' , \dot{y}' , \dot{z}' , ω'_ξ , ω'_η , ω'_ζ calculated from (3.92), (3.93), and (3.94) and the same initial position (x , y , z) and orientation (ψ , ϑ , φ) as before the impacts.

3.3 Equations of the Roulette Run

In literature there is a lack of works concerning the dynamic analysis of a roulette wheel mechanical model (see [9]). There are books, papers, and notes devoted to mathematics, probability theory, and statistical analysis of casino roulette spins [10, 11].

As Small and Tse [9] stated

Unlike most casino games, the game of roulette is entirely mechanical and therefore deterministic. Of course, the outcome of a spin depends with extreme sensitivity on initial conditions. Nonetheless, the spin of the wheel and the roll of the ball are perfectly well described by rather fundamental mechanical principles, and Newton's second law.

We agree with this opinion. Although, we want to add that the formulation of the mathematical model of a roulette is not a simple mechanical problem. On the other hand, there are some difficulties in the modeling of the ball–wheel interaction, especially in the formulation of constraint equations depending on velocities. Such nonholonomic constraints are unavoidable in the case of a ball rolling.

We must point out that the main difficulty in predicting the outcome of a real roulette on the basis of the mechanical model analysis is the lack of precise data of the ball and the wheel initial conditions and for energy dissipation due to air resistance, friction, and collisions.

In the dynamic analysis of a roulette model these are the following mechanical problems to solve:

- free body general motion dynamics (including air resistance),
- constraint motion of a body (including air resistance),
- collision of bodies with superimposed nonholonomic constraints.

A coin tossing and a die throw analysis have been treated as a series of sequences of free falls (F) and collisions (C) and the whole process is described symbolically as $\{F - C\}_n$, where n is the number of collisions with the ground (or the table). Similarly, we describe the roulette ball motion as a sequence of particular problems (ball rolling, the collisions of a ball with the deflectors placed on the wheel, the fall of a ball from the rim, collisions of a ball with the frets dividing the pockets on the rotating wheel, etc.) These problems are solved in sequences depending on the results of actually solved work (in our algorithm decision about the solution path selection depends on previous results). In parallel, the wheel motion is analyzed.

We will use the following symbols to denote particular tasks in the roulette ball motion analysis:

- $R_{(T)}$ – rolling of the ball on the toroidal surface,
- $R_{(FC)}$ – rolling of the ball on the fixed conical surface,
- $C_{(Dk)}$ – collision of the ball with deflector number k ,
- $R_{(Dk)}$ – rolling of the ball on the edge of deflector number k ,
- $O_{(Dk)}$ – the ball coming off the vertex of deflector number k ,
- F – free fall of the ball,

- $C_{(FC)}$ – collision of the ball with the fixed conical surface,
- $C_{(T)}$ – collision of the ball with the fixed toroidal surface,
- $C_{(RC)}$ – collision of the ball with the rotating conical surface after landing on the spinning wheel,
- $C_{(CC)}$ – collision of the ball with the rotating conical surface at the instant of crossing the rim between two different surfaces (due to the discontinuity of the inclination angle between fixed and rotating conical surfaces),
- $R_{(RC)}$ – rolling of the ball on the rotating conical surface (rolling of the ball on the spinning wheel),
- $B_{(Dk)}$ – the ball break away the edge of deflector,
- $C_{(Fk)}$ – collision of the ball with the fret number k ,
- $C_{(P)}$ – collision of the ball with the pocket surfaces.

The combinations with repetition of some of these task sequences (for example, $\{R_{(T)} - R_{(FC)}\}$, $\{F - C_{(FC)}\}$, $\{C_{(RC)} - R_{(RC)}\}$) allow to define the problem of the roulette wheel run. It should be pointed out that the combination (set) of tasks strongly depends on initial conditions for the ball and the roulette wheel motion. The sequence of problems to solve is not known at the beginning of the ball motion; it is built during the motion depending on current results. Solving the succeeding tasks we are able to predict the final outcome of the roulette wheel run.

An exemplary set of tasks for the roulette run simulation can be symbolically described as the sequence (see Fig. 4.48):

$$\{R_{(T)} - R_{(FC)}\}_5 - C_{D2} - R_{D2} - F - C_{(FC)} - R_{(FC)} - C_{D3} - R_{D3} - F - C_{(FC)} - R_{(FC)} - C_{(RC)} - R_{(RC)} - C_{(P)}.$$

The presented model of the roulette wheel is shown in Fig. 3.19.

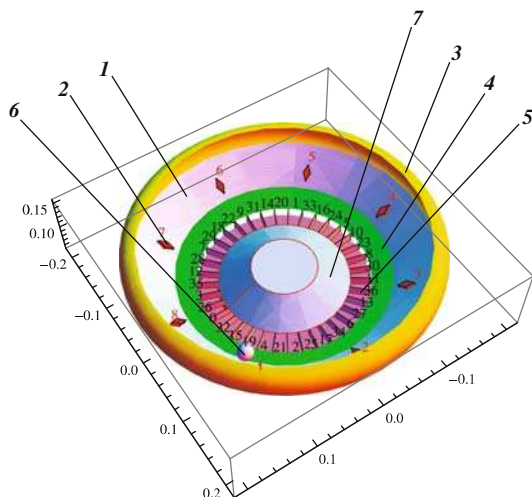


Fig. 3.19 Mechanical model of a roulette: fixed frame (the stator) (1), deflectors (2), toroidal surface abutting the wheel (3), spinning wheel (4), frets separating the pockets (5), the ball (6), central conical part (7)

The stator consists of some parts. One is assumed as a body of toroidal inner surface and two other bodies having conical top (upper) surfaces (cross section of the wheel is shown in Fig. 3.22). Our model consists of the following rigid bodies: fixed frame (1) with deflectors (2), surface abutting the wheel (3), spinning wheel with pockets (4) and central conical part (7), frets separating (dividing) the pockets (5), the ball (6).

3.3.1 Spinning Wheel Motion Analysis

The spinning wheel model with pockets, separating frets and central part, is presented in Figs. 3.20 and 3.21.

After the dealer's spin of the roulette wheel it gradually loses momentum, and its angular velocity decreases. In our model we assume that the drag moment M_r is constant ($M_r = \text{sign}(\Omega_w)M_0 = \text{const}$) or depends on the value of the angular

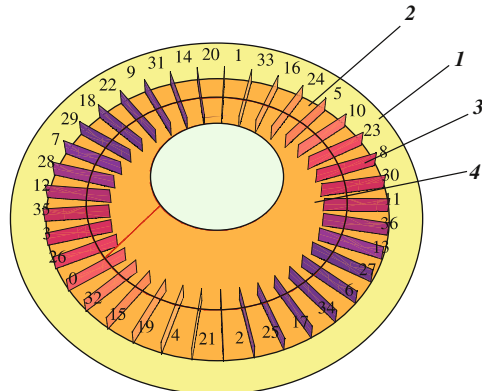


Fig. 3.20 Spinning wheel model: the rotating conical surface (1), pockets (2), frets separating the pockets (3), the central conical part (4)

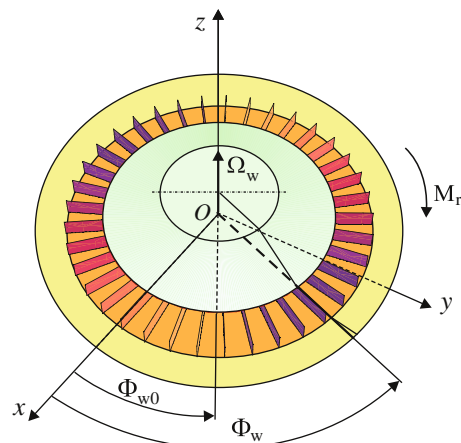


Fig. 3.21 Description of the spinning wheel rotation

velocity of the wheel ($M_r = \text{sign}(\Omega_w)M_r(\Omega_w)$). At the first stage of the analysis we solve the equation

$$J_w \dot{\Omega}_w = M_w , \quad \text{with} \quad M_w = -M_r = \begin{cases} -\text{sign}(\Omega_w)M_0 , \\ -\text{sign}(\Omega_w)M_r(\Omega_w) , \end{cases} \quad (3.95)$$

where J_w is the spinning wheel moment of inertia, Ω_w the wheel angular velocity. Knowing the initial conditions of the wheel $\Omega_w(0) = \Omega_{w0}$, $\Phi_w(0) = \Phi_{w0}$ we find from (3.95) the rotation angle of the spinning wheel $\Phi_w(t)$. It should be pointed out that the solution of (3.95) is valid only for the perfect (statically and dynamically balanced) spinning wheel while the rotation is free. The ball collisions with the rotating wheel and pockets as well as the ball rolling on the wheel cause rapid changes in the wheel angular velocity.

To describe stepwise angular velocity transition due to the collisions we use the angular momentum theorem (2.1) in the form

$$J_w(\dot{\Omega}_w - \Omega_w) = S_x r_y - S_y r_x , \quad (3.96)$$

where S_x, S_y are the components of the reaction impulse at collision instant obtained on the basis of Newton hypothesis (2.49), and r_x, r_y are the collision point coordinates.

3.3.2 The Ball Motion on Fixed Wheel Surfaces

The ball spin in the rim of the roulette wheel is analyzed as a rolling (without sliding) of the spherical body on fixed surfaces. (Notice that in the solution presented in [9] the ball was modeled as a particle sliding on the wheel surfaces.) Air resistance force and moment acting on the ball is considered in the analysis.

The descriptions of the ball motion on conical and toroidal surfaces are generally similar. The differences are only in the relations representing particular surfaces (a cone or a toroid). First, we present the set of equations describing the ball motion on conical surface, and – in the next paragraph – on toroidal surface.

3.3.2.1 The Ball Rolling on Fixed Conical Surface ($R_{(FC)}$)

The ball mass center acceleration and velocity components are obtained in the frame $A\xi\eta\xi$ with the origin (A) in the contact point of ball and fixed conical surface (Figs. 3.22 and 3.23). The axis ξ is normal to the cone surface and outward the cone, η is horizontal axis tangent to the cone horizontal cross section circle and ζ is tangent axis directed along the cone generatrix outward the apex O (Figs. 3.22 and 3.23).

The ball mass center (C) acceleration components (respectively, in ξ, η, ζ directions) are described by

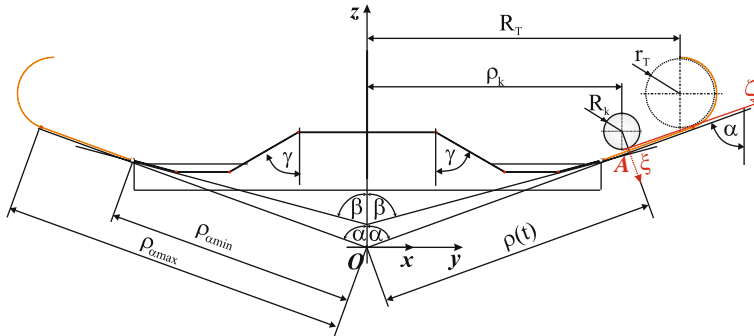


Fig. 3.22 Cross section of the roulette wheel and basic dimensions

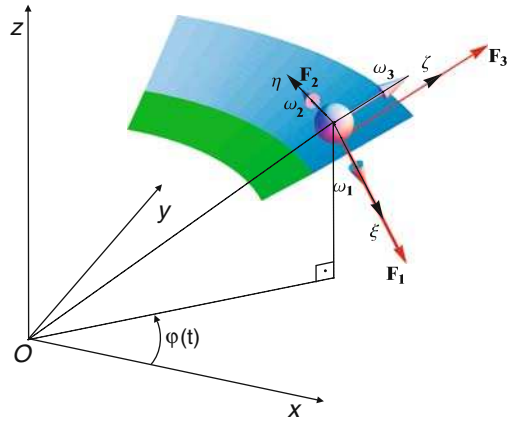


Fig. 3.23 Fixed frame $Oxyz$ and $A\xi\eta\zeta$ frame in contact point of ball and fixed conical surface, the angular coordinate of the contact point, the ball angular velocity, and reaction force components

$$a_{C\xi} = \cos(\alpha)v_\varphi^2(R_k \cos(\alpha) - \rho \sin(\alpha)) ,$$

$$a_{C\eta} = 2 \sin(\alpha)v_\rho v_\varphi + (\rho \sin(\alpha) - R_k \cos(\alpha)) \dot{v}_\varphi , \quad (3.97)$$

$$a_{C\zeta} = \sin(\alpha)v_\varphi^2(R_k \cos(\alpha) - \rho \sin(\alpha)) + \dot{v}_\rho ,$$

and velocity components of the contact point (A) of the ball and the fixed conical surface are obtained as follows:

$$v_{A\xi} = \sin(\alpha)v_\varphi\rho + R_k\omega_3 , \quad v_{A\eta} = \sin(\alpha)v_\varphi\rho , \quad v_{A\zeta} = 0 , \quad (3.98)$$

where v_ρ and v_φ are time derivatives of the contact point coordinates $\rho(t)$ and $\varphi(t)$ shown in Figs. 3.22 and 3.23, respectively.

The constraint equations arising from the ball rolling condition are described by functions

$$f_1 = R_k\omega_3 + v_\varphi\rho \sin(\alpha) , \quad f_2 = v_\rho - R_k\omega_2 . \quad (3.99)$$

Solving equations $f_1 = 0$, $f_2 = 0$ we have

$$\omega_2 = \frac{v_\rho}{R_k}, \quad \omega_3 = -v_\varphi \frac{\sin(\alpha)\rho}{R_k}, \quad (3.100)$$

and

$$v_{C\xi} = 0, \quad v_{C\eta} = v_\varphi (\sin(\alpha)\rho - \cos(\alpha)R_k), \quad v_{C\zeta} = v_\rho. \quad (3.101)$$

The dynamic equations of the ball rolling on conical surface have the form

$$\begin{aligned} m \cos(\alpha)v_\varphi^2 (\cos(\alpha)R_k - \sin(\alpha)\rho) &= -F_1 - mg \sin(\alpha), \\ m (2 \sin(\alpha)v_\rho v_\varphi + (\sin(\alpha)\rho - \cos(\alpha)R_k) \dot{v}_\varphi) &= \\ &= -F_2 - \frac{2}{3}\pi R_k^2 (\lambda_n + 2\lambda_\tau) v_\varphi (-\cos(\alpha)R_k + \sin(\alpha)\rho), \\ m (g \cos(\alpha) + \sin(\alpha)v_\varphi^2 (\cos(\alpha)R_k - \sin(\alpha)\rho) + \dot{v}_\rho) &= \\ &= -F_3 + \frac{1}{3}(-2)\pi R_k^2 (\lambda_n + 2\lambda_\tau) v_\rho, \end{aligned} \quad (3.102)$$

and

$$\begin{aligned} \frac{1}{5}2mR_k (R_k \dot{\omega}_1 - \cos(\alpha)v_\rho v_\varphi) &= \frac{1}{3}(-8)\pi R_k^4 \lambda_\tau \omega_1, \\ \frac{1}{5}R_k (5F_3 + 2m (-\sin^2(\alpha)v_\varphi^2 \rho + \cos(\alpha)R_k v_\varphi \omega_1 + \dot{v}_\rho)) &= \\ &= \frac{1}{3}(-8)\pi R_k^3 \lambda_\tau v_\rho, \\ \frac{1}{5}R_k (-5F_2 - 2m \sin(\alpha) (\rho \dot{v}_\varphi + v_\varphi (v_\rho + \dot{\rho}))) &= \\ &= \frac{1}{3}(-8)\pi R_k^4 \lambda_\tau v_\varphi \left(\cos(\alpha) - \frac{\sin(\alpha)\rho}{R_k} \right). \end{aligned} \quad (3.103)$$

where λ_τ , λ_n are air pressure and air friction coefficients for the ball. (More details on description of the air resistance force and moment can be found in (Section 3.3.4)).

Solving (3.102) we find reaction forces F_2 and F_3 , i.e., friction force components

$$\begin{aligned} F_2 &= -m(2 \sin(\alpha)v_\rho v_\varphi + (\sin(\alpha)\rho - \cos(\alpha)R_k) \dot{v}_\varphi) + \\ &\quad -\frac{2}{3}\pi R_k^2 (\lambda_n + 2\lambda_\tau) v_\varphi (-\cos(\alpha)R_k + \sin(\alpha)\rho), \\ F_3 &= -m(g \cos(\alpha) + \sin(\alpha)v_\varphi^2 (\cos(\alpha)R_k - \sin(\alpha)\rho) + \dot{v}_\rho) + \\ &\quad +\frac{1}{3}(-2)\pi R_k^2 (\lambda_n + 2\lambda_\tau) v_\rho. \end{aligned} \quad (3.104)$$

The numerical solution of (3.102)–(3.103) together with (3.100) allow to find time series of $\rho(t)$, $\varphi(t)$, $\omega_1(t)$, $v_\rho(t)$, $v_\varphi(t)$ and then $\omega_2(t)$, $\omega_3(t)$. Some results of the exemplary numerical solution of the ball rolling on the conical as well as on the toroidal surfaces of the fixed roulette wheel are presented in Figs. 3.29 and 3.30.

3.3.2.2 Rolling of the Ball on Fixed Toroidal Surface (R_T)

Next considered task in the roulette wheel analysis is the description of the ball motion on fixed toroidal surface (Fig. 3.24). The solution method of this problem is similar to the analysis of the ball on the fixed conical surface (presented in the previous paragraph).

The ball mass center acceleration components in $A\xi\eta\zeta$ frame are described by

$$\begin{aligned} a_{C\xi} &= (R_k - r_T) \dot{\theta}^2 - (\cos(\theta) (\cos(\theta) (r_T - R_k) + R_T)) \dot{\varphi}^2, \\ a_{C\eta} &= 2 \sin(\theta) (R_k - r_T) \dot{\theta} \dot{\varphi} + (\cos(\theta) (r_T - R_k) + R_T) \ddot{\varphi}, \\ a_{C\zeta} &= \sin(\theta) (\cos(\theta) (r_T - R_k) + R_T) \dot{\varphi}^2 + (r_T - R_k) \ddot{\theta}. \end{aligned} \quad (3.105)$$

The contact point of the ball and the surface (A) velocity components have the form

$$v_{A\xi} = 0, \quad v_{A\eta} = (\cos(\theta) r_T + R_T) \dot{\varphi}, \quad v_{A\zeta} = r_T \dot{\theta}. \quad (3.106)$$

The functions describing nonholonomic constraints are obtained as

$$f_1 = R_k \omega_3 + (\cos(\theta) r_T + R_T) \dot{\varphi}, \quad f_2 = -R_k \omega_2 + r_T \dot{\theta}, \quad (3.107)$$

and from $f_1 = 0$, $f_2 = 0$ follows that

$$\omega_2 = \frac{r_T \dot{\theta}}{R_k}, \quad \omega_3 = -\frac{(\cos(\theta) r_T + R_T) \dot{\varphi}}{R_k}. \quad (3.108)$$

The ball mass center velocity components are equal to

$$v_{C\xi} = 0, \quad v_{C\eta} = (\cos(\theta) r_T - \cos(\theta) R_k + R_T) \dot{\varphi}, \quad v_{C\zeta} = (r_T - R_k) \dot{\theta}. \quad (3.109)$$

The dynamic equations describing the center mass motion of the ball rolling on toroidal surface have the form

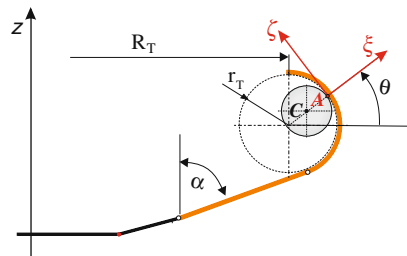


Fig. 3.24 The frame $A\xi\eta\zeta$ and coordinate θ describing position of the ball contact point with toroidal surface

$$\begin{aligned}
m((R_k - r_T)\dot{\theta}^2 - \cos(\theta)(\cos(\theta)(r_T - R_k) + R_T)\dot{\varphi}^2) &= F_1 - mg \sin(\theta), \\
2m \sin(\theta)(R_k - r_T)\dot{\theta}\dot{\varphi} + m(\cos(\theta)(r_T - R_k) + R_T)\ddot{\varphi} &= \\
&= F_2 - \frac{2}{3}\pi R_k^2(\lambda_n + 2\lambda_\tau)v_\varphi(-\cos(\alpha)R_k + \sin(\alpha)\rho), \\
m(\sin(\theta)(\cos(\theta)(r_T - R_k) + R_T)\dot{\varphi}^2 + (r_T - R_k)\ddot{\theta}) &= \\
&= F_3 - mg \cos(\theta) + \frac{1}{3}(-2)\pi R_k^2(\lambda_n + 2\lambda_\tau)v_\rho,
\end{aligned} \tag{3.110}$$

where F_1, F_2, F_3 are the reaction components (Fig. 3.25).

Solving these equations with respect to F_1, F_2, F_3 and using the results in the equations describing the ball rotations we have the following equations:

$$\begin{aligned}
\frac{2}{5}mR_k(R_k\dot{\omega}_1 + R_T\dot{\theta}\dot{\varphi}) &= -\frac{8}{3}\pi R_k^4\lambda_\tau(\sin(\theta)\dot{\varphi} + \omega_1), \\
\frac{1}{15}R_k(3m(5g \cos(\theta) + 7R_T \sin(\theta)\dot{\varphi}^2) + r_T(10\pi R_k^2(\lambda_n + 2\lambda_\tau)\dot{\theta} + \\
&+ 21m(\ddot{\theta} + \sin(\theta)\cos(\theta)\dot{\varphi}^2)) + 3mR_k(\cos(\theta)\dot{\varphi}(2\omega_1 - 5\sin(\theta)\dot{\varphi}) - 5\ddot{\theta}) + \\
&- 10\pi R_k^3(\lambda_n + 2\lambda_\tau)\dot{\theta}) &= \frac{8}{3}\pi R_k^3\lambda_\tau\dot{\theta}(R_k - r_T), \\
\frac{1}{15}R_k(3mR_k(2\dot{\theta}(\omega_1 - 5\sin(\theta)\dot{\varphi}) + 5\cos(\theta)\dot{\varphi}) + \\
&- 10\pi R_k^2(\lambda_n + 2\lambda_\tau)\dot{\varphi}(r_T \cos(\theta) + R_T) + 10\pi R_k^3(\lambda_n + 2\lambda_\tau)\cos(\theta)\dot{\varphi} + \\
&- 21m\dot{\varphi}(r_T \cos(\theta) + R_T) + 42mr_T\dot{\theta}\sin(\theta)\dot{\varphi}) &= \\
&= \frac{8}{3}\pi R_k^3\lambda_\tau\dot{\varphi}(\cos(\theta)(r_T - R_k) + R_T).
\end{aligned} \tag{3.111}$$

Some results obtained from the numerical solution of the presented equations are depicted in Figs. 3.26 and 3.27. Changes in the ball position angle θ and the normal reaction force F_1 during the motion on the toroidal surface are shown in these figures.

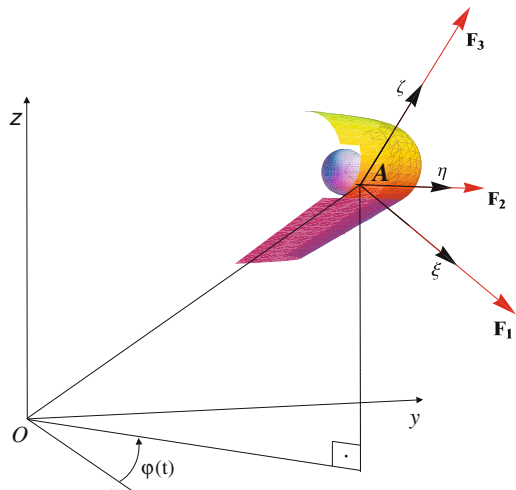


Fig. 3.25 Fixed frame $Oxyz$, $A\xi\eta\zeta$ frame, angular coordinate of contact point (φ) , and reaction force components in contact point of ball with toroidal surface

Fig. 3.26 Result of the ball motion simulation on toroidal surface – angle θ obtaining position of the ball on toroidal surface as the function of the angular coordinate of contact point φ

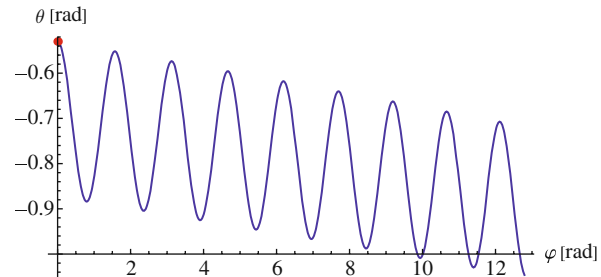


Fig. 3.27 Result of the ball motion simulation on toroidal surface – normal component of the reaction force on toroidal surface. Initial reaction value is marked by the point

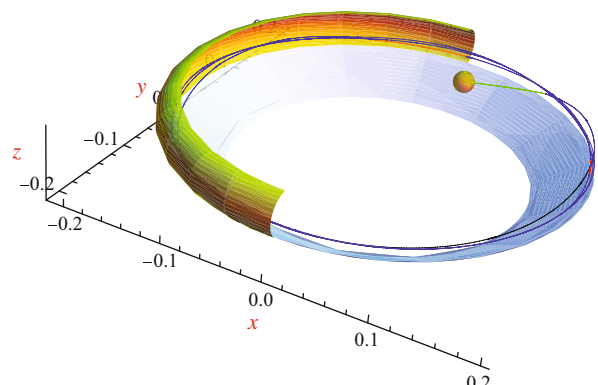
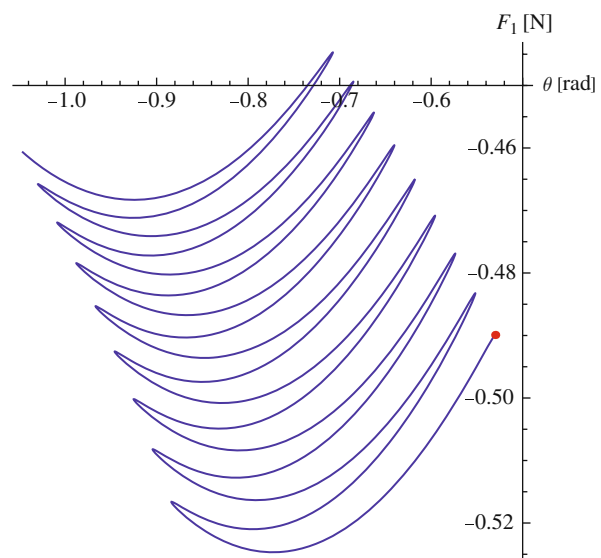


Fig. 3.28 Trajectory of the ball rolling on toroidal and conical surfaces

Fig. 3.29 Normal component of the reaction force on toroidal and conical surfaces as the function of the coordinate φ

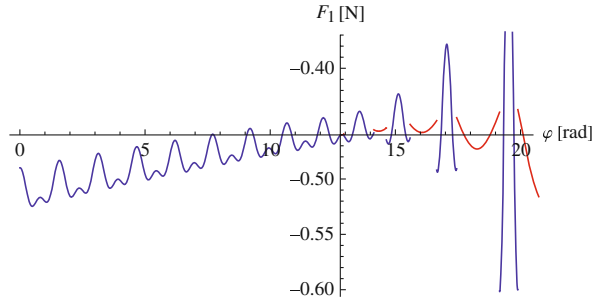
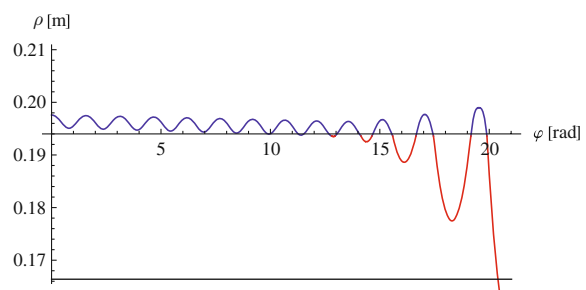


Fig. 3.30 Position (ρ) of the ball on toroidal and conical surfaces as the function of the coordinate φ



In Figs. 3.28, 3.29, and 3.30 the results summarizing the ball motion on the toroidal and fixed conical surfaces are presented (during its motion the ball five times crosses the border between these surfaces, i.e., the motion sequence is described as $\{R_{(T)} - R_{(FC)}\}_5$).

Notice that the normal component of the reaction force (F_1) of toroidal and conical surfaces is not a continuous function (Fig. 3.29). Crossing the border between these surfaces the reaction force changes stepwise due to the discontinuity of the surface curvature radius on the border.

3.3.3 Collision of the Ball with a Deflector ($C_{(Dk)}$)

The roulette wheel stator with deflectors is shown in Fig. 3.19. In Fig. 3.31 we present the exemplary result of the first stage of the ball motion – till the collision with deflector number 2.

The analysis of the ball collision with deflector is examined in detail as three stages: collision of the ball with a deflector edge, motion of the ball on the edge of deflector, the ball coming off the vertex of deflector. In the following paragraphs we describe these stages.

3.3.3.1 Collision of the Ball with a Deflector Edge

First, we find the column matrix representing the vector $\mathbf{r}_{uc} = \mathbf{r}_c - \mathbf{r}_u$ connecting the collision point and the ball mass center (Fig. 3.32) as follows:

Fig. 3.31 Trajectory of the ball mass center before the collision with deflector number 2

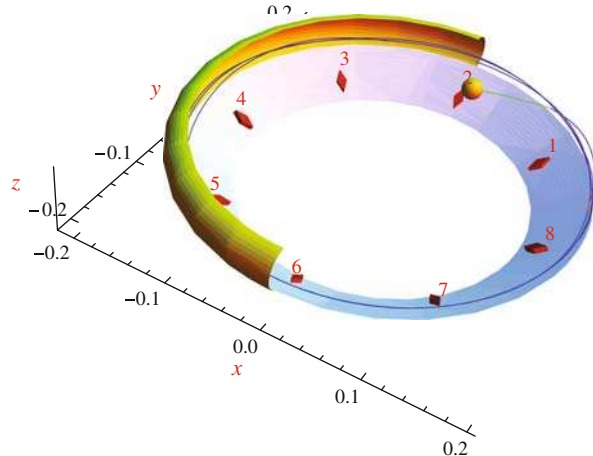
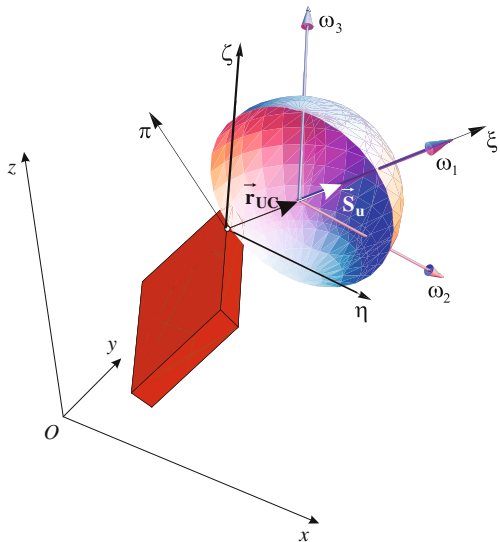


Fig. 3.32 The ball collision with the deflector edge (the vector \mathbf{r}_{uc} obtaining the direction of collision and the impulse of reaction force \mathbf{S}_u)



$$\mathbf{r}_u = \begin{bmatrix} x_u \\ y_u \\ z_u \end{bmatrix}, \quad \mathbf{r}_c = \begin{bmatrix} x \\ y \\ z \end{bmatrix}, \quad \mathbf{r}_{uc} = \mathbf{r}_c - \mathbf{r}_u. \quad (3.112)$$

The unit vector (\mathbf{e}) of \mathbf{r}_{uc} has the components obtained by

$$\mathbf{e} = \begin{bmatrix} e_x \\ e_y \\ e_z \end{bmatrix} = \frac{1}{\sqrt{(x - x_u)^2 + (y - y_u)^2 + (z - z_u)^2}} \begin{bmatrix} x - x_u \\ y - y_u \\ z - z_u \end{bmatrix}. \quad (3.113)$$

Assuming that the collision of the ball with the deflector edge is perfectly plastic ($\chi = 0$) we have the set of equations:

$$\begin{aligned} m(-v_{Cx} + v'_{Cx}) &= e_x S_u, & m(-v_{Cy} + v'_{Cy}) &= e_y S_u, \\ m(-v_{Cz} + v'_{Cz}) &= e_z S_u, & e_x v'_{Cx} + e_y v'_{Cy} + e_z v'_{Cz} &= 0. \end{aligned} \quad (3.114)$$

Solving (3.114) we find the impulse of reaction force S_u and the ball mass center velocity components after the collision ($v'_{Cx}, v'_{Cy}, v'_{Cz}$).

3.3.3.2 Motion of the Ball on the Edge of Deflector ($R_{(Dk)}$)

The motion of the ball on the edge of the deflector after the collision is treated as the body motion on the frictionless line.

We use the local frame $(\xi\eta\zeta)$ defined by unit vectors $\mathbf{e}_\xi, \mathbf{e}_\eta, \mathbf{e}_\zeta$. Axis ζ has the direction of the deflector edge (Figs. 3.32, 3.33). To obtain the directions of axes ξ and η we introduce two unit vectors \mathbf{e}_π (perpendicular to the deflector top plane) and $\mathbf{e}_{\eta 1}$ and use the following relations:

$$\mathbf{e}_{\eta 1} = \mathbf{e}_\zeta \times \mathbf{e}_\pi, \quad \mathbf{e}_\xi = \mathbf{e}_{\eta 1} \sin(\theta_d) + \mathbf{e}_\pi \cos(\theta_d), \quad \mathbf{e}_\eta = \mathbf{e}_{\eta 1} \times \mathbf{e}_\xi. \quad (3.115)$$

Dynamic equations of the ball motion have the form

$$\begin{aligned} m\dot{v}_{\lambda d} + mg e_{3\zeta} &= 0, \\ mR_k \dot{v}_{\theta d} + mg e_{2\eta} &= 0, \\ mR_k v_{\theta d}^2 + mg e_{1\xi} &= F_d, \end{aligned} \quad (3.116)$$

where $v_{\lambda d} = \dot{\lambda}_d$ is the ball mas center velocity in ζ direction, $v_{\theta d} = -\dot{\theta}_d$ is the angular velocity of the ball rotation about ζ -axis and F_d is the reaction force.

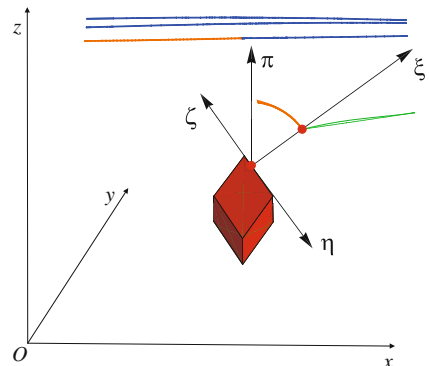


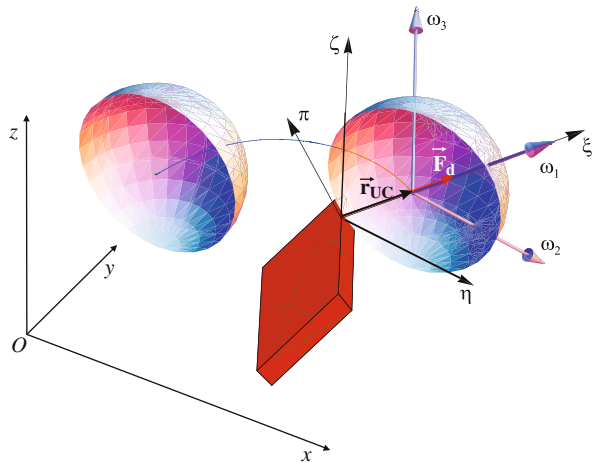
Fig. 3.33 Trajectory of the ball mass center before the collision with the deflector and during the motion on the edge

The trajectory of the ball mass center before the collision with the deflector edge and during the motion on the edge – obtained from (3.116) – is shown in Fig. 3.33.

3.3.3.3 The Ball Coming off the Vertex of Deflector ($O_{(Dk)}$)

Checking up the value of the reaction force F_d obtained from (3.116) we find the time instant (for $F_d = 0$) at which the ball is coming off the vertex of the deflector. In Fig. 3.34 the trajectory and the positions of the ball at the instants of coming off the vertex of the deflector and landing on the fixed conical surface are shown. (Free fall of the ball is described below.)

Fig. 3.34 The ball positions at the instants of coming off the vertex of deflector and landing on (collision with) the fixed conical surface



3.3.4 Free Fall of the Ball (F)

The ball thrown by a croupier or “jumping” due to the collisions is treated as a free fall motion of the body forced by gravity and air resistance. The following equations are used to describe the components of air resistance force and moments:

$$F_{nx} = \int_0^{\frac{\pi}{2}} \lambda_n 2\pi R_k^2 v_x \sin^2(\vartheta) \cos(\vartheta) d\vartheta = \frac{2}{3}\pi R_k^2 v_x \lambda_n , \quad (3.117)$$

$$F_{\tau x} = \int_0^{\frac{\pi}{2}} \lambda_\tau 2\pi R_k^2 v_x \cos^3(\vartheta) d\vartheta = \frac{4}{3}\pi R_k^2 v_x \lambda_\tau , \quad (3.118)$$

$$F_x = \frac{2}{3}\pi R_k^2 v_x \lambda_n + \frac{4}{3}\pi R_k^2 v_x \lambda_\tau , \quad (3.119)$$

where F_{nx} , $F_{\tau x}$ are the x components of normal and tangent (to the ball surface) air drag force, R_k is the ball radius, v_x the ball velocity component, and λ_τ , λ_n are the tangent and normal coefficients of air drag. In the same way we obtain other components as follows:

$$F_y = \frac{2}{3}\pi R_k^2 v_y \lambda_n + \frac{4}{3}\pi R_k^2 v_y \lambda_\tau , \quad (3.120)$$

$$F_z = \frac{2}{3}\pi R_k^2 v_z \lambda_n + \frac{4}{3}\pi R_k^2 v_z \lambda_\tau . \quad (3.121)$$

and components of moments as follows:

$$M_x = \int_{-\frac{\pi}{2}}^{\frac{\pi}{2}} \lambda_\tau \omega_x R_k \cos(\vartheta) R_k \cos(\vartheta) 2\pi R_k \cos(\vartheta) R_k d\vartheta = \frac{8}{3}\pi R_k^4 \lambda_\tau \omega_x , \quad (3.122)$$

$$M_y = \frac{8}{3}\pi R_k^4 \lambda_\tau \omega_y , \quad M_z = \frac{8}{3}\pi R_k^4 \lambda_\tau \omega_z . \quad (3.123)$$

In (3.122)–(3.123) the symbols ω_x , ω_y , ω_z denote the ball angular velocity components in the inertial frame.

Juxtaposing the results of the ball free motion with the rotation of the wheel we found the relative position of the ball with respect to the spinning wheel.

3.3.5 Landing of the Ball

3.3.5.1 Landing of the Ball on Fixed Conical Surface

To obtain the position of the colliding point we check up the distance f_c from the ball to the fixed conical surface. If $f_c = 0$ the ball collides with the conical surface.

The distance f_c from the outer ball surface to the fixed conical surface of the roulette wheel can be obtained from

$$f_c = z(t) - \frac{\sqrt{x(t)^2 + y(t)^2}}{\tan(\alpha)} - \frac{R_k}{\sin(\alpha)} , \quad (3.124)$$

where $x(t)$, $y(t)$, $z(t)$ are the coordinates of the ball mass center and α is the inclination of conical surface with respect to the vertical axis (z).

Knowing the exact time ($f_c(t_c) = 0 \rightarrow t_c$) of a collision, the position and the velocity of the ball before the impact we are able to calculate the velocity components after the impact.

3.3.5.2 Landing of the Ball on Fixed Toroidal Surface

The method of analysis of the ball collision with the fixed toroidal surface surrounding the wheel is the same as presented in the former paragraph but the formulas are more complicated:

$$\rho_K = \sqrt{x(t)^2 + y(t)^2}, \quad z_T = \rho_{\alpha max} \cos(\alpha) + r_T \sin(\alpha), \quad (3.125)$$

$$d_{TK} = \sqrt{(z(t) - z_T)^2 + (\rho_K - R_T)^2}, \quad (3.126)$$

$$x_{Tm} = \left(\frac{(\rho_K - R_T) r_T}{d_{TK}} + R_T \right) \frac{x(t)}{\rho_K}, \quad (3.127)$$

$$y_{Tm} = \left(\frac{(\rho_K - R_T) r_T}{d_{TK}} + R_T \right) \frac{y(t)}{\rho_K}, \quad z_{Tm} = z_T + \frac{(z(t) - z_T)r_T}{d_{TK}}, \quad (3.128)$$

$$f_t = \sqrt{(x_{Tm} - x(t))^2 + (y_{Tm} - y(t))^2 + (z_{Tm} - z(t))^2} \quad (3.129)$$

(basic dimensions of the wheel: ρ_K , $\rho_{\alpha max}$, R_T , r_T are shown in Fig. 3.22).

On the basis of these equations the distance (f_t) of the colliding point of the ball from the fixed toroidal surface is found, and in the next step the velocity components after the impact can be obtained.

3.3.5.3 Landing of the Ball on Rotating Conical Surface

In a similar manner as for the fixed conical surface we obtain the position of the ball colliding point with the rotating conical surface.

The distance f_r from the outer ball surface to the rotating conical surface of the roulette wheel can be obtained as

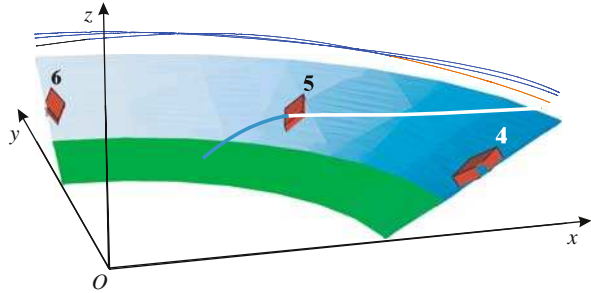
$$f_r = z(t) - \frac{\sqrt{x(t)^2 + y(t)^2}}{\tan(\beta)} - \frac{R_k}{\sin(\beta)} - z_{\beta min}. \quad (3.130)$$

Knowing the exact time ($f_r(t_c) = 0 \rightarrow t_c$) of a collision, the position and the velocity of the ball before the impact we are able to calculate the velocity components after the impact.

3.3.5.4 Collision of the Ball with Rotating Conical Surface ($C_{(RC)}$)

The ball trajectory before the collision with rotating conical surface is shown in Fig. 3.35.

Fig. 3.35 The ball trajectory before the collision with rotating conical surface



After the ball landing on rotating conical surface we obtain the position of the mass center and the initial velocities of the ball using column matrices:

$$\mathbf{r}_{cu} = \begin{bmatrix} x_c \\ y_c \\ z_c \end{bmatrix}, \quad \mathbf{v}_{cu} = \begin{bmatrix} v_{xc} \\ v_{yc} \\ v_{zc} \end{bmatrix}, \quad \boldsymbol{\Omega}_{\beta c} = \begin{bmatrix} \omega_{c1} \\ \omega_{c2} \\ \omega_{c3} \end{bmatrix}. \quad (3.131)$$

In the collision point we introduce the local frame $\xi_c \eta_c \zeta_c$ defined by the following unit vectors (in the matrix form):

$$\begin{aligned} \mathbf{e}_{\beta 3} &= [\sin(\beta) \cos(\varphi_c) \quad \sin(\beta) \sin(\varphi_c) \quad \cos(\beta)]^T, \\ \mathbf{e}_{\beta 1} &= [\cos(\beta) \cos(\varphi_c) \quad \cos(\beta) \sin(\varphi_c) \quad -\sin(\beta)]^T, \\ \mathbf{e}_{\beta 2} &= [-\sin(\varphi_c) \quad \cos(\varphi_c) \quad 0]^T, \end{aligned} \quad (3.132)$$

(where the vector $\mathbf{e}_{\beta 2} = \mathbf{e}_{\beta 3} \times \mathbf{e}_{\beta 1}$).

The components of the ball center velocity in $\xi_c \eta_c \zeta_c$ frame before the collision are obtained as follows:

$$\begin{aligned} v_{\rho c} &= v_{xc} \sin(\beta) \cos(\varphi_c) + v_{yc} \sin(\beta) \sin(\varphi_c) + v_{zc} \cos(\beta), \\ v_{\varphi c} &= v_{yc} \cos(\varphi_c) - v_{xc} \sin(\varphi_c), \\ v_{nc} &= v_{xc} \cos(\beta) \cos(\varphi_c) + v_{yc} \cos(\beta) \sin(\varphi_c) - v_{zc} \sin(\beta). \end{aligned} \quad (3.133)$$

We use the following equations to find the ball mass center velocity ($\mathbf{v}'_{C\beta c} = [v'_{C\beta 1} \quad v'_{C\beta 2} \quad v'_{C\beta 3}]^T$) and angular velocity ($\boldsymbol{\Omega}'_{\beta c} = [\omega'_{c1} \quad \omega'_{c2} \quad \omega'_{c3}]^T$) after the collision as well as the reaction impulse ($\mathbf{S}_{\beta c} = [S_{\beta 1} \quad S_{\beta 2} \quad S_{\beta 3}]^T$):

$$\begin{aligned} m \left(v'_{C\beta 1} - v_{xc} \cos(\beta) \cos(\varphi_c) - v_{yc} \cos(\beta) \sin(\varphi_c) + v_{zc} \sin(\beta) \right) - S_{\beta 1} &= 0, \\ m \left(v'_{C\beta 2} + v_{xc} \sin(\varphi_c) - v_{yc} \cos(\varphi_c) \right) - S_{\beta 2} &= 0, \end{aligned} \quad (3.134)$$

$$\begin{aligned} \frac{2}{5} m R_k \left(\omega'_{\beta 1} - \omega_{c1} \right) &= 0, \\ S_{\beta 3} + \frac{2}{5} m R_k \left(\omega'_{\beta 2} - \omega_{c2} \right) &= 0, \\ \frac{1}{5} \left(2m R_k \left(\omega'_{\beta 3} - \omega_{c3} \right) - 5S_{\beta 2} \right) &= 0. \end{aligned} \quad (3.135)$$

The equation of the rotating wheel angular momentum (3.136) allows to find its angular velocity after the collision

$$S_{\beta 2} \rho_c + J_w (\Omega'_w - \Omega_w) = 0. \quad (3.136)$$

Constraint equations describing the rolling (without sliding) of the ball on the spinning wheel have the form

$$v'_{C\beta 1} = 0, \quad \omega'_{\beta 3} R_k - \rho_c \Omega'_w + v'_{C\beta 2} = 0, \quad v'_{C\beta 3} - \omega'_{\beta 2} R_k = 0. \quad (3.137)$$

Solving (3.134), (3.135), (3.136), and (3.137) we find the components of the reaction impulse at the instant of collision as

$$\begin{aligned} S_{\beta 1} &= m(v_{zc} \sin(\beta) - \cos(\beta)(v_{xc} \cos(\varphi_c) + v_{yc} \sin(\varphi_c))), \\ S_{\beta 2} &= \frac{2J_w m (-\omega_{c3} R_k + \rho_c \Omega_w + v_{xc} \sin(\varphi_c) - v_{yc} \cos(\varphi_c))}{7J_w + 2m\rho_c^2}, \\ S_{\beta 3} &= -\frac{2}{7} m (-\omega_{c2} R_k + \sin(\beta)(v_{xc} \cos(\varphi_c) + v_{yc} \sin(\varphi_c)) + v_{zc} \cos(\beta)), \end{aligned} \quad (3.138)$$

the ball mass center velocity components:

$$\begin{aligned} v'_{C\beta 1} &= 0, \\ v'_{C\beta 2} &= \frac{-2J_w \omega_{c3} R_k + (5J_w + 2m\rho_c^2)(v_{yc} \cos(\varphi_c) - v_{xc} \sin(\varphi_c)) + 2J_w \rho_c \Omega_w}{7J_w + 2m\rho_c^2}, \\ v'_{C\beta 3} &= \frac{1}{7} (2\omega_{c2} R_k + 5v_{xc} \sin(\beta) \cos(\varphi_c) + 5v_{yc} \sin(\beta) \sin(\varphi_c) + 5v_{zc} \cos(\beta)) \end{aligned} \quad (3.139)$$

the angular velocities of the ball after the collision:

$$\omega'_{\beta 1} = \omega_{c1},$$

$$\omega'_{\beta 2} = \frac{5(\sin(\beta)(v_{xc} \cos(\varphi_c) + v_{yc} \sin(\varphi_c)) + v_{zc} \cos(\beta))}{7R_k} + \frac{2\omega_{c2}}{7}, \quad (3.140)$$

$$\omega'_{\beta 3} = \frac{2\omega_{c3} R_k (J_w + m\rho_c^2) + 5J_w(\rho_c \Omega_w + v_{xc} \sin(\varphi_c) - v_{yc} \cos(\varphi_c))}{R_k (7J_w + 2m\rho_c^2)},$$

and the angular velocity of the wheel after the collision:

$$\Omega'_w = \frac{7J_w \Omega_w + 2m\rho_c \omega_{c3} R_k - 2m\rho_c v_{xc} \sin(\varphi_c) + 2m\rho_c v_{yc} \cos(\varphi_c)}{7J_w + 2m\rho_c^2}. \quad (3.141)$$

3.3.6 Collision of the Ball with Rotating Conical Surface ($C_{(CC)}$)

The next problem to describe is the impact of the ball crossing a border line (discontinuity line) between two different surfaces. In the model of the roulette wheel (Fig. 3.22) two conical surfaces – fixed circular conical surface of aperture 2α and rotating conical surface of aperture 2β – are adjoined. There is a small gap between these surfaces (Fig. 3.36a).

The motion of the roulette wheel is described by (3.95) and actualized after each collision as we show in the previous section (3.134), (3.135), (3.136), and (3.137).

The coordinate system used in the following equations is shown in Fig. 3.36. The ball mass center velocity components before the collision in $\xi_\beta \eta_\beta \zeta_\beta$ frame are as follows:

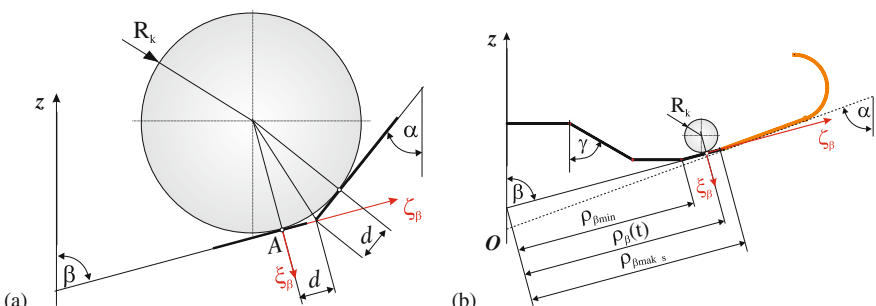


Fig. 3.36 The ball collision with rotating conical surface (a) and coordinates and frames (b)

$$\begin{aligned} v_{C\xi} &= \dot{x} \cos(\beta) \cos(\varphi) + \dot{y} \cos(\beta) \sin(\varphi) - \dot{z} \sin(\beta) , \\ v_{C\eta} &= \dot{y} \cos(\varphi) - \dot{x} \sin(\varphi) , \\ v_{C\zeta} &= \dot{x} \cos(\varphi) \sin(\beta) + \dot{y} \sin(\beta) \sin(\varphi) + \dot{z} \cos(\beta) , \end{aligned} \quad (3.142)$$

where $\varphi = \varphi(t)$ is the angular coordinate of the contact point and $\dot{x}, \dot{y}, \dot{z}$ are the ball mass center velocity components in the inertial frame $Oxyz$. The angular velocity components of the ball before the collision in $\xi_\beta \eta_\beta \zeta_\beta$ frame are described by

$$\begin{aligned} \omega_\xi &= \omega_1 \cos(\beta) \cos(\varphi) + \omega_2 \cos(\beta) \sin(\varphi) - \omega_3 \sin(\beta) , \\ \omega_\eta &= \omega_2 \cos(\varphi) - \omega_1 \sin(\varphi) , \\ \omega_\zeta &= \omega_1 \cos(\varphi) \sin(\beta) + \omega_2 \sin(\beta) \sin(\varphi) + \omega_3 \cos(\beta) , \end{aligned} \quad (3.143)$$

where $\omega_1, \omega_2, \omega_3$ denote the ball angular velocity components in $Oxyz$ frame.

The ball momentum changes, affected by the collision ($m\mathbf{v}'_C - m\mathbf{v}_C = \int \mathbf{F} dt$), allow us to find the reaction impulses S_ξ, S_η, S_ζ from the following relations:

$$\begin{aligned} S_\xi &= m \left(v'_{C\xi} - \cos(\beta) \cos(\varphi) \dot{x} - \cos(\beta) \sin(\varphi) \dot{y} + \sin(\beta) \dot{z} \right) , \\ S_\eta &= m \left(v'_{C\eta} + \sin(\varphi) \dot{x} - \cos(\varphi) \dot{y} \right) , \\ S_\zeta &= m \left(v'_{C\zeta} - \cos(\varphi) \sin(\beta) \dot{x} - \sin(\beta) \sin(\varphi) \dot{y} - \cos(\beta) \dot{z} \right) , \end{aligned} \quad (3.144)$$

in which $S_\xi = \int F_\xi dt, S_\eta = \int F_\eta dt, S_\zeta = \int F_\zeta dt$ are the reaction impulse components and $v'_{C\xi}, v'_{C\eta}, v'_{C\zeta}$ are the components of the ball mass center velocity after the impact.

The equations describing the changes in the ball rotation ($\mathbf{K}'_C - \mathbf{K}_C = \int \mathbf{M}_C dt$) due to the impulse components S_ξ, S_η, S_ζ can be transformed to the following form:

$$\begin{aligned} \frac{2}{5} m R_k (\omega'_\xi - \sin(\alpha - \beta) \omega_2 - \cos(\alpha - \beta) \omega_3) &= 0 , \\ S_\zeta + \frac{2}{5} m R_k (\omega'_\eta - \omega_1) &= 0 , \\ \frac{1}{5} (2m R_k (\omega'_\zeta - \cos(\alpha - \beta) \omega_2 + \sin(\alpha - \beta) \omega_3) - 5S_\eta) &= 0 , \end{aligned} \quad (3.145)$$

where symbols $\omega'_\xi, \omega'_\eta, \omega'_\zeta$ are used for the ball angular velocity components after the collision (in $\xi_\beta \eta_\beta \zeta_\beta$ frame).

The changes in angular momentum of the spinning wheel due to the ball interaction are obtained from the following equation:

$$J_w(\Omega'_w - \Omega_w) = S_\eta(\rho_{\alpha min} \sin(\alpha) - d \sin(\beta)) . \quad (3.146)$$

The constraints enclosing the ball motion within the rotating cone (rolling without sliding) are described by velocity-dependent equations in the form

$$v'_{C\xi} = 0 ,$$

$$\Omega'_w(\rho_{\alpha min} \sin(\alpha) - d \sin(\beta)) + \omega'_\zeta R_k + v'_{C\eta} = 0 , \quad (3.147)$$

$$v'_{C\xi} - \omega'_\eta R_k = 0 .$$

The numerical solution of (3.144), (3.145), (3.146), and (3.147) gives the values of the ball and spinning wheel velocity components $v'_{C\xi}$, $v'_{C\eta}$, $v'_{C\zeta}$, ω'_ξ , ω'_η , ω'_ζ , Ω'_w and the reaction impulse components S_ξ , S_η , S_ζ . On the basis of the reaction impulse components we find the value of minimum friction coefficient that is necessary to ensure that the ball is rolling without sliding. This minimum friction coefficient is equal to

$$\mu_{min} = \frac{\sqrt{S_\eta^2 + S_\zeta^2}}{-S_\xi} . \quad (3.148)$$

The sign minus in the denominator of this equation is due to axis ξ_β direction outward from the conical surface ($N = -S_\xi$ is the normal reaction force).

If the value (μ_β) of the friction coefficient between the ball and the roulette wheel is lower than μ_{min} it is necessary to change former assumption and to solve the next problem – the sliding of a ball on a wheel surface. For such a case instead of using (3.144) the following relations are used:

$$\begin{aligned} S_\xi &= m \left(v'_{C\xi} - \cos(\beta) \cos(\varphi) \dot{x} - \cos(\beta) \sin(\varphi) \dot{y} + \sin(\beta) \dot{z} \right) , \\ S_\eta &= \frac{\mu_\beta S_\xi (\cos(\varphi) \dot{y} - \sin(\varphi) \dot{x})}{\sqrt{(\cos(\varphi) \dot{y} - \sin(\varphi) \dot{x})^2 + (\cos(\varphi) \sin(\beta) \dot{x} + \sin(\beta) \sin(\varphi) \dot{y} + \cos(\beta) \dot{z})^2}} , \\ S_\zeta &= \frac{\mu_\beta S_\xi (\cos(\varphi) \sin(\beta) \dot{x} + \sin(\beta) \sin(\varphi) \dot{y} + \cos(\beta) \dot{z})}{\sqrt{(\cos(\varphi) \dot{y} - \sin(\varphi) \dot{x})^2 + (\cos(\varphi) \sin(\beta) \dot{x} + \sin(\beta) \sin(\varphi) \dot{y} + \cos(\beta) \dot{z})^2}} , \end{aligned} \quad (3.149)$$

which are obtained from friction force relationships:

$$S_\eta = S_\xi \mu_\beta \frac{v_{C\eta}}{\sqrt{v_{C\eta}^2 + v_{C\xi}^2}} , \quad S_\zeta = S_\xi \mu_\beta \frac{v_{C\zeta}}{\sqrt{v_{C\eta}^2 + v_{C\xi}^2}} , \quad (3.150)$$

together with the ball mas center velocity components given by (3.142).

Using S_η and S_ζ from (3.149) in (3.145), (3.146), and (3.147) we obtain a set of eight nonlinear algebraical equations with unknowns $v_{C\xi}$, $v_{C\eta}$, $v_{C\zeta}$, ω_ξ , ω_η , ω_ζ , Ω_w , S_ξ .

Having end results of the above presented problem of a ball collision with the rotating conical surface we are ready to analyze the ball motion on the spinning wheel.

3.3.7 Rolling of the Ball on the Spinning Wheel ($R_{(RC)}$)

The coordinate systems used in constructing the kinematic equations are shown in Fig. 3.36b. The velocity of the ball and wheel contact point components before the collision in xyz frame are obtained as follows:

$$\begin{aligned} v_{Ax} &= v_\rho \cos(\varphi) \sin(\beta) - v_\varphi \rho_\beta \sin(\beta) \sin(\varphi) , \\ v_{Ay} &= v_\rho \sin(\beta) \sin(\varphi) + v_\varphi \rho_\beta \sin(\beta) \cos(\varphi) , \\ v_{Az} &= v_\rho \cos(\beta) , \end{aligned} \quad (3.151)$$

where $v_\rho = \dot{\rho}$, $v_\varphi = \dot{\varphi}$.

The ball mass center acceleration components before the collision have the following form (in xyz frame):

$$\begin{aligned} a_{Cx} &= (\dot{v}_\rho - \rho_\beta \dot{v}_\varphi^2) \sin(\beta) \cos(\varphi) - (\rho_\beta \dot{v}_\varphi + 2v_\varphi \dot{\rho}_\beta) \sin(\varphi) , \\ a_{Cy} &= (\dot{v}_\rho - \rho_\beta \dot{v}_\varphi^2) \sin(\beta) \sin(\varphi) - (\rho_\beta \dot{v}_\varphi + 2v_\varphi \dot{\rho}_\beta) \cos(\varphi) , \\ a_{Cz} &= (\dot{v}_\rho - \rho_\beta \dot{v}_\varphi^2) \cos(\beta) . \end{aligned} \quad (3.152)$$

The ball mass center velocity components before the collision in $\xi_\beta \eta_\beta \zeta_\beta$ frame are obtained as follows:

$$v_{C\xi} = 0 , \quad v_{C\eta} = v_\varphi (\sin(\beta) \rho_\beta - \cos(\beta) R_k) , \quad v_{C\zeta} = v_\rho . \quad (3.153)$$

The constraints enclosing the ball motion on the rotating cone are described by velocity-dependent equations in the form

$$f_1 = R_k (\omega_3 - \cos(\beta) v_\varphi) + \sin(\beta) v_\varphi \rho_\beta - \Omega_w \rho_\beta \sin(\beta) , \quad f_2 = v_\rho - \omega_2 R_k . \quad (3.154)$$

The solution of equations $f_1 = 0$, $f_2 = 0$ leads to

$$\omega_2 = \frac{v_\rho}{R_k} , \quad \omega_3 = \frac{\cos(\beta) R_k v_\varphi + \sin(\beta) \rho_\beta (\Omega_w - v_\varphi)}{R_k} , \quad (3.155)$$

where $\omega_1, \omega_2, \omega_3$ denote the ball angular velocity components in $Oxyz$ frame and $\Omega_w = \dot{\Phi}$ is the roulette wheel angular velocity.

The ball mass center dynamic equations allow to present the reaction forces acting on the ball in the form:

$$\begin{aligned} F_1 &= mv_\varphi^2 \cos(\beta) (R_k \cos(\beta) - \rho_\beta \sin(\beta)) - mg \sin(\beta), \\ F_2 &= \frac{1}{3} (-2\pi \cos(\beta) \lambda_n v_\varphi R_k^3 - 4\pi \cos(\beta) \lambda_\tau v_\varphi R_k^3 + 2\pi \sin(\beta) \lambda_n v_\varphi \rho_\beta R_k^2 + \\ &\quad + 4\pi \sin(\beta) \lambda_\tau v_\varphi \rho_\beta R_k^2 - 3m \cos(\beta) \dot{v}_\varphi R_k + 6m \sin(\beta) v_\rho v_\varphi + \\ &\quad + 3m \sin(\beta) \rho_\beta \dot{v}_\varphi), \\ F_3 &= \frac{1}{3} (2\pi \lambda_n v_\rho R_k^2 + 4\pi \lambda_\tau v_\rho R_k^2 + 3m \cos(\beta) \sin(\beta) v_\varphi^2 R_k + \\ &\quad + 3mg \cos(\beta) - 3m \sin^2(\beta) v_\varphi^2 \rho_\beta + 3m \dot{v}_\rho). \end{aligned} \quad (3.156)$$

The changes in the ball angular momentum due to forces (3.156) lead to following equations:

$$\begin{aligned} \frac{2}{15} R_k (20\pi \lambda_\tau \omega_1 R_k^3 + 3m \dot{\omega}_1 R_k - 3m \cos(\beta) v_\rho v_\varphi) + \frac{8}{3}\pi R_k^4 \lambda_\tau \omega_1 &= 0, \\ \frac{1}{15} R_k (10\pi (\lambda_n + 6\lambda_\tau) v_\rho R_k^2 + 3m \cos(\beta) v_\varphi (7 \sin(\beta) v_\varphi + 2\omega_1) R_k + \\ &\quad + 3m (-7v_\varphi^2 \rho \sin^2(\beta) + 2v_\varphi \rho \Omega r \sin^2(\beta) + 5g \cos(\beta) + 7\dot{v}_\rho)) + \\ &\quad + \frac{8}{3}\pi R_k^3 \lambda_\tau v_\rho &= 0, \\ \frac{1}{15} R_k (10\pi \cos(\beta) (\lambda_n + 6\lambda_\tau) v_\varphi R_k^3 - 10\pi \sin(\beta) \rho (\lambda_n v_\varphi + 2\lambda_\tau (3v_\varphi - 2\Omega r)) R_k^2 + \\ &\quad + 21m \cos(\beta) \dot{v}_\varphi R_k - 3m \sin(\beta) (12v_\rho v_\varphi + 2(v_\varphi - \Omega r)\dot{\rho} + \\ &\quad + \rho (7\dot{v}_\varphi - 2\dot{\Omega}_w))) + \frac{8}{3}\pi R_k^3 \lambda_\tau (\cos(\beta) R_k v_\varphi + \sin(\beta) \rho (\Omega r - v_\varphi)) &= 0, \end{aligned} \quad (3.157)$$

where $\dot{v}_\rho = \ddot{\rho}$, $\dot{v}_\varphi = \ddot{\varphi}$, $\dot{\Omega}_w = \ddot{\Phi}$.

The changes in the angular momentum of a spinning wheel are obtained by the equation

$$\begin{aligned} J_w \dot{\Omega}_w - \frac{1}{3} \sin(\beta) \rho (-2\pi \cos(\beta) (\lambda_n + 2\lambda_\tau) v_\varphi R_k^3 + 2\pi \sin(\beta) (\lambda_n + \\ &\quad + 2\lambda_\tau) v_\varphi \rho R_k^2 - 3m \cos(\beta) \dot{v}_\varphi R_k + 3m \sin(\beta) (2v_\rho v_\varphi + \rho \dot{v}_\varphi)) &= 0. \end{aligned} \quad (3.158)$$

Solving (3.156), (3.157), and (3.158) we can find time series of seven unknowns $\rho, \varphi, \omega_1, \Phi, F_1, F_2, F_3$ which are the final results of this part of the dynamic analysis of a roulette wheel.

The sample results of the presented analysis of the ball rolling on the spinning wheel are shown in Figs. 3.37 and 3.38. We can see the differences in the ball trajectory for two values of the initial velocity $v_\varphi = 1.32037$ m/s and $v_\varphi = 1.320709$ m/s.

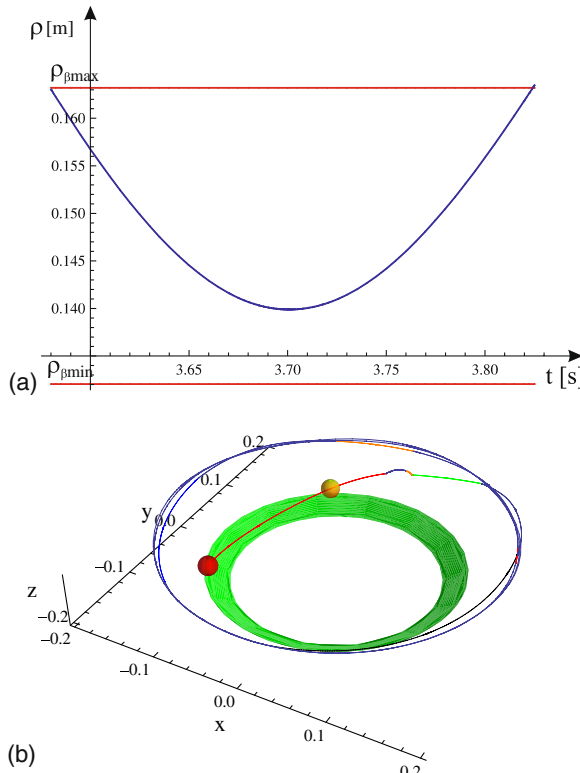


Fig. 3.37 The ball position on the rotating wheel (for the initial velocity $v_\phi = 1.32037$ m/s): (a) coordinate $\rho(t)$ ($\rho_{\beta\max}$ and $\rho_{\beta\min}$ are outer and inner edges of the spinning wheel) and (b) trajectory of the ball mass center

From Fig. 3.37 follows that during the analyzed time interval the ball mass center trajectory does not cross the lower border of the rotating conical surface (the line $\rho_{\beta\min}$ in Fig. 3.37a). For the second case shown in Fig. 3.38 the ball mass center trajectory crosses the line $\rho_{\beta\min}$ for $t \cong 3.81$ s and the ball lands in the pocket.

3.3.8 The Ball Landing in the Pocket ($L_{(PK)}$)

For the position coordinate on the rotating wheel $\rho(t) = \rho_{\beta\min}$ the ball lands in the pocket. Such a case is illustrated in Figs. 3.38 and 3.39.

The results of the roulette run for various initial conditions are shown in Sect. 4.5.

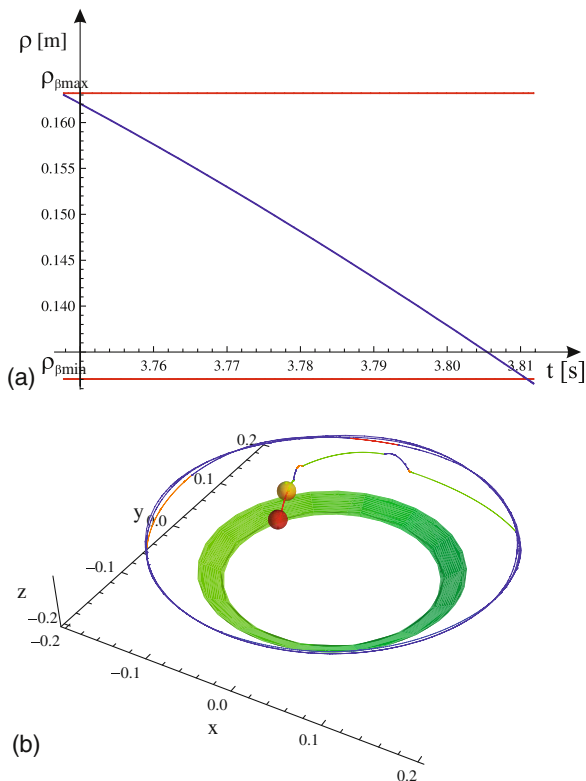


Fig. 3.38 The ball position on the rotating wheel (for the initial velocity $v_\phi = 1.320709$ m/s): (a) coordinate $\rho(t)$ ($\rho_{\beta\max}$ and $\rho_{\beta\min}$ are outer and inner edges of the spinning wheel) and (b) trajectory of the ball mass center

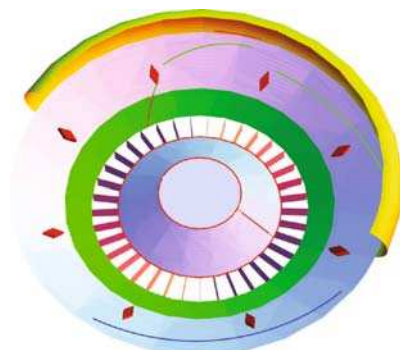


Fig. 3.39 Ball trajectory and outcome result on roulette wheel (number 29)

References

1. Mizuguchi, T., Suwashita, M.: Dynamics of coin tossing. *Progr. Theoret. Phys. Suppl.* **161**, 274 (2006) 42, 46, 56, 58
2. Vulović, V.Z., Prange, R.E.: Randomness of true coin toss. *Phys. Rev. A* **33/1**, 576 (1986) 42, 46, 56
3. Keller, J.B.: The probability of heads. *Amer. Math. Monthly* **93**, 191 (1986) 42
4. Strzałko, J., Grabski, J., Stefański, A., Perlikowski, P., Kapitaniak, T.: Dynamics of coin tossing is predictable. *Phys. Rep.* **469**, 59–92 (2008) 43
5. Neimark, J.I., Fufaev, N.A.: Dynamics of nonholonomic systems Translations of Mathematical Monographs, vol. 33. American Mathematical Society, Providence, Rhode Island, 518 (1972) 65, 70
6. Shaw, S., Holmes, P.: Periodically forced linear oscillator with impacts: Chaos and long-periodic motions. *Phys. Rev. Lett.* **51**, 623–626 (1983)
7. Mirtich, B.: Fast and accurate computation of polyhedral mass properties. *J. Graphics Tools* **1**, 2 (1996) 67, 68
8. Wolfram, S.: The Mathematica Book, 5th edn. Wolfram Media, Inc., Champaign, IL (2004) 68
9. Small, M., Tse, Ch. K.: Feasible implementation of a prediction algorithm for the game of roulette. In: Asia Pacific Conference on Circuits and Systems (IEEE), Macau, 30 November–3 December 2008. 71, 74
10. Schreiber, M.: "Expectations for Roulette" from The Wolfram Demonstrations Project. [http://demonstrations.wolfram.com/ExpectationsForRoulette/\(2009\)](http://demonstrations.wolfram.com/ExpectationsForRoulette/(2009)). Cited 10 May 2009 71
11. MacLin, O.H., Dixon, M.R.: A computerized simulation for investigating gambling behavior during roulette play. *Behav. Res. Methods, Instrum. Comput.* **36**(1), 96–100 (2004) 71

Chapter 4

Dynamics and Predictability

Abstract We present the results of the experimental observations and the numerical simulations of the coin toss, die throw, and roulette run. We give arguments supporting the statement that the outcome of the mechanical randomizer is fully determined by the initial conditions, i.e., no dynamical uncertainties due to the exponential divergence of initial conditions or fractal basin boundaries occur. We point out that although the boundaries between basins of attraction of different final configurations in the initial condition space are smooth, the distance of a typical initial condition from a basin boundary is so small that practically any uncertainty in initial conditions can lead to the uncertainty of the outcome.

4.1 Experimental Observations

We have performed some laboratory experiments that allow to monitor the motion of the tossed coin [1] and the thrown die.

In low-tech experiment (Fig. 4.1) photoelectric sensors (light curtains) are used to measure coin falling time.

In Fig. 4.1 experimental data are compared with theoretical curves showing $z(t)$ – the position of the coin in dependence of falling time. These curves represent theoretical results of the coin position for (i) air resistance force proportional to the coin velocity (v_z), (ii) air resistance force proportional to the square of coin velocity (v_z^2), (iii) air resistance omitted but gravity reduced ($g = 9.28 \text{ m/s}^2$), (iv) air resistance omitted and gravity reduced ($g = 9.52 \text{ m/s}^2$). As follows from the results presented in Fig. 4.1 (for two measurement series) the differences between particular curves are negligible, so we cannot conclude which method of computing air resistance force is adequate for such a coin.

Speed camera (Photron APX RS with the film speed at 1500 frames per second) has been used to observe the motion of a coin in our high-tech experiments. We observed the tossing of three coins; former Polish 1 zloty, current Polish 5 zloty and current British 2 pounds.

In the first experiment the coins were released at the height of 186 cm by a special device which allows for fixing the coin orientation at the beginning of motion. The examples of the coin motion during the free fall without rotation are

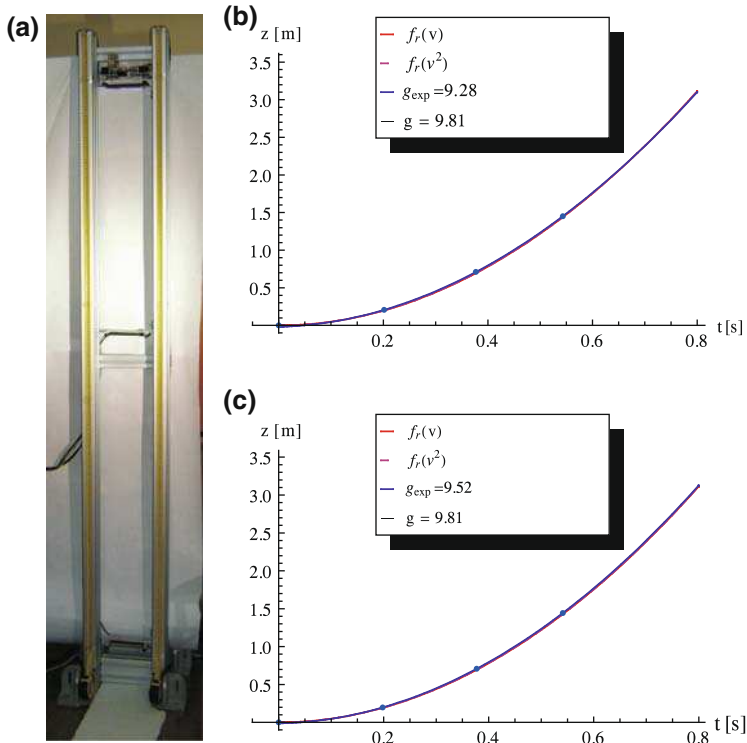


Fig. 4.1 Experimental rig (a) and results for Polish 5 zloty coin: (b) series I, (c) series II

shown in Fig. 4.2. Black points in this figure denote the positions of the coin center (they have been read from successive film frames). The experimental results are compared in Fig. 4.2 with theoretical curves obtained for coin free fall with no air resistance ($f_n = 0$), coin fall for air resistance proportional to the velocity ($f_n = f(v)$), and coin fall for air resistance proportional to the square of velocity ($f_n = f(v^2)$).

These experiments allow us to estimate the air resistance coefficients in normal and tangent directions (λ_n, λ_τ). For former Polish 1 zloty coin these coefficients are equal, respectively, to $\lambda_\tau \cong 0.4$ and $\lambda_n \cong 1.5$.

In Fig. 4.3 snapshots presenting the behavior of the coin before and after the impacts against the floor. In this case the coin rotates around all possible axes (the motion with precession), slides on the floor, and can change its side during the motion between successive collisions. Our observations suggest that the bouncing of the coin on the floor introduces sensitive dependence of the final state (heads or tails) on the coin orientation at the moment of the impact. The phenomena, which take place during the impacts, can play a major role in the determination of the outcome of the toss. Generally, the coin bouncing on the floor is more fair than the coin landing on the soft floor or caught in the hand.

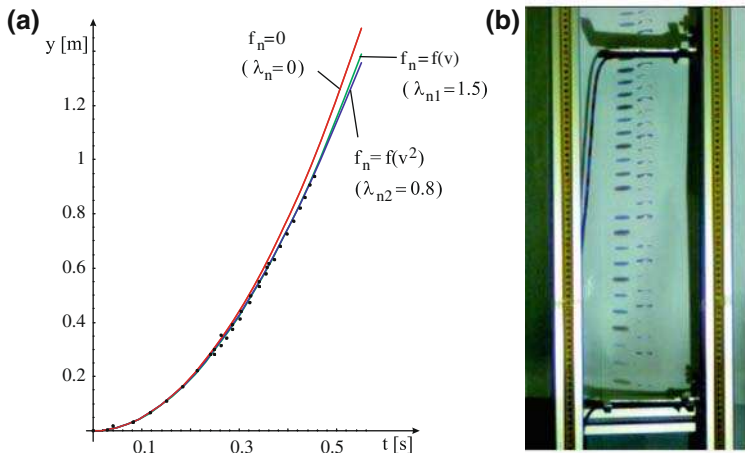
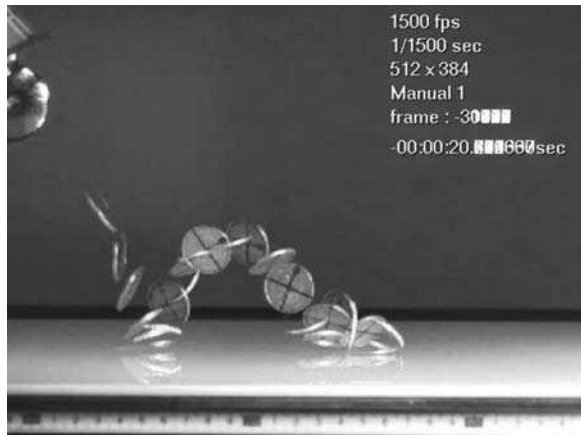


Fig. 4.2 Coin free fall: (a) comparison of experimental data and simulation results for “1 zloty” coin and (b) collections of subsequent positions of the coin during free fall

Fig. 4.3 Collections of snapshots presenting the behavior of tossed coin (Polish 1 zloty) before and after the impacts



From our experiments carried out for the falling coins follows that

1. for the realistic coin it is sufficient to consider a simplified model of the ideal thin coin,
2. the 1D coin model can be employed to analyze its dynamics even if the air resistance is to be taken into account.

In order to perform the experimental examination of dice tossing we build a rig which is shown in Fig. 4.4. Its construction lets us change the angle of the plate on which the die is sliding and introduce the different initial velocities of the die at the edge. Moreover, it is possible to change the distance between the plate and the table by which we can vary the time of falling and the velocity at the first collision. A scale is showing the distance between the starting point and the current position

Fig. 4.4 Experimental rig for dice tossing



of the die. To investigate an influence of the restitution coefficient we changed the table sheets between acrylic, plywood ($\chi = 0.62$), glass ($\chi = 0.67$), and cork ($\chi = 0.58$). These coefficients of restitution were determined experimentally.

We examined the tetrahedron, cube, octahedron, dodecahedron, and icosahedron dice. In Fig. 4.5 we present the tetrahedron die falling on the acrylic sheet from a height of 15 cm. In the considered toss we observed 24 collisions with time intervals between succeeding collisions: 0.158666, 0.006, 0.116667, 0.004667, 0.034, 0.02, 0.018, 0.040666, 0.01, 0.03, 0.032, 0.008667, 0.032667, 0.016, 0.012, 0.017333, 0.008, 0.005333, 0.004667, 0.012, 0.009333, 0.007334, 0.005333 [s]. Some of them are grouped – one corner of the die hits the table and immediately after it the other one also hits it. After every collision the energy of the die is smaller. The die is bouncing lower and its rotation vanishes. Finally, last 10 collisions have no influence on the die's final configuration.

In Fig. 4.6a we show the snapshots for the cube die in the case of the plywood table sheet (there were 12 collisions, the distance between the starting point and the final position was 19.5 cm). We made the same observations in the case of glass (25 collisions, 22.5 cm) and acrylic (15 collisions, 20 cm). In Fig. 4.6b we show an octahedron die with cork table sheet. There were 13 collisions and 26 cm distance and in the last one – Fig. 4.6c – the icosahedron die (20 faces) is presented, we detected 17 impacts and 46 cm distance.

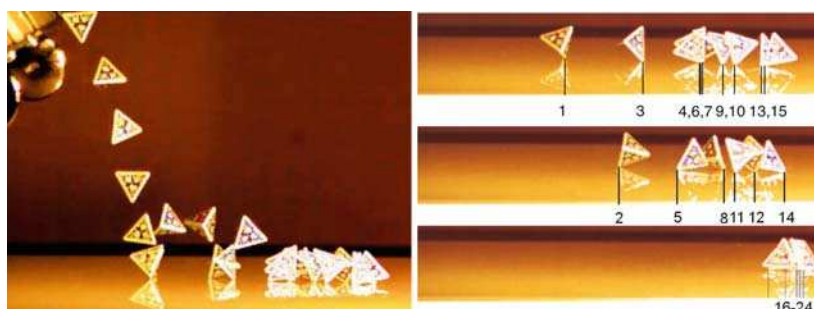


Fig. 4.5 Selected positions of the tetrahedron die during free fall and collisions. Subsequent collision points with the table are marked with the *black lines* and *collision numbers*

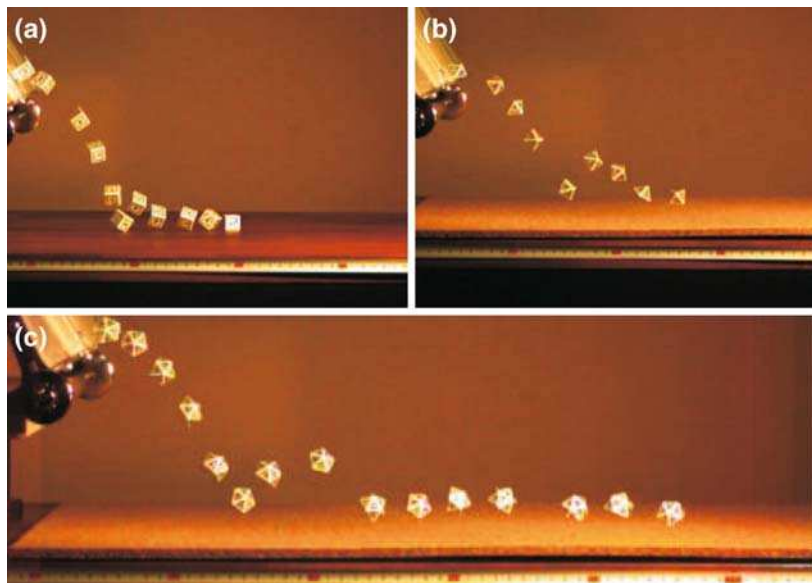


Fig. 4.6 Selected positions of dice during free fall and collisions: (a) cube; (b) octahedron; and (c) icosahedron

When the number of the die faces increases and the shape of the die becomes closer to the ball one can observe that the die motion is “rolling-like” and the distance between the starting point and the final position is bigger.

4.2 Simplified Models

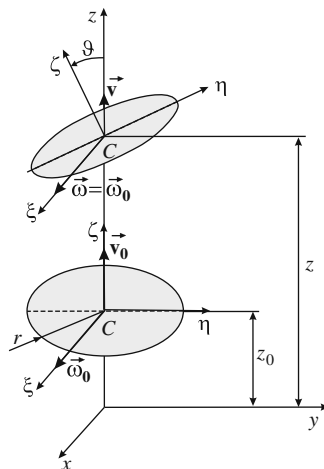
4.2.1 Keller’s Model

The detailed studies of the tossed coin dynamics started with the work of Keller [2]. His results can be summarized in the following way. Consider an ideal coin and assume that the center of the mass which can move vertically is at the height $z(t)$ at time t . In addition to its vertical motion, the coin is assumed to be rotating about a horizontal axis that lies along the diameter of the coin. Let x be the axis which is parallel to this rotation axis. One can describe the angular position of the coin at time t by the angle $\vartheta(t)$ between the positive z -axis and the normal to the side of the coin which is up at $t = 0$ (see Fig. 4.7). When $\vartheta(0) = 0$ the coin rotates with n_0 revolutions per second (angular velocity $\omega_0 = 2\pi n_0$).

If the initial velocity in the upward direction z is v_0 , after t seconds, a coin tossed at the initial height z_0 will be at the height

$$z = z_0 + v_0 t - \frac{1}{2} g t^2, \quad (4.1)$$

Fig. 4.7 Keller's [2] coin tossing model (rotation around axis (ξ) parallel to x)



where g is the acceleration due to gravity. If the coin is caught when it returns to the initial height z_0 , the elapsed time t^* of the coin motion satisfies $t^* = 2v_0/g$, so the coin has revolved $n = 2n_0v_0/g$ times. If n is between $2j$ and $2j + 1$, where $j = 0, 1, 2, \dots$ the initial side will be up-most and if $n \in (2j + 1, 2j + 2)$ the opposite side will be up-most. Figure 4.8 shows the decomposition of the phase space $(\omega_0/\pi, v_0/g)$ into regions where the coin comes up as it started (gray regions) or opposite (white regions). These two regions are separated by the hyperbola $2n_0v_0/g = j$ (or $\frac{\omega_0 v_0}{\pi g} = j$). Assuming that coin starts with the head side up gray and white regions in Fig. 4.8 describe the sets H and T of initial conditions which lead to head and tail outputs of the toss.

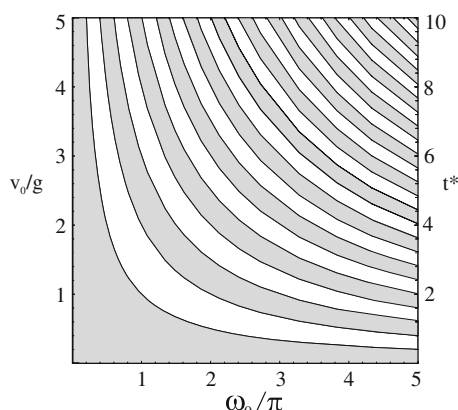


Fig. 4.8 Initial conditions in the phase space $(\omega_0/\pi, v_0/g)$ and in the phase space $(\omega_0/\pi, t^*)$ leading to heads (white regions) and tails (gray regions) [2, 3]

Now we suppose that a pair of initial conditions¹ ω, v is a random variable with a continuous probability density $p(\omega, v)$ with support in the region $\omega > 0, v > 0$. Then the probability of heads P_H is given by

$$P_H = \int \int_H p(\omega, v) d\omega dv . \quad (4.2)$$

Thus the outcome is random because we assumed that the initial conditions are random.

For any value P_H in the interval 0–1, there are densities p for which integral (4.2) has that value, so (4.2) does not place any restriction on P_H . However, we shall now show that when the support of p is shifted to sufficiently large values of v and possibly to large values of ω , then P_H tends to a fixed limit which is independent of the density $p(\omega, v)$. These observations can be summarized in the following theorem [2].

Theorem 4.1. *Let $p(\omega, v)$ be a continuous probability density with support in the region $\omega > 0, v > 0$, and let β be a fixed constant satisfying $0 \leq \beta \leq \pi/2$. Then*

$$\lim_{U \rightarrow \infty} P_H = \lim_{U \rightarrow \infty} \int \int_H p(v - U \cos \beta, \omega - r^{-1} U \sin \beta) d\omega dv = \frac{1}{2} . \quad (4.3)$$

Proof. The proof can be found in [2], although the conclusions are evident from Fig. 4.8. \square

The significance of this theorem is that there is a unique probability of heads which is approximately achieved by any continuous probability density of the initial values ω, v that is shifted to sufficiently large values of ω and v . The approximation improves as the density $p(\omega, v)$ is translated to larger values of ω, v .

The limiting value of P_H is 1/2, despite the fact that the initial condition is not symmetric in heads and tails, since the coin always starts out with heads up. Therefore the traditional method of calculating P_H , based on the symmetry, is not applicable.

The reason why P_H has a limit as U increases is that the sets H and T both consist of many strips which become very narrow at infinity. Thus both H and T occupy the fixed fractions of the area of any disk which is shifted to infinity.

Here is the Engel–Kemperman theorem from [3], specialized to the coin tossing case. Let $f(\omega, t)$ be a probability density on the (t, ω) plane. Thus $f(\omega, t) \geq 0$ and

$$\int \int f(\omega, t) d\omega dt = 1 . \quad (4.4)$$

¹ For the ideal model of coin (no air interaction) the angular velocity is constant during the free fall ($\omega = \omega_0$). In (4.2), (4.3), (4.4), (4.5), (4.6), (4.7), (4.8), (4.9), (4.10), (4.11), and (4.12) we use the symbols ω, v for initial conditions (instead of ω_0, v_0) and the symbol t for time t^* at which the coin lands.

The marginal densities $f_1(\omega)$, $f_2(t)$ are defined by

$$f_1(\omega) = \int f(\omega, t) dt \quad (4.5)$$

and

$$f_2(t) = \int f(\omega, t) d\omega . \quad (4.6)$$

The conditional densities $f_\omega(t)$ and $f_t(\omega)$ are defined by

$$f_\omega(t) = \frac{f(\omega, t)}{f_1(\omega)} , \quad (4.7)$$

$$f_t(\omega) = \frac{f(\omega, t)}{f_2(t)} . \quad (4.8)$$

Thus $f_\omega(t)$ is the probability density which gives the chance that a random quantity with density $f(\omega, t)$ is in the interval $(t, t + dt)$ given an observed, fixed value of ω . The following theorem applies to the case where $\psi = \pi/2$. The translation of f is the probability density $\bar{f}(\omega, t) = f(\omega + \omega_0, t + t_0)$.

Theorem 4.2. *Let $f(\omega, t)$ be a probability density on the plane (t, ω) with marginal densities $f_1(\omega)$, $f_2(t)$, and differentiable conditional densities $f_\omega(t)$ and $f_t(\omega)$. Translate f to $f(\omega + \omega_0, t + t_0)$. Then, the probability over the heads region in Fig. 4.8 satisfies*

$$\left| P(\text{heads}) - \frac{1}{2} \right| \leq 4\pi \min \left(\frac{W_v}{t_0}, \frac{W_\omega}{\omega_0} \right) , \quad (4.9)$$

where

$$W_v = \int \int |f'_t(\omega)| f_1(\omega) d\omega dt , \quad (4.10)$$

and

$$W_\omega = \int \int |f'_\omega(t)| f_2(t) dt d\omega . \quad (4.11)$$

To see if this theorem is useful for natural coin tosses, an empirical measurement has been carried out in [3]. These measurements show that natural coin tosses (approximately one foot tosses of duration about 1/2 s) have initial conditions that satisfy $36 \leq \omega \leq 40$, $7 \leq v \leq 9$ equivalent to $0.44 < t < 0.56$, with ω measured

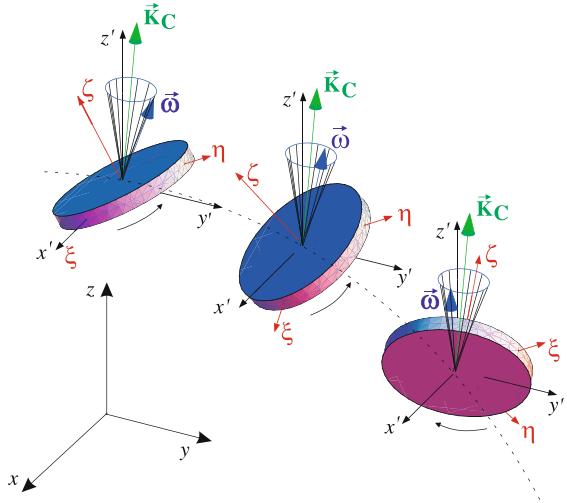
in rev/s, v in ft/s, and t in seconds. Assuming a uniform distribution in this region, Theorem 4.2 gives

$$\left| P(\text{heads}) - \frac{1}{2} \right| \leq 0.056 . \quad (4.12)$$

4.2.2 Precession of a Coin

The ideal model of a coin (no air interaction) is the body classified as symmetric top. The precession of such a body is described in Sect. 2.2 and shown in Fig. 4.9.

Fig. 4.9 The precessing coin: vectors of angular velocity (ω) and angular momentum (\mathbf{K}_c) in the spatial frame xyz



In Sect. 2.2 it is shown that for torque-free motion (body force moment $\mathbf{M}_c = \mathbf{0}$) the angular momentum vector \mathbf{K}_c has constant value (2.19) and direction in the spatial frame xyz . The angular velocity vector ω has constant value (2.15) and rotates. Presented in Sect. 2.2 solution of problem (2.13) allows us to state that for ideal coin the angle γ (Fig. 4.10) between the vector \mathbf{K}_c and the normal to the coin (axis ξ) stays constant (2.20).

As follows from Fig. 4.10b the vector of body angular velocity (ω) can be resolved into two components ω_n and ω_p ($\omega_n + \omega_p = \omega$), and the values of these vectors are obtained from relations:

$$\frac{\omega_n}{\omega_\tau} = \frac{K_c}{K_\tau} , \quad \frac{\omega_p}{\sin(\alpha - \gamma)} = \frac{\omega}{\sin(\gamma)} , \quad (4.13)$$

where $K_\tau = J_1 \sqrt{\omega_{\xi 0}^2 + \omega_{\eta 0}^2}$. Taking into account (2.17), (2.19), and (2.20) we find that

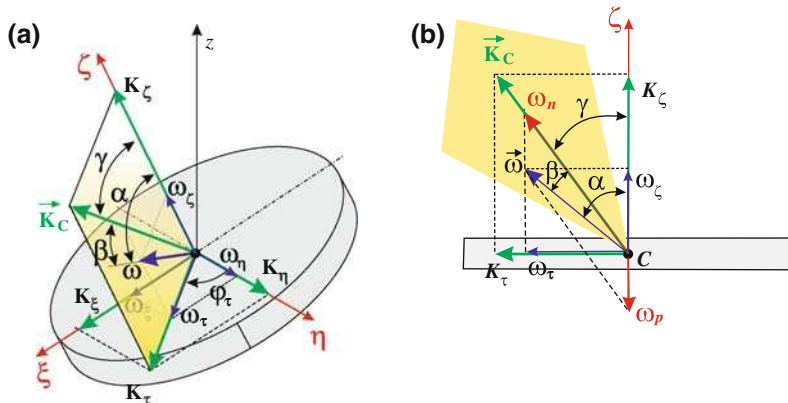


Fig. 4.10 Torque-free precession of a coin (a symmetric top): (a) vectors of angular velocity ($\tilde{\omega}$), angular momentum (\mathbf{K}_c), and their components and (b) the plane rotating with angular rate ω_n about the angular momentum vector

$$\omega_n = \frac{K_c}{J_1}, \quad \omega_p = \frac{J_3 - J_1}{J_1} \omega_{\xi 0}. \quad (4.14)$$

Changes of the angular velocity vector $\boldsymbol{\omega}$ we can describe in the following form

$$\frac{d\boldsymbol{\omega}}{dt} = \hat{\frac{d\boldsymbol{\omega}}{dt}} + \boldsymbol{\omega} \times \boldsymbol{\omega}, \quad (4.15)$$

where $\boldsymbol{\omega} \times \boldsymbol{\omega} = \mathbf{0}$, whereas the changes of the vector $\boldsymbol{\omega}$ due to rotation with velocity $\boldsymbol{\omega}_p$ in the local frame $\xi\eta\zeta$ (Fig. 4.10b) are obtained as

$$\frac{d\boldsymbol{\omega}}{dt} = \hat{\frac{d\boldsymbol{\omega}}{dt}} = \boldsymbol{\omega}_p \times \boldsymbol{\omega} = \boldsymbol{\omega}_p \times (\boldsymbol{\omega}_n + \boldsymbol{\omega}_p) = -\boldsymbol{\omega}_n \times \boldsymbol{\omega}_p. \quad (4.16)$$

It means that the absolute time derivative of the vector $\boldsymbol{\omega}$ can be calculated as

$$\frac{d\boldsymbol{\omega}}{dt} = -\boldsymbol{\omega}_n \times \boldsymbol{\omega}, \quad (4.17)$$

since $\boldsymbol{\omega}_n \times \boldsymbol{\omega}_p = \boldsymbol{\omega}_n \times \boldsymbol{\omega}$.

The influence of precession on the tossed coin motion for ideal model of coin was investigated by Diaconis et al. [3]. They show that if the angle γ is less than $\pi/4$ ($\gamma < \pi/4$), the coin never turns over if it started head up: “It wobbles around and always comes up the way it started. In all of these cases there is precession. Magicians and gamblers can carry out such controlled flips which appear visually indistinguishable from normal flips.”

4.2.2.1 Coin Tossed without Precession

There are two cases of the ideal coin motion with no precession: a “total cheat coin” and Keller’s case [3].

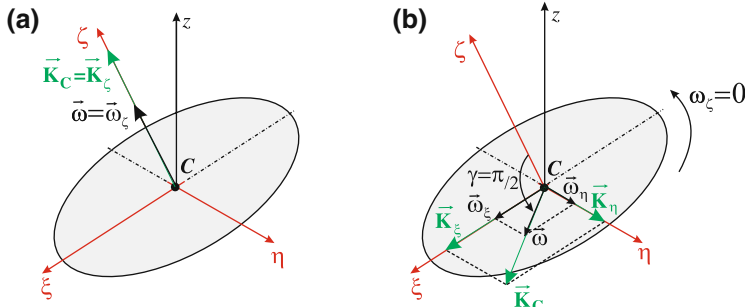


Fig. 4.11 Coin motion without precession: (a) total cheat coin toss ($\omega_\xi = 0, \omega_\eta = 0, \omega_\zeta \neq 0, K_c = J_3\omega_{\zeta 0}, \gamma = 0$) and (b) Keller’s case – “fair tossed” coin ($\omega_\zeta = 0, \omega = \sqrt{\omega_{\xi 0}^2 + \omega_{\eta 0}^2}, K_c = J_1\sqrt{\omega_{\xi 0}^2 + \omega_{\eta 0}^2}, \gamma = \pi/2$)

“Total cheat coin” (Fig. 4.11a) rotates about its normal axis (ζ) but moves without turning (like a spinning pizza). In this case $\mathbf{K}_c = J_3\boldsymbol{\omega}$, where $\boldsymbol{\omega} = \omega_\zeta$ ($\omega_\xi = \omega_\eta = 0$). The angle $\gamma = 0$ and vectors $\boldsymbol{\omega}, \mathbf{K}_c$ are collinear with direction of ζ -axis.

In the case analyzed by Keller (Figs. 4.7 and 4.11b) it is assumed that the angular momentum vector (\mathbf{K}_c) lays in the plane of the coin ($\gamma = \pi/2$) and has the same direction as the coin angular velocity vector ($\boldsymbol{\omega}$).

The toss of coin will be called “fair” if $\omega_{\zeta 0} = 0$. For the “fair tossed” ideal coin from (2.17) we have $\omega_p = 0, \sin \varphi_t = \omega_{\xi 0}/\omega_t, \cos \varphi_t = \omega_{\eta 0}/\omega_t$, and its rotation is described by constant angular velocity components

$$\omega_\xi(t) = \omega_{\xi 0}, \quad \omega_\eta(t) = \omega_{\eta 0}, \quad \omega_\zeta(t) = 0. \quad (4.18)$$

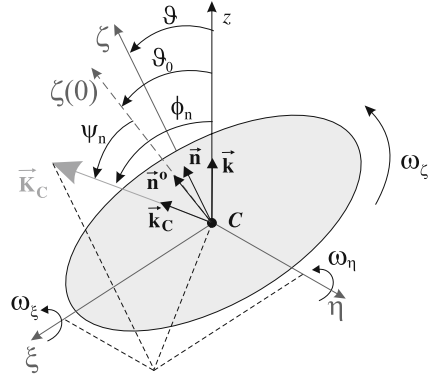
It means that for the “fair tossed” ideal coin the angular momentum vector (\mathbf{K}_c) has constant value components ($K_\xi = J_1\omega_{\xi 0}, K_\eta = J_1\omega_{\eta 0}, K_\zeta = 0$) and is perpendicular to the ζ -axis ($\gamma = \pi/2$) (Fig. 4.11b). The vectors $\boldsymbol{\omega}, \mathbf{K}_c$ are constant and collinear.

4.2.2.2 Probability of Heads

Here we present two theorems proved by Diaconis et al. [3] that allow to obtain the probability of the coin coming up as started. They are valid for ideal model of coin with no air interaction (Fig. 4.12).

Theorem 4.3. Let $f_\vartheta(t) = \mathbf{n} \cdot \mathbf{k}$ be the quantity which determines “heads” or “tails,” i.e., the cosine of the angle (ϑ) between the normal \mathbf{n} to the coin at time t and up direction \mathbf{k} . Define ψ_n and ϕ_n by

Fig. 4.12 The precessing coin: vector of angular momentum (\mathbf{K}_C) and the unit vectors \mathbf{k} , \mathbf{n} , \mathbf{k}_C and $\mathbf{n}^o = \mathbf{n}(0)$



$$\cos \psi_n = \mathbf{n}^o \cdot \mathbf{k}_c , \quad \cos \phi_n = \mathbf{k} \cdot \mathbf{k}_c , \quad (4.19)$$

then

$$f_\vartheta(t) = A + B \cos(\omega_n t + \vartheta_0) , \quad (4.20)$$

with $A = \cos \psi_n \cos \phi_n$, $B = \sin \psi_n \sin \phi_n$, $\omega_n = K_c / J_1$ for $J_1 = \frac{1}{4}(mr^2 + \frac{1}{3}mh^2)$, $K_c = \sqrt{J_1^2(\omega_{\xi 0}^2 + \omega_{\eta 0}^2) + J_3^2\omega_{\zeta 0}^2}$ and phase ϑ_0 is determined by $\mathbf{k} \cdot \mathbf{n}(0)$ (Fig. 4.12).

Theorem 4.4. Let ψ_n , ϕ_n , $0 \leq \psi_n$, $\phi_n \leq \pi/2$, be defined as in Theorem 4.3. As ω and t tend to infinity, let $p(\psi_n, \phi_n)$ be limiting probability of heads for coin toss, starting with heads up, with angle ψ_n between the normal $\mathbf{n}(0)$ to the coin and angular momentum \mathbf{K}_c , and angle ϕ_n between the up direction \mathbf{k} and \mathbf{K}_c . Then

$$p(\psi_n, \phi_n) = \begin{cases} \frac{1}{2} + \frac{1}{\pi} \sin^{-1} (\cot(\phi_n) \cot(\psi_n)) & \text{if } \cot(\phi_n) \cot(\psi_n) \leq 1 , \\ 1 & \text{if } \cot(\phi_n) \cot(\psi_n) \geq 1 . \end{cases} \quad (4.21)$$

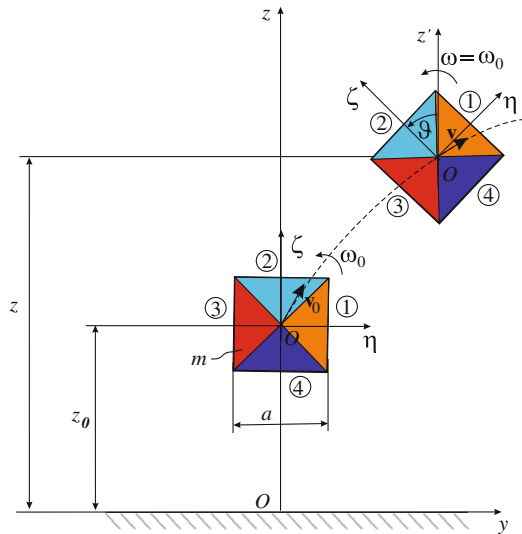
4.2.3 Plane Motion Model of a Cubic Die

The mapping approach has been used by Feldberg et al. [4] and Mosekilde [5] in the analysis of plane motion of a cubic die (the model of cubic die with two faces parallel to the vertical plane – see Fig. 4.13).

Nonlinear iterating mapping technique relates the position of one point on the trajectory to the coordinates of another point. The sequence of a die free fall (F) and collisions (C) with a table allows to obtain the trajectory of the die by iteration between two maps.

In Fig. 4.14a we present $F-C-F$ map (F means free fall, C a collision with the table) showing the die throw outcome distributions before the second collision for

Fig. 4.13 Feldberg–Mosekilde's model of a cubic die



plane motion of the cube die model. The die throw outcome distributions before the third collision ($F-C-F-C-F$ map) for the same model is shown in Fig. 4.15a. These results are quite close (qualitatively) to the results from the work [4]. (They are not identical because of the lack of complete data used in the calculations reported in [4].)

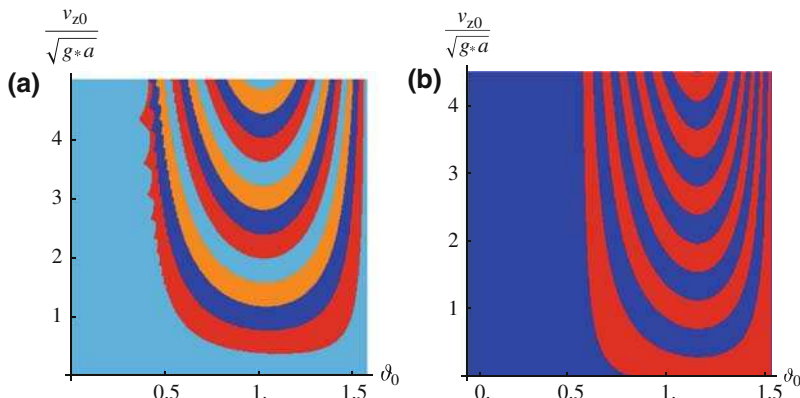


Fig. 4.14 Comparison of the die throw outcome distributions ($F-C-F$ maps) for (a) cube die plane motion model (Feldberg–Mosekilde's model) and, (b) the barbell model (Nagler–Richter's model). Results for the data ($m = 0.016 \text{ kg}$, $a = 0.02 \text{ m}$, $J_\eta = 1.06667 \times 10^{-6} \text{ kg m}^2$, $\chi = 0.5$, $\omega_{\eta 0} = 0$, $0 < v_{z0}/\sqrt{ga} < 5$, $0 < \vartheta_0 < \pi/2$)

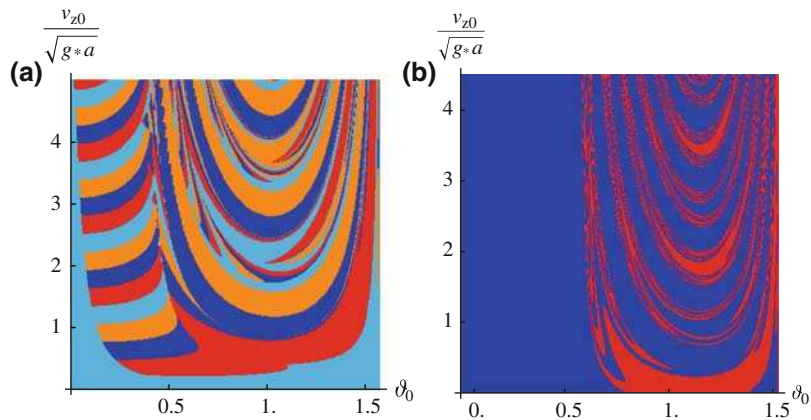


Fig. 4.15 Comparison of the die throw outcome distributions ($F-C-F-C-F$ maps) for: (a) the cube die plane motion model (Feldberg–Mosekilde’s model), (b) the barbell model (Nagler–Richter’s model). The data are the same as for Fig. 4.14

4.2.4 Nagler–Richter’s Model of a Die

An interesting analysis of a die as a random number generator was presented by Nagler and Richter [6]. The model used in [6] was a massless rod with two particles of mass m_1 and m_2 at its ends (the barbell model). It is shown in Fig. 4.16.

The authors of [6] assumed that it is admissible to reduce a cube die having one of its axis parallel to the table (like a square in plane motion). Further reduction rests on assigning the same numbers to opposite sides of the square. There are two outcomes of the barbell toss – it is laying on the table with one of two masses on the

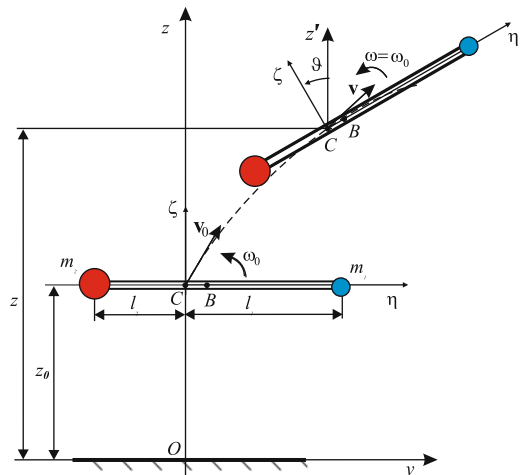


Fig. 4.16 Nagler–Richter’s model of cubic die

right. Using the mapping method the authors presented final state diagrams of the model for different values of the restitution coefficient.

In our opinion the model proposed by Nagler and Richter [6] and the results obtained using this model are adequate for no precession “fair tossed” coin (see Sect. 4.2.2) rather than for a die throw. The barbell model and the bar model (see Sect. 3.1.1) are suitable for plane motion analysis of a coin.

Disadvantages of the barbell model in the analysis of cube die are as follows. First, a change of a cube die throw outcome takes place for the rotation angle increment equal to $\pi/2$ ($\Delta\vartheta = \pi/2$) whereas for the barbell model for $\Delta\vartheta = \pi$ (Fig. 4.17). Second, the mass center coordinates of cube die are different from coordinates for the barbell so the gravity force effect in these two cases will be different.

Exemplary trajectories simulated for the models under consideration are shown in Fig. 4.18. We can compare the results for the barbell model and the cube model (in

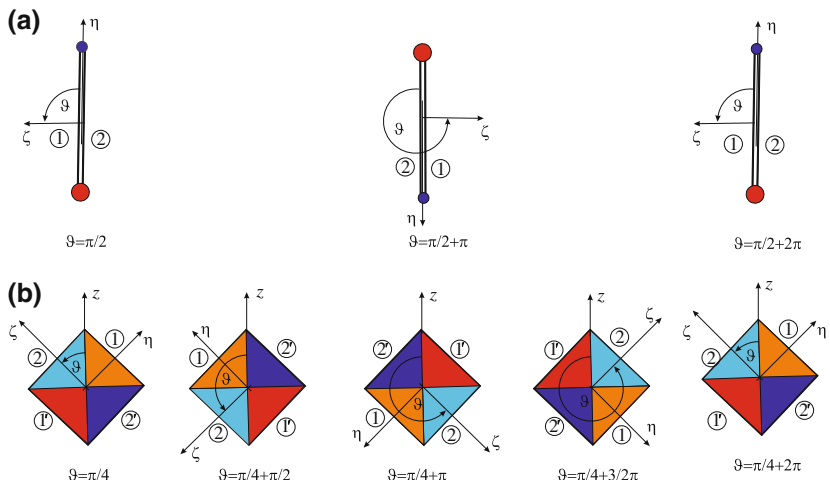


Fig. 4.17 Positions affecting changes in the outcome of dice throw for (a) barbell model ($\Delta\vartheta = \pi$) and (b) plane motion of cube die model ($\Delta\vartheta = \pi/2$)

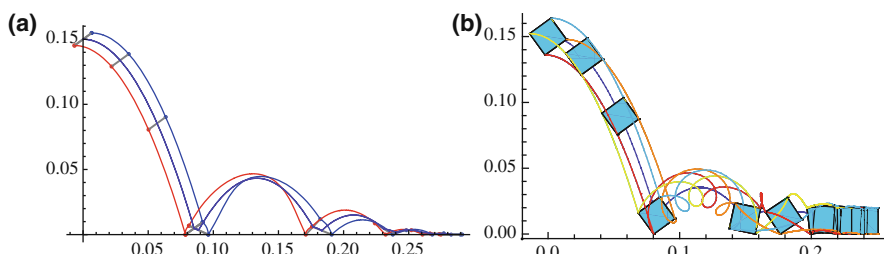


Fig. 4.18 Die throw results for (a) barbell model ($m_1 = 0.008 \text{ kg}$, $m_2 = 0.008 \text{ kg}$, $l_1 = 0.00816 \text{ m}$, $l_2 = 0.00816 \text{ m}$, $J_C = 1.0667 \times 10^{-6} \text{ kg m}^2$, $z_0 = 0.15 \text{ m}$, $\omega_{\eta 0} = 0$, $\vartheta_0 = \pi/5$) and, (b) plane motion of cube die model ($m = 0.016 \text{ kg}$, $a = 0.02 \text{ m}$, $J_C = 1.0667 \times 10^{-6} \text{ kg m}^2$, $z_0 = 0.15 \text{ m}$, $\omega_{\eta 0} = 0$, $v_x = 0.5 \text{ m/s}$, $v_z = 0$, $\vartheta_0 = \pi/5$, $\chi = 0.5$)

plane motion) of die for the same dynamical characteristics and identical initial conditions. Corresponding basins of attraction for both models after subsequent collisions are shown, respectively, in Figs. 4.14 and 4.15. We can see that the structure of mappings in both cases is qualitatively similar but the regions representing outcomes 1' and 2' for the Feldberg–Mosekilde’s model (Fig. 4.17b) are indistinguishable for Nagler–Richter’s model.

4.3 Coin Tossing Simulation

We assume that the coin is thrown at the height z_0 (the mass center initial position vector $\mathbf{r}_{(t=0)} = [x_0 \ y_0 \ z_0]^T$), coin initial orientation $\boldsymbol{\psi}_{(t=0)} = [\psi_0 \ \theta_0 \ \varphi_0]^T$ with the initial angular velocity $\boldsymbol{\omega}_{\xi(t=0)} = [\omega_{\xi 0} \ \omega_{\eta 0} \ \omega_{\zeta 0}]^T$ and the mass center initial velocity $\mathbf{v}_{c(t=0)} = [\dot{x}_0 \ \dot{y}_0 \ \dot{z}_0]^T$. After a free fall when z coordinate of one of coin points is equal to zero, say $z_d = 0$, the coin collides with the horizontal base (floor). It is assumed that at the collision a portion of the coin energy is dissipated, i.e., the collision is described by the restitution coefficient $\chi < 1$. After the collision, the coin mass center moves to the height z_1 in which the total mechanical energy of the coin $E = T + V$ is equal to its total energy in the moment after the collision $E' = T' + V'$. (In the case when air resistance is taken into account total mechanical energy of the coin at height z_1 is less than its value after the collision $E < E'$.) Next, the coin moves on until it collides with the floor again. The calculations are terminated when after the n th collision the total mechanical energy of the coin $E = T + V$ is smaller than the potential energy at the coin center level equal to its radius r , i.e., $E < mgr$, as this condition disables the change of the coin face during further motion. The no-turning-over condition $E < mgr$ can be modified in particular cases of the coin–base collision model. For example, for symmetric, perfectly smooth – frictionless – coin and floor the condition is $E(z, \dot{z}, \omega_{\xi}, \omega_{\eta}) < mgr$, that means that only the part of kinetic energy is taken into account, i.e., the term $\frac{1}{2}J_{\zeta}\omega_{\zeta}^2$ is neglected. This improved criterion has the form

$$T + V - \frac{1}{2}(m\dot{x}^2 + m\dot{y}^2 + J_{\zeta}\omega_{\zeta}^2) < mgr . \quad (4.22)$$

In our numerical calculations we consider the following coin data: $m = 2$ g, $r = 1.25$ cm, $h = 0.2$ cm (former Polish 1 PLN coin made of light aluminum-based alloy) with $\xi_c = 0$, $\eta_c = 0$, $\zeta_c = 0$ – for an ideal coin, and $\xi_c = -0.1$ cm, $\eta_c = -0.1$ cm, $\zeta_c = -0.02$ cm – for an imperfect coin. For numerical simulations we used a standard *Mathematica*[®] package [7, 8].

The results of simulations of the coin motion during the free fall for neglected air resistance are shown in Fig. 4.19a–d. Figure 4.19a,b shows a simulation of the motion of the 3D imperfect and ideal (Fig. 4.19b) coin models ((3.1), (3.2), (3.3), (3.4), (3.5), (3.6), (3.7), and (3.8), respectively). Figure 4.19c,d presents the results for a 2D model of imperfect (Fig. 4.19c) and ideal (Fig. 4.19d) thin coins ((3.9), (3.10), and (3.11)).

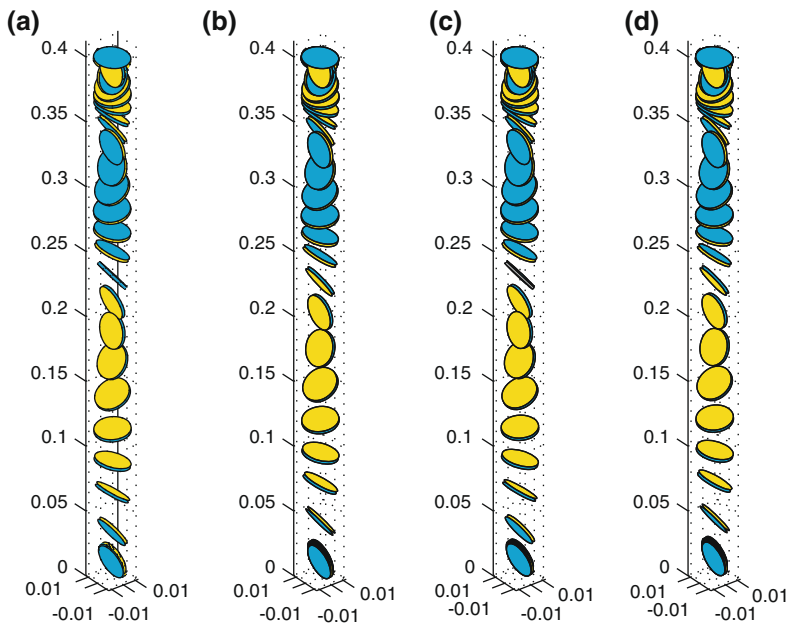


Fig. 4.19 Coin motion simulation results: (a) 3D imperfect coin model, (b) 3D ideal coin model, (c) 2D imperfect coin model, and (d) 2D ideal coin model

A comparison of different coin models in the presence of air resistance is shown in Fig. 4.20 where the trajectories calculated with different models are presented for 3D imperfect coin, 3D ideal coin, 2D imperfect coin, and 2D ideal coin.

Equations (3.1), (3.2), (3.3), (3.4), and (3.15) describe the case where the free fall of different coin models are differentiable so that one can calculate transient Lyapunov exponents. By transient Lyapunov exponents we mean values obtained for

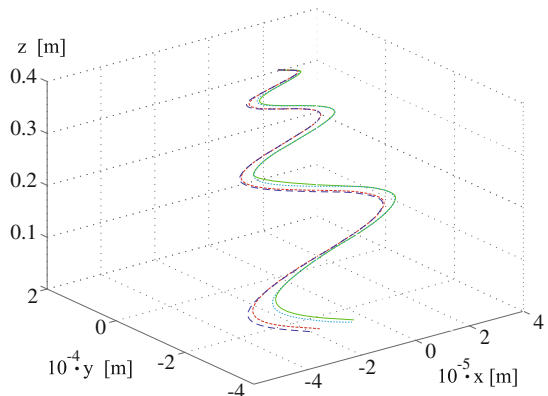
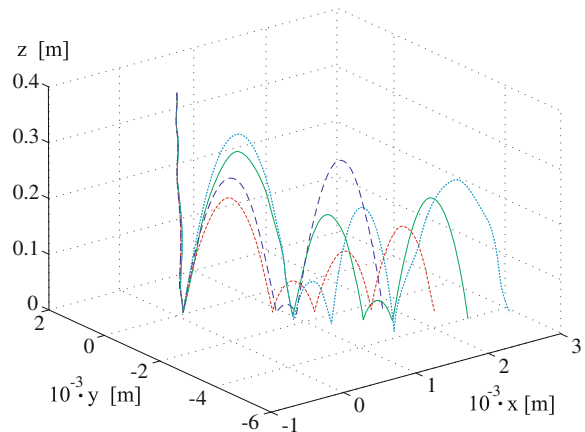


Fig. 4.20 Free fall coin mass center trajectories for 3D imperfect coin (—), 3D ideal coin (---), 2D imperfect coin (· · ·), and 2D ideal coin (- · -)

Fig. 4.21 Coin mass center trajectories after collisions for 3D imperfect coin (—), 3D ideal coin (---), 2D imperfect coin (···), and 2D ideal coin (- - -)



a finite t not large enough to ensure a satisfactory reduction of fluctuations but small enough to reveal slow trends [9–11]. Our calculations show that for sufficiently large t all transient Lyapunov exponents tend to zero, so there is no sensitive dependence on initial conditions during the free fall.

The results for the simulation of the coin bouncing on the floor are shown in Fig. 4.21. Trajectories of the coin mass center calculated for different models are indicated in the same way as in Fig. 4.20. Figure 4.22 presents the trajectories of

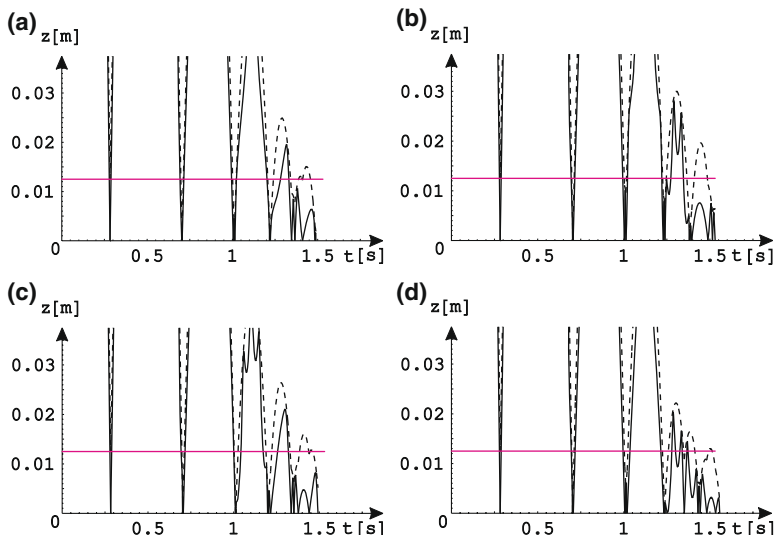


Fig. 4.22 Trajectories of the coin mass center and the position of the lowest point of the coin for (a) $z_0 = 0.40001$, (b) $z_0 = 0.40002$, (c) $z_0 = 0.40003$, (d) $z_0 = 0.40004$. In all cases: $\omega_{\eta 0} = 40.15 \text{ rad/s}$, $x_0 = y_0 = 0$, $\dot{x}_0 = \dot{y}_0 = \dot{z}_0 = 0$, $\varphi_0 = \psi_0 = 0$, $\vartheta_0 = 7\pi/180 \text{ rad}$, $\omega_{\xi 0} = \omega_{\eta 0} = 0$, $\omega_{\eta 0} = 40.15 \text{ rad/s}$, $\lambda_n = 0.8$, $\lambda_\tau = 0.2$, $\chi = 0.8$ (--- coin mass center trajectories, — the lowest point of the coin position)

the coin mass center and the position of the lowest point of the coin calculated for slightly different initial conditions z_0 : $z_0 = 0.40001$ (Fig. 4.22a), $z_0 = 0.40002$ (Fig. 4.22b), $z_0 = 0.40003$ (Fig. 4.22c), $z_0 = 0.40004$ (Fig. 4.22d). Other initial conditions have been fixed to $x_0 = y_0 = 0$, $\dot{x}_0 = \dot{y}_0 = \dot{z}_0 = 0$, $\varphi_0 = \psi_0 = 0$, $\vartheta_0 = 7\pi/180$ rad, $\omega_{\xi 0} = \omega_{\zeta 0} = 0$, and $\omega_{\eta 0} = 40.15$ rad/s.

The sequences indicating which face of the coin is up after the successive impact in the simulations shown in Fig. 4.22 are as follows:

- (a) $H \circ HHH \circ HHH \circ HHH \circ T \circ T \circ T \circ HH$ for $z_0 = 0.40001$,
- (b) $H \circ HHH \circ HH \circ TT \circ HHH \circ T \circ T \circ T$ for $z_0 = 0.40002$,
- (c) $H \circ HHH \circ HHH \circ HH \circ H \circ T \circ T \circ T \circ T \circ T$ for $z_0 = 0.40003$,
- (d) $H \circ HHH \circ TTT \circ TTT \circ T \circ H \circ H \circ H \circ H \circ H$ for $z_0 = 0.40004$.

Some of the collisions are not visible in the scale of Fig. 4.22 as they occur in small time intervals. More details are visible at the enlargements shown in Fig. 4.23.

In the presented examples one can notice that bouncing on the floor introduces a dependence on the initial conditions. This dependence is better visible in Fig. 4.24.

The trajectories of the coin mass center starting from slightly different initial conditions are shown in this figure. One can notice that after a few initial impacts trajectories differ significantly from each other.

The dependence on the initial conditions due to the impact can lead to unpredictability and chaotic behavior in mechanical systems [12, 13]. To quantify the dependence on the initial conditions we introduced the following map.

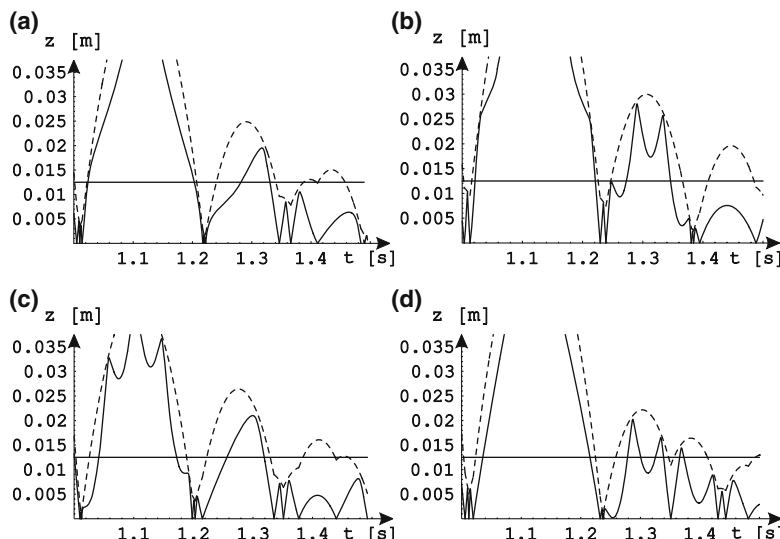


Fig. 4.23 Detailed view ($t \in (1, 1.5)$) of Fig. 4.22 for (a) $z_0 = 0.40001$, (b) $z_0 = 0.40002$, (c) $z_0 = 0.40003$, (d) $z_0 = 0.40004$. In all cases: $\omega_{\eta 0} = 40.15$ rad/s, $x_0 = y_0 = 0$, $\dot{x}_0 = \dot{y}_0 = \dot{z}_0 = 0$, $\varphi_0 = \psi_0 = 0$, $\vartheta_0 = 7\pi/180$ rad, $\omega_{\xi 0} = \omega_{\zeta 0} = 0$, $\omega_{\eta 0} = 40.15$ rad/s, $\lambda_n = 0.8$, $\lambda_\tau = 0.2$, $\chi = 0.8$, (--- coin mass center trajectories, —— the lowest point of the coin position)

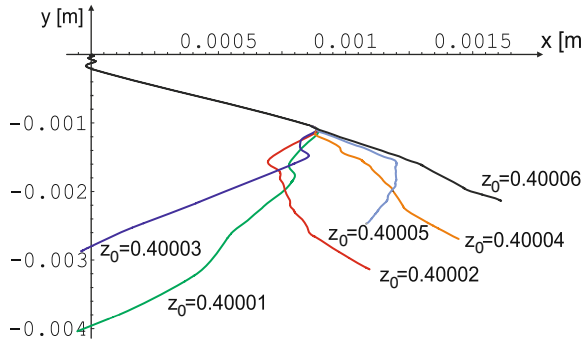


Fig. 4.24 Trajectories of the coin mass center: $z_0 = 0.40001$, $z_0 = 0.40002$, $z_0 = 0.40003$, $z_0 = 0.40004$, $z_0 = 0.40005$, $z_0 = 0.40006$ (in all cases: $\omega_{\eta 0} = 40.15$ rad/s, $x_0 = y_0 = 0$, $\dot{x}_0 = \dot{y}_0 = \dot{z}_0 = 0$, $\varphi_0 = \psi_0 = 0$, $\vartheta_0 = 7\pi/180$ rad, $\omega_{\xi 0} = \omega_{\zeta 0} = 0$, $\omega_{\eta 0} = 40.15$ rad/s, $\lambda_n = 0.8$, $\lambda_\tau = 0.2$, $\chi = 0.8$)

Let $U : [0, 2\pi] \rightarrow [0, 2\pi]$ be a map which maps the point ϕ_n on the edge of the coin which hits the floor at the n th impact to the point ϕ_{n+1} which hits the floor at the $n+1$ th impact. The example of such a map is shown in Fig. 4.25. The left part of Fig. 4.25 shows the points on the edge of the coin which collide with the floor at successive collisions. Numbers around the coin edge indicate the points of the few initial collisions. The analysis of the time series of points ϕ_1, ϕ_2, \dots , shows that the dynamics of U is characterized by transient chaotic behavior as the largest transient Lyapunov exponent is positive (equal to 0.024).

Our simulations reveal that from the point of determining the final outcome (heads or tails) two types of collisions shown in Fig. 4.26 are possible. In the first scenario after many soft chattering collisions (occurring in exponentially decreasing time intervals) which orient the coin closer to being perpendicular to the surface the

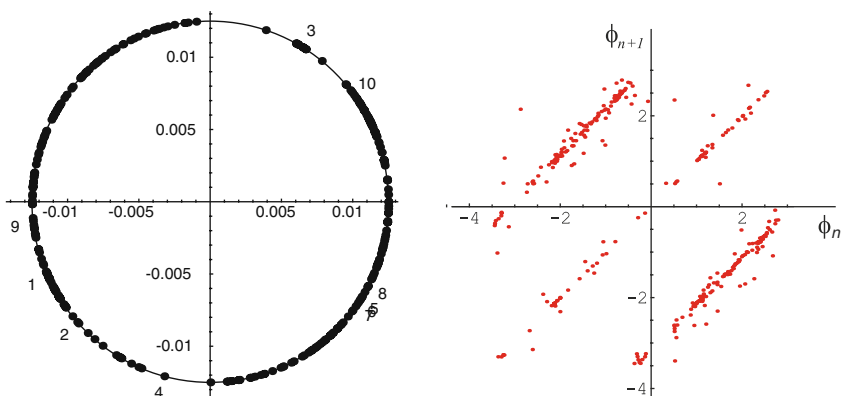
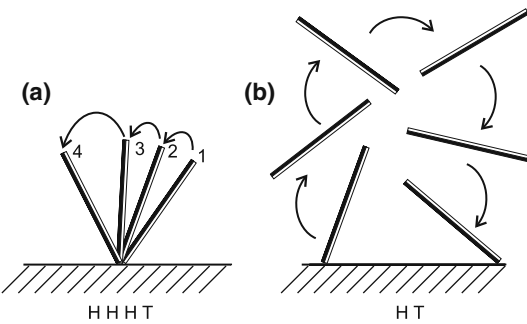


Fig. 4.25 Numerical simulation of the map U : (a) positions of collision point on the coin and (b) map U illustrated as $\phi_n - \phi_{n+1}$; $\vartheta = 25.021 \cdot \pi/180$, coefficient of restitution $\chi = 1$, air resistance considered, number of collisions 316

Fig. 4.26 Two types of collisions leading to the change of the coin face:
(a) sequence of soft chattering collisions with small angular momentum transfer and **(b)** collision with large angular momentum transfer



coin finally flips over (Fig. 4.26a). After the n th collision the coin flips over during the free motion before the next $n+1$ th collision. The second type is characterized by larger momentum transfer during the collision which allows the coin to flip around during the motion over the floor (Fig. 4.26b). The observation of the side of the coin which is up after a successive collision allows us to identify both types of collisions. If the same side (say heads) is up in a number of collisions after which, one observes a flip to another side (say tails), the sequence of soft chattering collisions takes place. When after a single tails side one observes a flip to heads we have a second type of collision. The analysis of time series shows that the first type is more frequent.

The 1D model [2, 14, 15] can be an adequate model for the coin only in a particular case: (i) the coin mass center moves along one plane, and (ii) the vector of the coin total angular velocity is perpendicular to the plane determined by its mass center trajectory.

The angle between the angular momentum and the normal to the coin is constant along the coin trajectory only when the air resistance is neglected so that the results of [3] which are based on this property cannot be always generalized.

Summarizing, we found that for the real coin, in which the distance between the center of the mass and the geometrical center is small, it is sufficient to consider a simplified model of the ideal thin coin. When the distance of the free fall is small, the effect of the air resistance is hardly visible and can be neglected.

4.4 Simulations of the Die Throw

In order to determine on which face the die lands we have analyzed the rotations of the die around the given rotation axis. During the die motion the projections of the vectors \mathbf{n}_i^o ($i = 1, \dots, n$) on the vertical axis $-\mathbf{k}^o$ (with the orientation toward the table) have been calculated. Here, n indicates a number of faces for the examined die model (some of them are shown in Fig. 3.17b). This allows the calculation of the cosines of the angles α_i

$$\cos \alpha_i = -\mathbf{k}^o \cdot \mathbf{n}_i^o . \quad (4.23)$$

The face j for which $\cos \alpha_j$ is the largest, i.e., $\cos \alpha_j = \max_i(\cos \alpha_i)$ is the lowest. The die lands on the face which is the lowest at the moment when the die stops on the table.

The aim of the numerical simulations of the die motion during its free fall was to determine

- the probability of the fall of the die on each face with the assumption that the table is perfectly plastic (after first collision with the table the die stops),
- the distribution of the probability of the die fall on each face (for perfectly plastic table) depending on the direction of the initial angular vector,
- maps of the die tossing results (understood as the final result of the die throw).

The results of the free fall calculations are presented in Sect. 4.4.1.

On the other hand, during the numerical simulations of dice bouncing on the table the analysis has been additionally concentrated on

- the sensitivity of the final result after the bounces on the initial position and rotational speed,
- the process of “unfinished fractalization” of coexisting basins of attraction of respective die faces.

The dynamical analysis of the bouncing dice is demonstrated in Sect. 4.4.2.

4.4.1 Free Fall Probability Distribution

First group of simulation results show a chance of die landing on each of its faces depending on the die initial orientation and its rotation axis orientation. The orientation of die rotation axis has been described by the angular velocity vector $\omega = I^o\omega$, whereas the direction of the unit vector I^o has been determined by the angles ψ_l, ϑ_l as $l_{0x} = \sin \vartheta_l \cos \psi_l, l_{0y} = \sin \vartheta_l \sin \psi_l, l_{0z} = \cos \vartheta_l$. The chance of the die landing on the face number i was called the probability $p(i)$.

Simulations have been carried out for all dice models and the results are shown in Figs. 4.27, 4.28, 4.29, 4.30, 4.31, 4.32, 4.33, 4.34, 4.35, and 4.36. The orientation of individual die faces has been described using the unit vectors \mathbf{n}_i^o ($i = 1, \dots, n$). In our research we have considered, the number $n = 4, 6, 8, 12, 20$, respectively, for tetrahedron, cube, octahedron, dodecahedron, and icosahedron.

The first landing face of the die for the assumed initial position and the angular velocity vector has been calculated by finding the maximum of $\cos \alpha_i$ (4.23). Some results of these simulations are shown in Figs. 4.28b, 4.30b, 4.32b, 4.34b, and 4.36b.

Maps of die tossing results for values of initial angular velocity $\omega \in (17.5, 42.5)$ and free fall duration time $t \in (0, 2.5)$, as well as probability values of landing on each of die faces (bar charts) for the mentioned simulation parameter ranges are presented in these figures.

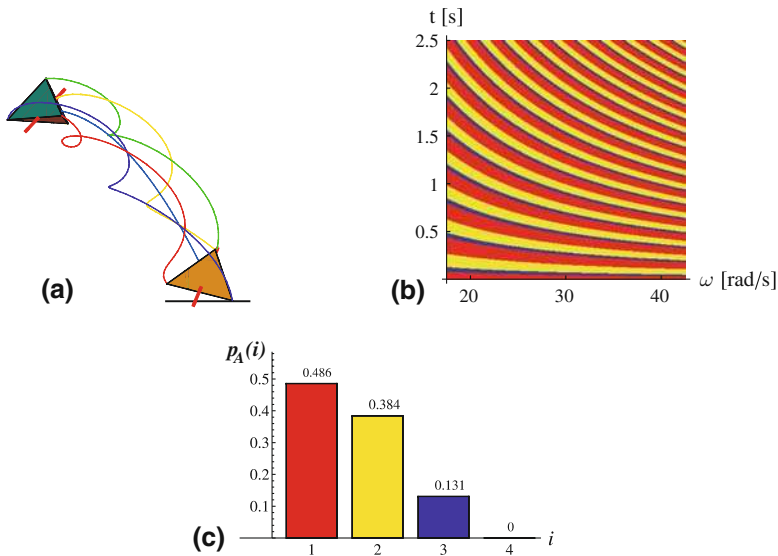


Fig. 4.27 First landing results (no bouncing toss) for tetrahedron die rotating about constant direction ($\psi_l = \pi/6.001$, $\vartheta_l = \pi/4.001$) axis: (a) trajectories of the die vertices; (b) map of results for various values of initial angular velocity ω and free fall duration time t ; and (c) $p_A(i)$ – probability of landing on each die face

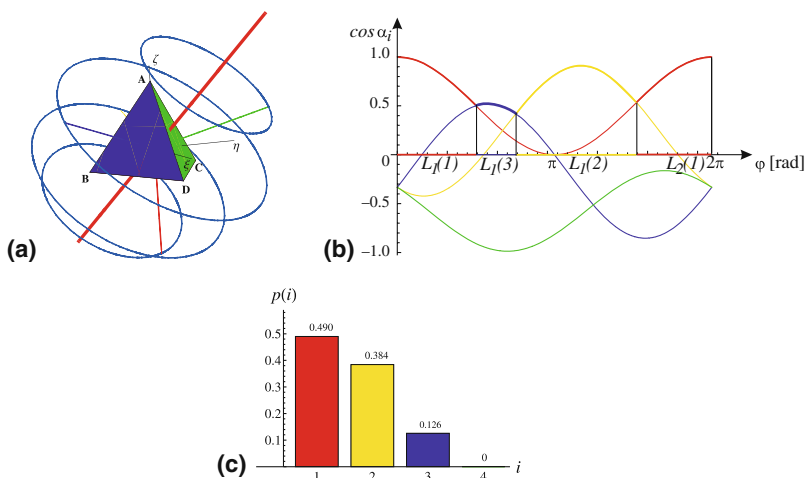


Fig. 4.28 Tetrahedron die: (a) assumed orientation of die rotation axis ($\psi_l = \pi/6.001$, $\vartheta_l = \pi/4.001$); (b) values of $\cos \alpha_i$ for face number $i = 1, \dots, 4$; and (c) $p_L(i)$ – probability of landing on each die face (for assumed orientation of die rotation axis – ψ_l , ϑ_l)

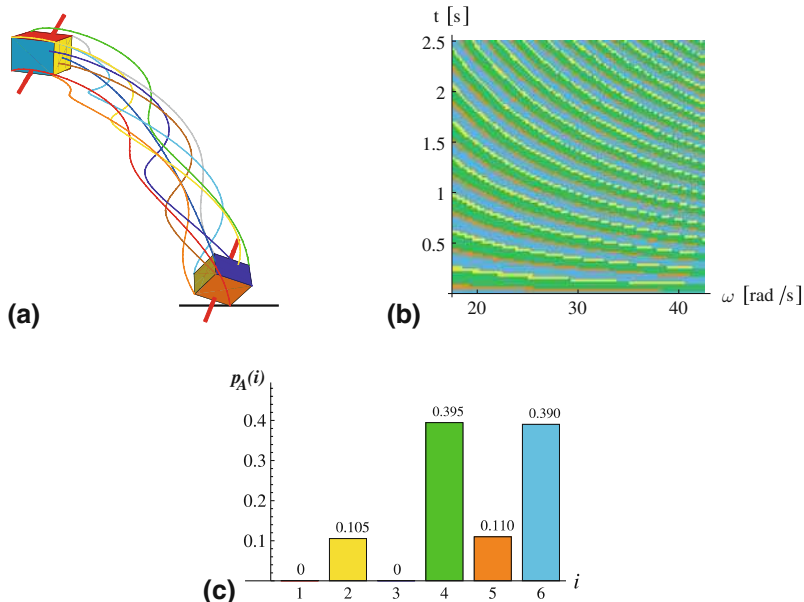


Fig. 4.29 Toss results for cube die rotating about constant direction ($\psi_l = 0$, $\vartheta_l = \pi/4$) axis: (a) falling cube die; (b) map of results for various values of initial angular velocity ω and free fall duration time t ; and (c) $p_A(i)$ – probability of landing on each of die faces

The probability of the die toss result has been calculated as follows:

$$p_A(i) = A(i)/A , \quad (4.24)$$

where $A(i)$ is the sum of areas of landing results on face i and A is the total area of the assumed simulation parameter region. For the results presented in bar charts (Figs. 4.27c, 4.29c, 4.31c, 4.33c, 4.35c) this value is $A = 62.5$.

However, the chance of winning die face can be estimated with a simpler approach. In practice, the same values of probability of landing on die face number

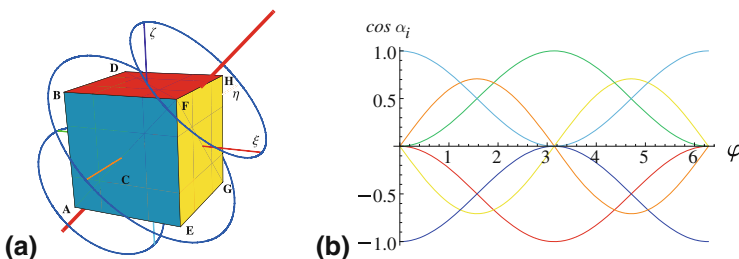


Fig. 4.30 Cube die: (a) assumed orientation of die rotation axis ($\psi_l = 0$, $\vartheta_l = \pi/4$); (b) values of $\cos \alpha_i$ for face number $i = 1, \dots, 6$

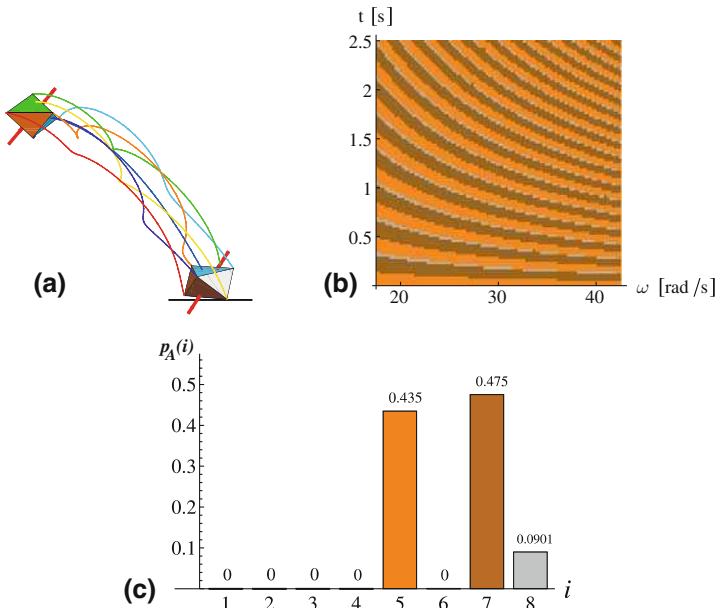


Fig. 4.31 No bouncing toss results for octahedron die rotating about constant direction ($\psi_l = \pi/6$, $\vartheta_l = \pi/6$) axis: (a) falling octahedron die; (b) map of results for various values of initial angular velocity ω and free fall duration time t ; and (c) $p_A(i)$ – probability of landing on each of die faces

i one can obtain by observing only one full rotation ($\varphi \in <0, 2\pi>$) about the die rotation axis and determining from the formula

$$p_L(i) = L(i)/L, \quad (4.25)$$

where $L(i)$ is the sum of lengths of regions in which $\cos \alpha_i$ is greater than $\cos \alpha_j$ for other j faces, and L is the total length of the analyzed range of rotation angle. The

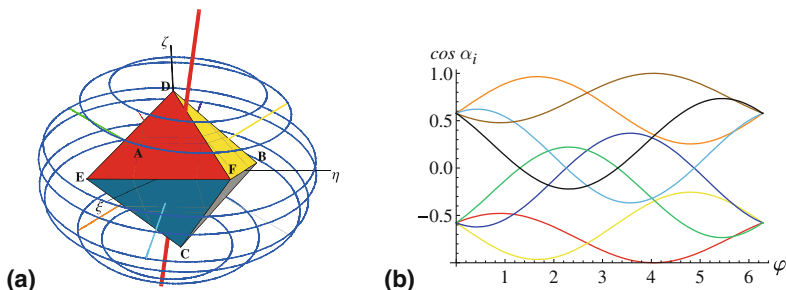


Fig. 4.32 Octahedron die: (a) assumed orientation of die rotation axis ($\psi_l = \pi/6$, $\vartheta_l = \pi/6$); (b) values of $\cos \alpha_i$ for face number $i = 1, \dots, 8$

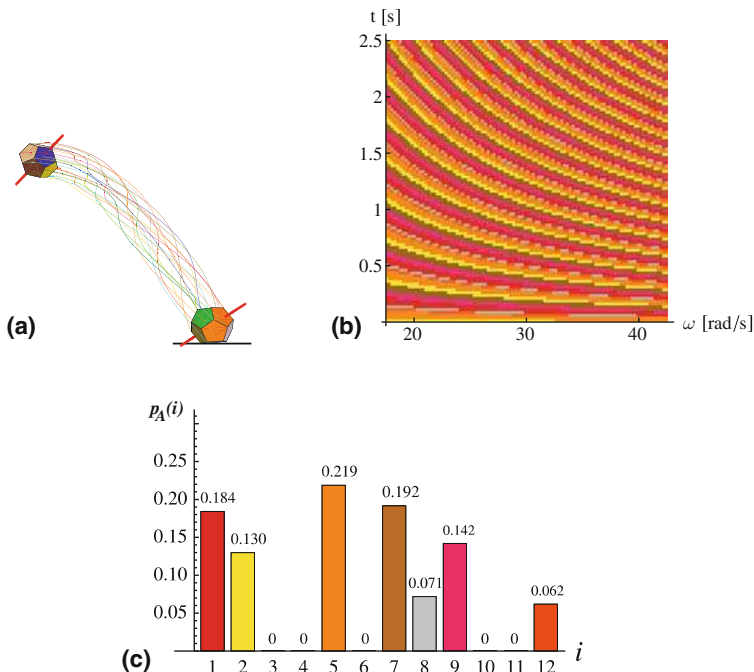


Fig. 4.33 No bouncing toss results for dodecahedron die rotating about constant direction ($\psi_l = \pi/1.615$, $\vartheta_l = \pi/1.3$) axis: (a) falling dodecahedron die; (b) map of results for various values of initial angular velocity ω and free fall duration time t ; and (c) $p_A(i)$ – probability of landing on each of die faces

idea of this method is presented in Fig. 4.28b. (We obtain $L(1) = L_1(1) + L_2(1) = 3.08$, $L(2) = L_1(2) = 2.41$, $L(3) = L_1(3) = 0.79$, $L(4) = 0$ and, since the value of L is corresponding to one cycle of the rotation $L = 2\pi$.) The approximated equality $p_A(i) \approx p_L(i)$ can be illustrated by comparison of the bar charts in Figs. 4.27c and 4.28c.

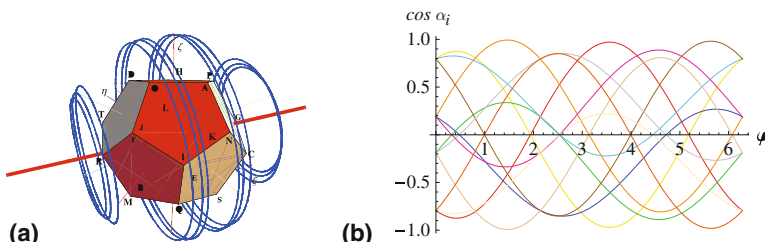


Fig. 4.34 Dodecahedron die: (a) assumed orientation of die rotation axis ($\psi_l = \pi/1.615$, $\vartheta_l = \pi/1.3$); (b) values of $\cos \alpha_i$ for face number $i = 1, \dots, 12$

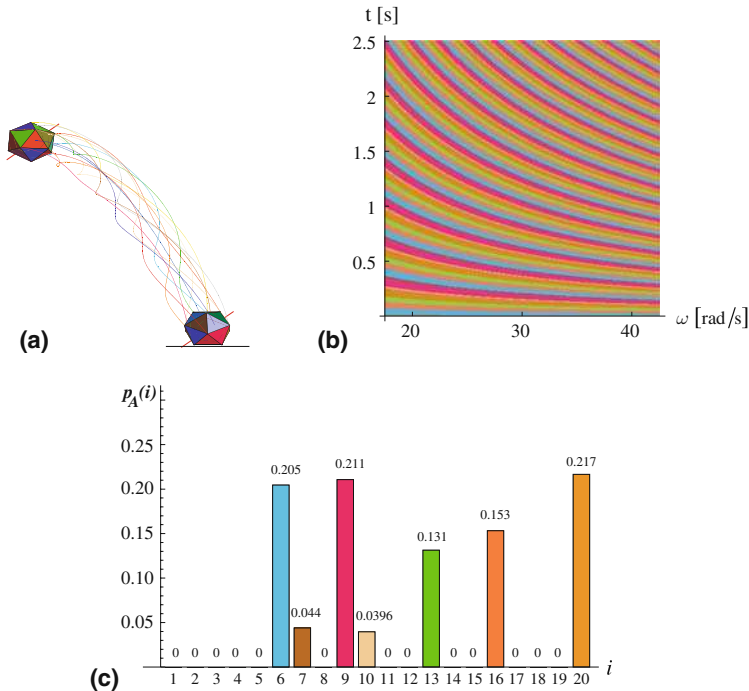


Fig. 4.35 No bouncing toss results for icosahedron die rotating about constant direction ($\psi_l = \pi/4$, $\vartheta_l = \pi/3.0001$) axis: (a) falling icosahedron die; (b) map of results for various values of initial angular velocity ω and free fall duration time t ; and (c) $p_A(i)$ – probability of landing on each of die faces

The results of first landing simulation of the die throw illustrated in Figs. 4.27, 4.28, 4.29, 4.30, 4.31, 4.32, 4.33, 4.34, 4.35, and 4.36 show its analogy to the free fall of the coin. In both these cases, a lack of bounces leads to the smooth structure of basins of attraction of respective die faces in initial condition space. On

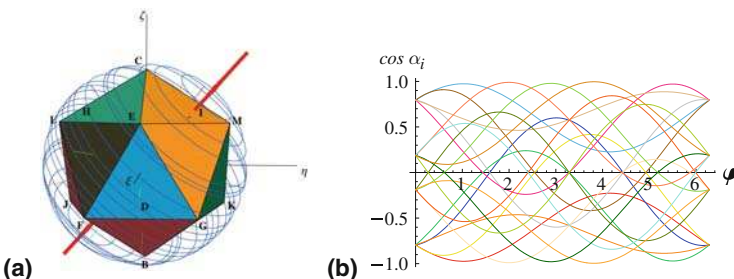


Fig. 4.36 Icosahedron die: (a) assumed orientation of die rotation axis ($\psi_l = \pi/4$, $\vartheta_l = \pi/3.0001$) and (b) values of $\cos \alpha_i$ for face number $i = 1, \dots, 20$

the other hand, significant differences in probability distribution between the die faces can be observed (Figs. 4.27c, 4.29c, 4.31c, 4.33c, and 4.35c). This fact is confirmed by corresponding “one rotation probe” presented in Figs. 4.28b, 4.30b, 4.32b, 4.34b, and 4.36b. It is clearly visible that for given, strictly defined, initial speed and direction of the rotation axis the probability of landing on some die faces is practically equal to zero. In most interesting cases even more than half of the die faces do not appear as a result of free die throw, e.g., 5 from 8 for octahedron (Fig. 4.31c) or 13 from 20 for icosahedron (Fig. 4.35c). Moreover, if we additionally consider the fact of the varied distribution of the probability between remaining, possibly winning faces, we can state that the die throw is usually an unfair event.

Unfair character of the free die toss result can also be visualized in the form of 3D diagram of probability distribution. An example of such diagrams for tetrahedron is shown in Fig. 4.37, where the surface representing the probability of landing on each of four faces over 2D space of angles ψ_l and ϑ_l , defining an initial orientation of rotation axis direction, is presented. These direction angles change in the range $\psi_l \in [0, 2\pi]$, $\vartheta_l \in [0, \pi]$ while $\varphi_l = 0$. The demonstrated results have been obtained applying “one rotation probe” described above. It can be observed that the probability of landing on red face tends to 1 for $\vartheta_l \rightarrow 0$ and $\vartheta_l \rightarrow \pi$ because for these values of angle ϑ_l the bottom face is red. (The calculations have been carried out for the following data: $\varphi_0 = 0$, $v_{0x} = 0$, $v_{0y} = 0$, $v_{0z} = 0$, $\omega_{0x} = \omega_0 \sin \vartheta_l \cos \psi_l$, $\omega_{0y} = \omega_0 \sin \vartheta_l \sin \psi_l$, $\omega_{0z} = \omega_0 \cos \vartheta_l$.)

General illustration of probability distribution in the case of tetrahedron is demonstrated in Fig. 4.38, where a superposition of the probability diagrams from Fig. 4.37 is shown. These simulation results show that the probability of landing on the red face is dominant in wide range of initial die inclination angles ψ_l and

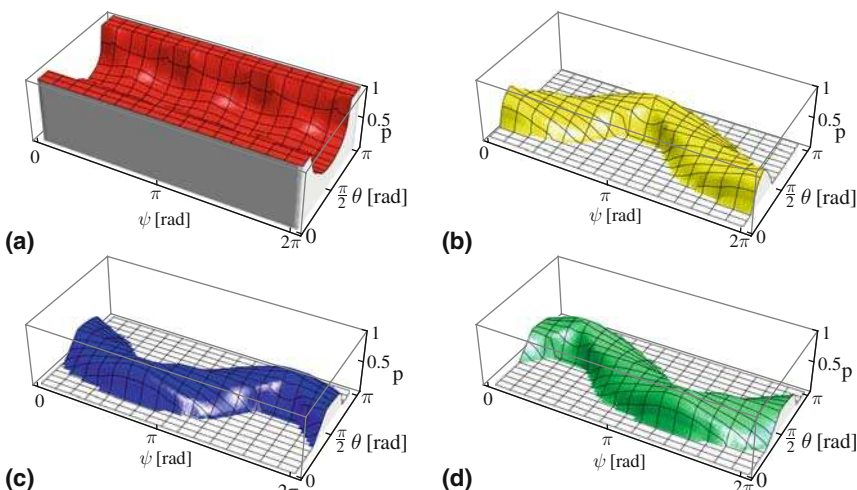
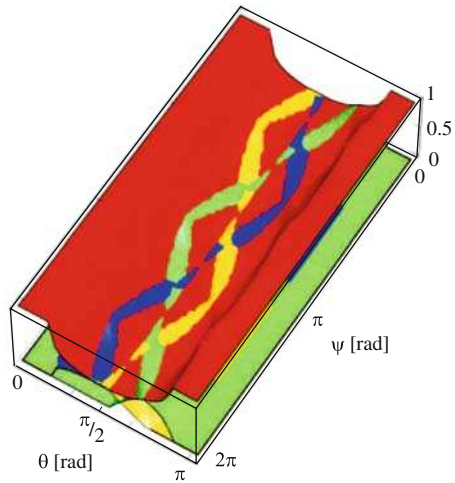


Fig. 4.37 Probability distribution of landing on each of faces for tetrahedron die (d4). Colors are corresponding to the die faces: (a) red – 1; (b) yellow – 2; (c) blue – 3; and (d) green – 4

Fig. 4.38 Maximum of probability distribution of landing on faces 1–4 for tetrahedron die (d4). Colors are corresponding to the die faces: red – 1, yellow – 2, blue – 3, and green – 4



ϑ_l except of the region for $\vartheta \in [\pi/4, 3\pi/4]$ where the chances for each face are similar.

The analogous analysis of the probability distribution between respective faces has been carried out for d6 (Fig. 4.39) and d8 (Fig. 4.40) dice. The calculations have been started from the following initial data: $\varphi_0 = 0$, $v_{0x} = 0$, $v_{0y} = 0$, $v_{0z} = 0$, $\omega_{0x} = \omega_0 \sin \vartheta_l \cos \psi_l$, $\omega_{0y} = \omega_0 \sin \vartheta_l \sin \psi_l$, $\omega_{0z} = \omega_0 \cos \vartheta_l$.

In these cases the unequal distribution of probability is also easily observable. Thus such an inequality can be considered as a typical feature of free die throw in wide regions of the initial die position.

Fig. 4.39 Maximum of probability distribution of landing on faces 1–6 for cubic die (d6). Colors are corresponding to the die faces: red – 1, yellow – 2, blue – 3, green – 4, orange – 5, light blue – 6

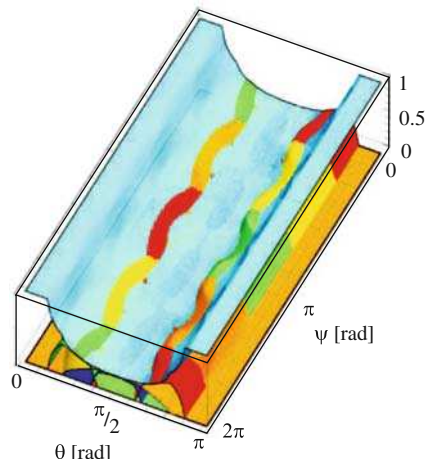
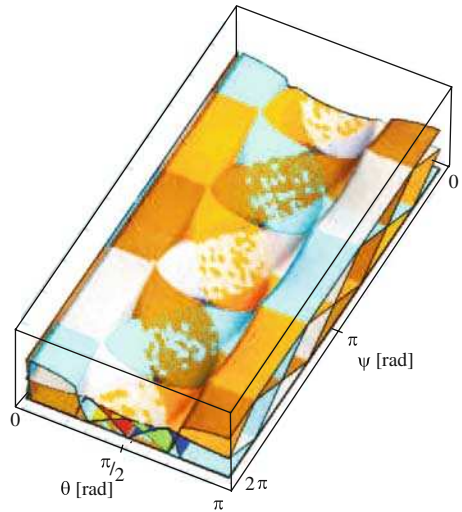


Fig. 4.40 Maximum of probability distribution of landing on faces 1–8 for octahedron die (d8). Colors are corresponding to the die faces: red – 1, yellow – 2, blue – 3, green – 4, orange – 5, light blue – 6, brown – 7, and gray – 8

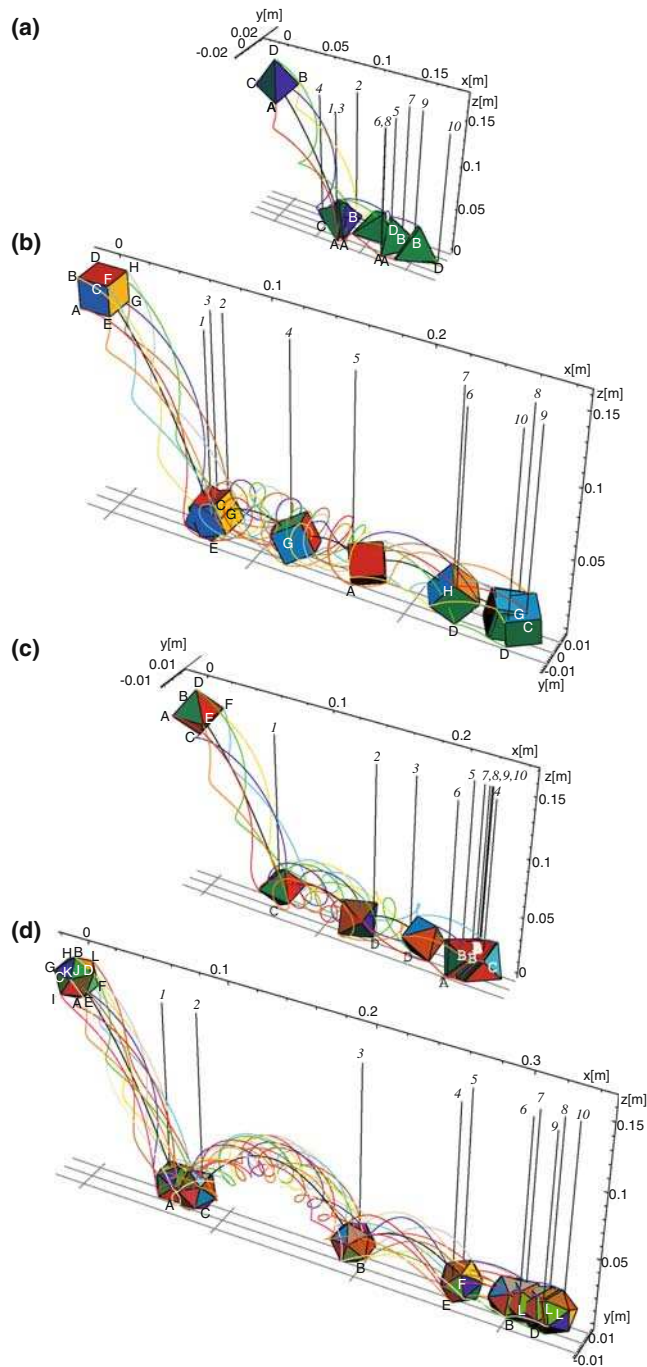


4.4.2 Simulation of Dice Bouncing on the Table

In order to simulate the dynamics of dice bouncing on the floor the classical Newton's hypothesis, where the transition from the state before to the state after the collision is defined by restitution coefficient χ (2.49), has been applied.

The examples of the trajectories of dice vertices calculated from (3.87)–(3.88) and (3.92), (3.93), and (3.94) are shown in Fig. 4.41a–d. In the numerical calculations we have assumed the following parameters: $m = 0.016 \text{ kg}$, $\chi = 0.5$, and initial conditions: $x_0 = y_0 = 0$, $v_{0x} = 0.6 \text{ m/s}$, $v_{0y} = 0$, $v_{0z} = -0.7 \text{ m/s}$, $\psi_0 = 0.001 \text{ rad}$, $\vartheta_0 = 0.00001 \text{ rad}$, $\varphi_0 = 0.0001 \text{ rad}$, $\omega_{\xi 0} = 0$, $\omega_{\eta 0} = 60 \text{ rad/s}$, $\omega_{\zeta 0} = 0$. The vertical lines indicate the position of the successive collisions. For the tetrahedron die ($a = 0.040793 \text{ m}$) during the successive bounces the following corners collide with the table: A,B,A,C,D,A,B,A,B,D as shown in Fig. 4.41a. The cube die ($a = 0.02 \text{ m}$) hits the table with E,G,C,G,A,D,H,G,C,D corners (Fig. 4.41b).

Fig. 4.41 Trajectories of dice vertices, dice orientations for first 10 collisions, sequences of dice colliding corners, and dice landing faces for (a) tetrahedron die (colliding corners: A,B,A,C,D,A,B,A,B,D; landing faces: 4,4,4,4,3,3,3,3,3); (b) cube die (colliding corners: E,G,C,G,A,D,H,G,C,D; landing faces: 5,5,5,2,5,1,1,3,3,3); (c) octahedron die (colliding corners: C,D,D,C,B,A,B,B,B; landing faces: 6,1,3,7,7,7,7,7,7,7); and (d) icosahedral die (colliding corners: A,C,B,E,F,B,L,L,D,L; landing faces: 7,12,4,17,17,5,5,15,15). Simulation results presented for dice mass $m = 0.016 \text{ kg}$, dice edge lengths: $a = 0.040793 \text{ m}$ (d4), $a = 0.02 \text{ m}$ (d6), $a = 0.025698 \text{ m}$ (d8), $a = 0.0154205 \text{ m}$ (d20), initial conditions: $\psi_0 = 0.001 \text{ rad}$, $\vartheta_0 = 0.00001 \text{ rad}$, $\varphi_0 = 0.0001 \text{ rad}$, $\omega_{\xi 0} = 0$, $\omega_{\eta 0} = 60 \text{ rad/s}$, $\omega_{\zeta 0} = 0$, $y_0 = 0$, $x_0 = 0$, $z_0 = 0.15 \text{ m}$, $v_y = 0$, $v_z = -0.7 \text{ m/s}$, $v_x = 0.6 \text{ m/s}$, and $\chi = 0.5$

**Fig. 4.41** (continued)

The sequences of the colliding corners for the octahedron ($a = 0.025698 \text{ m}$) (Fig. 4.41c) and icosahedron ($a = 0.0154205 \text{ m}$)² dice are, respectively, C,D,D,C, B,A,B,B,B (Fig. 4.41c), and A,C,B,E,F,B,L,L,D,L (Fig. 4.41d). Notice that not all collisions result in the change of the die face which is the lowest one before and after the collision. For the tetrahedron die we observe such a face change only once after the fourth collision. Four changes take place for the cube die (after third, fourth, fifth, and seventh collisions). During the simulation of the throw of the octahedron and icosahedral dice one observes, respectively, three (after first, second, and third collisions) and five (after first, second, third, fifth and eighth collisions) face changes.

Figure 4.42a–d describes the dissipation of the energy along the trajectories shown in Fig. 4.41a–d. Total mechanical energy $E_{tot} = \frac{1}{2}m(v_x^2 + v_y^2 + v_z^2) + \frac{1}{2}J(\omega_\xi^2 + \omega_\eta^2 + \omega_\zeta^2) + mgz$ (solid line), rotational kinetic energy $E_{rot} = \frac{1}{2}J(\omega_\xi^2 + \omega_\eta^2 + \omega_\zeta^2)$ (dashed line), and the sum of kinetic energy of translation and potential $E_{tr} = \frac{1}{2}m(v_x^2 + v_y^2 + v_z^2) + mgz$ (dotted line) are shown. The horizontal dashed lines indicate the level of the minimum energy necessary to change the throw result $E_{min} = \frac{1}{2}m(v_x^2 + v_y^2) + \frac{1}{2}J\omega_z^2 + mgh_{rot}$, where h_{rot} is the distance between mass center and the die edge. Notice that although the total energy decreases with the successive collisions, after particular collisions the rotational energy E_{rot} can increase what results in the unexpected increase of the rotation speed. Such phenomena are easily visible in real (experimental) die throws.

In order to analyze the sensitivity of the final toss result on the initial conditions we have compared the dice motion trajectories starting from very similar initial conditions.

Consider the cube die ($m = 0.016 \text{ kg}$, $a = 0.02 \text{ m}$, $J = 1.067 \times 10^{-6} \text{ kg m}^2$). Comparison of two throws of the die for similar initial conditions is shown in Fig. 4.43a – for $z_o = 0.15 \text{ m}$ and in Fig. 4.43b for $z_o = 0.151 \text{ m}$.

The vertical lines in these figures denote instances of impacts (for small intervals between impacts some lines overlap).

As follows from Fig. 4.43 the die motion in these two cases is quite close to each other only in the free fall motion. However, after a few collisions with the table the differences become significant. Additionally, the divergence of trajectories connected with the sensitivity on initial conditions is illustrated with sequences of colliding corners and landing faces shown in description of Figs. 4.43 and 4.44.

The similar effect has been observed for tetrahedral and octahedral dice.

Tetrahedral die ($m = 0.016 \text{ kg}$, $a = 0.040793 \text{ m}$, $J = 1.3313 \times 10^{-6} \text{ kg m}^2$) has been analyzed. The comparison of two throws of the die for similar initial conditions ($\psi_0 = 0.001 \text{ rad}$, $\vartheta_0 = 0.00001 \text{ rad}$, $\varphi_0 = 0.0001 \text{ rad}$, $\omega_{\xi 0} = 0$, $\omega_{\eta 0} = 60 \text{ rad/s}$, $\omega_{\zeta 0} = 0$, $y_o = 0$, $x_o = 0$, $z_o = 0.15 \text{ m}$, $v_y = 0$, $v_z = -0.7 \text{ m/s}$, $v_x = 0.6 \text{ m/s}$) is shown in Fig. 4.45a for $z_o = 0.15 \text{ m}$ and in Fig. 4.45b for $z_o = 0.151 \text{ m}$.

Octahedral die ($m = 0.016 \text{ kg}$, $a = 0.025698 \text{ m}$, $J = 1.05662 \times 10^{-6} \text{ kg m}^2$) has been analyzed. The comparison of two throws of the die for similar initial conditions

² The length of the die edge for all analyzed dice was obtained assuming that the mass and density of dice have the same value ($m = 0.016 \text{ kg}$).

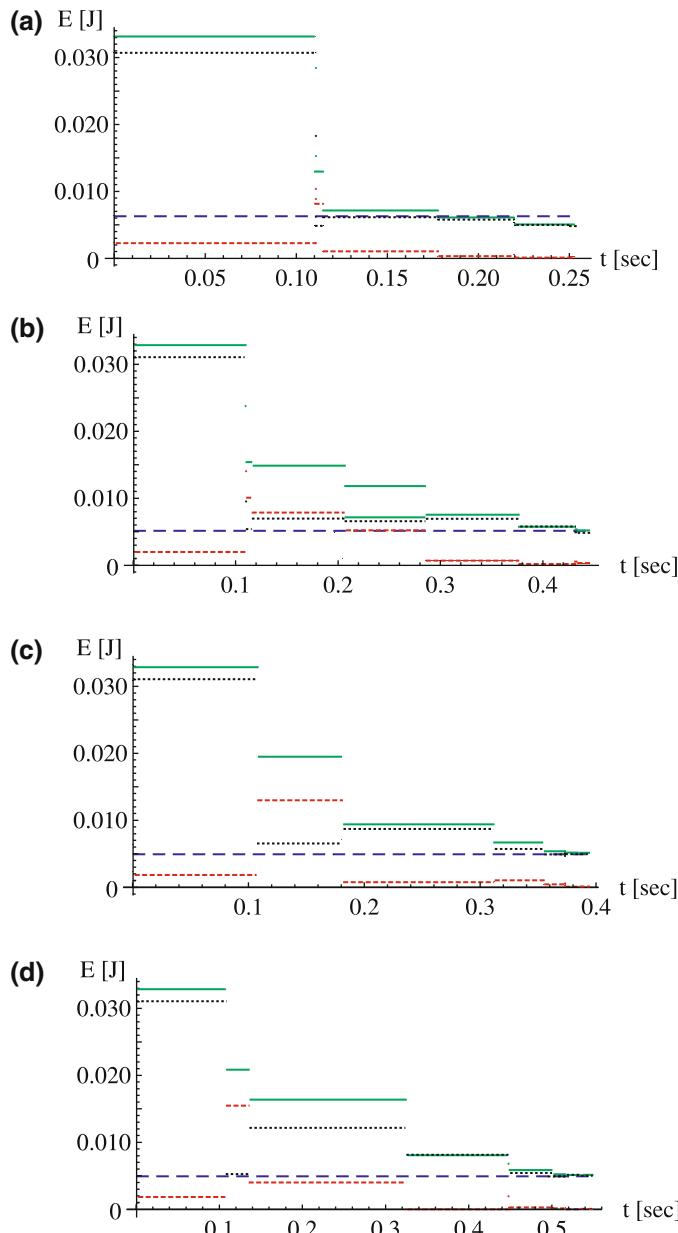


Fig. 4.42 Changes in dice energy for first 10 collisions of (a) tetrahedron die (d4); (b) hexahedron (cube) die (d6); (c) octahedron die (d8); and (d) icosahedral die (d20). Results presented for the same parameter values as in Fig. 4.41. Solid lines (—) denote total mechanical energy — E_{tot} , dashed lines (- - -) are for rotational kinetic energy — E_{rot} , dotted lines (· · ·) are used for kinetic energy of translation plus potential — E_{tr} , and horizontal dashed line (---) denotes minimum of energy necessary to change of toss outcome — E_{min}

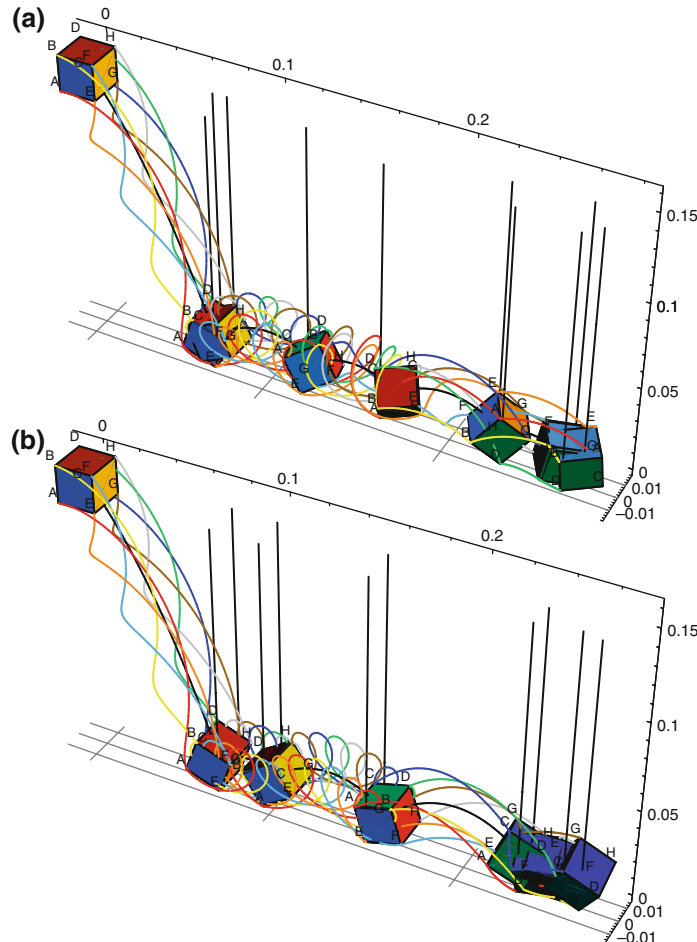


Fig. 4.43 Cube die throw – trajectories of die vertices and die orientations in the collision sequence for $\psi_0 = 0.001 \text{ rad}$, $\vartheta_0 = 0.00001 \text{ rad}$, $\varphi_0 = 0.0001 \text{ rad}$, $\omega_{\xi 0} = 0$, $\omega_{\eta 0} = 60 \text{ rad/s}$, $\omega_{\zeta 0} = 0$, $y_o = 0$, $x_o = 0$, $v_y = 0$, $v_z = -0.7 \text{ m/s}$, $v_x = 0.6 \text{ m/s}$ and (a) $z_o = 0.15 \text{ m}$, (b) $z_o = 0.151 \text{ m}$. Sequence of die colliding corners: (a) E,G,C,G,A,D,H,G,C,D and (b) E,G,C,A,G,E,F,A,B,B; die landing faces: (a) 5,5,5,2,5,1,1,3,3,3 and (b) 5,5,5,5,2,2,6,6,6,6

($\psi_0 = 0.001 \text{ rad}$, $\vartheta_0 = 0.00001 \text{ rad}$, $\varphi_0 = 0.0001 \text{ rad}$, $\omega_{\xi 0} = 0$, $\omega_{\eta 0} = 60 \text{ rad/s}$, $\omega_{\zeta 0} = 0$, $y_o = 0$, $x_o = 0$, $z_o = 0.15 \text{ m}$, $v_y = 0$, $v_z = -0.7 \text{ m/s}$, $v_x = 0.6 \text{ m/s}$) is shown in Fig. 4.46a for $z_o = 0.15 \text{ m}$ and in Fig. 4.46b for $z_o = 0.151 \text{ m}$.

4.5 Simulation of the Roulette Run

In Fig. 4.47 the exemplary result of the roulette run simulation for initial values of the ball center velocity $v_0 = 1.32709 \text{ m/s}$ and for angular velocity of the roulette wheel $\Omega_w = -2.0944 \text{ rad/s}$ is shown. (Additional data describing the roulette wheel

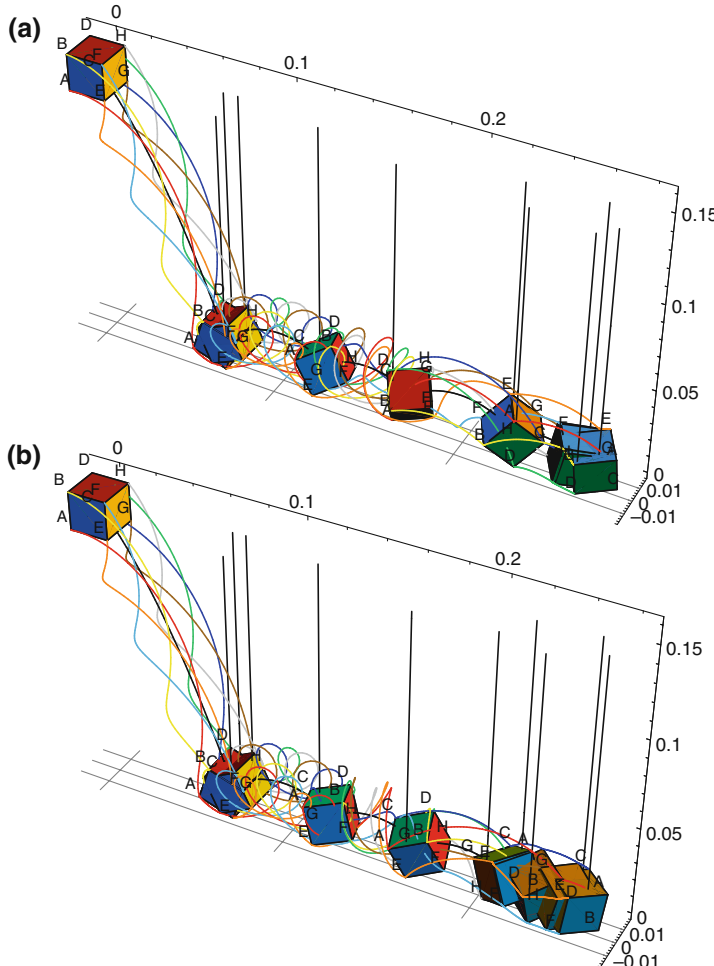
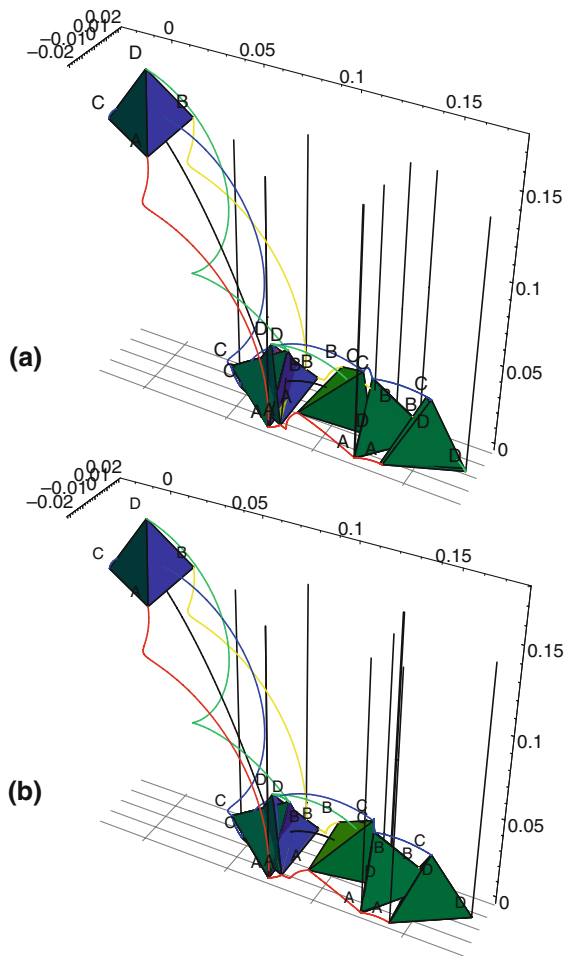


Fig. 4.44 Cube die (d6) throw – trajectories of die vertices and die orientations in the collision sequence: (a) $\psi_0 = 0.001$ rad, $\vartheta_0 = 0.00001$ rad, $\varphi_0 = 0.0001$ rad, $\omega_{\xi 0} = 0$, $\omega_{\eta 0} = 60$ rad/s, $\omega_{\zeta 0} = 0$, $y_o = 0$, $x_o = 0$, $z_o = 0.15$ m, $v_y = 0$, $v_z = -0.7$ m/s, $v_x = 0.6$ m/s (sequence of die colliding corners: E,G,C,G,A,D,H,G,C,D; die landing faces: 5,5,5,2,5,1,1,3,3,3) and (b) initial conditions are the same as for case (a) except of $z_o = 0.1502$ m (sequence of die colliding corners: E,G,C,G,E,D,H,F,B,D; die landing faces: 5,5,5,2,2,1,1,1,1,1)

are as follows: $m = 0.039$ kg, $R_k = 0.011$ m; $R_T = 0.188$ m, $r_T = 0.022$ m, $\alpha = 60^\circ$, $\beta = 62^\circ$.) The outcome is 29. The ball rolls approximately 3.41 rounds on toroidal (R_T) and fixed conical (R_{FC}) surfaces, collide with deflector number 2 (C_{D2}), rolls on the sharp edge of this deflector (R_{D2}), falls (F) and collide with fixed conical surface (with $\chi = 0$) (C_{FC}), rolls on conical surface (R_{FC}), bounce with deflector number 3 (C_{D3}), rolls on the edge of the deflector (R_{D3}), falls (F) and collide with fixed conical surface (C_{FC}), rolls on conical surface (R_{FC}), collide

Fig. 4.45 Tetrahedron die (d4) throw – trajectories of die vertices and die orientations in the collision sequence:
(a) $\psi_0 = 0.001 \text{ rad}$,
 $\vartheta_0 = 0.00001 \text{ rad}$,
 $\varphi_0 = 0.0001 \text{ rad}$, $\omega_{\xi 0} = 0$,
 $\omega_{\eta 0} = 60 \text{ rad/s}$, $\omega_{\zeta 0} = 0$,
 $y_o = 0$, $x_o = 0$, $z_o = 0.15 \text{ m}$,
 $v_y = 0$, $v_z = -0.7 \text{ m/s}$,
 $v_x = 0.6 \text{ m/s}$ (sequence of
die colliding corners:
A,B,A,C,D,A,B,A,B,D; die
landing faces:
4,4,4,4,3,3,3,3,3) and **(b)**
initial conditions are the same
as for case **(a)** except of
 $z_o = 0.151 \text{ m}$ (sequence of
die colliding corners:
A,B,A,C,D,B,A,B,D,A; die
landing faces:
4,4,4,4,3,3,3,3,3)



with rotating conical surface ($C_{(RC)}$), rolls on rotating conical surface ($R_{(RC)}$), collide and lands in the pocket ($C_{(P)}$). It can be symbolically described as the sequence of following tasks:

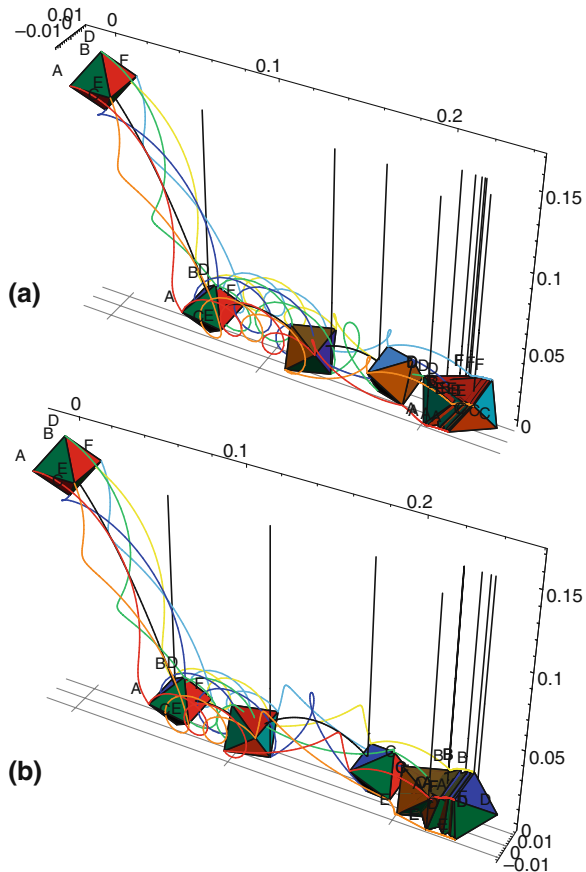
$$\{R_{(T)} - R_{(FC)}\}_5 - C_{D2} - R_{D2} - F - C_{(FC)} - R_{(FC)} - C_{D3} - R_{D3} - F - C_{(FC)} - R_{(FC)} - C_{(RC)} - R_{(RC)} - C_{(P)}.$$

The comparison of the roulette ball mass center trajectories for two initial values of the ball center velocities ($v_0 = 1.32709 \text{ m/s}$ and $v_0 = 1.327229 \text{ m/s}$) and the angular velocity of the roulette wheel $\Omega_w = -2.0944 \text{ rad/s}$ is shown in Fig. 4.48. The final outcome for these two runs is the same – the ball lands in the pocket number 29.

The trajectories of the roulette ball mass center for initial values of the ball center velocities $v_0 = 1.32913$ and $v_0 = 1.32919$ are shown in Fig. 4.49 (the angular velocity of the roulette wheel $\Omega_w = -2.0944 \text{ rad/s}$). We observe the change in

Fig. 4.46 Octahedron die (d8) throw – trajectories of die vertices and die orientations in the collision sequence:

(a) $\psi_0 = 0.001 \text{ rad}$,
 $\vartheta_0 = 0.00001 \text{ rad}$,
 $\varphi_0 = 0.0001 \text{ rad}$, $\omega_{\xi 0} = 0$,
 $\omega_{\eta 0} = 60 \text{ rad/s}$, $\omega_{\zeta 0} = 0$,
 $y_o = 0$, $x_o = 0$, $z_o = 0.15 \text{ m}$,
 $v_y = 0$, $v_z = -0.7 \text{ m/s}$,
 $v_x = 0.6 \text{ m/s}$ (sequence of
die colliding corners:
C,D,D,C,B,A,B,B,B; die
landing faces:
6,1,3,7,7,7,7,7,7) and
(b) initial conditions are the
same as for case (a) except of
 $z_o = 0.151 \text{ m}$ (sequence of
die colliding corners:
C,C,C,D,F,E,F,F,F; die
landing faces:
6,7,6,1,1,1,1,6,6)



the final outcome – the ball lands in the pocket number 19 for $v_0 = 1.32919$. The sequence of tasks to solve for the velocity value $v_0 = 1.32919$ is as follows:

$\{R_{(T)} - R_{(FC)}\}_5 - C_{D2} - R_{D2} - F - C_{(FC)} - R_{(FC)} - R_{(T)} - R_{(FC)} - C_{(D5)} - R_{D5} - F - R_{(RC)} - C_{(P)}$. The trajectories of the roulette ball mass center for initial values of the ball center velocities $v_0 = 1.32037 \text{ m/s}$, $v_0 = 1.32919 \text{ m/s}$ and final results are presented in Fig. 4.50 (for the angular velocity of the roulette wheel $\Omega_w = -2.0944 \text{ rad/s}$). The final outcomes are, respectively, 9 and 19.

The trajectories of the roulette ball mass center for initial values of the ball center velocities, $v_0 = 1.327229$, $v_0 = 1.32735$, $v_0 = 1.32841$, $v_0 = 1.32913$, and $v_0 = 1.32919$ are shown in Fig. 4.51 (the angular velocity of the roulette wheel $\Omega_w = -2.0944 \text{ rad/s}$). The final outcomes are 29 for $v_0 \in [1.32709, 1.32913]$ and 19 for $v_0 = 1.32919$. Notice that the rotating wheel position slightly differs for each of these cases but in Fig. 4.50 we show only one position of the roulette wheel – for the case $v_0 = 1.32709$.

We can summarize the results presented in Figs. 4.48, 4.49, and 4.51 in one picture (Fig. 4.52) presenting the final outcome of the roulette run for certain values

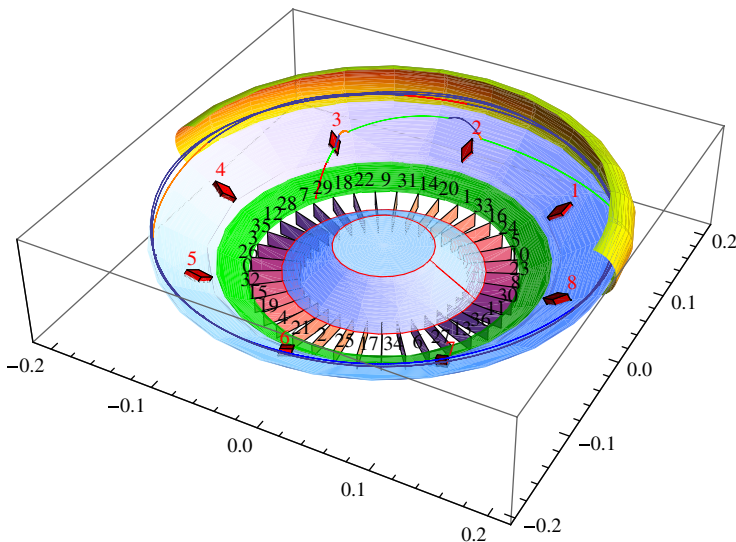


Fig. 4.47 Simulation result of the roulette run (the ball mass center trajectory) for initial values of the ball center velocity $v_0 = 1.32709$ m/s and the angular velocity of the roulette wheel $\Omega_w = -2.0944$ rad/s

of the ball center initial velocity and established other parameters of the roulette wheel and initial conditions.

Final outcomes for initial velocity values of the ball center from the range (1.32709, 1.32913) are the same (the ball lands in the pocket number 29) but for initial velocity values out of this range the ball lands in other pockets (9, 19, ...).

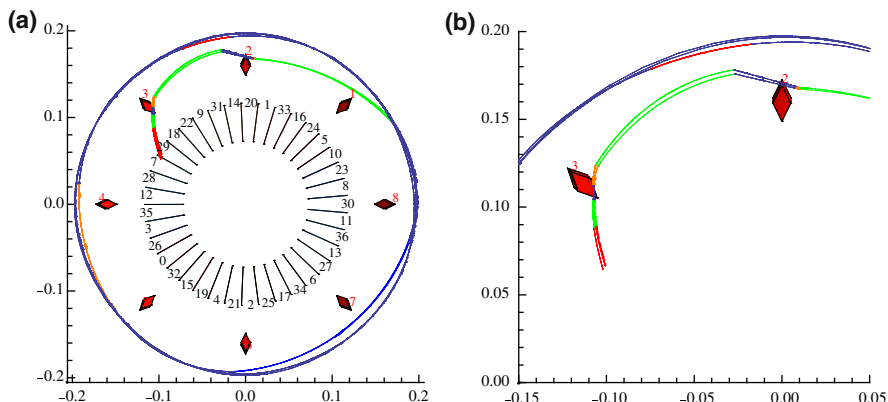


Fig. 4.48 Comparison of the roulette ball mass center trajectories for $v_0 = 1.32709$ and $v_0 = 1.327229$ (a) and their zoom (b)

Fig. 4.49 Comparison of the roulette ball mass center trajectories for $v_0 = 1.32913$ and $v_0 = 1.32919$ ($\Omega_w = -2.0944 \text{ rad/s}$)

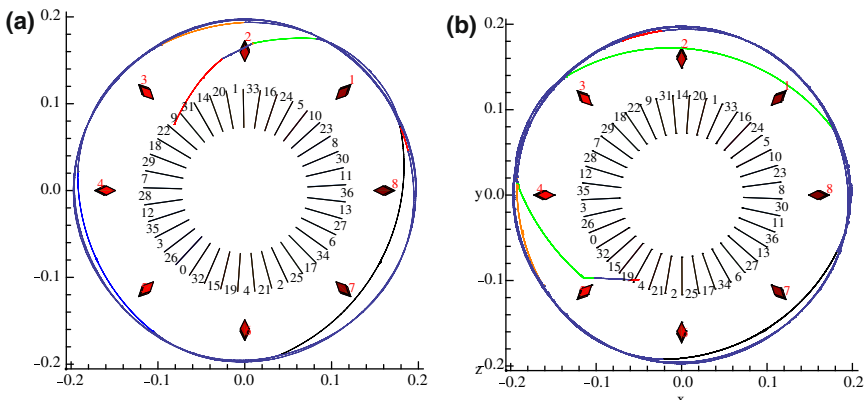
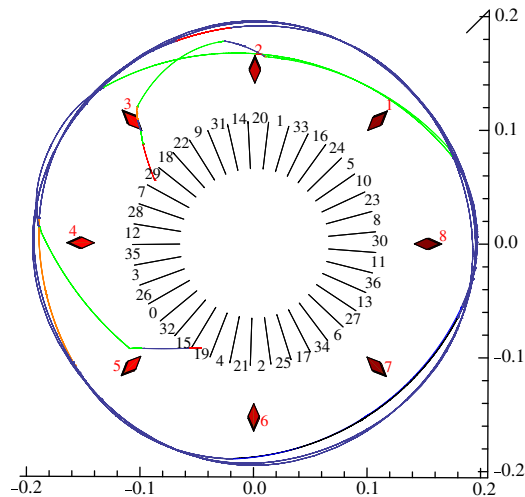
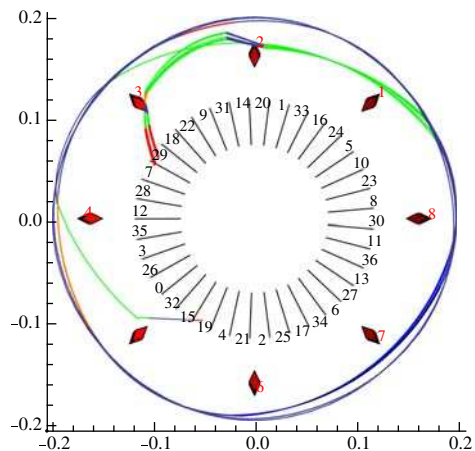


Fig. 4.50 Comparison of the roulette ball mass center trajectories and pocket positions for (a) $v_0 = 1.32037 \text{ m/s}$, (b) $v_0 = 1.32919 \text{ m/s}$ ($\Omega_w = -2.0944 \text{ rad/s}$)

Fig. 4.51 Comparison of the roulette ball mass center trajectories for $v_0 = 1.32709$, $v_0 = 1.327229$, $v_0 = 1.32735$, $v_0 = 1.32841$, $v_0 = 1.32913$, and $v_0 = 1.32919$ ($\Omega_w = -2.0944 \text{ rad/s}$)



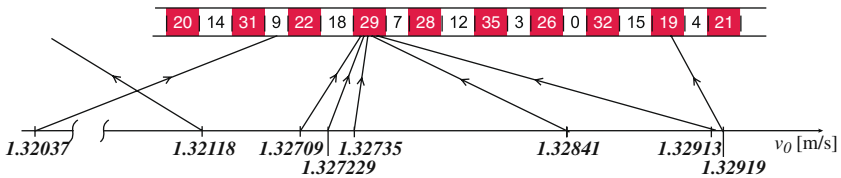


Fig. 4.52 Final outcome of the roulette run for particular values of the ball center velocity

4.6 On the Predictability of Mechanical Randomizer

The equations of motion of tossing a coin (3.1), (3.2), (3.3), (3.4), (3.5), (3.6), (3.7), (3.8), (3.9), (3.10), (3.11), (3.12), (3.13), (3.14), and (3.15), throwing a die (3.87–3.88), and the roulette ball run given in Chap. 3 are Newton–Euler’s equations, with no external source of random influence, i.e., the fluctuations of air, thermodynamic or quantum fluctuations of the coin. One can construct a mapping of the initial conditions to a final observed configuration (face of the coin and the die or a roulette pocket). First, let us consider the coin toss. The initial conditions are position, configuration, momentum, and angular momentum at the beginning of the free fall motion. There are three possible final configurations after bouncing on the floor: the coin terminates flat on the surface with its heads side up, its tails side up, or the coin balances on its edge. The first two configurations are stable. In some studies these are called stable point attractors [15, 16], but the term attractor does not exactly coincide with the definition known in nonlinear dynamics. The flow given by the equations of motion maps all possible initial conditions into one of the final configurations. The set of initial conditions which is mapped onto heads configuration creates *heads basin of attraction* while the set of initial conditions mapped onto tails configuration creates *tails basin of attraction*. The boundary which separates heads and tails basins consists of initial conditions mapped onto the coin standing on the edge configuration. For an infinitely thin coin this set is a set of zero measure and thus with probability 1 the coin ends up either heads or tails. For the finite thinness of the coin this measure is not zero but the probability of edge configuration to be stable is low.

If the outcome of the long sequence of the coin tossing is to give a random result, it can only be because the initial conditions vary sufficiently from toss to toss. Assume the one that can set the initial conditions $\Phi = \{x_0, y_0, z_0, \dot{x}_0, \dot{y}_0, \dot{z}_0, \psi, \vartheta, \varphi, \omega_{\xi 0}, \omega_{\eta 0}, \omega_{\zeta 0}\}$ with uncertainty ε . If the ball B in the phase space centered at Φ contains only points which go to one of the final states, the outcome is predictable and repeatable. If in the ball B there are points leading to different final states (denote the set of points leading to heads as H and the set of points leading to tails as T), then the result of tossing is not predictable. One can calculate the probability of heads (tails) as

$$\text{prob}(\text{heads}) = \mu(H)/\mu(B), \quad (\text{prob}(\text{tails}) = \mu(T)/\mu(B)), \quad (4.26)$$

where μ is a measure of the sets H , T , and B .

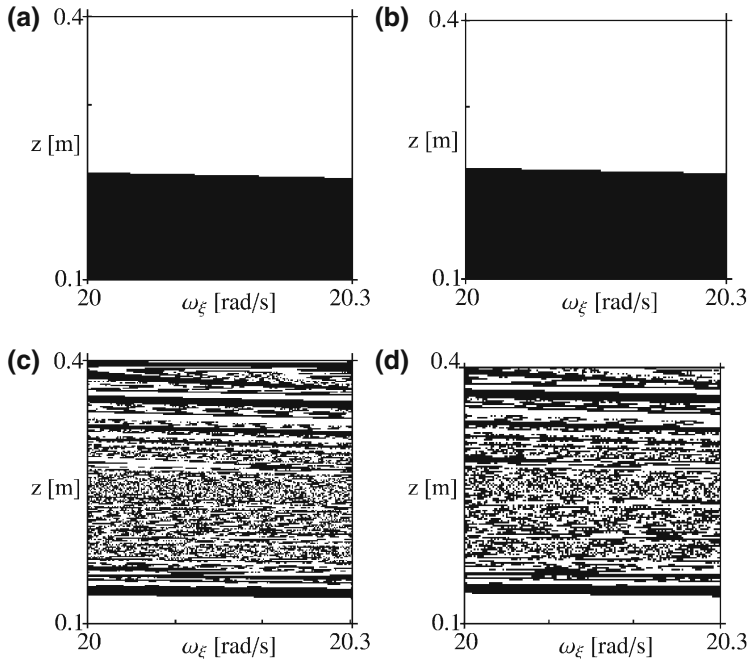


Fig. 4.53 Basins of attraction of heads (black) and tails (white). Two-dimensional model of an ideal thin coin described by (3.1), (3.6), (3.7), and (3.8) has been simulated: (a,b) impactless motion; (c,d) motion with bouncing on the floor, (a,c) air resistance neglected; and (b,d) air resistance considered $\lambda_n = 0.8$, $\lambda_\tau = 0.2$. Simulation results for $m = 0.002 \text{ kg}$, $r = 0.0125 \text{ m}$, $h = 0$, $J_\xi = 0.788 \times 10^{-7} \text{ kg m}^2$, $\vartheta_0 = \pi/5 \text{ rad}$, $v(t = 0) = 0$, $\chi = 0.6$

Figure 4.53a–d shows the basins of attraction of heads and tails calculated for various coin models (in the first model the air resistance is neglected and the second model includes air resistance force). The dark regions correspond to heads and the white ones to tails. The case of the coin terminating on the soft floor (restitution coefficient $\chi = 0$) in which the air resistance effect has been neglected is shown in Fig. 4.53a. The same case with the air resistance is presented in Fig. 4.53b. The models that allow the bouncing of the coin on the floor surface ($\chi = 0.6$) are shown in Fig. 4.53c, d. In Fig. 4.53c, d the air resistance has been, respectively, neglected and considered. Figure 4.53a–d has been calculated by numerically integrating (3.1), (3.6), (3.7), and (3.8) together with the constraint equation (3.5). We fixed all initial conditions except two, namely the position of the coin mass center z_0 and the angular velocity ω_ξ . We check that similar structures of the basin boundaries are observed when different initial conditions are allowed to vary. So in Fig. 4.53a–d the 2D sections of the phase space are the good indications of what happens in the entire phase space.

The structure of the basin boundaries for the coin models without bouncing on the floor is similar to the boundaries in the Keller model (Fig. 4.8) [2].

It seems that the influence of the air resistance or the dimensionality of the model can be neglected (compare Fig. 4.8 with Fig. 4.53a, b).

One can notice that the structure of the basin boundaries is more complicated (looks like fractal or intermingled) when the coin is allowed to bounce on the floor as can be seen in Fig. 4.53c,d. To check the possibility that these basins are fractal (intermingled) the appropriate enlargements are presented in Fig. 4.54a–d. It can be seen that apart from the graininess due to the finite number of points, the boundaries are smooth (see Fig. 4.54c,d). Under further magnification no new structures can be resolved, i.e., no evidence of intermingled or even fractal basin boundaries is visible. The same conclusion has been reached in [14, 15, 17] where simple 1D models of the coin have been considered.

The same property of the basin of attraction is observed in the die throw simulations in which (3.87)–(3.88) have been numerically integrated. In Figs. 4.55 and 4.56 we present the results of the tetrahedral and cube dice throw with basins of attraction for each of the die faces in 2D space of initial conditions (z_0, ω_0) . Basins of attraction of the given die face are shown in different colors. For the tetrahedron (Fig. 4.55) the left column has been reconstructed for free fall case (the result before first collision with the table), while the diagrams in right columns depict the final

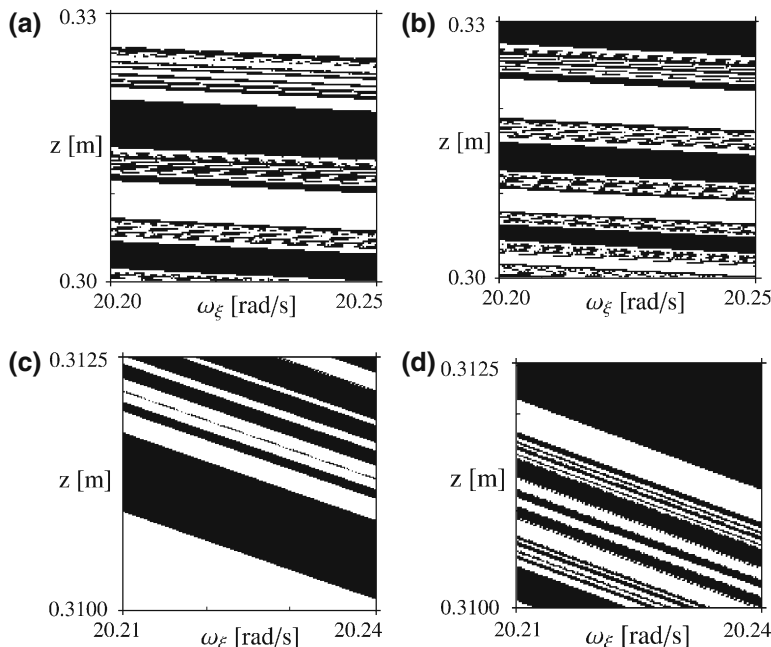


Fig. 4.54 Basins of attraction of heads (black) and tails (white). Two-dimensional model of an ideal thin coin described by (3.1), (3.6), (3.7), and (3.8) has been simulated; **(a,b)** enlargements of Fig. 4.53c; **(c,d)** enlargements of Fig. 4.53d; **(a,c)** air resistance neglected, and **(b,d)** air resistance considered $\lambda_n = 0.8$, $\lambda_\tau = 0.2$. Simulation results for $m = 0.002$ kg, $r = 0.0125$ m, $h = 0$, $J_\xi = 0.788 \times 10^{-7}$ kg m², $\vartheta_0 = \pi/5$ rad, $v(t = 0) = 0$, $\chi = 0.6$

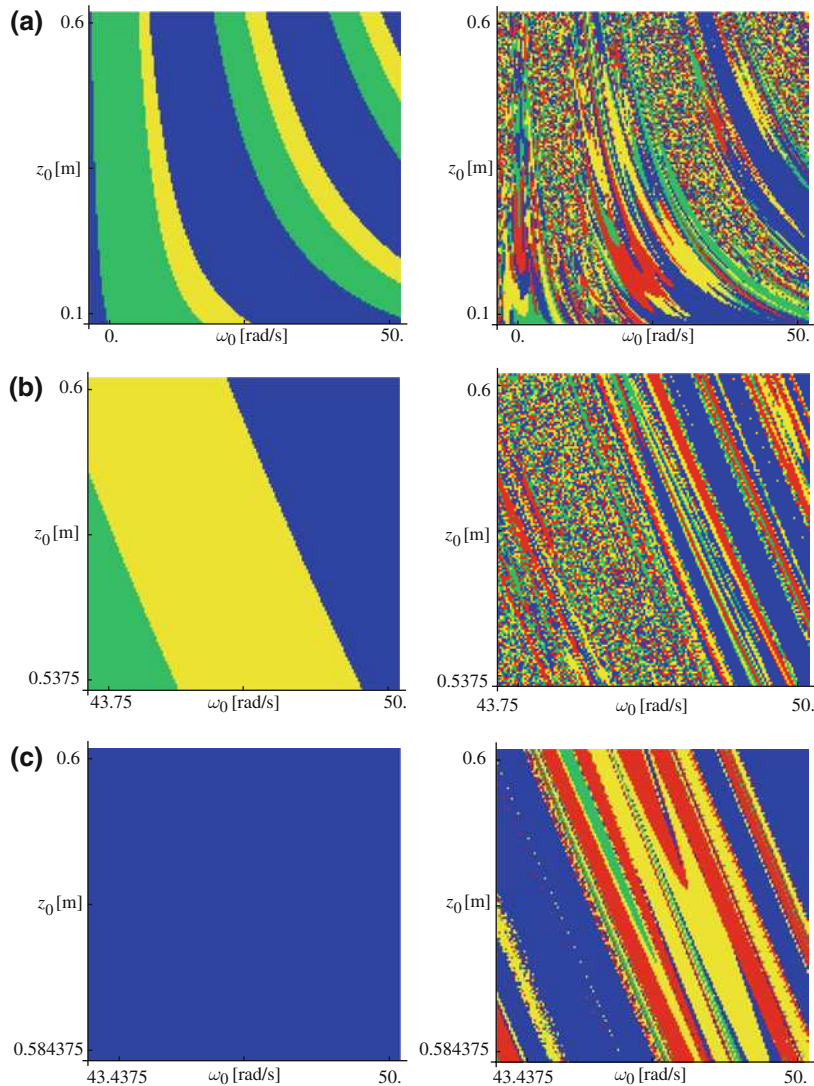


Fig. 4.55 Outcome results for tetrahedron die throw with basins of attraction for each of the die faces: **(a)** for parameter ranges $z_0 \in [0.1, 0.6]$ and $\omega_0 \in [0, 50]$; **(b)** for parameter ranges $z_0 \in [0.5375, 0.6]$ and $\omega_0 \in [43.75, 50] - 1/64$ of the area from **(a)**; and **(c)** for parameter ranges $z_0 \in [0.584375, 0.6]$, $\omega_0 \in [43.43475, 50] - 1/1024$ of the area from **(a)**. Further data: $m = 0.016$ kg, $a = 0.040793$ m, $J = 1.33125 \times 10^{-6}$ kg m², $\varphi_0 = 0.3$ rad, $\psi_0 = 1.2$ rad, $\vartheta_0 = 0.6$ rad, $v_{0x} = 1.4$ m/s, $\omega_\xi = 0$, $\omega_\eta = \omega_0$, $\omega_\zeta = 2.5$ rad/s, $\chi = 0.5$ (left column – free fall, right column – final results)

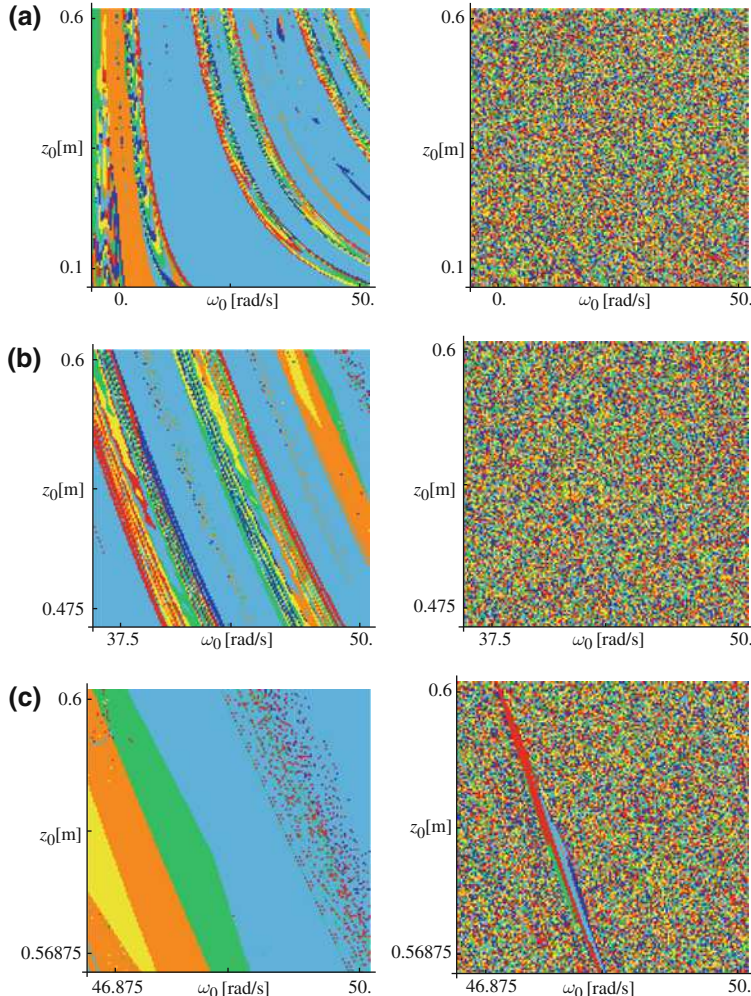


Fig. 4.56 Outcome results for cube die throw with basins of attraction for each of the die faces: **(a)** for parameter ranges $z_0 \in [0.1, 0.6]$ and $\omega_0 \in [0, 50]$; **(b)** for parameter ranges $z_0 \in [0.5375, 0.6]$ and $\omega_0 \in [43.75, 50]$ – $1/16$ of the area from **(a)**; and **(c)** for parameter ranges $z_0 \in [0.584375, 0.6]$, $\omega_0 \in [43.43475, 50]$ – $1/256$ of the area from **(a)**. Further data: $m = 0.016 \text{ kg}$, $a = 0.02 \text{ m}$, $J = 1.06667 \times 10^{-6} \text{ kg m}^2$, $\varphi_0 = 0.3 \text{ rad}$, $\psi_0 = 1.2 \text{ rad}$, $\vartheta_0 = 0.6 \text{ rad}$, $v_{0x} = 1.4 \text{ m/s}$, $\omega_\xi = 0$, $\omega_\eta = \omega_0$, $\omega_\zeta = 2.5 \text{ rad/s}$, $\chi = 0.5$ (Left column – die landing positions before the second collision, right column – final results)

structure of basins of attraction (after all collisions). For the cube die the result for free fall case (i.e., before first collision with the table) is the same in the whole range of initial conditions ($z_0 \in [0.1, 0.6]$ and $\omega_0 \in [0, 50]$). The left column in Fig. 4.56 contains the die landing positions before the second collision (more interesting than before the first collision) and the right column depicts the structure of basins for the

end result. Each next pair of diagrams represents zoom of previous ones. In the case of tetrahedron the successive zooms lead to an appearance of relatively uniform and separated regions of attraction (with nonzero Lebesgue measure) of given die faces (right map in Fig. 4.55c). Thus we can observe the “fractalization death” process due to the limited number of collisions, i.e., map iterations. However, increasing the number of faces (see the cube case shown in Fig. 4.56) causes that “fractalization death” effect is not so clearly visible like for the tetrahedron die in spite of large zoom (compare right column in Figs. 4.55c and 4.56c).

In the case of the roulette run one can observe that the initial conditions are not completely washout. Figure 4.52 shows that if the initial conditions are set with a finite inaccuracy the final result is predictable and repeatable. However this inaccuracy although finite has to be very small.

This allows us to state that *for almost any initial condition Φ there exists such $\varepsilon > 0$ that the ball with radius ε centered at Φ contains the points which belong only to one basin of attraction.* In other words, if one can settle the initial condition with appropriate accuracy, the outcome of the coin tossing procedure is predictable and repeatable.

This result is not correct when Φ lies on the basin boundary, but the set of initial conditions which is on the basin boundaries is of zero, or almost of a very small Lebesgue measure. As it has already been mentioned such initial conditions lead to unstable configurations such as a die or a coin balancing on the edge.

The data presented in this chapter show that the results of the coin toss, die throw, and roulette run are predictable in the sense of our Definition 1.1 and unfair by dynamics according to Definition 1.2. However Definition 1.1 is theoretical and in practice to obtain predictability one has to set the initial condition with such a small uncertainty that cannot be obtained in real experiments.

References

1. Strzałko, J., Grabski, J., Stefański, A., Perlikowski, P., Kapitaniak, T.: Dynamics of coin tossing is predictable. *Phys. Rep.* **469**, 59–92 (2008) 97
2. Keller, J.B.: The probability of heads. *Amer. Math. Monthly* **93**, 191 (1986) 101, 102, 103, 117, 137
3. Diaconis, P., Holmes, S., Montgomery, R.: Dynamical bias in the coin toss. *SIAM Rev.* **49**(2), 211–235 (2007) 102, 103, 104, 106, 107, 117
4. Feldberg, R., Szymkat, M., Knudsen, C., Mosekilde, E.: Iterated-map approach to die tossing. *Phys. Rev. A*, **42**(8), 4493–4502 (1990) 108, 109
5. Mosekilde, E.: Topics in Nonlinear Dynamics: Applications to Physics, Biology and Economic Systems. World Scientific, Singapore (1996) 108
6. Nagler, J., Richter, P.: How random is dice tossing? *Phys. Rev. E*, **78**, 036207 (2008) 110, 111
7. Wolfram, S.: The Mathematica Book, 5th edn. Wolfram Media, Inc., Champaign, IL (2004) 112
8. Weisstein, E.W.: Coin Tossing (from MathWorld: A Wolfram Web Resource.) <http://mathworld.wolfram.com/CoinTossing.html>. Cited 10 Apr 2009 112
9. Kapitaniak, T.: Generating strange nonchaotic attractors. *Phys. Rev. E* **47**, 1408 (1993) 114
10. Kapitaniak, T.: Distribution of transient Lyapunov exponents of quasi-periodically forced systems. *Prog. Theor. Phys.* **93**, 831 (1995) 114
11. Tel, T.: Transient chaos. *J. Phys. A* **22**, 691 (1991) 114

12. Isomaki, H. M., von Boehm, J., Raty, R.: Devil's attractors and chaos of a driven impact oscillator. *Phys. Lett.* **107A**, 343 (1985) 115
13. Isomaki, H. M., von Boehm, J., Raty, R.: Fractal basin boundaries of an impacting particle. *Phys. Lett.* **126A**, 484 (1988) 115
14. Mizuguchi, T., Suwashita, M.: Dynamics of coin tossing. *Progr. Theoret. Phys. Suppl.* **161**, 274 (2006) 117, 138
15. Vulović, V.Z., Prange, R.E.: Randomness of true coin toss. *Phys. Rev. A* **33/1**, 576 (1986) 117, 136, 138
16. Bhatia, N.P., Szego, G.P.: *Dynamical Systems: Stability Theory and Applications*. Springer, New York (1967) 136
17. Kechen, Z.: Uniform distribution of initial states. *Phys. Rev. A* **41**, 1893 (1990) 138

Chapter 5

Nature of Randomness in Mechanical Systems

Abstract We discuss the nature and origin of randomness in mechanical systems. We argue that nonsmoothness of the system plays a key role in the occurrence of dynamical uncertainties. The explanation why for practically small uncertainties in the initial conditions mechanical randomizer approximates the random process is given.

5.1 Randomness and Determinism

The essential property characterizing random phenomena is the impossibility of predicting any individual outcome. Generally, it is assumed that when we toss a coin, throw a die, or run a roulette ball this condition is fulfilled and all predictions have to be based on the laws of large numbers. In practice the only thing one can tell with a given degree of certainty is the average outcome after a large number of experiments.

However, in the previous chapters we show that the dynamics of the coin, die, or roulette ball can be described by the deterministic equations of motion. Knowing the initial condition with a finite accuracy ε , viscosity of the air, the value of the acceleration due to the gravity at the place of experiment, and the friction and elasticity factors of the ground one can predict the outcome. The predictability of the considered randomizer is based on Definition 1.1 (see p. 20) and the assumption that $\varepsilon > 0$. In real experiment the predictability is possible only for very small ε , i.e., for the accuracy which is practically extremely difficult to implement.

Another system that seems to be typically random is Brownian motion, i.e., the perpetual irregular motions of the small grains or particles of colloidal size immersed in a fluid, which were first noticed by the British botanist Brown in 1826. The irregular perpetual motion of a Brownian particle is the result of its collisions with molecules of the surrounding fluid. The colloidal particle is much bigger and heavier than the colliding molecules of the fluid, so that each collision has a negligible effect, but the superposition of many small interactions produces an observable effect. The molecular collisions of a Brownian particle occur in a very rapid succession and their number is tremendous. This frequency is too high and the small changes in the particle's path caused by each single impact are too fine to be

discerned by the observer. Thus, the exact path of the particle cannot be followed in any detail and this is the only reason why we have to consider this problem as the random phenomena, so we have a deterministic system that we cannot fully describe.

Typical mechanical phenomenon for which the description stochastic methods are used is vertical oscillations of a vehicle moving on a nonsmooth surface. But why is this system random? The answer is that we cannot drive twice on exactly the same line with identically the same velocity, and it is much simpler to consider a stochastic model.

Where else do we use stochastic processes in mechanical system? One case is modeling the responses of structures to earthquake, wind, etc., but again we do not know the full mechanism of these processes and their complete deterministic descriptions.

In all of the above random processes the system has been deterministic, and so in principle can be completely described. In practice, we are using stochastic processes as an approximate description of a deterministic system that has the unknown initial conditions and may have high sensibility to initial conditions.

When we try to identify and model the real systems sometimes we obtain as the result of the modeling process a model that shows very regular behavior while a real system has an irregular behavior. In that case we add random noise and this noise represents nothing more than our lack of knowledge of the system structure or of the identification procedure as it is described in Fig. 5.1.

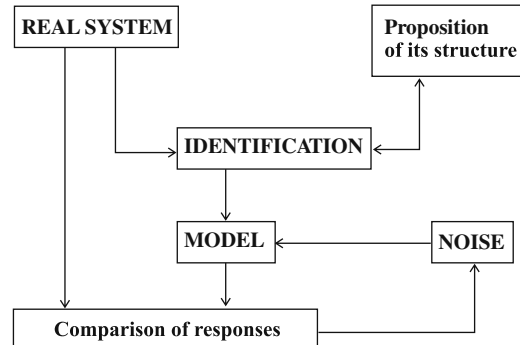


Fig. 5.1 Noise as a component of modeling

The same conclusion has been formulated by Pierre-Simon Laplace in his treatise on probability theory [1]:

If an intelligence knew at a given instant all the forces animating matter, as well as the position velocity of any of its molecules, and if moreover it was sufficiently vast to submit these data to analysis, it would comprehend in a single formula the movements of the largest bodies of the Universe and those of the tiniest atom. For such intelligence nothing would be irregular, and the curve described by an air or vapor molecule would appear to be governed in as precise a way as is for us the course of the Sun. But, due to our ignorance of all the data needed for the solution of this grand problem, and the impossibility, due to our limited abilities, of subjecting most of the data in our possession to calculation, even when

the amount of data is very limited, we attribute the phenomena that seem to us and succeed without any particular order to changeable and hidden causes, whose action is designated by the word chance, a word that after all is only the expression of our ignorance. Probability relates partly to this ignorance and in other parts to our knowledge.

In the early years of the previous century there was a general conviction that the laws of the universe were completely deterministic. The development of the quantum mechanics originating with the work of such physicists as Max Planck, Albert Einstein, and Louis de Broglie changes the Laplacian conception of the laws of nature as for the quantum phenomena the stochastic description is not just a handy trick, but an absolute necessity imposed by their intrinsically random nature. For the examples of quantum probability, see [1].

Currently, the vast majority of the scientists support the vision of a universe where random events of objective nature exist. Contradicting Albert Einstein's famous statement it seems that God plays dice after all. But going back to mechanical randomizers where quantum phenomena have at most negligible effect we can say that God does not play dice in the casinos.

5.2 Why the Tossed Coin or Die Can Approximate the Random Process?

The results presented in the previous chapters show that if the outcome of the long sequence of coin (die) tosses is to give random results, it can only be because the initial conditions vary from toss to toss. We show numerically that for each initial condition there exists the accuracy $\varepsilon > 0$ for which the final state is predictable. Now we try to explain why for practically small (but not infinitely small) ε the coin (die) tossing procedure can approximate the random process. Consider again Fig. 4.8. A sequence of coin tosses will be random if the uncertainty ε is large in comparison to the width W of the stripes characterizing the basins of attraction, so the condition $\varepsilon >> W$ is essential for the outcome to be random [2]. It is interesting to notice that uncertainty ε depends on the mechanism of coin tossing while the quantity W is determined by the parameters of the coin.

As it has been already shown in the case of the coin bouncing on the floor the structure of the heads and tails basin boundary becomes complicated (Fig. 5.2b-d) with the increase of impacts number. In Fig. 5.2a-d we show the calculations of these basins for different number of impacts n . The face of the coin which is up after the n th collision has been observed. The initial conditions leading to heads and tails are indicated, respectively, in black and white. The 2D model of an ideal thin coin described by (3.1), (3.6), (3.7), and (3.8) has been simulated. In Fig. 5.2a-d the air resistance has been considered while in Fig. 5.2e-h the air resistance has been neglected. Figure 5.2a,e; b,f; c,g; and d,h shows the results for, respectively, 0, 2, 4, and 9 collisions.

With the increase of the collision numbers it is possible to observe that the complexity of the basin boundaries increases with the number of impacts. The increase

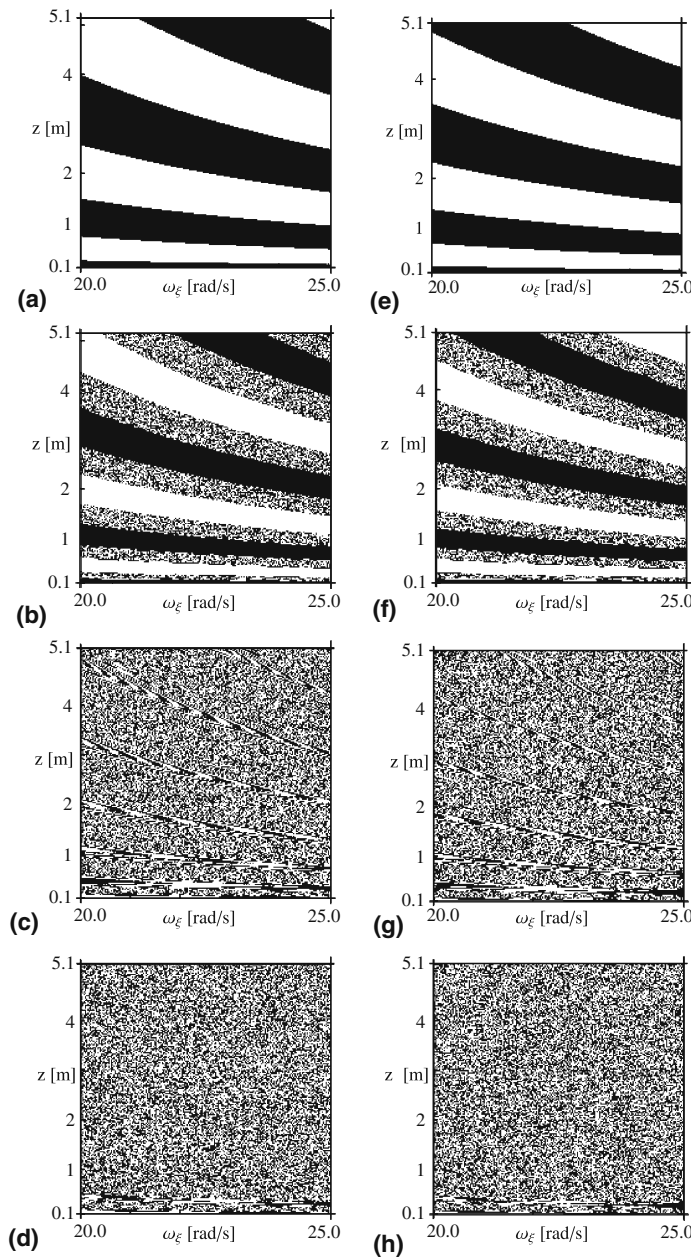


Fig. 5.2 Basins of attraction indicating the face of the coin which is up after n th collision ($\{F - C\}_n - F$). Two-dimensional model of an ideal thin coin described by (3.1), (3.6), (3.7), and (3.8) has been simulated. *Black* and *white* indicate, respectively, basins of heads and tails; (a,e) $n = 0$, (b,f) $n = 2$, (c,g) $n = 4$, (d,h) $n = 9$; (a-d) air resistance considered $\lambda_n = 0.8$, $\lambda_\tau = 0.2$, (e-h) air resistance neglected. Simulation results for $m = 0.002$ kg, $r = 0.0125$ m, $h = 0$, $J_\xi = 0.788 \times 10^{-7}$ kg m², $\vartheta_0 = \pi/5$ rad, $v(t = 0) = 0$, $\chi = 0.6$

of complexity is better visible when one considers the line in the phase space projection shown in Fig. 5.2a–d and counts the number of crossings from one basin to another one N . It is possible to show that the function $N(n)$ grows faster than the exponential. With the finite graininess (resolution) of Fig. 5.2a–d these basin boundaries look fractal and one can speak about fractalization-like process which can be observed with the increase of impacts. Sensitivity to the initial conditions introduced during the impacts (see Fig. 4.22) is responsible for this “fractalization.” It seems that this mechanism is similar to the fractalization route to strange non-chaotic dynamics [3].

To explain this process consider the limit case of the infinite number of impacts which is possible in unreal coin tossing model which neglects the air resistance and assumes the elastic impacts, i.e., $\chi = 1$. Consider the map $U : [0, 2\pi] \rightarrow [0, 2\pi]$ introduced in Sect. 4.3 shown in Fig. 5.3. The analysis of the time series of points ϕ_1, ϕ_2, \dots , shows that the dynamics of U is chaotic as the largest Lyapunov exponent is positive (equal to 0.08). In this limit case the basins of heads and tails are intermingled and the outcome of the coin tossing is unpredictable. Numerically, this can be observed when in the successive enlargements of the heads–tails basin boundaries the new structure is visible.

In the real case, the infinite number of impacts cannot be realized due to the dissipation (inelastic impacts and air resistance), so the fractalization-like process has to be stopped by the fulfillment of condition (4.22). The existence of the chaotic process described by the map U explains why the coins behave in practice as perfect randomizers.

The process of the coin bouncing on the floor has a significant influence on the final state (heads or tails). It has been observed that the successive impacts introduce sensitive dependence on the initial conditions leading to transient chaotic behavior.

The basin of attraction of heads and tails (the sets of the initial conditions leading to both outcomes) shows that the boundaries between heads and tails domains are

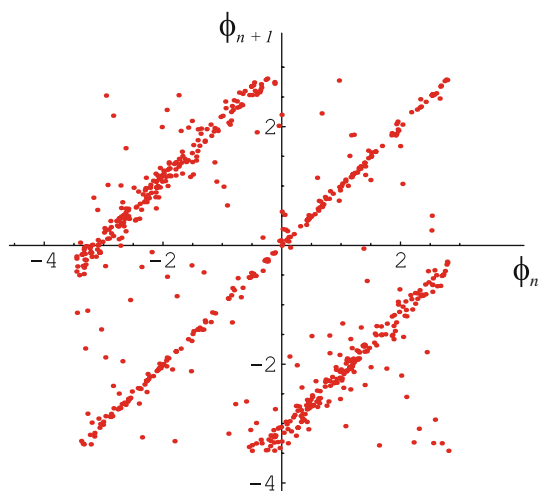


Fig. 5.3 Numerical simulation of the map U
 $\phi_n - \phi_{n+1}$;
 $\vartheta = 25.021 \cdot \pi / 180$
coefficient of restitution
 $\chi = 1$, air resistance
neglected, number of
collisions 700

smooth. This allows us to state our main result; there exists an open set of initial conditions for which the outcome of the coin tossing is predictable.

In practice, although heads and tails boundaries are smooth, the distance of a typical initial condition from a basin boundary is so small that practically any finite uncertainty in initial conditions can lead to the uncertainty of the result tossing. This is especially visible in the case of the coin bouncing on the floor, when with the increase of the number of impacts the basin boundaries become more complicated. In this case one can consider the tossing of a coin as approximately random process. Similar conclusions are valid for thrown dice (Fig. 4.56).

5.3 Why the Impacts Induce Pseudorandomness?

In all presented examples it has been shown that the impacts have a significant influence on the predictability of mechanical randomizers. With the increase of the number of impacts the accuracy in the initial conditions necessary for predicting the outcome increases rapidly. Now we explain why this occurs.

The equations of motion of the described mechanical randomizers belong to the class of the so-called piecewise-smooth systems (also known as the systems with discontinuities).

Definition 5.1. Consider the dynamical system

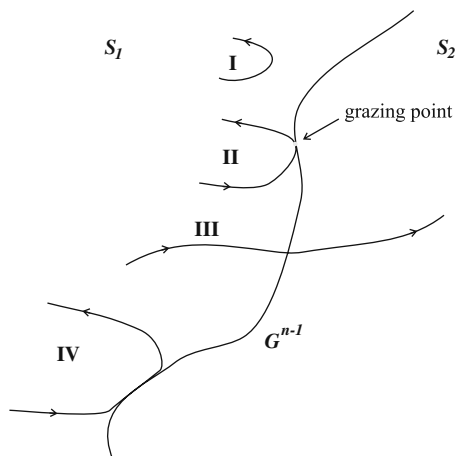
$$\frac{dx}{dt} = f(x, \eta), \quad (5.1)$$

where $x \in R^n$, $\eta \in R^m$ and assume that the function $f : R^{n+m+1} \rightarrow R$ is a piecewise-smooth function, t is a time variable, $\eta \in R^m$ a parameter vector, and $x \in r^n$ the state vector. Such a system is called a piecewise-smooth system or system with discontinuities.

Definition 5.2. The set of points in which the function f is not smooth is in the points $x \in G^{n-1}$, where G^{n-1} is $(n-1)$ -dimensional manifold $G^{n-1} \in R^n$ which consists of the points in which the function f is termed a switching manifold.

Manifold G^{n-1} is smooth and divides the phase space R^n into domains S_1, S_2, \dots with differently defined vector fields. Schematic description of the evolution of the phase space trajectory near a smooth switching manifold is shown in Fig. 5.4. For simplicity we assume that only two regions S_1 and S_2 with differently defined vector fields exist. The trajectory can evolve entirely in the region S_1 (case I), hit it tangentially at a grazing point (case II), cross the boundary and start evolving in the region S_2 (case III), or after hitting the boundary slides on it and return to evolve in the region S_1 (case IV). Case III is typical for the class of piecewise-linear systems. Case IV occurs when the vector field does not exist in the region S_2 . It is characteristic for the systems with impacts and in particular for the considered in this book mechanical randomizers.

Fig. 5.4 Schematic description of the evolution of the phase space trajectory near a smooth switching manifold



It is well known that systems like (5.1) can exhibit a plethora of complicated dynamical regimes. Several different bifurcation scenarios are known including the sudden transition from stable periodic motion to fully developed chaotic behavior [4–9]. In particular, a qualitative change of the system behavior is usually observed when a part of the system trajectory hits tangentially the switching manifold G^{n-1} . When this occurs the system is said to undergo a grazing bifurcation [10–17].

As it has been already stated in Sect. 1.7 mechanical randomizers cannot show chaotic behavior as its evolution is finite due to the energy dissipation. In this case the phenomena connected with the grazing bifurcation result in the occurrence of the transient chaos and fractalization of the boundaries between basins of the different final configurations.

References

1. Marques de Sa, J.P.: *Chance: The Life of Games and the Game of Life*. Springer, Berlin (2008) 144, 145
2. Vulović, V.Z., Prange, R.E.: Randomness of true coin toss. *Phys. Rev. A* **33**(1), 576 (1986) 145
3. Datta, S., Ramakrishna, R., Prasad, A.: Fractalization route to strange nonchaotic dynamics. *Phys. Rev. A* **70**, 046203 (2004) 147
4. Shaw, S., Holmes, P.: Periodically forced linear oscillator with impacts: Chaos and long-periodic motions. *Phys. Rev. Lett.* **51**, 623–626 (1983) 149
5. Thompson, J., Ghaffari, R.: Chaotic dynamics of an impact oscillator. *Phys. Rev. A* **27**, 1741–1743 (1983) 149
6. Peterka, F.: Part 1: Theoretical analysis of n-multiple (l/n)-impact solutions. *CSAV Acta Technica* **26**(2), 462–473 (1974) 149
7. Brogliato, B.: *Nonsmooth Mechanics*. Springer Verlag, London (1999) 149
8. Feigin, M.I.: Fundamental dynamic models and criteria of C-bifurcation structures for piecewise smooth systems. In *Proceedings of the International Symposium on Analysis and Synthesis of Nonlinear Dynamical Systems*, pp. 30–40. Riga, Latvia (1996) 149
9. Isomaki, H.M., von Boehm, J., Raty, J.: Devils attractors and chaos of a driven impact oscillator. *Phys. Lett. A* **107**, 343–346 (1985) 149

10. Nordmark, A.B.: Non-periodic motion caused by grazing incidence in impact oscillators. *J. Sound Vib.* **2**, 279–297 (1991) 149
11. Nordmark, A.: Universal limit mapping in grazing bifurcations. *Phys. Rev. E* **55**, 266–270 (1997) 149
12. Nusse, L.E., Yorke, J.A.: Border-collision bifurcations including period two to period three for piecewise smooth systems, *Physica D* **57**, 39–57 (1992) 149
13. Frederiksson, M., Nordmark, A.: Bifurcations caused by grazing incidence in many degrees of freedom impact oscillators. *Proc. R. Soc. London, Ser. A* **453**, 1261–1276 (1997) 149
14. Frederiksson, M., Nordmark, A.: On normal form calculations in impact oscillators. *Proc. R. Soc. London, Ser. A* **456**, 315–329 (2000) 149
15. di Bernardo, M., Champneys, A.R., Budd, C.J.: Grazing, skipping and sliding: Analysis of the nonsmooth dynamics of the DC/DC buck converter. *Nonlinearity* **11**, 858–890 (1998) 149
16. di Bernardo, M., Feigin, M., Hogan, S., Homer, M.: Local analysis of C-bifurcations in n-dimensional piecewise smooth dynamical systems. *Chaos, Solitons Fractals* **10**, 1881–1908 (1999) 149
17. Feigin, M.I.: The increasingly complex structure of the bifurcation tree of a piecewise-smooth system. *J. Appl. Maths. Mech.* **59**, 853–863 (1995) 149

Index

A

Air resistance, 18, 23, 25, 36, 37, 42, 46, 48, 53, 56, 57, 62, 63, 68, 71, 83, 112, 113, 145, 147
coefficients, 47, 60
force, 36, 37, 43, 47, 50–53, 83, 97
moment, 43, 52, 53, 55, 56, 58, 59, 83, 84

B

Basin, 18, 146
of attraction, 19, 20, 97, 112, 118, 123, 136–141, 145, 147
boundary, 19, 20, 97, 136–138, 141, 145, 147, 148
intermingled, 147
Body dynamics
equations, 23
Buffon's needle, 14–16

C

Chaos, 149
Chaotic, 6, 18, 147
behavior, 18, 115, 116, 147, 149
Coefficient of restitution, 37
Collision, 16, 23
of bodies, 37–39
elastic, 38
time, 38

E

Euler
angles, 23, 26, 31–34, 45
parameters, 23, 34, 35, 42–44, 46, 64

F

Fair
coin, 6, 7
by continuity, 9
die, 7

by dynamics, 21

by symmetry, 7

tossed coin, 107, 111

Fractal basin boundary, 18–20, 97, 138, 147

Fractalization, 118, 141, 147, 149

G

Grazing, 148
bifurcation, 149

I

Ideal coin, 7, 27, 45, 46, 56, 57, 67, 101, 105, 107, 112, 113

Imperfect coin, 7, 41, 43–46, 64, 112–114

Inertia

matrix, 41, 44

Products, 67

Intermingled
basin of attraction, 21
Isohedra, 7, 8, 67, 68

L

Lyapunov exponent, 18, 113, 116, 147

M

Moment of inertia, 27, 46, 58, 63, 67, 68, 74
Momentum, 11, 17, 19, 117, 136
angular, 17, 19, 23, 25–30, 38, 117, 136
linear, 23, 25, 38

N

Newton's
hypothesis, 64, 69, 70, 74
law, 71
Newton-Euler
equations, 19, 25, 42, 67, 68, 136
laws, 41
Noise, 144

P

Pinball machine, 14, 16, 17
Precession, 26, 27, 29, 30, 55, 105–107, 111
Predictability, 18, 21, 141, 143, 148
Probability, 2, 5, 6, 9, 11, 13–16, 19, 103, 104,
 107, 108, 118, 120–126, 136, 144, 145
Product of inertia, 41, 44

Q

Quaternions, 23, 26, 34, 35, 42

R

Randomizer, 1, 14, 17–21, 41, 46, 143, 145,
 147, 148
Riddled
 basin of attraction, 21
Rolling, 4, 71, 72, 74–77, 79, 87, 90, 92

U

Unpredictability, 18, 20, 115